

NASA Contractor Report 187068

LEWIS GRANT  
IN-34

330112  
P.266

# Experimental Study of Boundary Layer Transition With Elevated Freestream Turbulence on a Heated Flat Plate

Ki-Hyeon Sohn and Eli Reshotko  
*Case Western Reserve University  
Cleveland, Ohio*

February 1991

Prepared for  
Lewis Research Center  
Under Grant NAG3-230

**NASA**

National Aeronautics and  
Space Administration

(NASA-CR-187068) EXPERIMENTAL STUDY OF  
BOUNDARY LAYER TRANSITION WITH ELEVATED  
FREESTREAM TURBULENCE ON A HEATED FLAT PLATE  
Final Report (Case Western Reserve Univ.)  
266 p

N91-17341

CSCD 20D 65/34

Unclass  
0330112



EXPERIMENTAL STUDY OF BOUNDARY LAYER TRANSITION WITH  
ELEVATED FREESTREAM TURBULENCE ON A  
HEATED FLAT PLATE

Ki-Hyeon Sohn and Eli Reshotko  
Case Western Reserve University  
Department of Mechanical and Aerospace Engineering  
Cleveland, Ohio 44106

**ABSTRACT**

A detailed investigation to document momentum and thermal development of boundary layers undergoing natural transition on a heated flat plate was performed. Experimental results of both overall and conditionally sampled characteristics of laminar, transitional and low Reynolds number turbulent boundary layers are presented. Measurements were acquired in a low-speed, closed-loop wind tunnel with a freestream velocity of 100 ft/s and zero pressure gradient over a range of freestream turbulence intensities (TI) from 0.4% to 6%.

The distributions of skin friction, heat transfer rate and Reynolds shear stress were all consistent with previously published data. Reynolds analogy factors for  $Re_\theta < 2300$  were found to be well predicted by laminar and turbulent correlations which accounted for an unheated starting length. The measured laminar value of Reynolds analogy factor was as much as 53% higher than  $Pr^{2/3}$ . A small dependence of turbulent results on TI was observed.

Conditional sampling performed in the transitional boundary layer indicated the existence of a near-wall drop in intermittency, pronounced at certain low intermittencies, which is consistent with the cross-sectional shape of turbulent spots observed by others. Non-turbulent intervals were observed to possess large magnitudes of near-wall unsteadiness and turbulent intervals had peak values as

much as 50% higher than were measured at fully turbulent stations. Non-turbulent and turbulent profiles in transitional boundary layers cannot be simply treated as Blasius and fully turbulent profiles, respectively. The boundary layer spectra indicate predicted selective amplification of T-S waves for  $TI \approx 0.4\%$ . However, for  $TI \approx 0.8\%$  and  $1.1\%$ , T-S waves are localized very near the wall and do not play a dominant role in the transition process.

## **ACKNOWLEDGEMENTS**

Our most sincere thanks to **Dr. James O'Brien** and **Dr. Khairul Zaman** of the **NASA Lewis Research Center** for their valuable advice and guidance with the facility, instrumentation and experimental techniques utilized in this work.

This study was supported by the **NASA Lewis Research Center** under grant number **NAG 3-230**.

## TABLE OF CONTENTS

	Page
Abstract	i
Acknowledgements	iii
Nomenclature	viii
CHAPTER I <u>INTRODUCTION</u>	1
CHAPTER II <u>EXPERIMENTAL FACILITY AND INSTRUMENTATION</u>	10
2.1 WIND TUNNEL	10
2.1.1 Flow conditioner/Turbulence grids	11
2.1.2 Test section/Heated surface	12
2.1.3 Probe traversing mechanism	14
2.2 INSTRUMENTATION	15
2.2.1 Test section instrumentation	16
2.2.2 Probes/Anemometers	16
2.2.3 Data acquisition equipment	19
CHAPTER III <u>EXPERIMENTAL PROCEDURE</u>	21
3.1 ESTABLISHMENT OF OPERATING CONDITIONS	21
3.2 PROBE CALIBRATION	22

3.2.1	Velocity-voltage calibration	22
3.2.1.1	Single-wire probe	22
3.2.1.2	Miniature 3-wire probe	23
3.2.2	Temperature calibrations	26
3.2.2.1	Single-wire probe	26
3.2.2.2	Temperature sensor of the 3-wire probe	26
3.2.3	Time constant of temperature sensor	28
3.3	MEASUREMENTS OF OVERALL VELOCITY/TEMPERATURE	29
3.4	HEAT TRANSFER MEASUREMENTS	30
3.5	HIGH-SPEED DATA ACQUISITION	30
3.6	SPECTRAL DATA ACQUISITION	31
CHAPTER IV	<u>DATA REDUCTION</u>	33
4.1	MOMENTUM BOUNDARY LAYER ANALYSIS	33
4.1.1	Mean velocity profiles	33
4.1.2	Determination of friction velocity	36
4.2	THERMAL BOUNDARY LAYER ANALYSIS	38
4.2.1	Heat transfer	38
4.2.2	Mean temperature profiles	39
4.2.3	Energy balance	42
4.3	COMPENSATION OF TEMPERATURE SENSOR	43
4.3.1	Thermal energy balance in a wire	43

4.3.2	Experimental determination of time constant	45
4.4	TEMPERATURE CORRECTION FOR CONSTANT TEMPERATURE BRIDGE OUTPUT VOLTAGE	46
4.5	CONDITIONAL SAMPLING TECHNIQUE	48
CHAPTER V	<u>RESULTS AND DISCUSSION</u>	51
5.1	FREESTREAM TURBULENCE INTENSITY	51
5.2	MOMENTUM BOUNDARY LAYER	52
5.2.1	Mean velocity profiles	52
5.2.2	Skin friction	55
5.2.3	Momentum integral quantities	58
5.2.4	Streamwise rms velocity profiles	60
5.2.5	Conditionally sampled profiles	63
5.2.5.1	Intermittency factor	64
5.2.5.2	Conditionally sampled mean velocity profiles	66
5.2.5.3	Conditionally sampled rms velocity profiles	70
5.2.6	3-wire measurements	75
5.2.6.1	Vertical component of rms velocity	76
5.2.6.2	Reynolds shear stress	78
5.3	THERMAL BOUNDARY LAYER	81
5.3.1	Mean temperature profiles	81
5.3.2	Heat transfer measurements	84

5.3.3 Reynolds analogy factor	86
5.3.4 Thermal energy balance	88
5.3.5 3-wire measurements	89
5.3.5.1 RMS temperature profiles	91
5.3.5.2 Turbulent heat flux	92
5.4 BOUNDARY LAYER SPECTRA	97
CHAPTER VI <u>SUMMARY AND CONCLUSIONS</u>	109
References	115
Tables	121
Figures	127

## NOMENCLATURE

A	Constants in thermal response equations of hot-wire [eq. 4-32, 4-37]
B	
$C_1$	Calibration constants in equation for time constant [eq. 4-35]
$C_2$	
$C_f$	Skin friction coefficient
$c_p$	Specific heat at constant pressure
$E_L$	Linearized voltage
f	Disturbance frequency
$f'(\eta)$	Blasius similarity variable [= $U / U_\infty$ ]
H	Shape factor
h	Heat transfer coefficient
i	Wire current
K	Yaw factor of Champagne's law [eq. 3-2]
k	Thermal conductivity
$l_w/d_w$	Length-to-diameter ratio of wire
$l_w^+$	Wire length normalized in wall units [= $u_\tau l_w / \nu$ ]
M	Time constant of temperature wire
Nu	Nusselt number [= $h X / k$ ]
OHR	Overheat ratio of hot-wire
Pr	Molecular Prandtl number [= $\mu c_p / k$ ]

$Pr_t$	Turbulent Prandtl number
PSD	Power spectral density [= $V^2 / \text{Hz}$ ]
$q_w''$	Wall heat flux
$Re_x$	Length Reynolds number [= $U_e X / \nu$ ]
$Re_\theta$	Momentum thickness Reynolds number [= $U_e \theta / \nu$ ]
$Re_{\delta^*}$	Displacement thickness Reynolds number [= $U_e \delta^* / \nu$ ]
$r_o$	Radius of wire
$R_w$	Resistance of wire at wire temperature, $T_w$
$R_a$	Resistance of wire at air temperature, $T_a$
$R_o$	Resistance of wire at reference temperature, $T_o$
S	Spanwise separation of the wires of the 3-wire probe [= 0.52 mm]
$S^+$	S in wall units [= $u_\tau S / \nu$ ]
St	Stanton number [= $h / \rho c_p U_e$ ]
$2 St/C_f$	Reynolds analogy factor
T	Instantaneous or mean temperature, depending on context
$T_o$	Reference temperature
$T_\tau$	Friction temperature [= $q_w'' / \rho c_p u_\tau$ ]
$T^+$	Mean temperature in wall units [= $(T_w - T) / T_\tau$ ]
t	Time
$t'$	Instantaneous or rms fluctuating temperature, depending on context
TI	Streamwise freestream turbulence intensity
U	Instantaneous or mean streamwise velocity, depending on context

$U_o$	Magnitude of actual velocity
$U_{eff}$	Effective cooling velocity
$u_r$	Friction velocity [= $(\tau_w / \rho)^{1/2}$ ]
$u^+$	Streamwise mean velocity in wall units [= $U / u_r$ ]
$u'$	Instantaneous or rms streamwise fluctuating velocity, depending on context
$V$	Bridge voltage of the hot-wire anemometer or instantaneous vertical velocity, depending on context
$v'$	Instantaneous or rms vertical fluctuating velocity, depending on context
$-\overline{u'v'}$	Reynolds shear stress
$\overline{v't'}$	Turbulent heat flux
$X$ or $x$	Streamwise distance from the leading edge of the test plate
$X_o$	Unheated starting length [= 1.375 inches]
$y$	Vertical distance from the wall
$Y_o$	Typical distance between the wall and the first measurement location
$y^+$	Vertical distance in wall units [= $u_r y / \nu$ ]

### Greek

$\alpha$	Temperature coefficient of resistance
$\Gamma$	Intermittency factor
$\Delta_2$	Enthalpy thickness

$\delta_{.995}$	Boundary layer thickness when $U = 0.995 U_e$
$\delta^*$	Integral displacement thickness
$\eta$	Hartree or Blasius similarity variable [= $y (U_e / 2\nu x)^{1/2}$ ]
$\Theta$	Mean temperature in outer coordinates [= $(T-T_e) / (T_w-T_e)$ ]
$\theta$	Integral momentum thickness
$\nu$	Kinematic viscosity
$\xi$	Instantaneous flow angle between $U_e$ and $U$ [see Fig. 8]
$\Pi$	Wake strength
$\rho$	Density
$\tau_w$	Wall shear stress
$\phi$	Angle between normal to the wire and $U_e$ [see Fig. 8]

### **Subscripts**

a	Evaluated at air temperature, $T_a$
e	At the edge of the boundary layer or at freestream
w	At the wall or of wire, depending on context
n	Non-turbulent part of the conditionally sampled quantities
o	Overall quantities
t	Turbulent part of the conditionally sampled quantities



## **CHAPTER I**

### **INTRODUCTION**

The understanding of boundary layer development under the influence of a highly disturbed freestream is important for many engineering applications. This is especially so for turbine blades of aircraft gas turbine engines. Heat transfer rates from hot gases to cooled turbine blades are largely dependent on whether the boundary layer is laminar, transitional or turbulent. Since boundary layer transition is characterized by a significant increase of skin friction and heat transfer rate, the determination of the transition location on the turbine blade becomes necessary to accurately predict local heat transfer rates and then to properly assess the cooling requirements for the turbine blade (Graham, 1979). On turbine blades, the transition process is protracted so that appreciable portions of the cooled surface are transitional. Heat transfer measurements by Turner (1971) indicated that transitional behavior was observed over about 80% of the suction side of a typical turbine blade for a freestream turbulence level of 5.9%. The accurate prediction of the transition pattern leads directly to the improvement of engine efficiency and hardware durability. More reliable information from systematic and well-controlled experiments are required to

provide fundamental information for improved modeling and computation of boundary layer transition as it occurs in turbomachinery. This is the motivation of the current work.

Boundary layer transition in a low disturbance flow is characterized by an initial amplification of linear 2D Tollmien-Schlichting (T-S) waves followed by secondary instabilities leading to the formation of 3D vortices and the subsequent development of turbulent spots and the turbulent flows. In a relatively quiescent environment, the rate at which the transition process proceeds is related to the growth rate of infinitesimal disturbances as described by linear considerations. The non-linear processes completing the transition occur rapidly and do not have much effect on the length to transition. Linear stability theory has been used to predict the critical Reynolds number, above which the selective amplification of disturbances may occur, and the growth rates of the amplified disturbances. The classical experiment performed by Schubauer & Skramstad (1948) with a very low freestream disturbance level of 0.03% was the first to clearly demonstrate the behavior of T-S waves in laminar flow. Following the linear 2D T-S waves, at least three types of 3D non-linearity can develop, depending on the magnitude reached by the primary amplified waves. These are peak-to-peak K-type observed by Klebanoff, Tidstrom & Sargent (1962), and either of two peak-to-valley staggered patterns, the H-type (Herbert) and the C-type (Craik).

However, for highly disturbed freestreams, the initial disturbance level is large enough to be considered non-linear so that amplification of linear T-S

waves is bypassed and the formation of turbulent spot occurs directly. Morkovin (1979) introduced the term bypass transition to describe the transition process which occurs in the presence of initially finite non-linear disturbances. The archetypical example of the bypass phenomenon is the transition in a fully developed Poiseuille pipe flow. In the experimental studies of Wignanski & Champagne (1973) and Wignanski, Sokolov & Friedman (1975), the formation of turbulent puffs were found in the range of  $Re_D$  less than 3000 due to large disturbances introduced into the entrance section, otherwise the flow is laminar. In highly disturbed flows as expected in gas turbine environments where freestream turbulence levels may be up to 20% no experimental study of boundary layer transition is available. Dyban, Epik & Suprun (1976) conducted an experiment in a very slow air flow to characterize the laminar boundary layer for freestream turbulence levels ranging from 0.3% to 25.2%. From the rms disturbance profiles measured in the boundary layer, they concluded that the depth of penetration of freestream disturbances into the boundary layer was not dependent on the freestream turbulence levels but only on the Reynolds number. The perturbation peak in the laminar boundary layer was highest at 4.41% of freestream turbulence level. They referred to this laminar boundary layer in the presence of high levels of freestream turbulence as a pseudo-laminar boundary layer.

Besides freestream turbulence level, there are many other factors affecting the boundary layer transition. They are: 1) the profile modifiers such as

pressure gradient, suction, blowing, surface curvature, surface temperature and bluntness, 2) the vehicle factors such as surface roughness and surface vibration, and 3) other environmental factors such as acoustic disturbances. The elements of boundary layer transition in quiescent environments have been summarized by Tani (1968) for the low speed regime, and by Reshotko (1976) for a rather broad range of speeds including the issues of boundary layer stability and receptivity. A general description together with a practical method for predicting transition in quiescent 2D incompressible flow was also presented by Arnal (1984).

Previous studies of the influence of pressure gradient and heat transfer rate as well as freestream disturbances on boundary layer transition were primarily concerned with the mean overall characteristics of intermittent boundary layers. In order to isolate the above three effects from many other possible parameters affecting transition, numerous analytical and experimental studies have focused on the flat plate case. Some empirical relations including the effects of freestream disturbance and pressure gradient were developed by van Driest & Blumer (1963), Hall & Gibbings (1972) and Abu-Ghannam & Shaw (1980), adjusting several constants from existing experimental data. The prediction of onset and end of the transition region was also proposed.

The effects of heat transfer in addition to freestream turbulence level and pressure gradient were considered experimentally by Junkhan & Serovy (1967) on a heated constant temperature wall, by Blair (1982) on a uniformly heated flat plate and by Rued & Wittig (1985) on a cooled isothermal wall. They observed

that the effect of heat transfer on boundary layer transition is not significant compared to the corresponding effects of freestream turbulence and pressure gradient. Transition Reynolds number was relatively insensitive to wall heat transfer rate and mild acceleration of the flow. Gaugler (1985) has summarized a number of bypass transition data sets that include the effects of heat transfer, covering a wide range of flow conditions and indicating strong effects of freestream turbulence level and pressure gradient on the location and length of the transition zone. He concluded that the transition length appeared to depend strongly on the freestream parameters within the zone rather than just on the conditions at the start of transition. McDonald & Fish (1973) developed a computational technique to predict transition behavior under the influence of surface roughness and curvature in addition to the effects of freestream turbulence level, pressure gradient and heat transfer with the solution procedure depending on the calculation of the streamwise development of a turbulent mixing length. Their results were in good agreement with the available experimental data. A general review of transition mechanisms (T-S and bypass modes) and of the prediction and control of transition was presented by Reshotko (1986).

Many studies have been conducted to recognize the intermittent character of laminar breakdown in a boundary layer. The turbulent spot was first observed by Emmons (1951). He also formulated a theory based on probability considerations, suggesting that the spot production process may occur randomly

throughout the boundary layer. Due to lack of experimental evidence, he simply proposed a constant spot production function. The existence of turbulent spots in boundary layer flow has been confirmed experimentally by Schubauer & Klebanoff (1955). Dhawan & Narasimha (1958) further developed the turbulent spot theory of Emmons (1951) by correcting the constant spot production function to the form of a delta function, based on the observation that laminar breakdown in a 2D flat plate boundary layer is very nearly point-like and the spots originate in only a restricted region. They also proposed the first simplified transition zone model for predicting the mean quantities based on intermittency, treating the non-turbulent part of the transitional flow as an extension of theoretical laminar flow and the turbulent part as the fully turbulent flow. This transition zone model has been widely accepted for simply predicting the skin friction and heat transfer in the transitional flow.

Detailed studies of individual turbulent spot structures have been performed by many researchers. The turbulent spot was generated artificially in otherwise laminar boundary layers by Wygnanski, Sokolov & Friedman (1976) and Antonia, Chambers, Sokolov & van Atta (1981) using the technique of electric sparks and by Cantwell, Coles & Dimotakis (1978) using small jets of short duration. Although the results of these studies played a big role in understanding turbulent spot structure in the transitional flow, they are applicable only in the very early stages of transition, before mixing of multiple turbulent spots occurs.

Limited results of conditional sampling in a transitional boundary layer were first reported by Arnal, Juillen & Michel (1978). They observed that a large fraction of a near-wall peak of overall streamwise velocity fluctuations are associated with the switching between the two significantly different mean levels of non-turbulent and turbulent flows. Several other very recent studies of Blair (1988) for mildly accelerating flow, of Kuan & Wang (1988) and Kim, Simon & Kestoras (1989) for flat plate boundary layer flow focused additionally on determination of the separate statistics of the non-turbulent and turbulent parts of the transitional boundary layer using conditional sampling techniques. Results of these studies clearly indicated that the non-turbulent and turbulent parts in the transitional flow cannot be thought of respectively as Blasius and fully turbulent flows. A review of the conditional sampling technique was presented by Antonia (1981).

The purposes of the present study are to experimentally document some of the characteristics of the naturally occurring boundary layer transition on a heated flat plate and to provide a well-controlled set of experimental data for improvement of transition modeling accounting for effects of freestream turbulence intensity and heat transfer rate. The present work is a continuation of previous studies initiated by Paik & Reshotko (1986) and Sohn & Reshotko (1986). In the former work the focus was shifted to the study of low Reynolds number turbulent boundary layers since the transition zone was too close to the leading edge to be measurable. In the latter study (Sohn & Reshotko, 1986) the

mean characteristics of bypass transition on an unheated flat plate were documented for a freestream turbulence level of 1.6%. The effects of freestream turbulence intensities ranging from 0.3% to 5% on boundary layer transition were investigated separately at NASA Lewis Research Center by Suder, O'Brien & Reshotko (1988) for an unheated flat plate in the same facility as used in the present study. They observed naturally generated T-S waves near the wall leading to transition for the lowest freestream turbulence level. However, the bypass mode was observed for freestream turbulence levels of 0.7% and above. The overall characteristics of the momentum boundary layer only were obtained by Sohn & Reshotko (1986) and by Suder, O'Brien & Reshotko (1988).

The present experimental study was conducted on a uniformly heated flat plate with zero pressure gradient for freestream turbulence intensities ranging from 0.4% to 6%. The first part of this experimental program is to document the momentum and thermal mean characteristics of laminar, transitional and low Reynolds number turbulent boundary layers. In addition to mean and rms velocity and temperature profiles, the Reynolds analogy factors are determined from skin friction information and surface heat transfer rates in the range of  $Re_\theta$  less than 2300 for six levels of freestream turbulence. Boundary layer spectra are also obtained to identify the nature of the transition process. To establish a better understanding of boundary layer transition, conditional sampling is applied to segregate the digitally recorded velocity signal into non-turbulent and turbulent parts. Conditionally sampled mean and rms velocity profiles as well as the

distribution of intermittency factor across the boundary layer are measured for two freestream turbulence levels of 1.1% and 2.4%. The results for freestream turbulence level of 1.1% (grid 1), in which the mean velocity and temperature profiles nearly span the entire transition from laminar to turbulent were summarized and presented by Sohn, O'Brien & Reshotko (1989). The second part examines correlations of instantaneous velocities and temperature measured simultaneously with a miniature 3-wire probe. Overall and conditionally sampled Reynolds shear stress and turbulent heat flux are obtained and discussed.

## **CHAPTER II**

### **EXPERIMENTAL FACILITY AND INSTRUMENTATION**

#### **2.1 WIND TUNNEL**

The experiments were performed in a low-speed, closed-circuit wind tunnel located at the NASA Lewis Research Center. This wind tunnel was designed to generate large-scale, two-dimensional, incompressible boundary layers and to study the effects of freestream turbulence, pressure gradient and heat transfer rates on the transitional boundary layer. A schematic of the wind tunnel is shown in Figure 1. This wind tunnel is similar to that of Blair et al. (1981) in design. The wind tunnel consists of 9 units which are 1) blower, 2) flow conditioner with turbulence grids, 3) two dimensional contraction nozzle, 4) bleed scoops, 5) test section with heated surface, 6) diffuser, 7) air heater, 8) air filter, 9) air cooler. The air velocity, temperature, pressure gradient and turbulence intensity in the test section can be controlled through adjustment of various components of the wind tunnel. This wind tunnel was used by Suder et al. (1988) for the experimental study of bypass transition in an unheated boundary layer.

### **2.1.1 Flow conditioner/Turbulence grids**

The tunnel is driven by a Chicago Blower Corporation, SISW Class III SQA centrifugal fan with a capacity of 10,000 CFM. Flow rate is controlled by a vortex valve located at the inlet of the blower. Upon exiting the blower, the air enters the flow-conditioning plenum chamber, where any flow irregularities introduced by the blower are removed and the freestream turbulence levels are reduced. This plenum chamber consists of the following: 1) perforated plate baffles, which force the highly nonuniform flow from the blower to spread across the entire plenum, 2) a series of honeycombs and soda straws to straighten the flow, and 3) a series of fine-mesh damping screens. A honeycomb-screen combination can produce a lower exit turbulence intensity than a honeycomb alone can, since the large-scale flow exiting from the honeycomb cells are broken into smaller scale eddies through the screens.

At the downstream end of the flow-conditioning chamber and upstream of the contraction nozzle, turbulence generating grids could be positioned to set the freestream turbulence in the test section. The benefits of this arrangement are that the grid-generated turbulence would be more homogeneous and have a lower decay rate along the test section since the effective distance from the grid to the test section entrance is increased (Blair et al., 1981). The turbulence grids are made up of rectangular-bar arrays with approximately 62% open area. The shape of the resulting mesh is square. The mesh size of the opening for grids 1 to 4 are 0.69-inch, 2.06-inch, 5.50-inch, and 7.0-inch respectively. With four

different turbulence grids (Grids 1 to 4), an arrangement of a 20 mesh screen just downstream of the grid 1 (Grid 0.5), and without any grids (Grid 0), six different turbulence intensities in the test section ranging from 0.4% to 6% can be achieved. For a more detailed description of the wind tunnel components and turbulence grid configurations, refer to the paper by Suder et al. (1988).

### **2.1.2 Test section/Heated surface**

The test section of the wind tunnel is rectangular in cross section and measures 27 inches wide, 60 inches long and 6 inches high. The test section consists of the flat lower wall of the tunnel instrumented for heat transfer measurements which serves as the boundary layer test surface, two vertical plexiglass sidewalls and a hinged upper wall. The upper wall is made up of a stainless steel frame holding three interchangeable panels: one probe-traversing mechanism and two plexiglass sections. The upper wall is hinged at the top of inlet frame. It can thus be pivoted to control the pressure gradient in the test section. In this study, the upper wall was adjusted for zero pressure gradient through the test section by monitoring static pressure tap readings on the test surface.

At the entrance to the test section, a double bleed scoop assembly is positioned. A sketch showing details of the scoop configuration is presented in Figure 2. The large scoop is intended to remove both the boundary layer which develops along the contraction nozzle and the vortices which develop in the

contraction corners. The small scoop, smoothly attached to the test surface, serves as the leading edge of the flat plate, which is a 4:1 ellipse. This arrangement results in a 1.375-inch unheated starting length. This small scoop bleeds off any boundary layer which develops on the large scoop. As shown in both figures 1 and 2, the flow drawn through the scoops by an auxiliary suction blower is returned to the main tunnel loop. The volume of flow through the scoops is controlled by a slide valve located at the return duct. Spanwise rows of the static pressure taps along the top and bottom of the two bleed scoops provide guidance in establishing spanwise uniformity at the leading edge of the flat plate. The location of static pressure taps on the two bleed scoops is given in Figure 3. In-situ pitot tube readings at the inlet and exit stations of the test section are monitored in order to verify appropriate boundary layer bleed rates.

The heated flat plate model is constructed using 12-inch sections of rigid polyurethane foam, 27 inches wide, 2 inches thick, and totaling 56 inches in length. These are mounted in a plexiglass frame with inconel foil cemented to the foam to form the test surface. Polyurethane foam was used for the test plate model due to its extremely low thermal conductivity. The last 4 inches of the test surface are unheated and made of a plexiglass block. The entire test surface is smoothly connected to the flange of the diffuser. A schematic of the test surface including dimensions is shown in Figure 4. The test surface is uniformly heated using nine strips of 6-inch wide, 24-inch long and 0.001-inch thick inconel foil. The inconel foil has relatively high resistivity and low thermal

coefficient of resistance which is advantageous compared to other materials. Consecutive inconel foils were electrically connected in series using copper bars arranged in a staggered fashion. Gaps between strips were approximately 0.01 inches wide and were smoothed with a polyester-based filler. The entire heated test surface was covered with a thin layer of fiber glass cloth (about 0.005 inches thick) and carefully sanded to make a hydrodynamically smooth surface. Flat black lacquer and liquid crystal were sprayed on top of the finished surface in the middle 24 inches of span in order to allow for visual inspection of thermal spanwise uniformity. The area of the heated surface is 9 ft<sup>2</sup>. The surface temperatures were measured by means of thermocouples spot-welded directly to the back side of the foil through small holes in the rigid foam plate. With this configuration, uniform heat flux is convected away from the working surface. Conduction losses through the polyurethane foam are less than 2% of heat convected.

The test surface is instrumented with 18 static pressure taps for monitoring of streamwise and spanwise pressure gradients and 59 thermocouples for measuring wall temperatures. The locations of the static pressure taps and thermocouples are also presented in Figure 4.

### **2.1.3 Probe traversing mechanism**

Flowfield measurements for this study were acquired using two types of boundary-layer type hot-wire probes. The probe can be precisely positioned in

three dimensions using a specially designed traversing system. A schematic of the probe traversing mechanism is shown in Figure 5. A remotely controlled stepping-motor-driven actuator enables vertical positioning of the probe using increments as small as 0.00033 inches (3 counts = 0.001 inch). Any streamwise and spanwise positioning within the 19-inch diameter circle can be easily achieved by rotating two eccentrically mounted circular plates, which are supported by ball bearings and are free to rotate in either direction independently. The section containing these two plates forms one of the three panels making up the inner top wall of the test section. The three panels are interchangeable so that the probe can be positioned at different streamwise distances from the leading edge of the flat plate. This double-eccentric plate arrangement maintains a flush surface on the test section roof.

Due to the circular shape of the rotating plate, there are certain corner areas which are inaccessible to the probe. The other major drawback of the traversing system is that probe cannot be positioned within the first 4.5 inches from the leading edge of the flat plate because of the relative positions of the probe traversing mechanism and the small scoop (the leading edge).

## **2.2 INSTRUMENTATION**

The wind tunnel is equipped with many pressure taps and thermocouples especially on the test surface to monitor the thermal operating conditions. The velocity signals from a single hot-wire probe were monitored on a digital

oscilloscope and mean values were measured with averaging voltmeter. Some appropriate signals were then digitally recorded with a waveform recorder for conditional sampling as a post-processing data reduction. Instantaneous velocities and temperatures were simultaneously measured using a miniature 3-wire probe and recorded for calculation of various statistical quantities. In addition, an FFT analyzer was used for obtaining boundary layer spectra. Detailed descriptions of the test section instrumentation, the hot-wire probes, anemometers and data processing equipment will be given in the following sections.

### **2.2.1 Test section instrumentation**

At both the test section inlet and exit planes, a pitot tube and thermocouple are located in the freestream at the center span of the test section. The freestream velocity and temperature entering and exiting the test section and also the rate of suction through the bleed scoops can thus be determined.

A Sorensen DC power supply DCR60-25A is used to supply power to the test surface. The voltage drop across the surface foils was directly measured using a digital voltmeter. The DC current was measured using a precision shunt resistor and a digital voltmeter.

### **2.2.2 Probes/Anemometers**

Two types of probes were used in this experimental work:

1) A commercially available TSI model 1218-T1.5 single sensor boundary layer hot-wire probe was used to measure the streamwise component of mean and fluctuating velocity. This probe was also operated in constant current mode to measure the mean temperature in the boundary layer. The safety leg of the single boundary layer type wire was removed to allow the probe to approach as close to the wall as possible.

2) A miniature 3-wire probe was used to simultaneously measure the instantaneous streamwise and vertical components of velocity and the temperature. This also allowed the determination of correlation quantities like Reynolds shear stress and turbulent heat flux in the boundary layer.

The 3-wire probe was designed based on the requirement of having good spatial resolution and the ability to make measurements as close to the wall as possible. In addition, the viscous length scale  $\nu/u_\tau$  is small (for the worst case of a fully turbulent boundary layer,  $u_\tau \approx 4.5$  ft/s then  $\nu/u_\tau \approx 11 \mu\text{m}$ ), thus in order to properly resolve the small-scale near-wall fluctuating turbulence without significant eddy averaging in the spanwise direction, a small separation distance between the wires is required. However, in order to minimize support prong conduction the hot wire should have a length-to-diameter ratio ( $l_w/d_w$ ) greater than 200. But to minimize vertical averaging in the shear flow, a short sensing length is also required. These conflicting requirements necessitate the use of miniature probe with small diameter wires.

A schematic of the miniature 3-wire probe is given in Figure 6. The two

velocity sensors have an X shape with  $\pm 45^\circ$  orientation. These X sensors are 2.5  $\mu\text{m}$  gold plated tungsten wires with a sensing length of 0.5 mm, which gives  $l_w/d_w=200$ . To reduce the prong interference and end-wall conduction, the wires were plated. The overall length of each X-wire including the plated portions is 1 mm. The temperature sensor is an unplated 1  $\mu\text{m}$  platinum wire with a length of 0.35 mm, yielding  $l_w/d_w=350$ . These three wires are separated 0.35 mm apart from each other. Thus, the spanwise separation of the wires of the 3-wire probe,  $S^+$ , is about 50 wall units for the worst case of a fully turbulent boundary layer.

A TSI model 1050 constant temperature anemometer and a TSI model 1052 fourth order polynomial linearizer were used to operate the hot-wire probes for the measurements of mean and rms velocities throughout the boundary layers. The same TSI model 1050 anemometer was operated in constant current mode in order to measure the mean temperatures in the boundary layers with a single-wire probe.

A DANTEC model 55M20 temperature bridge with a DANTEC model 55M01 main unit was operated in constant current mode to measure instantaneous temperature using the 1  $\mu\text{m}$  temperature sensor of the miniature 3-wire probe. Statistical quantities such as Reynolds shear stress, turbulent heat flux and correlations can be determined from the digitally recorded signals of instantaneous velocities and temperatures.

### 2.2.3 Data acquisition equipment

Steady-state tunnel conditions such as freestream velocity, pressure, temperature, and wall temperatures etc. were monitored and updated about every 2 seconds by means of a multichannel data acquisition system, Escort. The Escort system, which is a real time data processing system, consists of a remote acquisition microprocessor (RAMP), data input and output device, 256-channel multiplexing digitizer and a minicomputer.

Time-averaged mean and rms velocity data were acquired using a Racal-Dana model 5004 precision averaging digital multimeter, set for 200 averages for each data point.

Spectral data were acquired using a Nicolet Scientific Corporation model 660A dual-channel FFT analyzer, which features 1024-point, 12-bit analog-to-digital conversion with a maximum sampling rate of 100 KHz. For the present study, data were acquired using the 2 KHz frequency range for grids 0 to 1 and the 5 KHz range for grid 2.

A high-speed multichannel digital data acquisition system, Datalab DL6000 Multitrap waveform recorder, was used to record instantaneous velocity and temperature signals. This waveform recorder is a 12-bit precision analog-to-digital converter with maximum sampling rate of 1 MHz and 128 Kbytes digital memory per channel for a maximum of 8 channels. For conditional sampling the sampling rate was set at 50 KHz and 32 Kbytes of data were stored for each waveform.

Control of the data acquisition process and subsequent data reduction were accomplished using a Hewlett Packard model 9000 series 300 personal computer, to which an HP 7550A Graphics plotter was hooked up for data plotting.

A digital oscilloscope, TEKTRONIX model 7603, was used to monitor the instantaneous velocity and temperature signals, and to pick up the bridge output signal of simulating a step-change of the flow temperature for the compensation of the temperature sensor of the 3-wire probe. After the signals were checked visually, they were, if desired, stored in the HP computer using a waveform recorder for later data reduction.

## **CHAPTER III**

### **EXPERIMENTAL PROCEDURE**

#### **3.1 ESTABLISHMENT OF OPERATING CONDITIONS**

Prior to any data acquisition, steady-state tunnel operating conditions were established by running the tunnel for approximately two hours, while all equipment was being warmed up by turning the power on. During this warm-up period, the Escort program was brought up and zero calibration was performed on the digital voltmeter. Electrical power of about 350 watts was supplied to the inconel foil to establish the steady-state test section condition with maximum temperature difference between the wall and freestream of about 15 °F. After the steady-state tunnel condition was reached, the velocity-voltage calibrations were performed. The settings of 4 coefficients on the linearizer were also determined for the single-sensor probe measurements. Zero pressure gradient in the test section was established by the adjustment of a hinged upper wall, while monitoring the pressure readings on the test surface. The freestream velocity of 100 ft/s was maintained by adjusting the vortex valve located at the blower inlet and the damper valve located at the diffuser exit. Spanwise uniformity of the static pressure distribution of the incoming flow was checked by reading the

pressure taps on both scoops. The appropriate bleed rate, resulting in the very close readings of both pitot tubes located at the inlet and exit of the test section was also determined by adjusting the slide valve on the bleed return duct line.

## **3.2 PROBE CALIBRATION**

Three kinds of calibrations were performed to properly characterize the momentum and thermal boundary layers, which were 1) velocity calibration, 2) temperature calibration, and 3) so called time constant calibration. More details of probe calibrations will be discussed in the following sections.

### **3.2.1 Velocity-voltage calibration**

For the analysis of the momentum boundary layer, two types of probes were used: 1) the single-wire probe for measurements of streamwise component of time-averaged mean and rms velocities, and 2) the special miniature 3-wire probe for instantaneous streamwise and vertical components of velocities. The wires were operated with the TSI 1050 constant temperature anemometers. The overheat ratio was set to 1.5 for calibration and operation of the single-wire probe and to 1.6 for the 3-wire probe.

#### **3.2.1.1 Single-wire probe**

The velocity calibration of the single-wire probe was done against the in-situ pitot tube at the inlet of the test section where the flow is usually quite

smooth and the corresponding turbulence intensity small without any grids. The bridge output voltages were recorded for about 20 different velocities ranging from 0 to 110 ft/s. To get maximum sensitivity, output voltages and velocities were normalized using a scale from 0 to 10. According to King's law, the square of output voltage is proportional to the square root of velocity. This calibration curve can thus be approximated by using a fourth order polynomial curve. One of the normalized velocity-voltage calibration curves is presented in Figure 7. The coefficients of a fourth order polynomial approximation curve were then set into the TSI model 1052 linearizer. The relationship between the linearized voltage and velocity is then as follows:

$$U = \frac{U_{\max}}{10} \times E_L \quad (3-1)$$

where  $E_L$  is the linearized voltage,  $U_{\max}$  is the maximum velocity for which the hot-wire was calibrated ( $U_{\max}=110$  ft/s) and  $U$  is the local velocity. Quite good linear relationship between  $U$  and  $E_L$  was achieved ( $U = 11 E_L$ ).

### 3.2.1.2 Miniature 3-wire probe

The velocity-voltage calibration of a 3-wire probe was performed at the free-jet calibrator. The two X-shaped velocity sensors were calibrated for velocity and angle in the following manner. First, the inner wire was oriented perpendicular to the flow and bridge output voltages were recorded for about 20 velocities ranging from 0 to 130 ft/s. The velocity-voltage data of the inner wire

were then fitted using a fourth order polynomial approximation. Since the outer wire could not be oriented perpendicular to the flow due to relative positions of a probe rotating device and the wall of jet calibrator, the probe was oriented with both wires at 45 degrees to the flow and bridge output voltages of both wires were recorded in pairs for about 20 velocities ranging from 0 to 170 ft/s. By applying the normal orientation inner wire calibration result to the 45-degree inner wire bridge voltage, the effective cooling velocity was obtained. The fourth order polynomial approximation relating the effective cooling velocity to the bridge voltage of the outer wire was then obtained from the 45-degree orientation voltage-pair calibration data. The actual velocity can be obtained from the effective cooling velocity using Champagne's law (1967),

$$U_{eff}^2 = U_o^2 (\cos^2 \phi + K^2 \sin^2 \phi) \quad (3-2)$$

Where  $U_o$  is the magnitude of actual velocity,  $\phi$  is the angle between normal to the wire and mean flow direction and  $K$  is the correction factor to account for deviation from the cosine law (see Figure 8).

Angle calibrations were performed on the inner wire with three different jet velocities ( $U_o$ ) for 20 angular orientations from -45 to 45 degrees using increments of 5 degrees. A least-squares fitting was then performed to evaluate  $K$  of the inner wire using the information of a fourth order polynomial curve (to get the effective cooling velocity) and the angle calibration data of inner wire. The values of  $K$  thus determined turned out to be very close to zero. The actual

velocity was thus calculated from the effective cooling velocity using the simple cosine law,  $U_{eff} = U_o \cos \phi$  rather than Champagne's law. Schubauer & Klebanoff (1946) experimentally tested the validity of the cosine law, concluded that it was valid for finite wires for angles of yaw,  $\phi$ , less than 70 degrees.

Two components of instantaneous velocity were then obtained using a cosine law in the following manner.

$$U_{eff_1} = U_o \cos \phi_1 \quad (3-3)$$

$$U_{eff_2} = U_o \cos \phi_2 \quad (3-4)$$

$$\phi_1 = 45 + \xi \quad (3-5)$$

$$\phi_2 = 45 - \xi \quad (3-6)$$

where  $\xi$  represented the instantaneous flow angle (see Figure 8). The streamwise and vertical components of instantaneous velocity,  $U$  and  $V$ , were obtained from the digital record of bridge voltages by simultaneously solving the equations (3-3) and (3-4) with the relations of (3-5) and (3-6).

$$U = U_o \cos \xi = \frac{(U_{eff_2} + U_{eff_1})}{\sqrt{2}} \quad (3-7)$$

$$V = U_o \sin \xi = \frac{(U_{eff_2} - U_{eff_1})}{\sqrt{2}} \quad (3-8)$$

The values of  $U_{eff}$  were obtained from the polynomial results of the velocity

calibrations.

### **3.2.2 Temperature calibrations**

Temperature calibrations were performed in an oil container submerged in a constant temperature water bath. The oil temperature was measured by direct reading of a platinum heat probe thermometer which was carefully leveled with the temperature sensor. With very low current heating (1.0 mA), the sensor worked as a resistance thermometer. Two types of probes were used to measure the mean and instantaneous temperatures.

#### **3.2.2.1 Single-wire probe**

The single-wire probe with the TSI 1050 anemometer in constant current mode was used to measure mean temperature in the boundary layers. Bridge output voltages were recorded for 40 different temperatures. A least-squares fit to the temperature calibration data yielded the slope,  $dV/dT$ , i.e. the sensitivity of the single-wire probe. Once the reference quantities were given (e.g. set 5 volts at freestream temperature known from the thermocouples located at the inlet and exit of the test section), mean temperatures in the boundary layers were then easily obtained using the slope from the calibration data.

#### **3.2.2.2 Temperature sensor of the 3-wire probe**

The temperature sensor with the DANTEC 55M20 temperature bridge

was used to measure instantaneous temperature. The wire resistance is linearly related to the temperature as follows:

$$R = R_o [1 + \alpha(T - T_o)] \quad (3-9)$$

where  $\alpha$  is the temperature coefficient of resistance and  $R_o$  is the wire resistance at reference temperature,  $T_o$ . In order to determine  $\alpha$  [ $= (dR/dT) / R_o$ ], the resistance was measured at 60 different temperatures ranging from 60 to 120 °F. A least-squares fit to the resistance-temperature calibration data yielded the slope,  $dR/dT$  and also  $\alpha(T)$ . One representative temperature calibration curve is shown in Figure 9.

The sensitivity in temperature measurements was obtained using two methods. In the first test, output voltages from the bridge were obtained at different temperatures. The slope,  $dV/dT$ , yielded the sensitivity directly. Once the sensitivity was known, temperature could be obtained by measuring the bridge output voltage. One of calibration curves yielding sensitivity is presented in Figure 10. In the second test, a resistance decade box was connected in place of the probe. The bridge was first set to balance with the resistance decade box set at 62 ohms, then the resistance of the decade box was increased from 60 to 67 ohms in steps of 0.2 ohms and the corresponding bridge output voltage recorded, which yielded the slope,  $dV/dR$ . This calibration curve is shown in Figure 11. Since  $\alpha$  had been obtained earlier, the change in resistance could be easily converted to the corresponding change in temperature and the sensitivity

also could be calculated using two slopes ( $dV/dT = dR/dT \cdot dV/dR$ ). The values of  $dV/dT$  obtained from the two methods were very closely matched as indicated in Figure 11.

### 3.2.3 Time constant of temperature sensor

Due to the thermal capacitance of the temperature sensor, the wire cannot respond quickly to a sudden change of temperature. There is a certain frequency limitation for the temperature wire so that compensation of the temperature wire is required to properly account for a high-frequency component in the temperature data.

To simulate a step-change of air temperature, experiments were carried out in the following way. The probe was first placed at the inlet of the test section where the velocity calibrations were performed. The temperature bridge was initially set to balance with a very low current of 0.3 mA in the air flow. The bridge current was then increased to about 2 to 3 mA in *the stand-by mode* depending on the flow speed to get the voltage response ranging from 0 to 10 volts. Suddenly feed the increased bridge current in *the stand-by mode* to the temperature sensor by turning the probe current switch to *the operate mode* of the temperature bridge. The temperature sensor was observed to respond in an exponential way as shown in Figure 14 (also see section 4.3). This simulation was checked on the oscilloscope before the signal was stored on an HP computer using a multichannel waveform recorder in the pre-trigger mode. The sampling

rate was set to 500 KHz and the recording length of sampling data was 4 Kbytes. The time constant was calculated as a post-processing data reduction. Time constant experiments were repeated with 8 different flow speeds ranging from 30 to 100 ft/s. A least-squares fitting was then performed to get the relationship between the time constant of the temperature wire and the flow speed.

### **3.3 MEASUREMENTS OF OVERALL VELOCITY AND TEMPERATURE**

In order to resolve the time-averaged overall characteristics of momentum and thermal boundary layers, the boundary-layer type single-wire probe was positioned at 5 to 8 different streamwise locations between 5 and 20 inches from the leading edge of the flat plate depending on the freestream turbulence intensities ranging from 0.4% to 6%. Once a probe was moved to a certain streamwise location in the freestream at center-span of the test section, the probe was then carefully lowered until it slightly touched the wall. The typical distance between wall and the first measurement point was about 0.005 inches. The first 10 data points were obtained with a vertical increment of 0.001 inches and the next 10 data points were acquired using steps of 0.002 inches. Increments of 0.005 inches for next 10 points and then 0.01 inches, thereafter, were applied until the edge of the boundary layer was reached. Quite good vertical resolution was achieved (40 to 50 data points depending on the thickness of the boundary layers). The Racal-Dana averaging voltmeter, set for 200 averages at each data point, was used to measure mean and rms voltages.

### **3.4 HEAT TRANSFER MEASUREMENTS**

After steady-state conditions of the test section were achieved by running the tunnel with the power-supply on, while monitoring the Escort display of wall and freestream temperature distribution, the wall temperature data with one power-supply polarity were recorded. Due to a small voltage-tap error resulting from the intimate contact of the thermocouples with the inconel foil, wall temperature data were acquired again with opposite power-supply polarity. Averaging of the two sets of wall temperature data was then performed to get the appropriate values of wall temperature. At the same time, the current and voltage drop of the power-supply across the inconel foils were measured using a voltmeter, which yielded the wall heat flux value.

### **3.5 HIGH-SPEED DATA ACQUISITION**

Conditional sampling, with which the signal can be segregated into turbulent and non-turbulent parts, was performed on the intermittent flows to get better understanding of the transitional boundary layers for two freestream turbulence intensities of 1.1% and 2.4% using grids 1 and 2 respectively. Six streamwise locations ranging from 9 to 20 inches from the leading edge of the test plate in the intermittent region for grid 1 and five locations ranging from 5 to 15 inches for grid 2 were selected based upon the results of time-averaged mean velocity profiles. At each streamwise location, a first set of 10 data points from the wall was measured with a 0.002-inch increment. Another 6 points

using 0.005-inch steps and then 0.01-inch increments were used until the edge of the boundary layer was reached. About 20 to 30 vertical data points were measured depending on the thickness of the boundary layer. Each intermittent signal was digitally recorded on the HP computer using a multichannel digital waveform recorder for later use. The sampling rate was set at 50 KHz and the recording length of data was selected as 32 Kbytes for each waveform.

The instantaneous streamwise and vertical components of velocity and temperature were measured simultaneously using a 3-wire probe in the intermittent regions for grid 1 where the conditional sampling was performed. Quite similar spatial resolutions (streamwise and vertical) to those of the single-wire conditional sampling were selected. The typical distance between the wall and the first measurement point ( $Y_0$ ) was about 0.02 inches for the 3-wire probe. Two signals from the X-shaped velocity sensors and one from a temperature sensor were simultaneously recorded using a multichannel waveform recorder with the sampling rate of 50 KHz and 32 Kbytes of data record length. As a post-processing data reduction, evaluation of statistical quantities such as Reynolds shear stress, turbulent heat flux, etc. was performed.

### 3.6 SPECTRAL DATA ACQUISITION

Spectral data were acquired with the single-sensor probe using a digital Nicolet FFT analyzer. Several boundary layer spectra including 1) the spectra at the very near-wall location ( $y=Y_0$ ), 2) at the location where the amplitude of

streamwise velocity fluctuations was maximum, and 3) the freestream spectra were obtained for four different freestream turbulence intensities ranging from 0.4% to 2.4% (grids 0 to 2). The spectra were obtained over streamwise distances from 5 to 20 inches from the leading edge of the heated flat plate with streamwise increments of 1 inch for several upstream locations and of 2 inches for the remainder, including the locations where the time-averaged velocity profiles were measured. For grids 0, 0.5 and 1, the spectral data were acquired over a 2 KHz frequency range, while for grid 2, data were obtained over a 5 KHz range. Every power spectral density curve for all four grid configurations was the result of at least 100 averages to get a representative power spectrum.

## CHAPTER IV

### DATA REDUCTION

#### 4.1 MOMENTUM BOUNDARY LAYER DATA ANALYSIS

For the momentum boundary layers, overall mean and rms velocity profiles were measured at selected streamwise locations on the flat plate with zero pressure gradient for six grid configurations. The measurements of the mean velocity profiles enabled calculation of the boundary layer integral parameters such as displacement thickness, momentum thickness and shape factor. The abrupt change of these parameters with streamwise distance is one rough way of determining the transition region.

##### 4.1.1 Mean velocity profiles

The mean velocity profiles were normalized with the Blasius similarity or Hartree variables, which are

$$\eta = y \sqrt{\frac{U_e}{2\nu x}}, \quad f'(\eta) = \frac{U}{U_e} \quad (4-1)$$

These profiles were compared to the well-known Blasius laminar solution. The

same mean velocity profiles were also normalized with wall units:

$$y^+ = \frac{u_\tau y}{\nu}, \quad u^+ = \frac{U}{u_\tau} \quad (4-2)$$

$$\text{where } u_\tau = \sqrt{\frac{\tau_w}{\rho}} \quad (4-3)$$

$u_\tau$  is referred to as friction velocity. The relationship between skin friction coefficient,  $C_f$ , and  $u_\tau$  is as follows:

$$\frac{C_f}{2} = \frac{\tau_w}{\rho U_e^2} = \left( \frac{u_\tau}{U_e} \right)^2 \quad (4-4)$$

The mean velocity profiles were then compared to the Blasius curve for laminar boundary layers and to the Musker (1979) law-of-the-wall curve for fully turbulent boundary layer flows. If the mean velocity data fall somewhere between the two curves, then the boundary layer is considered to be transitional.

The correlations for laminar boundary layers are as follows:

$$Re_\theta = Re_x \frac{\theta}{X} = 0.664 \sqrt{Re_x} \quad (4-5)$$

$$C_f = \frac{0.664}{\sqrt{Re_x}} = \frac{(0.664)^2}{Re_\theta} \quad (4-6)$$

Combining equations (4-4) and (4-6), the Blasius solution is expressed in wall units as follows:

$$u^+ = \frac{U_e}{u_\tau} f'(\eta) = 2.12984 \sqrt{Re_\theta} f'(\eta) \quad (4-7)$$

With the definition of  $\eta$  expressed in eq. (4-1),

$$y^+ = \frac{u_\tau}{\nu} \sqrt{\frac{2\nu X}{U_e}} \eta = \sqrt{2 Re_x} \frac{u_\tau}{U_e} \eta \quad (4-8)$$

Substituting equations (4-4) to (4-6) into eq. (4-8), the following expression for  $y^+$  is obtained:

$$y^+ = \sqrt{Re_\theta} \eta \quad (4-9)$$

In using eqs. (4-7) and (4-9),  $Re_\theta$  is the measured, not the calculated momentum thickness Reynolds number at the streamwise location of the measurements. The turbulent law-of-the-wall curve used for data analysis is that of Musker (1979):

$$u^+ = 5.424 \tan^{-1} \left[ \frac{(2y^+ - 8.15)}{16.7} \right] + \log_{10} \left[ \frac{(y^+ + 10.6)^{9.6}}{(y^{+2} - 8.15y^+ + 86)^2} \right] - 3.52 \quad (4-10)$$

This expression includes the viscous sublayer, the buffer layer and log-linear region (but no wake). For large  $y^+$ , it becomes the following familiar equation:

$$u^+ = \frac{1}{0.41} \ln y^+ + 5.0 \quad (4-11)$$

#### 4.1.2 Determination of friction velocity

The use of wall units implies the evaluation of friction velocity,  $u_\tau$ , which could in principle be directly acquired from measurements of wall shear stress,  $\tau_w$ . Determination of  $u_\tau$  is thus very important for characterizing the boundary layers since the wall shear stress changes significantly from laminar to turbulent through the transition regime. However, the exact measurement of  $\tau_w$  requires mean velocity gradient information at the wall, which is almost impossible to measure directly with a hot-wire system because of the limit on the approach of the hot-wire probe to the wall. Alternative ways of estimating  $u_\tau$  are considered based on the nature of each boundary layer.

For laminar boundary layers, the mean velocity varies linearly with distance from the wall in the near-wall region. The value of  $\Delta U/\Delta y$  from a couple of mean velocity data points close to the wall is used to approximate the value of  $\partial U/\partial y$  at the wall to calculate  $\tau_w$ . Once  $\tau_w$  is inferred from the near-wall data points ( $y^+ < 10$ ), then  $u_\tau$  can be easily determined.

For turbulent boundary layers, the mean velocity gradient near the wall is so large that the linear approximation of mean velocity gradient near the wall definitely leads to an error. The value of  $u_\tau$  is, instead, estimated from the law-of-the-wall relation (eq. 4-11), since the distinct log-linear region is known to exist in the fully turbulent boundary layers. A least-squares fitting of  $u^+$  falling within the log linear region of  $100 < y^+ < 250$  to the eq. (4-11) was performed with an initial value of  $u_\tau$  assumed from the empirical correlation of fully

turbulent boundary layers suggested by Schlichting (1979),

$$C_f = 0.0256 Re_\theta^{-\frac{1}{4}} \quad (4-12)$$

While slightly changing the value of  $u_\tau$  from the initial guess, the data fitting was repeated until the best fit having the least variance was found. The value of  $u_\tau$  for the turbulent boundary layer was thus estimated. This technique is sometimes called a Clauser fit (Clauser, 1956).

For transitional boundary layers, the above methods of determining  $u_\tau$  can not be applied. Therefore, the integral momentum equation for a flat plate was used to estimate  $u_\tau$ .

$$\frac{\tau_w}{\rho} = U_e^2 \frac{d\theta}{dx} \quad \left( \frac{u_\tau}{U_e} \right)^2 = \frac{d\theta}{dx} \quad (4-13)$$

The momentum thickness,  $\theta$ , was determined from numerical integration of the mean velocity profiles. One representative plot of  $\theta$  variation with streamwise distance,  $x$ , is shown in Figure 12. The values of  $u_\tau$  were determined from the slope of momentum thickness in the transitional region. The mean velocity profiles plotted in wall units with the values of  $u_\tau$  determined using the above method in the transitional boundary layer were also checked to see that the near-wall data ( $y^+ < 10$ ) were bounded by  $u^+ = y^+$  and the Musker law-of-the-wall curves.

The values of  $u_\tau$  obtained in the laminar, transitional and low Reynolds

number turbulent boundary layers for six levels of freestream turbulence are summarized in Tables I ~ VI.

## **4.2 THERMAL BOUNDARY LAYER DATA ANALYSIS**

In order to analyze the thermal characteristics of the boundary layers, the following quantities were measured: 1) heat transfer from the wall, 2) mean and rms temperature profiles. Also a check of the energy balance was performed. The data acquisition and reduction techniques for the above mentioned quantities will be explained in the following sections.

### **4.2.1 Heat transfer**

The heated flat plate was heavily instrumented with thermocouples along the center-span especially close to the leading edge. The values of wall and freestream temperature were directly obtained from the readings of the corresponding thermocouples. The measurements of the voltage and current of the power supply yield the wall heat flux. A correction for radiation heat loss was then applied to the wall heat flux. From measurements of the wall and freestream temperatures as well as the wall heat flux, the variation of Stanton number along the streamwise direction is obtained.

A quantity which combines information from both momentum and thermal boundary layers is the Reynolds analogy factor,  $2 St/C_f$ . The Reynolds analogy factor is simply the ratio of two values at the edge of the momentum and thermal

boundary layers expressed in wall units as indicated in the following equations:

$$\begin{aligned} \frac{2 St}{C_f} &= \frac{q_w''}{\rho C_p U_e (T_w - T_e)} \cdot \frac{U_e^2}{u_\tau^2} \\ &= \frac{q_w''}{\rho C_p u_\tau (T_w - T_e)} \cdot \frac{U_e}{u_\tau} = \frac{U_e^+}{T_e^+} \end{aligned} \quad (4-14)$$

#### 4.2.2 Mean temperature profiles

Special care was taken to account for the drift of wall temperature readings during the acquisition of data, which affected the distribution of boundary layer temperatures. Due to the boundary condition of uniform wall heat flux,  $T_w - T_e$  can be assumed constant with time at any given station. The amount of wall temperature correction was applied to correct the reference freestream temperature. With corrected  $T_e$ , the temperature distribution in the boundary layer was obtained by converting the anemometer output voltages.

The mean temperature profiles thus acquired with a single-sensor probe were plotted in wall units,

$$T^+ = \frac{(T_w - T)}{T_\tau}, \quad T_\tau = \frac{q_w''}{\rho C_p u_\tau} \quad (4-15)$$

where  $T_\tau$  is referred to as friction temperature. The dimensionless temperature  $T^+$  is a function of both wall heat flux and the skin friction represented by  $u_\tau$ .

The friction velocity used for the determination of friction temperature was the same  $u_\tau$  as used for the plot of non-dimensional velocity profiles, which was inferred from the mean velocity profiles on the heated flat plate as mentioned in section 4.1.2.

Due to the finite unheated starting length, laminar temperature profiles deviate from the well-known correlation of  $T^+ = Pr \cdot y^+$  even in the near-wall region ( $y^+ > 5$ ). In order to properly resolve the laminar correlation, the effects of uniform heat flux and unheated starting length will be considered successively. First, the constant property momentum and energy equations for a flat plate with zero pressure gradient and uniform heat flux can be written in non-dimensional forms as follows:

$$f''' + ff'' = 0 \quad (4-16)$$

$$\Theta'' + Pr f \Theta' - Pr f' \Theta = 0 \quad (4-17)$$

with boundary conditions of

$$\Theta(0) = 1, \quad \Theta(\infty) = 0 \quad (4-18)$$

$$\text{where } \Theta = \frac{T - T_e}{T_w - T_e} = \Theta(\eta) \quad (4-19)$$

Note that the derivatives are with respect to the similarity variable  $\eta$  (eq. 4-1) and Prandtl number,  $Pr$ , was assumed as 0.708. Eq. (4-17) already incorporates the laminar condition  $T_w - T_e \sim X^{1/2}$  appropriate to uniform heat flux.

The two ordinary differential equations, (4-16) and (4-17), were solved using a fourth order Runge-Kutta method. Once the non-dimensional temperature,  $\Theta$ , was obtained as function of  $\eta$ , then  $\Theta$  can be converted to  $T^+$  as follows:

From the definition of  $T^+$  expressed in eq. (4-15),

$$T^+ = \frac{\rho C_p u_\tau (T_w - T)}{q_w''} = \frac{1}{St} \left( \frac{u_\tau}{U_e} \right) \left( \frac{T_w - T}{T_w - T_e} \right) \quad (4-20)$$

The heat transfer correlation for the laminar boundary layer flow with uniform wall heat flux considering the effect of unheated starting length was expressed in the following form suggested by Kays & Crawford (1980):

$$St = 0.453 Pr^{-\frac{2}{3}} Re_x^{-\frac{1}{2}} \left[ 1 - \left( \frac{X_o}{X} \right)^{\frac{3}{4}} \right]^{-\frac{1}{3}} \quad (4-21)$$

Combining eqs. (4-20) and (4-21) with laminar relation of  $C_f$  (eq. 4-6), then the laminar temperature relation can be written in wall units as follows:

$$T^+ = \frac{Pr^{\frac{2}{3}} \sqrt{Re_\theta}}{0.453 \sqrt{2}} \left[ 1 - \left( \frac{X_o}{X} \right)^{\frac{3}{4}} \right]^{\frac{1}{3}} (1 - \Theta) \quad (4-22)$$

The above expression which accounts for the unheated starting length and the same correlation with no unheated starting length ( $X_o=0$ ) were compared with the measured temperature data in Figure 13. The excellent agreement of the laminar expression which accounted for the unheated starting length with the

measured data is noticeable.

The fully developed turbulent temperature law-of-the-wall formula also suggested by Kays & Crawford (1980) is written as follows:

$$T^* = 13.2 Pr + \frac{Pr_t}{0.41} \ln\left(\frac{y^*}{13.2}\right) \quad (4-23)$$

The value of turbulent Prandtl number,  $Pr_t$  was assumed constant as 0.9.

#### 4.2.3 Energy balance

In order to check the energy closure, values of enthalpy thickness,  $\Delta_2$ , were calculated from the integration of boundary layer temperature profiles (profile measurement), which can be expressed as follows for constant property, incompressible flows:

$$\Delta_2 = \frac{\int_0^{\infty} \rho C_p U (T - T_e) dy}{\rho C_p U_e (T_w - T_e)} = \frac{\int_0^{\infty} U (T - T_e) dy}{U_e (T_w - T_e)} \quad (4-24)$$

The values of  $\Delta_2$  were also obtained from a direct calculation of the uniform wall heat flux (wall measurement) as follows:

$$\Delta_2 = \frac{\int_{X_0}^X q_w'' dx}{\rho C_p U_e (T_w - T_e)} = \frac{q_w'' (X - X_0)}{\rho C_p U_e (T_w - T_e)} \quad (4-25)$$

where  $X_0$  is the unheated starting length (1.375 inches).

The energy closure was checked by simply comparing the two values obtained from both profile and wall measurements.

### 4.3 COMPENSATION OF TEMPERATURE SENSOR

In non-isothermal flow, the temperature gradient affects the output voltage of a hot wire anemometer, making the segregation of the output voltages of the single-wire probe into instantaneous velocity and temperature impossible without additional information. A miniature 3-wire probe is thus used to properly obtain the velocity and temperature information. Due to the heat capacitance of the temperature wire operated in constant-current mode, compensation becomes necessary to properly resolve the high-frequency temperature data. In this study, a digital method, basically following the analog technique suggested by Hishida & Nagano (1978), is used to compensate for the deficient frequency response of the temperature wire. The basic principle of the compensation of the temperature wire will be given in the following sections.

#### 4.3.1 Thermal energy balance in a wire

The thermal energy equation with the assumption of uniform radial temperature distribution within a fine wire and of negligible axial conduction and radiation, is in the following form:

$$\pi r_o^2 l_w \rho_w C_w \frac{dT_w}{dt} + 2 \pi r_o l_w h (T_w - T_a) - i^2 R_w = 0 \quad (4-26)$$

where  $h$  is the heat transfer coefficient,  $r_o$  is the wire radius and subscripts  $w$  and  $a$  correspond to the wire (not to the wall) and to air flow, respectively.

Since a negligible current heating with 1.0 mA was applied to the wire, therefore

the last term of  $i^2 R_w$  can be neglected. The equation for a temperature wire in the constant-current mode then becomes as follows:

$$r_o \rho_w C_w \frac{dT_w}{dt} + 2h(T_w - T_a) = 0 \quad (4-27)$$

Using the relation (3-9) for the temperature dependence of the wire resistance, the above equation is rewritten in terms of resistance,  $R$ .

$$\frac{r_o \rho_w C_w}{2h} \frac{dR_w}{dt} + R_w - R_a = 0 \quad (4-28)$$

Multiplying equation (4-28) by the constant current  $i_w$  yields

$$M \frac{dV_w}{dt} + V_w - V_a = 0 \quad (4-29)$$

$$\text{where } M = \frac{r_o \rho_w C_w}{2h} \quad (4-30)$$

$M$  is called the time constant of temperature wire.

Even though the empirical relation obtained by Collis and Williams (1959) well represents the heat transfer from a fine wire to the flow, for the sake of simplicity, the relation suggested by Kramers (1946) is chosen.

$$Nu_f = 0.42 Pr_f^{0.2} + 0.57 Pr_f^{0.33} Re_f^{0.5} \quad (4-31)$$

$$h = A + B\sqrt{U} \quad (4-32)$$

The fluid properties are evaluated at the film temperature in the above expression. For air flow, the coefficient  $A$  is slightly dependent on temperature,

but B is almost constant. In this study,  $(T_w - T_o)_{\max} < 15$  °F, therefore both A and B can be assumed constants, which yields  $h = h(U)$ .

#### 4.3.2 Experimental determination of time constant

The time constant of the temperature wire is strongly dependent on streamwise velocity but is weakly dependent on the flow temperature in this study. To experimentally determine M, a step-change of flow temperature from an initial temperature  $T_i$  to a final temperature  $T_f$  (i.e.  $T_a = T_f$ ) was simulated by a sudden feeding of increased current into the constant-current anemometer at a certain flow speed (see section 3.2.3 for a detailed procedure). The wire response to the step-change of flow temperature can be determined by solving eq. (4-29) with the proper initial and boundary conditions of  $V_w = V_i$  at  $t=0$  and  $V_w = V_f$  as  $t \rightarrow \infty$ . Then the solution becomes

$$V_w(t) = V_i + (V_f - V_i) \left(1 - e^{-\frac{t}{M}}\right) \quad (4-33)$$

The exponential response of wire temperature to a step change of temperature at a certain flow speed can be seen in Figure 14. The time constant M can be expressed by the following rearrangement of eq. (4-33):

$$M = \frac{t}{-\ln\left(1 - \frac{V_w(t) - V_i}{V_f - V_i}\right)} \quad (4-34)$$

In Figure 15, the quantity which is in the denominator of eq. (4-34) was plotted

with respect to time. The slope of curve shown in Figure 15 becomes the time constant at that flow speed. A set of data  $(M_i, U_i)$   $i=1,2 \dots N$  was obtained by repeating the above procedures with  $N$  different flow speeds. With the definition of time constant (eq. 4-30) and eq. (4-32), the following relation is obtained:

$$\frac{1}{M_i} = C_1 + C_2 \sqrt{U_i} \quad (4-35)$$

$C_1$  and  $C_2$  are the constants experimentally determined from a least-squares fit of time constant data  $(1/M_i, U_i^{1/2})$ . The calibration curve of time constant for several different flow speeds is shown in Figure 16. Once the calibration coefficients,  $C_1$  and  $C_2$  are determined, the time constant for each flow velocity is obtained according to eq. (4-35). The compensated temperature voltages are then obtained by solving eq. (4-29) with known time constants. The effect of compensation which is the increased frequency response up to 6 KHz according to the result of Hishida & Nagano (1978) is shown in Figure 17(a,b). The compensated voltage was converted to the corresponding temperature, since the sensitivity,  $dT/dV$ , was already obtained in the calibration (see section 3.2.2.2).

#### **4.4 TEMPERATURE CORRECTION FOR CONSTANT-TEMPERATURE BRIDGE OUTPUT VOLTAGE**

Since the hot-wire voltage signals were directly affected by the flow temperatures, the correction for hot-wire bridge voltage measured in the shear flow with temperature gradient is thus necessary. Perry (1982) suggested the

following simple relation for this correction:

$$\frac{V_{correct}}{V_{meas}} = 1 + \frac{\alpha}{2(OHR - 1)} (T_a - T_{cal}) \quad (4-36)$$

where  $T_a$  is the flow temperature,  $T_{cal}$  is the freestream temperature during the calibration,  $\alpha$  is the temperature coefficient of resistance which is  $0.0035 / ^\circ\text{C}$  at  $20 ^\circ\text{C}$  and  $OHR$  is the overheat ratio of the constant-temperature anemometer which is set at 1.6. The maximum correction made by eq. (4-36) is about 3%.

A more accurate but much more complicated alternative of getting instantaneous velocities and temperatures would involve the solution of three simultaneous nonlinear equations. The heat transfer equation for a constant-temperature wire suggested by Collis and Williams (1959) was algebraically manipulated to the following equation for both X-shaped wires:

$$V_w^2 = A T^{0.76} (T_w - T) + B (T_w - T) U_{eff}^{0.45} \quad (4-37)$$

With more complicated calibration data including the temperature effect, the coefficients A and B for both X wires can be obtained. The streamwise and vertical components of instantaneous velocity and the temperature are obtained by solving two equations (4-37), one for each X-wire together with the temperature wire response eq. (4-29) iteratively until some stopping criterion is satisfied. This alternate data reduction technique requires significantly increased computer time, but gives an improvement of only 3%. The method that involves the separate calculations of instantaneous velocities and subsequent correction is

satisfactory for the present study.

#### 4.5 CONDITIONAL SAMPLING TECHNIQUE

In the transition of a laminar shear flow to turbulence over a streamwise distance, intermittency is observed. Conditional sampling based on intermittency allows segregation of the intermittent signals into non-turbulent and turbulent parts. The distinctive feature of the turbulent fluid is its highly rotational nature. Thus vortical fluctuation is one very appropriate choice for discrimination between non-turbulent and turbulent flow but this technique requires a very complex probe. The alternative method used herein is to differentiate the velocity fluctuation (detector function) and emphasize the high frequency component for turbulent flow. Then smoothing of the detector function is applied. After some threshold values are determined, the signal is defined as turbulent if the value of the smoothed detector function is greater than the threshold value, otherwise the signal is defined as non-turbulent.

For the detector function, squares of the first and second derivatives of the velocity signal were used. For the single-wire measurements, the detector function was based on derivatives of the streamwise velocity as follows:

$$\text{Detector function:} \quad \left( \frac{\partial u}{\partial t} \right)^2 \quad \text{and} \quad \left( \frac{\partial^2 u}{\partial t^2} \right)^2$$

For the 3-wire measurements, there are several choices of detector function. A

detector function involving the derivatives of  $u$  and  $v$  separately rather than say the derivatives of the product of two velocity components such as Reynolds shear stress, was chosen following the suggestion by Hedley & Keffer (1974).

$$\text{Detector function: } \left(\frac{\partial u}{\partial t}\right)^2 + \left(\frac{\partial v}{\partial t}\right)^2 \quad \text{and} \quad \left(\frac{\partial^2 u}{\partial t^2}\right)^2 + \left(\frac{\partial^2 v}{\partial t^2}\right)^2$$

There will be some period of time when the detector function might have some zeros within the turbulent zone since the first derivative of the fluctuation signal alternates its signs very rapidly. Therefore, smoothing the derivatives over a short period of time becomes necessary to eliminate excessive zero-crossing.

The smallest possible value of smoothing time depends on the sampling rate of data acquisition and the resolution of the probe. The smoothing time is about 15 to 35 times the Kolmogorov scale. Setting the smoothing time as 10 times the sampling rate ( $20 \mu\text{s}$ ), the smoothing window size is approximately 30 times the Kolmogorov scale in this study.

Picking up the threshold value turned out to be trickier than selecting the smoothing time. Attempts were made to adopt a completely systematic way of quantifying the threshold value using the cumulative distribution function of the smoothed detector function described by Hedley and Keffer (1974). This method proved only partially successful and fine tuning of the threshold value was required at each measurement location in order to obtain an accurate indicator function as determined by careful direct comparison with an instantaneous signal.

For more details of detector and smoothing function, refer to the paper by Hedley and Keffer (1974).

The procedure used for accomplishing the necessary non-turbulent and turbulent decisions is illustrated in Figure 18(a) for streamwise velocity signals and in Figure 18(b) for Reynolds shear stress and turbulent heat flux. Even though first derivative detector and smoothing functions were not shown in the figures, but they were treated similarly to their second derivative counterparts. For the 3-wire measurements, all three instantaneous fluctuating signals of velocities ( $u'$  and  $v'$ ) and temperature ( $t'$ ) were compared to the indicator function to properly choose the threshold value. If both first and second derivative smoothing functions were smaller than their respective threshold values, the signal was declared as non-turbulent flow. Otherwise, it was defined as turbulent flow.

## **CHAPTER V**

### **RESULTS AND DISCUSSION**

#### **5.1 FREESTREAM TURBULENCE INTENSITY**

Detailed momentum and thermal boundary layer measurements have been performed on a heated flat plate with zero pressure gradient for six different levels of freestream turbulence. The freestream turbulence intensity data were acquired at streamwise locations between  $X=5$  and 20 inches from the leading edge of the heated flat plate. The vertical measurement location above the test surface was approximately 1.2 inches. The distribution of the streamwise freestream turbulence intensity generated by grids 0, 0.5, 1, 2, 3 and 4 within the test section is presented in Figure 19. The nominal values of the freestream turbulence intensity are 0.4% for grid 0, 0.8% for grid 0.5, 1.1% for grid 1, 2.4% for grid 2, 5% for grid 3 and 6% for grid 4. Note that for grids 0, 0.5, 1, and 2, the data are almost constant with streamwise distance, which means that the grid-generated freestream turbulence becomes nearly homogeneous quickly for the relatively moderate levels of freestream turbulence less than 2%. However, the data for grids 3 and 4 indicate a slow decay of the freestream turbulence intensity (freestream turbulent kinetic energy level) with distance

downstream due to larger eddies generated by the coarser grids. Turbulent cascading is still in progress. Somewhat higher levels of freestream turbulence are measured in this study compared to the corresponding levels obtained by Suder et al. (1988) for the unheated test surface.

For more detailed description of characteristics of freestream turbulence such as integral length scale and frequency spectra, refer to the paper by Suder et al. (1988).

## **5.2 MOMENTUM BOUNDARY LAYER**

In order to characterize the momentum boundary layer development, the distribution of inferred skin friction coefficient and shape factor as well as time-averaged overall mean and rms velocity profiles were measured with a boundary-layer type single-wire probe in the laminar, transitional, and low Reynolds number turbulent boundary layers. Based on these measurements, the transition region for each level of freestream turbulence can be determined. Conditional sampling was also performed on the above mentioned quantities to get a thorough understanding of the intermittency characteristics of the boundary layers for grids 1 and 2. In addition, the conditionally sampled as well as overall data of Reynolds shear stress,  $-\overline{u'v'}$  were acquired with the miniature 3-wire probe.

### **5.2.1 Mean velocity profiles**

Mean velocity profiles were measured at various streamwise locations

from  $X=5$  to 20 inches from the leading edge of the heated test surface along the center line for six levels of freestream turbulence. The mean velocity profiles normalized with the Hartree similarity variables,  $\eta$  and  $f'(\eta)$ , are presented in Figure 20(a-f). The two profiles at the farthest upstream locations in Figure 20(a-c) for grids 0, 0.5 and 1 lay on top of each other and agreed well with the Blasius profile (solid line) due to the similarity of the laminar boundary layers. The velocity profiles then begin to deviate from the Blasius profile with distance downstream, which indicates the start of boundary layer transition. For example, the transition region is apparently initiated at  $X=9$  inches from the leading edge for grid 0.5 and grid 1 as presented in Figure 20(b,c), but the transition region has already begun prior to the first measurement station of  $X=5$  inches for both grids 3 and 4 as shown in Figure 20(e,f).

To capture the end of the transition region and to stretch a thin layer very close to the wall, the same mean velocity profiles were normalized in terms of wall units,  $u^+$  and  $y^+$  and plotted using a logarithmic scale for the  $y^+$  axis. As shown in Figure 21(a-f), the mean velocity profiles plotted in wall units are compared to three types of reference curves: 1)  $u^+ = y^+$ , 2) the Blasius solution with a measured  $Re_\theta$  for a laminar boundary layer, and 3) the Musker (1979) continuous law-of-the-wall curve for a fully turbulent boundary layer. However, in Figure 21(f) for grid 4, as all the mean velocity profiles deviated from the Blasius curve, the latter curve was omitted. To be noted in these reference curves is that the Blasius profile is very well matched with the  $u^+ = y^+$  curve

near the wall especially for  $y^+ < 20$ . Excellent agreement of the two upstream profiles with the Blasius curve is observed in profiles taken between  $X=5$  and 10 inches for grids 0, 0.5 and 1. Also note that the data points near the wall ( $y^+ < 10$ ) are tightly bounded by  $u^+ = y^+$  and the Musker law-of-the-wall curves in all cases. The values of  $u_r$  required to construct these plots were inferred from the mean velocity profiles depending on the characteristics of the boundary layers. The laminar values of  $u_r$  were obtained from a laminar theory, the fully turbulent values were inferred using a Clauser fit and for the transition cases,  $u_r$  is acquired from the momentum integral theory (see section 4.1.2 for a detail).

Farther downstream, the data fell in the region between the Blasius curve and the Musker law-of-the-wall curve. The profiles for grids 0.5, 1 and 2 span nearly the entire range from laminar to turbulent boundary layers. Due to similarity of the turbulent boundary layer, mean velocity profiles for the larger grids fell on top of each other in the log-linear region as shown in Figure 21(e,f). Once the mean velocity profile fell close to the Musker law-of-the-wall curve especially in the log-linear region, it can be said that this might be the location of the end of transition. Thus, for example, the transition region ends at around  $X=15$  inches from the leading edge for grid 2.

For turbulent boundary layers, the existence of a log-linear region is an inherent characteristic (Purtell et al., 1981; Paik & Reshotko, 1986), which can be clearly depicted at some downstream locations for grids 1 ~ 4. One more trend detected in Figure 21(d-f) is that as the level of freestream turbulence

increased, the wake strength which is the amount of deviation of mean velocity profile from the law-of-the-wall curve of eq. (4-11) in the outer portion of turbulent boundary layer is getting diminished. This trend is consistent with the previously reported data for the turbulent boundary layer. The more detailed explanation of wake strength will be given in the following section.

### 5.2.2 Skin friction

The value of non-dimensional mean velocity at the edge of the boundary layer,  $u_e^+$ , is directly related to the skin friction coefficient,  $C_f$  (eq. 4-4). The plot of the variation of  $U_e/u_\tau$  with  $Re_\theta$  for the entire set of freestream turbulence intensity cases is shown in Figure 22(a). Also shown is the Blasius curve for comparison with the data in the laminar boundary layers.

$$\frac{U_e}{u_\tau} = 2.12984 \sqrt{Re_\theta} \quad (5-1)$$

For turbulent boundary layers, the empirical relation of  $C_f$  suggested by Schlichting (1979) is converted to  $U_e/u_\tau$ :

$$\frac{U_e}{u_\tau} = \frac{Re_\theta^{\frac{1}{4}}}{\sqrt{0.0128}} \quad (5-2)$$

To be noted in this turbulent correlation is that no effect of wake strength due to the variation of the freestream turbulence level was considered.

The effect of the increased freestream turbulence intensity on the

decreased magnitude of  $U_e/u_e$  in the boundary layers at the same streamwise distance is quite obvious. One more trend observed in these skin friction profiles is that the boundary layer transition occurs at increasingly lower values of Reynolds number as the freestream turbulence level increases. For example, the boundary layer transition starts at  $Re_\theta \approx 550$  for grid 0, at  $Re_\theta \approx 400$  for grid 0.5, and at  $Re_\theta \approx 380$  for grid 1, and ends at  $Re_\theta \approx 1150$  for grid 2 and at  $Re_\theta \approx 900$  for grid 3.

The effects of wake strength,  $\Pi$ , which were clearly observed in the mean velocity profiles for turbulent boundary layers, are quantified as follows. The Musker relation for turbulent boundary layer with wake strength effect is written in the following form:

$$u^+ = 5.424 \tan^{-1} \left[ \frac{(2y^+ - 8.15)}{16.7} \right] + \log_{10} \left[ \frac{(y^+ + 10.6)^{9.6}}{(y^{+2} - 8.15y^+ + 86)^2} \right] \quad (5-3)$$

$$- 3.52 + \frac{\Pi}{\kappa} \left[ 6 \left( \frac{y}{\delta} \right)^2 - 4 \left( \frac{y}{\delta} \right)^3 \right] + \frac{1}{\kappa} \left( \frac{y}{\delta} \right)^2 \left( 1 - \frac{y}{\delta} \right)$$

The first three terms on the right hand side are an expression for the law-of-the-wall curve of eq. (4-10). The term having the coefficient of  $\Pi/\kappa$  is an algebraic form of the Coles wake function and the last term is an additional wake term obtained by Granville (1977) providing a zero velocity derivative at the edge of the boundary layer.

$Re_\theta$  can be expressed in wall units with simple algebraic manipulation

from the definition of  $\theta$  as follows:

$$u_e^+ = u^+(\delta^+) = \frac{U_e}{u_\tau} \quad (5-4)$$

$$Re_\theta = \int_0^{\delta^+} u^+ dy^+ - \frac{1}{u_e^+} \int_0^{\delta^+} u^{+2} dy^+ \quad (5-5)$$

$Re_\theta$  can be obtained by performing an integration using eq. (5-3) with a specific value of  $\Pi$  and assumed values of  $\delta^+$ . Two sets of turbulent boundary layer data for  $u_e^+$  and  $Re_\theta$  as a function of  $\Pi$  were obtained: one with the Granville term and the other without it.

Three Musker-Coles (MC) curves with  $\Pi=0.55$ , 0.4 and 0.35 are compared with the experimental data for grids 2, 3, and 4 in Figure 22(b). For  $Re_\theta > 1000$ , MC curves with  $\Pi=0.4$  and  $\Pi=0.35$  are in good agreement with the data of grids 3 and 4, respectively. Note that the wake strength diminishes with increasing freestream turbulence intensity, as expected. In Figure 22(c), three Musker-Coles-Granville (MCG) curves with  $\Pi=0.5$ , 0.35 and 0.3 are again compared with the same experimental data of grids 2, 3, and 4 respectively. For the  $Re_\theta$  range considered, each set of data agreed well with the corresponding MCG curves. The difference in  $U_e/u_\tau$  values between the MC and MCG curves is minimal in this range of  $Re_\theta$ . For more detailed values and lists of properties of the two models for the turbulent boundary layer on a flat plate, refer to the paper by Paik & Reshotko (1986).

The variation of the experimentally determined skin friction coefficient,

$C_f$ , with  $Re_\theta$  is presented in Figure 23(a). The present  $C_f$  data are again compared with theoretical Blasius curve of eq. (4-6) in the laminar boundary layer. The empirical correlation of turbulent boundary layer without considering the effect of freestream turbulence intensity expressed in eq. (4-12) is also plotted for rough comparison to the experimental data. For more detailed comparisons at the higher  $Re_\theta$ , MC and MCG curves with proper values of  $\Pi$  were used. In Figure 23(b,c), the deduced values of  $C_f$  are compared to the corresponding MC and MCG curves with constant  $\Pi$ . A similar discussion applies for  $C_f$  as for  $U_e/u_\tau$ . One thing to be noted is that the values of  $C_f$  for laminar and turbulent boundary layers are so different that  $C_f$  can be used to determine the transition region. The transition region thus determined is in good agreement with the region obtained from the mean velocity profiles.

### 5.2.3 Momentum integral quantities

The integral quantities such as momentum ( $\theta$ ) and displacement thickness ( $\delta^*$ ) were obtained by numerical integration of the mean velocity profiles using Simpson's rule, and the resulting shape factors ( $H = \delta^*/\theta$ ) were determined. The distributions of  $\theta$  with streamwise distance for the entire set of freestream turbulence levels are presented in Figure 24. The solid line in this figure is the least-squares approximation by polynomials of experimental data and the broken line is the Blasius solution. The location of the beginning of the transition region is also approximately predicted by checking the deviation of the experimental  $\theta$

curves from the Blasius growth. The beginning of transition thus determined is quite consistent with the location acquired from variations of mean velocity profiles and  $C_f$ .

Figure 25 shows the variation of shape factor with  $Re_\theta$  for the six grid configurations. Also plotted in this figure is the laminar value of 2.595 and the Musker-Coles-Granville curve with  $\Pi=0.3$  for a fully turbulent boundary layer. In some calculations of downstream development of turbulent boundary layers, the shape factor is often assumed to be constant. However,  $H$  is slightly decreasing with increasing  $Re_\theta$  in the turbulent boundary layers as shown in Figure 25.

The shape factors of the farthest three upstream locations for grid 0 and of two upstream locations for grid 0.5 and grid 1, are very close to the Blasius value of 2.595. The values of  $H$  are decreasing with increasing  $Re_\theta$  and finally level out when  $Re_\theta > 1000$  for grids 2, 3 and 4. The boundary layer profiles are getting fuller as Reynolds number increases. The shape factor is another rough way of determining the transition region.

The effect of heating the air flow on transition can be observed from the basic measurements of macroscopic quantities like profiles of mean and rms velocities, inferred skin friction and shape factor. The air flow in the heated boundary layer becomes more unstable than in the unheated boundary layer especially for low levels of freestream turbulence according to the boundary layer stability theory (Schlichting, 1979). For example, the transition region

starts at around  $X=17$  inches from the leading edge of the heated flat plate for grid 0. However, it begins at around  $X=40$  inches for the unheated case as indicated in the data of Suder et al. (1988) for the same grid configuration. For the coarse grids (grid 3 or grid 4), the transition locations for heated and unheated cases become quite similar. It can be thus said that the effect of heating on transition of the boundary layer becomes less sensitive for the freestream turbulence intensities associated with bypass transition.

#### 5.2.4 Streamwise rms velocity profiles

The streamwise rms velocity fluctuations,  $u'$ , (streamwise component of turbulence intensities) within the boundary layer were measured by the single-sensor probe at the same time as the mean velocity data were acquired. The profiles of the overall streamwise velocity fluctuations normalized with respect to  $U_e$  across the boundary layer are presented in Figure 26(a-f) for six levels of freestream turbulence. Recall that the corresponding mean velocity profiles for each grid were presented in Figure 20(a-f). The boundary layer profiles from  $X=5$  to 15 inches for grid 0, at  $X=5$  and 7 inches for grids 0.5 and grid 1 are believed to be laminar in the presence of freestream turbulence (pseudo-laminar boundary layer) with a peak value of rms  $u'$  occurring at  $y/\delta^* \approx 1.3$ , which is quite typical for the laminar boundary layer (Suder et al., 1988; Sohn & Reshotko, 1986; Wang et al., 1985).

The peak value of  $u'/U_e$  within the boundary layers grows rapidly and the

peak moves toward the wall as the flow develops downstream in the transition region. The magnitude of near-wall peak is largest in the transition region. The maximum peak value of  $u'/U_e \approx 0.13$  occurs at  $y/\delta^* \approx 0.5$  in the early stages of transition process as shown in the profiles of  $X=12$  inches for grid 0.5, of  $X=11$  inches for grid 1 and of  $X=7$  inches for grid 2. As the transition proceeds, another peak begins to appear at  $y/\delta^* \approx 2$ . While the near-wall peak diminishes, the second peak grows for a while and then decreases before both peaks reach some constant plateau value of  $u'/U_e \approx 0.075$  in the immature stage of the turbulent boundary layer. Also to be noticed in the turbulent profiles of  $u'$  throughout the boundary layer is that the values of  $u'$  rise to a peak, followed by a rather constant plateau value and then decrease to the freestream value with increasing distance from the wall. The freestream rms values are nearly constant over all streamwise locations measured for grids 0~2, but for grids 3 and 4 these values decrease as the flow develops downstream, which was also seen in the profiles of freestream turbulence intensity of Figure 19. The double peak in the transitional boundary layer is typical and has been reported by many other researchers (Arnal et al., 1978; Suder et al., 1988; Kuan & Wang, 1988; Kim et al., 1989). This double peak in the overall rms velocity profiles is believed to be due to the velocity jumping quickly between laminar and turbulent levels in the passage of turbulent spots, introducing some artificial overall rms velocity values at that specific location. This kind of velocity behavior can be seen from the direct hot-wire signals measured at near-wall locations as shown in Figure

32(a). Further discussion of the double peak in the transitional boundary layer will be given in conjunction with the presentation of the conditionally sampled rms velocity profiles in section 5.2.5.3.

The same rms velocity profiles scaled with wall units are presented in Figure 27(a-f) for the entire set of freestream turbulence intensities. The peak value of  $u'/u_\tau$  in the laminar boundary layer occurs at  $y^+ \approx 30$ . As the flow develops downstream, a double peak appears. The near-wall peak moves toward the wall from  $y^+ \approx 30$  to  $y^+ \approx 17$ , but the second peak moves outward roughly from  $y^+ \approx 60$  to  $y^+ \approx 150$  as shown in profiles for grids 0.5, 1 and 2. The magnitude of  $u'/u_\tau$  in the turbulent boundary layer is relatively constant at 1.8 in the region of  $20 < y^+ < 200$  and finally drops off to the freestream value as shown in Figure 27(c-f). From Figure 27(d-f), similarity of  $u'/u_\tau$  is found in the inner portion ( $y^+ < 180$ ) of the turbulent boundary layer just as the similarity of  $u^+$  was detected throughout the law-of-the-wall region of the turbulent boundary layer. Also in the same figures, note the phenomenon of rms velocity profiles being thinner (decrease of  $u'$ ) with decreasing Reynolds number in the outer portion ( $y^+ > 180$ ) of turbulent boundary layer. Purtell et al. (1981) argued that this decrease of  $u'$  may primarily reflect the suppression of all but the largest scales of the turbulence, because the large fluctuation scales become increasingly dominant in the turbulence as Reynolds number is decreased.

Note that the magnitude of  $u'/u_\tau$  in the near-wall peak at  $y^+ \approx 17$  for turbulent boundary layer shown in Figure 27(c-f) for grids 1 ~ 4 is low compared

to the expected value of 2.5 to 3.0 for a fully turbulent boundary layer as reported by Ligrani & Bradshaw (1987). The conclusion of Ligrani & Bradshaw (1987) from the measurement of turbulence intensity within the viscous sublayer of a turbulent boundary layer using hot-wire probes of various sizes is that the hot-wire sensing length of  $l_w^+$  should be less than 20 to properly resolve the small-scale near-wall turbulence. However,  $l_w^+$  of the commercially available hot-wire used in the present measurements is approximately 80 with  $u_\tau \approx 4.5$  ft/s. The peak value of  $u'/u_\tau$ , obtained in the near-wall region is thus measured to be less than the expected value for a fully turbulent boundary layer due to spanwise averaging of small eddies over the length of the standard hot-wire. Fortunately, the turbulent length scales present in transitional turbulent spots are much larger than the viscous length scale of a fully turbulent boundary layer. Consequently, the near-wall turbulence measurements acquired in the transition region should be more accurate than those acquired in the fully turbulent region.

### **5.2.5 Conditionally sampled profiles**

The intermittent signals from the hot-wire probe for two levels of freestream turbulence (1.1% and 2.4%) were sampled continuously with the high speed A/D data converter. The conditional sampling technique was employed to distinguish the digitally recorded signals into turbulent-like and laminar-like sections. The method for making turbulent/non-turbulent decisions from the intermittent velocity signals was explained in section 4.5

### 5.2.5.1 Intermittency factor

Once the threshold values for the first and second derivatives of smoothed detector function are determined at each data point, the indicator function can be obtained. Determination of the indicator function allows for calculation of an intermittency factor,  $\Gamma$ . The profiles of intermittency factor  $\Gamma(y)$  across the boundary layer at some streamwise locations for grids 1 and 2 are shown in Figure 28(a,b). In these figures the solid curve represents an error function distribution of intermittency factor which is a Gaussian integral curve, for the fully turbulent boundary layer as suggested by Klebanoff (1955):

$$\Gamma = \frac{1}{2} (1 - \text{erf } \zeta) \quad (5-6)$$

$$\text{where } \zeta = 5 \left[ \left( \frac{y}{\delta} \right) - 0.78 \right] = 5 \left[ \frac{1}{8} \left( \frac{y}{\delta^*} \right) - 0.78 \right] \quad (5-7)$$

Note that the relation of  $\delta = 8 \delta^*$  was obtained from the assumed  $1/7^{\text{th}}$  power law of mean velocity in a fully turbulent boundary layer. The intermittency distribution in a fully turbulent boundary layer indicates that instantaneous position of the edge of the boundary layer has a random characteristic with a mean position at  $y/\delta \approx 0.78$ .

As shown in Figure 28(a,b), the intermittency profiles in the transition region do not decrease monotonically across the boundary layer. Instead, a peak is observed near the wall at relatively low intermittencies ( $\Gamma < 0.8$ ). For grid 1, the intermittency value increases from 0.22 at the near wall position to a

maximum value of 0.34 at  $y/\delta^* \approx 1$  and then drops off toward zero approaching the edge of the boundary layer at  $X=9$  inches. Similarly,  $\Gamma$  increases from a near-wall value of 0.4 to a peak value of 0.55, occurring at  $y/\delta^* \approx 1$  for  $X=11$  inches. The same behavior is observed for grid 2, that is  $\Gamma_{\max} \approx 0.25$  at  $X=5$  inches and  $\Gamma_{\max} \approx 0.61$  at  $X=7$  inches for  $y/\delta^* \approx 1$  as shown in Figure 28(b). It can be suspected that the most frequent turbulent activity in the transitional boundary layer is taking place at one displacement thickness away from the wall in the early stages of transition. This near-wall drop-off of  $\Gamma$  is in good agreement with a vertical cross-sectional shape of turbulent spots which exhibits the leading and trailing edge overhangs as observed by Cantwell et al.(1978) and is also consistent with a recent result obtained by Kuan & Wang (1988). However, the data of Kim et al. (1989) for flat plate boundary layer with zero pressure gradient and of Blair (1988) for a moderately accelerating boundary layer do not exhibit a well-defined near-wall intermittency drop-off.

For higher intermittency cases at the farther downstream locations of  $X=17.5$  and 20 inches for grid 1 and of  $X=11$  and 13 inches for grid 2, a peak is followed by a plateau of nearly constant intermittency near the wall and then gradually decays to zero. This decay of  $\Gamma$  toward zero in the outer region is possibly due to the entrainment of the freestream flow into the boundary layer and the peaked-top shape of turbulent spots, i.e. the flow passes the turbulent spots less frequently in the region of  $y/\delta^* > 4$ .

### 5.2.5.2 Conditionally sampled mean velocity profiles

Plots of conditionally sampled mean velocity profiles normalized with wall units, obtained at the same streamwise locations as the intermittency profiles are shown in Figure 29(a-f) for grid 1 and in Figure 30(a-e) for grid 2. Three profiles: non-turbulent, overall and turbulent parts of intermittent flow are shown in each of these figures along with the Blasius,  $u^+ = y^+$  and the Musker curves for reference. The non-turbulent profiles represent the average of velocity data obtained during time segments when the indicator function was zero. The overall profiles were determined from a direct long time average of the digitally recorded data which include both non-turbulent and turbulent parts. The turbulent parts were obtained from the average of instantaneous velocities acquired during time segments when the indicator function was equal to one. The values of  $u_c$  used respectively to plot these three profiles were determined by using the same method described in section 4.1.2 according to laminar (non-turbulent), transitional (overall), and turbulent boundary layers respectively. Note that near-wall data ( $y^+ < 10$ ) were matched with the Blasius or  $u^+ = y^+$  curves for non-turbulent profiles and to the Musker curve for turbulent parts. For the cases of  $\Gamma < 0.9$ , the corresponding Blasius curves are shown. Note that the  $Re_c$  used for the Blasius profile was the result from the non-turbulent mean velocity profiles, not from the overall profiles.

Low-intermittency non-turbulent profiles at  $X=9$  inches for grid 1 and at  $X=5$  inches for grid 2 agree well with the corresponding Blasius profiles.

However, the non-turbulent profiles increasingly deviate from Blasius curves as the intermittency increases as shown in Figure 29(b-f) for grid 1 and in Figure 30(b-e) for grid 2. For the highest intermittency cases as shown in Figure 29(f) and Figure 30(e), the non-turbulent profiles fall considerably below the Blasius values. The turbulent profile has its maximum deviation from the log-linear profile early in the transition process, having the appearance of low Reynolds number turbulent boundary layers with a large wake region as shown in Figure 29(a) for grid 1 and in Figure 30(a) for grid 2. As the transition proceeds, the deviation from the log-linear region in the turbulent profiles is diminished. When  $\Gamma \approx 0.99$ , the shape of turbulent profiles looks quite like that of fully turbulent boundary layers as shown in Figure 29(f) and Figure 30(e). One thing to be noted in the turbulent profiles having low intermittency ( $\Gamma < 0.8$ ) is that the log-linear region does not seem to exist. This trend is consistent with the data of Kim et al. (1989) for low level of freestream turbulence and Cantwell et al. (1978). But on the contrary, the log-linear region of the turbulent parts exists in the results of Kuan & Wang (1988) and Blair (1988), even though this log-linear region was small when the transition process initiates. The conditionally sampled mean velocity results clearly indicate that the non-turbulent and turbulent flows during the transition cannot be treated simply as Blasius or fully turbulent flows, respectively.

The distribution of conditionally sampled  $C_f$  is shown in Figure 31(a,b) for grids 1 and 2, respectively. The well-known laminar solution of  $C_f$  for

Blasius profile and turbulent correlations accounting for the effect of freestream turbulence intensities suggested by Simonich & Bradshaw (1978):

$$\frac{C_f}{C_{f_0}} = 1 + 2 \frac{u'}{U_\infty} \quad (5-8)$$

were compared to conditionally sampled data, where  $C_{f_0}$  is the turbulent skin friction coefficient with zero freestream turbulence intensity (eq. 4-12).

The skin friction corresponding to the non-turbulent flow has the Blasius value at the lowest  $\Gamma$  measured for both grids 1 and 2, but increasingly deviates from the corresponding Blasius value as  $\Gamma$  increases. The increasing skin friction at the wall in the non-turbulent flow as transition proceeds could be explained as follows. A series of hot-wire voltage signals throughout the intermittent boundary layer at  $X=11$  inches for grid 1 is shown in Figure 32(a). The near-wall voltage trace [upper left plot in Figure 32(a) or top trace of Figure 18(a)] indicates that the transition from non-turbulent to turbulent flow takes place very quickly (very sharp increase of voltage from non-turbulent to turbulent signal at the front interface of each turbulent bursting). However, once the turbulent spot passes the wire, it takes a relatively longer time for the flow to return to the original non-turbulent level. This phenomenon, which was referred to as a *calming effect*, was also observed in the oscillogram of artificially generated turbulent spot traces obtained by Schubauer & Klebanoff (1955). These time segments of post-burst relaxation periods during which the transport

is laminar were declared as non-turbulent, although the magnitude of the instantaneous velocities in these time segments is larger than the non-turbulent baseline values. As  $\Gamma$  increases, the flow changes its status more frequently between non-turbulent and turbulent levels due to the increased number of turbulent spots. Therefore, more portions of post-burst relaxation periods are included in the non-turbulent parts as the transition proceeds. The higher velocities in non-turbulent flows near the wall show up as higher values of  $C_f$  than the Blasius values.

The skin friction coefficients for turbulent flow at the early stages of transition (low  $\Gamma$ ) is quite different from that of the fully turbulent boundary layer as shown in Figure 31(a,b). However, the values of  $C_f$  in turbulent parts get closer to those of the fully turbulent boundary layer as  $\Gamma$  increases. Although the deviation of  $C_f$  for the turbulent parts at low  $\Gamma$  from that of fully turbulent flow cannot be clearly explained, it can be speculated that only relatively large eddies are present at the early stages of transition so that the turbulence cascading as well as the dissipation is not yet fully established (Kim et al., 1989).

The distribution of conditionally sampled shape factor as determined from numerical integration of the conditionally sampled mean velocity profiles is shown in Figure 33(a,b) for grids 1 and 2, respectively. The similar behavior of each part of  $H$  to the corresponding variation of mean velocity or  $C_f$  is observed. The laminar  $H$  value of 2.595 at the lowest  $\Gamma$  for both grids and the decrease of

H with increasing  $\Gamma$  are detected in the non-turbulent flow. The approach of turbulent values of H to the fully turbulent value is observed as  $\Gamma$  increases. It is clear again that the non-turbulent and turbulent flows during transition cannot be thought of simply as the corresponding Blasius or fully turbulent flows.

The effect of higher freestream turbulence intensity on the conditionally sampled profiles is the quick strong deviation from the Blasius curve for non-turbulent flow and an early approach to the fully turbulent boundary layer for turbulent flow. For example, comparing the turbulent and non-turbulent profiles measured at  $X=11$  inches for grid 1 shown in Figure 29(b) to those for grid 2 shown in Figure 30(d), the effect of freestream turbulence intensity can be observed. These trends are reflected in the conditionally sampled profiles of  $C_f$  shown in Figure 31(a,b) and of H shown in Figure 33(a,b). At  $Re_x \approx 4.2 \cdot 10^5$ , the values of  $C_f$  and H for non-turbulent flow are almost laminar for grid 1, however, the corresponding values of  $C_f$  and H for grid 2 are quite deviated from the Blasius values. Also the values for the turbulent flow of grid 1 are quite different from the values for a fully turbulent boundary layer, but the corresponding values for grid 2 are very close to the fully turbulent ones.

#### **5.2.5.3 Conditionally sampled rms velocity profiles**

After the non-turbulent, turbulent and overall mean velocities were obtained from the digitally recorded velocity data, the rms values were directly calculated from the digital data with respect to the corresponding mean values.

Conditionally sampled turbulence intensity ( $u'/U_e$ ) profiles at six streamwise locations from  $X=9$  to 20 inches for grid 1 are presented in Figure 34(a-f). The overall rms values obtained from the digital records with sampling rate of  $20 \mu\text{s}$  and 32 Kbytes of record length which totaled about 640 ms of sampling time, were in very good agreement with the rms values directly acquired from the analog rms voltmeter. Recall that the laminar rms profiles presented in Figure 26(a-c) for the farthest upstream stations have a rounded shape and exhibit a peak at  $y/\delta^* \approx 1.3$  with a magnitude of  $u'/U_e$  less than 0.05.

The peak magnitudes of the non-turbulent flow are greater, however, than those observed for any of the strictly laminar profiles [see the non-turbulent profile at  $X=9$  inches shown in Figure 34(a)]. The peak values of  $u'/U_e$  increase gradually as the flow develops downstream ( $X=11$  and 13 inches), and stay at rather constant value of approximately 0.1 for the remaining streamwise locations ( $X=13, 15, 17.5,$  and 20 inches). The location of the peak value for non-turbulent flow gradually moves toward the wall from  $y/\delta^* \approx 1.3$  at  $X=9$  inches to  $y/\delta^* \approx 0.6$  at  $X=17.5$  inches. Note that the non-turbulent values at  $X=20$  inches are quite scattered, possibly due to the small time portion of non-turbulent flow at high intermittency ( $\Gamma \approx 0.99$ ). Some non-turbulent rms values exceed both turbulent and overall values especially in the range of  $0.5 < y/\delta^* < 1$  at some downstream locations ( $X=15, 17.5$  and 20 inches). This observation was supported by direct inspection of intermittent waveforms which revealed high levels of low-frequency unsteadiness in the non-turbulent intervals between

turbulent spots at those vertical locations, especially pronounced near  $y/\delta^* \approx 1$  as shown in the 4<sup>th</sup> traces of Figure 32(b) where the hot-wire velocity signals acquired within the boundary layer at  $X=15$  inches for grid 1 are presented.

For the farthest upstream location at  $X=9$  inches shown in Figure 34(a), the turbulent rms profile has a peak  $u'/U_e$  value of about 0.12 at  $y/\delta^* \approx 0.5$  indicating a high production of turbulence, which is larger than both peak values of overall and non-turbulent profiles. This near-wall turbulent rms peak is also bigger than the rms peak of fully turbulent boundary layer flow, which is  $u'/U_e \approx 0.08$  at  $y/\delta^* \approx 0.5$ . It can be speculated that the turbulent part is the main contributor to the near-wall peak of the overall signal in the early stages of transition. The magnitude of the near-wall turbulent peak is the highest at the lowest intermittency measured, and decreases significantly with downstream distance. This result indicates that the transport process occurring in the turbulent spots will not be well modeled by standard turbulence models used for the equilibrium turbulent boundary layer. For the farthest downstream location at  $X=20$  inches, the turbulent part has a shape which is similar to the shape expected for a fully turbulent boundary layer, with a peak very close to the wall followed by a relatively flat region and then a drop-off to the freestream values at the edge of the boundary layer.

Some of the profiles of directly calculated overall turbulence intensity exhibit a peculiar behavior. Overall rms values are higher than the rms values of intermittency-weighted averages of the respective non-turbulent and turbulent

parts at some locations, i.e. very near the wall ( $y/\delta^* \leq 0.6$  for  $X=11, 13$  and  $15$  inches) and also farther out in the boundary layer ( $1.5 < y/\delta^* < 4$ ). This result indicates the presence of the *mean-step* contribution to the overall rms value, which is associated with the switching between two significantly different mean values of non-turbulent and turbulent at these specific vertical measurement locations. For the instantaneous velocity signals shown in Figure 32(a), the velocity waveforms at near-wall locations ( $y/\delta^* < 0.6$ ) are characterized by large positive excursions during the passage of turbulent spots so correspondingly large apparent overall rms values are observed, resulting in the near-wall peak of overall rms profiles. Similarly, negative velocity excursions occur during the passage of a turbulent spot, which results in a large rms contribution to the second hump in the overall profiles at vertical measurement stations located farther out in the boundary layer ( $1.5 < y/\delta^* < 4$ ). See the overall rms profiles at  $X=13$  and  $15$  inches shown in Figure 34(c,d).

The *mean-step* contribution to overall rms velocity can be expressed using the formula developed by Hedley & Keffer (1974) following the procedure of conditional averaging suggested by Kovaszny et al. (1970).

$$\overline{u_o'^2} = \Gamma \overline{u_t'^2} + (1 - \Gamma) \overline{u_n'^2} + \Gamma(1 - \Gamma) (\overline{U_t} - \overline{U_n})^2 \quad (5-9)$$

where the subscripts  $o$ ,  $t$  and  $n$  represent overall, turbulent and non-turbulent parts respectively and  $\Gamma$  indicates the time-averaged intermittency function.

The *mean-step* contribution is given by the last term in the expression. The

magnitude of this term is the largest for intermediate values of intermittency and for large differences between turbulent and non-turbulent mean values. The contribution of this term becomes negligible at the crossover elevation within the boundary layer near  $y/\delta^* \approx 1.2$ , where the mean velocities of the non-turbulent and turbulent flows are nearly equal.

The conditionally sampled streamwise rms velocity profiles at five streamwise locations from  $X=5$  to 13 inches for the higher level of freestream turbulence with grid 2 are presented in Figure 35(a-e). The effect of the higher level of freestream turbulence can be seen in the profiles of the non-turbulent flows as an increase of the rms peak magnitude. Some portions of the non-turbulent rms values begin to exceed both turbulent and overall values even at  $X=7$  inches, while this behavior occurs at  $X=13$  inches for grid 1. The shapes of the turbulent rms profiles approach the rms profiles of the fully turbulent boundary layer at  $X=9$  inches for grid 2, while this behavior is observed at  $X=15$  inches for grid 1. Due to the *mean-step* contribution, values of overall rms velocity in excess of the non-turbulent and turbulent parts are observed again near the wall ( $y/\delta^* < 0.5$ ) and farther out in the boundary layer ( $2 < y/\delta^* < 4$ ) at streamwise locations of  $X=7, 9$  and 11 inches for grid 2. Therefore, it can be said that the turbulence intensity represented by the overall rms values in the transitional boundary layer is not a good indicator of true turbulent transport activity.

### 5.2.6 3-wire measurements

One of main objectives of this experimental study is to provide a momentum and thermal data base for transitional and low Reynolds number turbulent boundary layer ( $Re_\tau < 2300$ ) especially in a highly disturbed environment. The freestream turbulence was varied by the six grid configurations in a controllable manner as described before. In order to capture the high-frequency components of fluctuating velocity and temperature as well as their correlations through transition, simultaneous measurements in non-isothermal flow with a miniature 3-wire probe were made. With this 3-wire probe, the distributions of cross-stream velocity and temperature fluctuations, Reynolds shear stress as well as turbulent heat flux in a transitional boundary layer for a freestream turbulence intensity of 1.1% (grid 1) were obtained. Using digitally stored simultaneous signals from each of the three wires, conditional sampling was also performed for the Reynolds shear stress and turbulent heat flux. A detailed presentation of thermal quantities such as temperature fluctuations and turbulent heat flux in a transitional boundary layer will be given in section 5.3.5.

One of the profiles of streamwise rms velocity fluctuations measured at  $X=13$  inches for grid 1 with both the single and the 3-wire probe is presented in Figure 36. Due to the vertical X-shape of the 3-wire probe, the near-wall peak of streamwise turbulence intensity obtained by the single-wire was not captured with the 3-wire probe. However, the location and magnitude of the second peak

of  $u'/U_e$  as observed by both probes are in agreement within 5%. This agreement of  $u'/U_e$  indicates that the 3-wire measurement obtained along with the digital data processing technique is within the acceptable range.

#### 5.2.6.1 Vertical component of rms velocity

The distribution of normalized vertical component of rms velocity with streamwise distance for grid 1 is shown in Figure 37. The magnitude of rms  $v'$  is measured to be much smaller than the corresponding values of rms  $u'$  near the wall ( $y/\delta^* < 2$ ). However, the two values are getting closer to each other in the outer region ( $y/\delta^* > 5$ ) and finally become identical outside the boundary layers. The evolution of the rms  $v'$  profiles is quite different from the corresponding rms  $u'$  profiles in the transitional region. Recall that the  $u'/U_e$  value of the near-wall peak increased suddenly to a maximum at  $X=11$  inches and then gradually decreased to the magnitude for the fully turbulent boundary layer in the latter stages of transition with distance downstream as shown in Figure 26(c). However, the peak magnitude of  $v'$  is observed to increase gradually from  $v'/U_e \approx 0.045$  at  $X=9$  inches to  $v'/U_e \approx 0.07$  at  $X=15$  inches as  $\Gamma$  increases from 0.34 to 0.93, but nearly maintains that maximum value of  $v'/U_e \approx 0.07$ , thereafter. This is quite consistent with the result of Kuan & Wang (1988) in terms of magnitude and trend. In addition, the similarity of  $v'$  in the outer portion of the boundary layer ( $y/\delta^* > 2$ ) in the latter stages of transition process, which was also seen in the profiles of  $u'$ , is observed.

The behavior of  $u'$  and  $v'$  in the transitional boundary layer can be viewed as the distribution of turbulent kinetic energy in the steady shear flow (Tennekes & Lumley, 1972). The  $u'$  component has more energy than the other components because it receives all of the kinetic energy production from the mean flow. The transfer of turbulent kinetic energy to the other components is then performed by the nonlinear pressure-velocity interaction,  $\overline{p' \partial u'_i / \partial x_i}$ . In the early stages of transition when the eddies are relatively large, due to the production of turbulent kinetic energy, the energy is first accumulated in the  $u'$  component and then some is transferred to the other components. The energy in  $u'$  and  $v'$  components thus gain in strength resulting in the increase of rms values of  $u'$  and  $v'$ . As the transition proceeds, the eddies are getting smaller and smaller resulting in the increase of viscous dissipation until it is globally balanced with the energy production. Due to redistribution of some portions of its energy to other components, the energy in the  $u'$  component is thus getting diminished which shows in the decreased magnitude of rms  $u'$ . However, the energy in  $v'$  gained from the  $u'$  component is being locally balanced with viscous dissipation, which is seen as a relative constant value in the rms  $v'$  profiles in the latter stages of transition (see the profiles at  $X=15$ ,  $17.5$ , and  $20$  inches shown in Figure 37). Both rms  $u'$  and  $v'$  components reach a similar energy level closer to the edge of the boundary layer, nearing isotropy of the turbulent fluctuations at the edge of the boundary layer in these latter stages of transition.

### 5.2.6.2 Reynolds shear stress

The development of Reynolds shear stress,  $-\overline{u'v'}$  in the transitional boundary layer for a freestream turbulence intensity of 1.1% was computed from digitally recorded instantaneous signals in a post-processing data reduction. Figure 38(a) shows the distribution of correlation coefficient of  $u'$  and  $v'$  within the boundary layer. These profiles represent Reynolds shear stress normalized with the product of rms velocity fluctuations. Note that the vertical distance from the wall was normalized with boundary layer thickness,  $\delta$  (the  $y$  value when  $U=0.995 U_e$ ). In the early stages of transition, the correlation coefficients have peak values of about 0.2 around  $y/\delta_{.995} \approx 0.65$  at  $X=9$  inches and of about 0.3 around  $y/\delta_{.995} \approx 0.45$  at  $X=11$  inches and then decrease to the freestream value as the profiles reach the edge of the boundary layer. The correlation coefficients in the outer portions of the boundary layer ( $y/\delta_{.995} > 0.7$ ) at two streamwise locations of  $X=9$  and 11 inches are rather scattered due to the very small rms values of  $u'$  and  $v'$ . It can be said that when the intermittency is less than some threshold value (about 0.5 in this study) the correlation coefficients are somewhat meaningless because the values of both numerator and denominator in the correlation coefficient are relatively small. However, with distance downstream, the correlation coefficient becomes larger and the locations of the constant plateau values of correlation coefficient move toward the wall. For profiles at  $X=20$  inches when the nominal intermittency factor is about 99% the plateau value of the correlation coefficient is 0.42 in the range of  $0.1 < y/\delta_{.995} < 0.4$  (this

is somewhat less than the fully turbulent correlation coefficient). A correlation coefficient for a fully turbulent boundary layer of between 0.45 and 0.54 was reported by other researchers (Chen & Blackwelder, 1978; Senda et al., 1980; Blair, 1984).

The distribution of Reynolds shear stress normalized with  $u_\tau^2$  for grid 1 is shown in Figure 38(b). The peak value of  $-\overline{u'v'}/u_\tau^2$ , which is about 0.5 at  $X=9$  inches, significantly increases as  $\Gamma$  increases, attaining a maximum peak value of about 2.0 at  $X=13$  inches and then decreases to a value of 1.0. In addition, the peak in each profile is observed to move progressively toward the wall as the transition proceeds. This behavior of the  $-\overline{u'v'}$  profiles which is consistent with the observations of Kuan & Wang (1988) for approximately the same levels of freestream turbulence, is seen to be similar to that of rms  $u'$  profiles presented in Figure 27(c).

One thing to be mentioned about the data measured with the 3-wire probe is that large effects of eddy averaging are possibly involved in the data obtained with the X-shaped sensing wires in the thin layer of shear flow at the early stages of transition ( $l_w/\theta \approx 1.35$  at  $X=9$  inches and  $l_w/\theta \approx 1.01$  at  $X=11$  inches). Thus, in order to obtain more accurate data in a thin boundary layer without having significant averaging effects, the wire should be shorter which would require a very fine sub-micron diameter wire. This is not feasible, however. As transition proceeds, the boundary layer is getting thicker and the effect of  $l_w/\theta$  is diminished ( $l_w/\theta \approx 0.41$  at  $X=20$  inches). To confirm that the probe size effect

in the thicker boundary layer is small, the Reynolds shear stress profile was measured also at  $X=20$  inches for grid 3, which is shown in Figure 39 together with data acquired with grid 1. The Reynolds shear stress profile for grid 3 agrees well with that of the fully turbulent boundary layer reported by others, having a near-wall peak value of  $-\overline{u'v'}/u_\tau^2$  of 1.0 and monotonically decreasing to zero in the freestream. Thus, the Reynolds shear stress data obtained with the present probe configuration seem to be free from severe probe size effects.

The conditionally sampled Reynolds shear stress profiles normalized with  $U_e^2$  are presented in Figure 40 (a-d) for 4 streamwise locations. The non-turbulent contribution to the shear stress is, as expected, observed to be quite small within the boundary layer which means that non-turbulent components of the velocity fluctuations are weakly correlated throughout the boundary layer. Due to an insufficient number of samples, some portions of non-turbulent part indicate small negative values of  $-\overline{u'v'}$ . The turbulent parts clearly show a decrease of near-wall peak value with increasing  $\Gamma$ , while the peak location is gradually moving toward the wall. This result again indicates that the transport process occurring in a turbulent spot cannot be modeled by the conventional turbulence model used in the equilibrium turbulent boundary layer. Recall that the same observation was made for the conditionally sampled rms  $u'$  velocity profiles (section 5.2.5.3). Overall profiles which are affected by the *switching* effect between two different mean values, show an increase of near-wall peak values with an increase of  $\Gamma$  until  $X=15$  inches and then a slight decrease as  $\Gamma$

gets closer to 1. The peak of the overall profiles is also seen to move progressively toward the wall as transition proceeds. The overall values of Reynolds shear stress contributed mainly by the turbulent parts during the passage of turbulent spots in the intermittent boundary layer is not a true indicator of turbulent shear stress.

### **5.3 THERMAL BOUNDARY LAYER**

The thermal characteristics of laminar, transitional and low Reynolds number turbulent boundary layers are analyzed by measuring the boundary layer mean temperature profiles with a single-wire probe and obtaining the Stanton number distribution from wall temperature and surface heat flux measurements for the six levels of freestream turbulence ranging from 0.4% to 6%. The variation of Reynolds analogy factor which combines the information of  $C_f$  and  $St$ , was also acquired in the range of  $Re_\eta < 2300$ . The energy balance was checked by comparing the enthalpy thickness obtained from the integration of temperature profiles across the boundary layer with integration of the surface heat flux along the boundary layer for all grid configurations. Finally measurements of the profiles of turbulent heat flux as well as the fluctuating temperature were performed with the miniature 3-wire probe.

#### **5.3.1 Mean temperature profiles**

The profiles of boundary layer mean temperature plotted in wall units,  $T^+$

vs.  $y^+$ , for the six grid configurations corresponding to the mean velocity profiles of Figure 21(a-f) with the same conditions, are shown in Figure 41(a-f). Three types of reference curves are also plotted along with the experimental data in these figures. These are: 1)  $T^+ = Pr \cdot y^+$ , 2) the theoretical laminar temperature profile of eq. (4-22) obtained by solving the momentum and energy equations simultaneously with proper boundary conditions, including a correction for unheated starting length as explained in section 4.2.2, and 3) the temperature law-of-the-wall curve for fully turbulent boundary layers expressed in eq. (4-23) with constant values of  $Pr=0.708$  and  $Pr_t=0.9$ . Due to the finite unheated starting length of 1.375 inches, the profiles of theoretical laminar temperature deviate from the  $T^+ = Pr \cdot y^+$  curve for almost all  $y$  locations which indicates that the  $T^+ = Pr \cdot y^+$  curve is not a good indicator for representing the laminar mean temperature profiles. However, the theoretical laminar curve gets closer to the  $T^+ = Pr \cdot y^+$  curve as  $Re_\delta$  increases, which can be seen in the behavior of the laminar curves for the three upstream stations shown in Figure 41(a-c). Note that the values of  $u$ , used to construct these temperature profiles are the same values used to plot the corresponding mean velocity profiles. Therefore, once the values of surface heat flux were measured, the profiles of non-dimensional temperature,  $T^+$ , are rather strictly obtained without introducing any subjective decision.

The mean temperature profiles exhibit a behavior that is qualitatively similar to the mean velocity data. Excellent agreement of the farthest upstream

laminar profiles with the corresponding theoretical laminar curves is observed. The temperature profiles for grids 0.5, 1 and 2, again span nearly the entire range from laminar to turbulent boundary layer as did the velocity profiles. The similarity of the temperature profiles for the turbulent boundary layer can be seen in the log-linear region for grids 1 ~ 4 as shown in Figure 41(c-f). The effect of higher levels of freestream turbulence which is the erosion of wake strength in the outer region of the turbulent boundary layer is also observed for the thermal wake in these figures. The wake strength of the temperature profiles for grids 3 and 4 is completely eroded, while that of the velocity profiles still exists even though it is small. It can be argued that the effect of freestream turbulent fluctuations penetrates more in the temperature profiles than it does for the velocity profiles, especially in the outer portion of turbulent boundary layer as the freestream turbulence level increases.

One more striking feature observed in the transitional boundary layer is that the velocity profiles slightly lag the respective temperature profiles. This velocity lag can be clearly observed by comparing the mean velocity profiles at  $X=15$  inches for grid 1,  $X=11$  inches for grid 2 and  $X=7$  inches for grid 3 shown in Figure 21(c-e) to the corresponding temperature profiles shown in Figure 41(c-e), where the temperature profiles are in close agreement with temperature law-of-the-wall curve but the velocity profiles are still developing in the transitional region. This velocity lag is also reflected in the higher values of Reynolds analogy factor than  $Pr^{-2/3}$  as explained in section 5.3.3. This result is,

however, opposite in trend to the observations of Wang et al. (1985) and Kim et al. (1989).

A representative case of non-dimensional mean temperature variation,  $(T_w - T)/(T_w - T_o)$  across the boundary layer is shown in Figure 42 for the grid 0.5 configuration. The solid curve in this figure again represents the same theoretical laminar temperature profile as the curve shown in the previous figures. Note the excellent agreement of this theoretical laminar temperature solution with the experimental data in the laminar boundary layer. The profiles are then observed to progressively deviate from the laminar curve with distance downstream.

### 5.3.2 Heat transfer measurements

Stanton number variations obtained directly from wall temperature measurements and uniform heat flux determinations for six levels of freestream turbulence are presented in Figure 43 as a function of  $Re_x$ . The two analytical solutions for uniform heat flux with a correction for unheated starting length,  $X_o$ , suggested by Kays & Crawford (1980) are included in this figure. These are:

1) the theoretical laminar Stanton number variation

$$St = 0.453 Pr^{-\frac{2}{3}} Re_x^{-\frac{1}{2}} \left[ 1 - \left( \frac{X_o}{X} \right)^{\frac{3}{4}} \right]^{-\frac{1}{3}} \quad (5-10)$$

2) the correlation for a fully turbulent boundary layer with zero freestream

turbulence intensity

$$St = 0.03 Pr^{-0.4} Re_x^{-0.2} \left[ 1 - \left( \frac{X_o}{X} \right)^{0.9} \right]^{-\frac{1}{9}} \quad (5-11)$$

Note that the effect of unheated starting length on the laminar correlation is much greater than that on the turbulent correlation. For grids 0 to 2, the measured laminar Stanton number distributions are in agreement with the laminar curve. For grids 3 and 4, the  $St$  data measured at the farthest upstream locations already fall into the transitional region. As  $Re_x$  increases,  $St$  deviates from the laminar correlation and progressively approaches the turbulent correlation past the transition region. The location of boundary layer transition, as expected, moves upstream with increasing freestream turbulence. The heat transfer data of Figure 43 also indicate that the freestream turbulence has a bigger effect on the turbulent boundary layer than it does for the laminar boundary layer flows. The values of  $St$  of the turbulent boundary layer flows are clearly increasing with increasing freestream turbulence. Very small effect of freestream turbulence is observed in the laminar boundary layer flows. These data are in very good agreement with the data of Blair (1983) both in terms of magnitude and transition locations. A little bump in the turbulent data, especially for  $Re_x > 10^6$  is believed to be due to the imperfect smoothness of the plate surface which was constructed from nine pieces of heating elements. The measurements of momentum and thermal boundary layer data were, thus, performed at stations of  $Re_x < 10^6$ .

### 5.3.3 Reynolds analogy factor

A plot of Reynolds analogy factor,  $2 \cdot St/C_f$  obtained for the condition of uniform heat flux in the range of  $Re_x < 10^6$  ( $Re_\theta < 2300$ ) for the six levels of freestream turbulence is shown in Figure 44. Recall that the Reynolds analogy factor in air for a flat plate with zero pressure gradient and a thermal boundary condition of constant wall temperature is well represented by  $Pr^{-2/3}$  for both laminar and turbulent flows. However, the reference curves shown in Figure 44, representing the expected  $2 \cdot St/C_f$  for laminar and turbulent regimes, are quite different from a conventional  $Pr^{-2/3}$  curve due to the effects of the thermal boundary condition of uniform wall heat flux and an unheated starting length. Appropriate laminar and turbulent theoretical results suggested by Kays & Crawford (1980) were combined in order to obtain the curves shown. The laminar correlation plotted in this figure can be written in the following formula:

$$\frac{2 St}{C_f} = \frac{0.453}{0.332} \left[ 1 - \left( \frac{X_o}{X} \right)^{3/4} \right]^{-1/3} Pr^{-2/3} \quad (5-12)$$

The value 0.332 comes from the laminar skin friction relation with constant fluid properties and 0.453 is from the laminar heat transfer relation with a uniform wall heat flux condition, resulting in a ratio of 1.365. The  $St$  is augmented by 36.5% solely due to the uniform wall heat flux condition over the constant wall temperature case, which indicates that the heat transfer rate is very sensitive to the thermal boundary condition in the laminar region. The term in the bracket

accounts for the effect of unheated starting length which produces an additional augmentation of 17% at the farthest upstream location ( $X=5$  inches) and diminishes to 5% at the far downstream measurement station ( $X=20$  inches). Consequently, values of  $2 \cdot St/C_f$  as high as 2.0, which is increased about 53% compared to the value for constant wall temperature without any unheated starting length, can be expected in the laminar region.

The turbulent correlation which was treated quite similarly to the laminar correlation can be expressed as follows:

$$\frac{2 \cdot St}{C_f} = \frac{0.0300}{0.0287} \left[ 1 - \left( \frac{X_o}{X} \right)^{0.9} \right]^{-\frac{1}{5}} Pr^{-0.4} \quad (5-13)$$

For turbulent boundary layers, heat transfer results are much less sensitive to both thermal boundary condition (4.5% augmentation due to uniform heat flux) and unheated starting length (1% increase at  $X=20$  inches). Thus, the turbulent values are much closer to the well known  $Pr^{2/3}$  value of 1.26 with  $Pr=0.708$ .

The experimentally determined laminar data agree very well with the laminar prediction of eq. (5-12). Examination of Figure 44 reveals that the effect of freestream turbulence on  $2 \cdot St/C_f$  in the laminar region is negligible, which can be easily deduced from the observation of negligible effect of freestream turbulence on both skin friction and convective heat transfer in the laminar region. A progressive decrease of  $2 \cdot St/C_f$  with increase of freestream turbulence level is also observed in the transition region. As known from the

variation of skin friction and heat transfer, shown in Figures 23(a) and 43, both  $C_f$  and  $St$  increase with increasing level of freestream turbulence in the transition region. The decreasing value of  $2 \cdot St/C_f$  with increasing level of freestream turbulence in the transition region can be thus interpreted as a larger increase in  $C_f$  than in  $St$ . For example, as the freestream turbulence level increases from 1.1% to 2.4% (from grid 1 to grid 2),  $C_f$  increases 120% but  $St$  increases 65% at  $X=11$  inches, resulting in a corresponding decrease in the Reynolds analogy factor by 25%. The values of  $C_f$ ,  $St$  and  $2 \cdot St/C_f$  for the six levels of freestream turbulence are listed in Table I ~ VI.

The values of  $2 \cdot St/C_f$  for higher freestream turbulence cases (grids 3 and 4) in the post-transitional region are better predicted by  $Pr^{2/3}$  than by eq. (5-13). The data for lower freestream turbulence cases (grids 0.5, 1 and 2), on the other hand, are closer to the values obtained from eq. (5-13) than  $Pr^{2/3}$ . A slight increase of  $2 \cdot St/C_f$  with freestream turbulence level in the turbulent region, which is consistent with the result of Blair (1983) can also be detected. The behavior of  $2 \cdot St/C_f$  with freestream turbulence in the transitional region shows an opposite trend to that in turbulent region.

#### 5.3.4 Thermal energy balance

The thermal energy balance is checked by comparing the values of the enthalpy thickness,  $\Delta_2$ , obtained from integration of the boundary layer temperature profiles (profile measurement) with the corresponding values

calculated from the wall heat flux (wall measurement).  $\Delta_2$  from the profile measurement is the result of thermal energy flux contained in the boundary layer per unit width at that measurement station, while  $\Delta_2$  from the wall heat flux is the result of the cumulative convective heat transferred per unit width from the upstream boundary of the heated section, i.e. 1.375 inches from the leading edge of the flat plate. The comparison between the two measurements for the six grid configurations is shown in Figure 45(a-f). The agreement is generally good over the streamwise distance for all six levels of freestream turbulence. For the upstream locations ( $Re_\theta < 500$ ) with relatively low freestream turbulence (grids 0, 0.5 and 1) the relative deviation is more like  $\pm 15\%$ , possibly due to the closeness of the measurement location to the unheated portion of the flat plate. The thermal boundary layer development started from the heated section for each level of freestream turbulence is also depicted by the data in Figure 45(a-f). The development of the laminar boundary layer is rather slow for grid 0. A fast increase of  $\Delta_2$  with streamwise distance in the transitional region for grids 0.5 and 1 can be observed, while rather steady linear increase in the turbulent region for grids 3 and 4 is apparent. This behavior of the thermal boundary layer is generally similar to that of the momentum boundary layer which was shown in Figure 24 for streamwise variation of  $\theta$ .

### 5.3.5 3-wire measurements

In order to directly obtain the instantaneous temperature without solving a

series of nonlinear heat transfer equations for a fine wire, the temperature sensor was operated with the constant current mode of the temperature bridge.

However, due to the heat capacity of a temperature wire operated in a constant current mode, adequate frequency resolution for the temperature fluctuations was difficult to achieve with commercially available 5  $\mu\text{m}$  diameter wire. Therefore, a miniature 3-wire probe having a 1  $\mu\text{m}$  diameter temperature wire was designed to properly achieve a good frequency response up to a few KHz. This frequency limit was considered adequate for the present experiment at low-speed, low-overheat flow with maximum temperature difference between wall and freestream of about 15 °F.

Although the results of the 3-wire measurements of mean temperature and velocity profiles within the heated boundary layer indicated quite good consistency with the data obtained with a single-wire probe, when the same data reduction technique was applied to the data obtained on the unheated boundary layer, an erroneous result of a non-zero temperature fluctuation was observed. Figure 46 shows one set of temperature fluctuation profiles measured on the heated and unheated fully turbulent boundary layer for the grid 3 configuration. The temperature difference used to normalize the rms temperatures on the unheated surface is the same as the  $\Delta T (=T_w - T_\infty)$  for the heated case. The residual measurement noise in the rms temperature is nearly constant throughout the boundary layer, and is about 1% of  $\Delta T$ . The values of rms  $t'$  for the heated turbulent boundary layer decreased monotonically to the noise level as the probe

approached the edge of the boundary layer. Consequently a small percentage of uncertainty is expected in the results for instantaneous temperature measured for the heated boundary layers.

#### 5.3.5.1 RMS temperature profiles

The distribution of fluctuating temperature normalized with  $\Delta T$  within the transitional boundary layer for 1.1% level of freestream turbulence is presented in Figure 47. In the early stage of transition at  $X=9$  inches, the rms  $t'$  profile merely shows the monotonic decrease from the value of 0.065 at  $y/\delta^* \approx 1$  to the freestream uncertainty level. Due to the vertical X shape of the 3-wire probe, locating the temperature probe closer to the wall was not possible. No near-wall peak is thus observed at any streamwise station. As the intermittency increases, a peak which is probably the second peak, begins to appear at  $y/\delta^* \approx 2$ . The magnitude of the peak  $t'/\Delta T$ , which is about 0.085 at the relatively small flat portion around  $y/\delta^* \approx 2$  at  $X=11$  inches, significantly increases to the maximum value of 0.11 at  $X=13$  and 15 inches and then gradually decreases to the magnitude of 0.075 at  $X=20$  inches as  $\Gamma$  approaches unity. A double peak can also be seen in the profile measured at  $X=17.5$  inches. In addition, the similarity of the rms temperature profiles in the outer portion ( $y/\delta^* > 4$ ) of the boundary layer is also observed in the latter stages of transition. The trend, especially the vertical location and the maximum value of second hump in the rms temperature profiles is quite similar to that of the corresponding streamwise

rms velocity profiles shown in Figure 26(c). Note also that the rms temperature values for the fully turbulent boundary layer obtained with grid 3 (Figure 46) is quite identical to the profile obtained by Blair (1984) and by Senda et al. (1980). Therefore, as far as the rms values are concerned, the time-averaged data obtained with the miniature 3-wire probe are acceptable.

#### 5.3.5.2 Turbulent heat flux

Turbulent heat flux, which is a correlation of fluctuating  $v'$  and  $t'$ , was obtained from the digitally recorded instantaneous velocity and temperature signals. The distribution of turbulent heat flux normalized with the product of respective rms values (correlation coefficient) in the transitional boundary layer for grid 1 is shown in Figure 48(a). The values of turbulent heat flux in the transitional boundary layer are found to be negative except in the region of  $y/\delta_{.995} > 0.4$  at  $X=20$  inches. The nominal intermittency factors corresponding to these data for grid 1, range from  $\Gamma \approx 0.34$  to 0.99. The negative correlation indicates that  $v'$  and  $t'$  are out of phase in these flows. Since the mean temperature gradient is negative in the boundary layer, the negative correlation between  $v'$  and  $t'$  seemingly indicates that the average heat flux generated by the fluctuating flow is directed toward the wall. This is a peculiar result not reported in any previous studies, but the validity and repeatability of the experimental observation has been checked as explained in the following.

The above behavior is observed principally in the transitional boundary

layers. The values of the turbulent heat flux increase, however, as intermittency or Reynolds number increases and finally become positive at  $y/\delta_{.995} \approx 0.4$  when  $\Gamma \approx 0.99$  and  $Re_\theta \approx 1150$  ( $X=20$  inches). The value of the correlation coefficient of  $\overline{v't'}$  over the most part of a fully turbulent boundary layer is measured to be 0.5 by other researchers (0.51 for Chen & Blackwelder (1978) at  $Re_\theta \approx 2900$  and 0.55 for Blair (1988) at  $Re_\theta \approx 5400$ ). Obviously, the presently measured small positive value of this quantity even when  $\Gamma \approx 0.99$  contrasts with these earlier experimental results. To check if the correlation coefficient would approach 0.5 with increasing  $Re_\theta$ , the flow was disturbed by the coarser grid 3 and measurements were performed at further downstream locations i.e. at  $X=20$ , 38, and 45 inches. The correlation coefficients measured at  $X=20$  inches ( $Re_\theta \approx 2000$ ),  $X=38$  inches ( $Re_\theta \approx 2800$ ) and at  $X=45$  inches ( $Re_\theta \approx 3200$ ) for grid 3 are shown in Figure 48(b) along with some selected profiles for grid 1 already shown in Figure 48(a). The measurements at  $X=45$  inches were performed with a boundary layer trip using a fine saw blade placed at about 0.8 inches from the leading edge of the plate to further thicken the boundary layer. The values of correlation coefficient clearly increase as  $Re_\theta$  increases. However, the profile of the correlation coefficient even at  $X=45$  inches ( $Re_\theta \approx 3200$ ) exhibit values lower than 0.5 as measured by others. The profile shows a constant plateau value of about 0.4 in the region of  $0.4 < y/\delta_{.995} < 0.8$  and small negative values very close to the wall ( $y/\delta_{.995} < 0.05$ ). These measurements were repeated and reproduced every time.

A double check of the negative sign of turbulent heat flux was performed with a Nicolet 660A analog correlator. The station  $X=20$  inches for grid 3 was chosen where depending on  $y$ , both negative and positive values of  $\overline{v't'}$  were observed as shown in Figure 48(b). The unlinearized instantaneous  $v$  signal and the  $t$  signal were correlated. The magnitude of the correlation is thus incorrect but the sign should be correct. The results of the cross-correlation  $\overline{v't'}$  are presented in Figure 49(a,b). Figure 49(a) clearly shows a negative value when  $\tau=0$  at  $y/\delta_{.995} \approx 0.08$ , where the correlation calculated from the digital analysis was negative as shown in Figure 48(b). The correlation, at a location farther out to the edge of the boundary layer at  $y/\delta_{.995} \approx 0.48$ , is positive as shown in Figure 49(b). This is also consistent with the positive value of digitally calculated correlation in the range of  $y/\delta_{.995} > 0.2$  as shown in Figure 48(b).

The sign check for  $\overline{v't'}$  was also performed at  $X=11$  inches for grid 1, where all the correlations obtained from the digital record throughout the boundary layer were negative. Figure 49(c) represents the correlation obtained at mid-span and Figure 49(d) shows the correlation off center by one inch at  $X=11$  inches and  $y=0.049$  inches for grid 1. Both correlations are quite similar to each other and are clearly negative at  $\tau=0$ . Thus, there is no variation of the correlation in the spanwise direction, i.e. two-dimensionality of the time-averaged quantities is confirmed.

In order to qualitatively check the accuracy of the phase read by the instrumentation, the following experiment was performed at  $X=11$  and 20 inches

for grid 1. The 3-wire probe was turned 90 degrees to locate the plane of the X-wire facing normal to the flow. Only the upstream wire of the hot-wire pair was activated and the temperature wire was in the thermal wake of the hot-wire. Since the hot-wire is operated in constant-temperature mode, when the air flow is slow, the thermal wake is hotter as less air has to transfer the same amount of heat from the hot-wire. Thus the temperature wire senses a higher air temperature and vice versa. The velocity and temperature waveforms obtained with the above mentioned probe arrangement at  $X=11$  inches and  $y \approx 0.03$  inches for grid 1 are shown in Figure 50(a). The top trace is the instantaneous velocity signal from the upstream slanted wire and the bottom one is the uncompensated temperature signal obtained in the thermal wake. These two signals are visually compared over a time period of 0.08 sec. From Figure 50(a), the two signals are found to be well aligned within the expected phase inversion. This confirms that there is no phase lag introduced by the instrumentation. The two waveforms are similarly compared for  $X=20$  inches and  $y \approx 0.08$  inches for grid 1 with the same probe arrangement as in the previous case. The two signals are shown in Figure 50(b). Although not quite as clear here, closer scrutiny leads to essentially the same conclusion, that there is no phase shift introduced by the anemometers. Thus the operation of the 3-wire probe and the data reduction schemes seem both to have been properly performed, and so the focus must shift to the 3-wire probe itself. Since the spanwise separation of the velocity and temperature sensors in the present 3-wire probe configuration is relatively large

( $S \approx 0.52$  mm), it is speculated that the correlation of  $v'$  and  $t'$  may be improper. For a fully turbulent boundary layer measured at  $X=20$  inches with grid 3 ( $U_e \approx 100$  ft/s,  $u_r \approx 4.6$  ft/s), the spanwise distance between these sensors in wall units,  $S^+$  is about 46. This value of  $S^+$  is larger than the criterion of 20 suggested by Ligrani & Bradshaw (1987) for resolving proper fine-scale turbulent fluctuations especially in the near-wall region. With the same probe geometry, the only way to reduce the value of  $S^+$  is to lower the freestream speed, which in turn decreases the value of  $u_r$ . Another set of  $\overline{v't'}$  data was obtained with a reduced freestream speed of 45 ft/s at the same streamwise location of  $X=20$  inches for grid 3, resulting in  $S^+ \approx 22$ . The profiles of correlation coefficient of  $v'$  and  $t'$  across the boundary layer with the two different values of  $S^+$  measured at  $X=20$  inches for grid 3 are shown in Figure 51. Noticeable improvement of  $\overline{v't'}$  with the smaller value of  $S^+$  is clearly observed in this figure, even though the shape is different from that of previously reported data for the fully turbulent boundary layer. No distinct constant plateau value around 0.5 is seen and there are still small portions of negative  $\overline{v't'}$  very close to the wall.

Of all the possible reasons for the negative correlation of turbulent heat flux in the boundary layer, excessive spanwise separation of the wires of the multiple-wire probe could well be the crucial factor affecting a proper correlation of  $v'$  and  $t'$ . To resolve this issue, additional carefully controlled measurements with various values of  $S^+$  as well as data using another specially well-designed 3-wire probe are required in both transitional and fully turbulent boundary layers.

#### 5.4 BOUNDARY LAYER SPECTRA

Boundary layer transition, whether it is in T-S mode or bypass mode, is believed to occur when the freestream turbulence penetrates and perturbs the laminar boundary layer. It is thus important to determine the disturbance energy level in the boundary layer, which can be quantified as the level of the time-averaged rms fluctuating velocity. This has already been presented. Due to the frequency content of the disturbances, it is also necessary to measure boundary layer spectra in order to see the distribution of disturbance spectral energy (square of the velocity fluctuation) as a function of frequency bandwidth in the boundary layers. The disturbance frequency band which contributes most to boundary layer transition can also be determined from the boundary layer spectra. In this experimental study, one-dimensional boundary layer spectra were acquired for 4 levels of freestream turbulence using grids 0~2 at various streamwise locations from  $X=5$  to 20 inches. Three sets of boundary layer spectra were acquired depending on the vertical  $y$  locations. These are: 1) spectra measured at the possible nearest station to the wall ( $y=Y_0$ ), 2) spectra obtained at the location of maximum rms velocity fluctuation, and 3) freestream spectra.

The onset of the transition region as determined from profiles of skin friction and heat transfer rates occurred at  $Re_{\delta}^* \approx 1500$  for grid 0,  $Re_{\delta}^* \approx 1050$  for grid 0.5, and  $Re_{\delta}^* \approx 1000$  for grid 1, which are all much larger than the minimum critical Reynolds number  $Re_{\delta}^* \approx 480$  predicted from non-parallel linear

stability theory by Gaster (1974), and the minimum critical Reynolds number predicted from the parallel flow linear stability theory (Schlichting, 1979), which is  $Re_s^* \approx 520$ . The freestream turbulence levels studied in the spectral analysis thus produced post-critical transitions. The minimum critical Reynolds numbers quoted are for unheated boundary layers. In the present experiments  $T_w/T_e$  may get as large as 1.03. While this slightly reduces the minimum critical Reynolds numbers and slightly enlarges the range of amplified T-S frequencies, the values for the unheated boundary layer are close enough to provide guidance for the arguments used in the discussion.

A series of power spectral density (PSD) curves obtained at the closest near-wall locations for grid 0~2 configurations are presented in Figure 52(a-d). The spectra for grid 0 in the frequency range of 0 to 2000 Hz presented in Figure 52(a) show the broad-band humps over the frequencies of 750 Hz to 1000 Hz at  $X=5$  inches with  $Re_s^* \approx 760$ . This unstable frequency range is predicted by the linear stability theory. This broad-band hump is shifted to a lower frequency range, decreasing the size of frequency range with distance downstream. This behavior is also consistent with linear stability theory. The number of very narrow-band spikes that are apparent in the near-wall spectra are the harmonics of 60 Hz electric noise, the acoustic disturbance at the blower blade-passing-frequency and its harmonics. In addition, a strong peak observed at  $X=5$  and 7 inches in the frequency range of 800 Hz to 1000 Hz centered around at 900 Hz. This peak is not related to any intentional excitation and also

appears in the near-wall spectra for grid 0.5 and grid 1. Therefore, this peak is not grid-related, either. Very similar, narrow-band near-wall disturbances at somewhat higher frequencies were observed by Blair (1988) in mildly accelerating flow at a freestream turbulence level of 0.85%. Even though the naturally generated T-S waves reported by Arnal et al. (1978) and Suder et al. (1988) in post-critical flows depict similar effects, this strong narrow-bandwidth disturbance occurring very close to the wall was not reported. The slight decrease in the PSD out of this unstable frequency range where  $f < 400$  Hz or  $f > 1400$  Hz is clearly detected in the laminar region, which is also consistent with linear stability theory. It can be thus said that strong amplification of T-S waves is first clearly observed very close to the wall in the perturbed laminar boundary layer as shown in the near-wall spectra. Once transition is initiated, the PSD value increases with distance downstream over all frequency bands selected from 0 to 2000 Hz and the PSD decreases monotonically with increasing frequencies, as shown in the spectra of  $X=15$ , 17.5 and 20 inches (curves 6, 7 and 8). The dominance of low-frequency disturbances is also observed in the early stages of transition.

Note that the overall energy level associated with the disturbance fluctuations is directly proportional to the integral of the PSD over all frequencies. It is observed that the disturbance energy is largely contained in the low frequency range (below 200 Hz) and in the unstable T-S frequency bands (broad-band hump). The increase of overall energy within the boundary layer

with distance downstream is indicated in this figure, which trend is also observed in the overall rms velocity profiles for grid 0 shown in Figure 26(a).

Figure 52(b) and 52(c) represent the distribution of PSD for grid 0.5 and grid 1, respectively. For grid 0.5 case, the preferred bandwidth amplification is in the frequency range of 750 Hz to 1700 Hz and is centered at around 1350 Hz at the farthest upstream location of  $X=5$  inches. This broad-band hump is shifted to slightly lower frequencies and amplified in the unstable frequency range with distance downstream. From the linear stability theory, the disturbances occurring in the frequency range of 700 Hz to 1800 Hz at  $Re_\theta^* = 790$  for grid 0.5 should be amplified, which trend is seen in Figure 52(b). The linear stability theory also indicates that the disturbances occurring outside of this frequency range would be damped. The spectra for grid 0.5 partially follow the behavior predicted by the linear stability theory in the frequency range below 250 Hz. However, the disturbance occurring at frequencies greater than 1700 Hz are not damped as predicted by the linear stability theory, but rather are amplified with increasing streamwise distance. Once the turbulent bursting was initiated (intermittency was first observed) at  $X=8$  inches (curve 4), the values of PSD increase rather dramatically at all frequencies including the frequencies below 250 Hz, which means that the disturbance energy level due to the bursts of broad-band turbulence overwhelms the energy level produced at the frequencies of T-S band in the boundary layer. As the intermittency increases with distance downstream, the energy level increases significantly over all frequencies. Once

the disturbance energy reached a peak value (curve 6), the energy level associated with the frequencies below 250 Hz drops off as the boundary layer develops, but the energy level corresponding to the frequencies greater than 300 Hz remains relatively constant (see curves 7 and 8). The trend of power spectra in the frequencies below 250 Hz is almost identical to that of overall rms velocity profiles for grid 0.5 shown in Figure 26(b). Therefore, it can be said that the disturbance fluctuations in the low frequency range especially below 250 Hz are the dominant portion of the overall rms velocities within the boundary layer.

The power spectra for the grid 1 case shown in Figure 52(c) indicate the same trends as for grid 0.5 case. The main difference between the two configurations is the value of PSD in the relatively high frequencies from 500 Hz to 2000 Hz especially in the laminar region. The energy level over the band of frequencies greater than 500 Hz between  $X=5$  and 7 inches (curves 1 to 3) for grid 1 is higher than the corresponding energy level for grid 0.5 due to higher freestream turbulence level. The PSD magnitudes below the frequencies of 300 Hz, the development and frequency range of broad-band humps in the laminar region as well as the PSD values after the initiation of turbulent bursts over all the frequencies are quite similar for these two grids.

The spectra for grid 2 in the frequency range of 0 to 5000 Hz shown in Figure 52(d) do not show any clear evidence of selective amplification, which can be seen in previous cases for lower levels of freestream turbulence. This is

expected because mean characteristics measured at the farthest upstream location indicate a deviation from the theoretical mean laminar boundary layer. Large-amplitude, low-frequency (below 200 Hz) disturbances at several upstream stations (curves 2 to 5) are observed. The PSD values in the low frequency range increase to a maximum at  $X=7$  inches (curve 3) during the burst of turbulence and then decrease to the freestream value as the boundary layer develops (curve 4, 5 and 6). This behavior of power spectra for grid 2 at the low frequencies is again consistent with that of the corresponding rms velocity profiles shown in Figure 26(d). The low-frequency disturbances are thus the main contributor to the overall fluctuating velocities in the boundary layer for all levels of freestream turbulence studied. Again, the PSD values for grid 2 decrease with increasing frequency.

Boundary layer spectra were also measured at other  $y$  locations. The spectra obtained farther out in the boundary layer where the rms velocity has its maximum are shown in Figure 53(a-d) for all 4 levels of freestream turbulence. Note that the vertical measurement locations for each grid were decided based on the overall rms velocity profiles shown in Figure 26(a-d). This location is shifted toward the wall from  $y \approx 1.3 \delta^*$  to  $y \approx 0.5 \delta^*$ , as transition proceeds.

The spectra for grid 0 shown in Figure 53(a) do not indicate any pronounced broad-band humps, which means almost all PSD values decrease with increasing frequency. The disturbances in the laminar boundary layer at streamwise locations of  $X=5$  to 11 inches (curves 1 to 4) are slightly damped

over all frequencies from 0 to 2000 Hz. The spectra in the laminar region do not show any selective amplification even in the predicted unstable frequency range, although the near-wall spectra shown in Figure 52(a) clearly indicated the selective amplification of T-S waves. This is possibly due to a large increase of unsteadiness level at the current measurement location (maximum rms velocity) compared to the disturbance levels at the near-wall location ( $y=Y_0$ ). Comparing the spectra shown in the two figures, the PSD values in the frequencies below 800 Hz are increased by two orders of magnitude ( $10^2$  times) and the PSD values in the frequencies above 800 Hz are increased by at least one order of magnitude ( $10^1$  times) in the perturbed laminar region. Therefore, the energy level produced at the frequencies associated with T-S waves becomes overshadowed by the large increase of PSD due to elevated location of  $y \approx 1.3 \delta^*$  at all frequencies. The increase of energy level due to elevation was largest at the farthest upstream location and then decreased slightly with distance downstream in the laminar region. In addition, the near-wall strong peak, centered at 900 Hz with the magnitude of PSD of  $10^{-6}$  V<sup>2</sup>/Hz is still observed at  $X=5$  inches (curve 1) because the increase of energy level due to elevation is insufficient to overshadow the near-wall peak, while all the harmonics of noise and blower blade-passing frequencies shown in the near-wall spectra are overshadowed. Once turbulent bursts are initiated, the effect of increasing energy level due to elevation is apparently diminished, which means that the energy level generated by the turbulent bursting in a wide band of frequencies is much higher than the

energy level increased by moving toward the location of maximum rms velocities. The PSD values at  $X=17.5$  and 20 inches (curves 7 and 8) are very similar to each other at the frequencies below 500 Hz and only very slightly different at frequencies over 500 Hz. For the low level of freestream turbulence with grid 0 (0.4%), the selective amplification of unstable frequency range of T-S waves is suspected to be the dominant mechanism in the process leading to the formation of turbulent spots, although the energy produced by the unstable T-S waves is already overshadowed by the large energy levels at  $y \approx 1.3 \delta^*$ .

The spectra for grid 0.5 measured at elevations corresponding to the maximum observed rms values indicate no broad-band hump as shown in Figure 53(b), which is consistent with the result of Blair (1988). Although the disturbances at frequencies below 400 Hz are not amplified in the laminar region, it is very difficult to select a preferred bandwidth showing selective amplification of disturbances in the laminar boundary layer. Comparing the boundary layer spectra at the two different  $y$  locations, the increased energy level by two orders of magnitude due to elevation over the frequency range of 500 Hz to 1000 Hz in the laminar region can be detected. Once turbulent bursting was initiated, the deviation of PSD values obtained at two different  $y$  locations is quite diminished. As the intermittency increases, the behavior of the two sets of boundary layer spectra is becoming more identical.

The power spectra for grid 1 shown in Figure 53(c) are similar in trend to the spectra for grid 0.5 presented in Figure 53(b). The only differences

detected are again in the magnitudes of PSD in the laminar region, i.e. the larger energy level due to elevation. No clear evidence of selective amplification is observed. Apparently the large-amplitude, low-frequency (less than 200 Hz) unsteadiness is not related to the unstable frequencies predicted by linear stability theory. The spectra of grids 0.5 and 1 indicate that the receptivity and selective amplification of disturbance frequencies in the range predicted by linear stability theory can occur only in laminar boundary layers perturbed by levels of freestream turbulence less than 1%. However, T-S waves thus generated are localized very near the wall and do not seem to play a dominant role in the ultimate transition process at this level of freestream turbulence.

The spectra for grid 2 measured at the  $y$  locations of maximum rms velocity that are shown in Figure 53(d) indicate very similar trends in the intermittent boundary layer to the near-wall spectra. Recall that due to the closeness of transition onset to the leading edge of the plate, no laminar boundary layers were observed for grid 2. The overall energy level is largely comprised of the velocity fluctuations at frequencies below 200 Hz and this low-frequency hump reaches its maximum at  $X=7$  inches, then drops off with increasing intermittency. The higher disturbance energy level due to elevation is the only main difference between the two sets of spectra obtained at the two different  $y$  locations. The post-critical transition process for a freestream turbulence level of 2.4 % (grid 2) can be termed a bypass transition in the sense that it does not follow the progression described by the selective amplification of

T-S waves for low freestream disturbance cases.

The spectra outside the boundary layer were also acquired at several different streamwise locations about 1.5 inches above the heated plate for the four grid configurations. The spectra measured at one streamwise location were nearly identical to those obtained at other locations for each level of freestream turbulence. This is quite consistent with the observation of almost constant levels of freestream turbulence throughout the streamwise locations for grids 0 to 2 as shown in Figure 19. A typical freestream spectrum for each grid configuration is shown in Figure 54. The freestream disturbance energy is comprised largely of low-frequency fluctuations less than 300 Hz. The PSD values are exponentially decreasing (linear decrease in semi-log plot means exponential decrease) with increasing frequency for each grid. The magnitude of freestream disturbance energy for grid 0.5 is increased by one order ( $10^1$  times) of magnitude over the corresponding levels for grid 0 over all frequencies. An additional order of magnitude increase of freestream energy level was also observed in going from grid 0.5 to grid 2. However, the increase from grid 0.5 to grid 1 is marginal, showing a slight increase in the relatively high frequency range of 200 Hz to 2000 Hz. The present freestream spectra for grids 0.5 and 1 are very close to those of Suder et al. (1988). The PSD values for grid 0 are about an order of magnitude above those of Suder et al. (1988) for frequencies above 50 Hz.

While the overall level of freestream unsteadiness is only increased from

0.4% for grid 0 to 0.8% for grid 0.5, the freestream spectral energy level is increased by an order of magnitude over almost the entire frequency range. This large increase of freestream disturbance energy level can definitely affect the disturbance generation mechanism in the laminar boundary layers. This relatively high level of freestream disturbance transmitted to the boundary layers can possibly trigger nonlinear wide-bandwidth disturbance growth, masking disturbances that might be amplified according to the linear growth of T-S waves in a perturbed frequency range. The mechanism of linear growth of T-S waves can thus be bypassed. However, the unsteady disturbance energy level very near the wall is relatively low due to strong action of viscous dissipation. The only locations where one can detect linear narrow-band disturbance growth attributable to T-S waves is near the wall for moderate levels of freestream turbulence below 1% (grids 0, 0.5 and 1).

For grids 3 and 4, the boundary layer transition is unambiguously caused by bypass mechanisms since the transition occurs upstream of the minimum critical Reynolds number predicted from linear stability theory. Detailed probing of the pre-transitional boundary layer was not possible in these cases because the transition occurred very close to the leading edge of the flat plate. Intermediate freestream turbulence levels ranging from 0.8% to 2% produced the post-critical transitions. These cases are still termed bypass, however, in the sense that they do not follow the classical progression predicted from linear stability theory over the most of the boundary layer ( $y > 1.3 \delta^*$ ), even though T-S modes are observed

very close to the wall. The lowest freestream turbulence intensity case of 0.4% (grid 0) perhaps produced a T-S mode transition process.

## CHAPTER VI

### SUMMARY AND CONCLUSION

A detailed investigation of momentum and thermal boundary layer development focusing on the boundary layer transition process in the presence of freestream turbulence and surface heat transfer, was carried out on a heated flat plate with zero pressure gradient as part of an ongoing research program. The freestream disturbance levels were measured to be nearly constant at values of 0.4% for grid 0, 0.8% for grid 0.5, 1.1% for grid 1, 2.4% for grid 2 which indicates the uniformity of the freestream fluctuating flow. For grid 3 the turbulence level falls from 5.5% to 4% over the test section and for grid 4, the range is from 6.5% to 5%, indicating that turbulent cascading is still in progress at the streamwise measurement locations.

For each level of freestream turbulence, the time-averaged overall quantities measured with a boundary-layer type single-sensor probe and thermocouples were used to determine the macroscopic momentum and thermal characteristics of laminar, transitional and low Reynolds number turbulent boundary layers. The instantaneous velocities and temperatures were measured simultaneously with a miniature 3-wire probe to determine correlation quantities

of the transitional boundary layers. Conditional sampling was also applied as a means of segregating the turbulent and non-turbulent parts from the digitally recorded velocity signals of both the single and 3-wire probes in the intermittent boundary layers for two levels of freestream disturbance of 1.1% and 2.4%.

The profiles of measured boundary layer mean velocity, inferred skin friction coefficient and calculated shape factor as well as the momentum and displacement thicknesses obtained at several streamwise locations were observed to be in good agreement with laminar theory for grids 0 to 1 and turbulent correlations with appropriate wake strength for grids 2 to 4 along with intermediate transitional values. Negligible effects of freestream turbulence intensity on the above mentioned quantities were observed for the laminar boundary layer. The turbulent wake strength was gradually diminished as freestream turbulence intensity increased which was observed in the turbulent boundary layer profiles of mean velocity,  $C_f$  and  $H$ . Transition was observed as a rapid increase of the near-wall peak of rms  $u'$  at  $y/\delta^* \approx 0.5$  and the occurrence of second peak at  $y/\delta^* \approx 2$  due to the switching effect between two different laminar and turbulent levels. This observation is consistent with other studies.

Intermittency profiles across the transitional boundary layers exhibited a peak at  $y/\delta^* \approx 1$ , especially pronounced with lower  $\Gamma$ , which is consistent with turbulent spot shapes observed in the previous studies indicating a maximum spot length away from the wall. The profiles of conditionally sampled mean velocity,  $C_f$  and  $H$  indicated that at the beginning of transition, the non-turbulent profile

had a Blasius shape but the turbulent parts had quite different shapes from the fully turbulent boundary layer. As  $\Gamma$  increased, the non-turbulent parts were observed to deviate increasingly from the corresponding Blasius shapes, while the turbulent parts were observed to approach the shape of fully turbulent profiles. Conditionally sampled rms velocity profiles revealed a very interesting feature. High levels of unsteadiness observed in the non-turbulent part overwhelmed the overall and turbulent counterparts at some streamwise locations as  $\Gamma$  increased. The turbulent part possessed peak turbulence intensities as much as 50% higher than the corresponding fully turbulent values at early stages of transition and then gradually approached a fully turbulent shape as  $\Gamma$  increased. From this observation of conditionally sampled profiles, it is clear that the non-turbulent and turbulent parts in the transitional flow cannot be treated as the theoretical laminar and fully turbulent flows, respectively.

The rms  $u'$  values obtained from direct voltmeter readings and from the calculation of digitally stored signals of both the single and 3-wire probe were all consistent. Data reduction for the 3-wire measurement was thus accurate and the flow was also well-behaved. The cross-stream velocity fluctuation ( $v'$ ) indicated that a large degree of anisotropy existed within the transitional boundary layer until isotropy was achieved near the edge of the boundary layer. Conditionally sampled Reynolds shear stress profiles indicated that the non-turbulent parts had negligible values throughout the boundary layer and the turbulent parts were gradually decreased until fully turbulent values were reached. Generally the

conditionally sampled and overall quantities of the momentum boundary layers were measured to be in good agreement with previously reported data.

Boundary layer mean temperature profiles and surface heat transfer in the laminar regions were in excellent agreement with laminar solutions accounting for uniform heat transfer rate and unheated starting length. The effect of short but finite unheated starting length was not significant for the turbulent correlations. Thermal wake strengths observed in the outer portion of turbulent boundary layers were diminished as the freestream disturbance level increased. Comparing the momentum and thermal boundary layers in the transitional region, the velocity profiles were observed to lag the temperature profiles, which was opposite to the observations of Kim et al. (1989) and of Blair (1988). Energy closure as checked by comparison of enthalpy thickness obtained from both profile and wall measurements was satisfactory. The effect of freestream turbulence level on surface heat transfer is identical to its effect on  $C_f$ . Increasing values of  $St$  with increasing levels of freestream turbulence in the turbulent region but negligible effect on the laminar values were observed. The location of boundary layer transition moved progressively upstream with increasing levels of freestream turbulence. Measured Reynolds analogy factors were found to be well predicted by combining appropriate correlations including the corrections for the thermal boundary condition of uniform heat flux and unheated starting length for the respective laminar and turbulent regimes. Consequently, Reynolds analogy factors were measured to be increased as much

as 53% compared to the value of  $Pr^{2/3}$  (1.26) in the laminar region but were not very sensitive to either thermal boundary condition or unheated starting length in the turbulent region.

The rms fluctuating temperature profiles measured with the 3-wire probe indicated the quite similar development to the streamwise rms velocity profiles in transitional boundary layers in terms of magnitude and peak location, showing, for example, double humps at the intermediate value of intermittency. The profiles of turbulent heat flux,  $\overline{v't'}$  acquired from the digitally recorded instantaneous velocity and temperature signals indicated negative values in certain cases, especially in the intermittent region. Even when  $\Gamma \approx 0.99$  and  $Re_\theta \approx 1150$  with freestream turbulence intensity of 1.1%, the measured turbulent heat flux was negative near the wall over about 30% of boundary layer thickness. However, the turbulent heat flux measurement became positive as  $Re_\theta$  increased and the profiles approached the shape observed by others in fully turbulent boundary layers at  $Re_\theta \approx 3200$ . Excessive spanwise separation of the wires of the 3-wire probe could well be the crucial factor affecting a proper correlation of  $v'$  and  $t'$ . Significant changes in  $\overline{v't'}$  were obtained in tests where the freestream velocity was reduced to 45 ft/s. At this reduced speed (and therefore reduced dimensionless separation in wall units)  $\overline{v't'}$  were more positive and approached the levels observed by others in turbulent boundary layers.

The near-wall boundary layer spectra indicate that some selective

amplification of disturbances in the frequency range predicted from linear stability theory occurred in the perturbed laminar boundary layer for 0.4% of freestream turbulence intensity (T-S mode). However, for freestream turbulence levels of 0.8% and 1.1%, T-S waves were localized very near the wall and did not seem to play a dominant role in the ultimate breakdown to turbulence. The post-critical transition process for a freestream turbulence level of 2.4% can be termed a bypass mode because the progression was quite different from the one observed for the lower freestream turbulence cases. The existence of low-frequency ( $f < 200$  Hz) disturbances in the early stages of transition was also observed for all levels of freestream turbulence studied. As the transition proceeds, boundary layer spectra indicate a continuous decrease of disturbance amplitude with increasing frequency at all locations, but a continuous increase of amplitude with distance downstream. The amplitude of the low-frequency disturbances diminishes, however, beyond a certain intermittency level.

## REFERENCES

- Abu-Ghannam, B.J. and Shaw, R. (1980), "Natural Transition of Boundary Layers - The effects of Turbulence, Pressure Gradient, and Flow History," *J. Mech. Engr. Sci.*, Vol. 22, No. 5, pp. 213-228.
- Antonia, R.A. (1981), "Conditional Sampling in Turbulence Measurement," *Ann. Rev. Fluid Mech.*, Vol. 13, pp. 131-156.
- Antonia, R.A., Chambers, A.J., Sokolov, M. and van Atta, C.W. (1981), "Simultaneous Temperature and Velocity Measurements in the Plane of Symmetry of a Transitional Turbulent Spot," *J. Fluid Mech.*, Vol. 108, pp. 317-343.
- Arnal, D., Juillen, J.C. and Michel, R. (1978), "Experimental Analysis and Computation of the Onset and Development of the Boundary Layer Transition," *NASA TM-75325*.
- Arnal, D. (1984), "Description and Prediction of Transition in Two-Dimensional, Incompressible Flow," *AGARD Rep. No. 709*, pp. 2-1 to 2-71.
- Blair, M.F., Bailey, D.A. and Schlinker, R.H. (1981), "Development of a Large-Scale Wind Tunnel for the Simulation of Turbomachinery Airfoil Boundary Layer," *ASME J. Engr. for Power*, Vol. 103, pp. 678-687.
- Blair, M.F. (1982), "Influence of Free-Stream Turbulence on Boundary Layer Transition in Favorable Pressure Gradients," *ASME J. Engr. for Power*, Vol. 104, pp. 743-750.
- Blair, M.F. (1983), "Influence of Free-Stream Turbulence on Turbulent Boundary Layer Heat Transfer and Mean Profile Development, Parts I & II," *ASME J. Heat Transfer*, Vol. 105, pp.33-47.
- Blair, M.F. and Bennett, J.C. (1987), "Hot-Wire Measurements of Velocity and Temperature Fluctuations in a Heated Turbulent Boundary Layer," *J. Physics Engr.*, Vol. 20, pp. 209-216.
- Blair, M.F. (1988), "Bypass-Mode Boundary Layer Transition in Accelerating Flows," *submitted to J. Fluid Mech.*, November.

- Cantwell, B.J., Coles, D. and Dimotakis, P.E. (1978), "Structure and Entrainment in the Plane of Symmetry of a Turbulent Spot," *J. Fluid Mech.*, Vol. 87, pp. 641-672.
- Champagne, F.H., Sleicher, C.A. and Wehrmann, O.H. (1967), "Turbulence Measurements with Inclined Hot-Wires, Parts 1 & 2," *J. Fluid Mech.*, Vol. 28, pp.153-182.
- Chen, C.H.P. and Blackwelder, R.F. (1978), "Large-Scale Motion in a Turbulent Boundary Layer: A Study Using Temperature Contamination," *J. Fluid Mech.*, Vol. 89, pp. 1-31.
- Clauser, F.H. (1956), "The Turbulent Boundary Layer," *Advances in Applied Mechanics*, Vol. IV, Academic Press, New York, pp. 1-51.
- Collis, D.C. and Williams, M.J. (1959), "Two-Dimensional Convection from Heated Wires at Low Reynolds Numbers," *J. Fluid Mech.*, Vol. 6, pp. 357-384.
- Dhawan, S. and Narasimha, R. (1958), "Some Properties of Boundary Layer Flow During the Transition from Laminar to Turbulent Motion," *J. Fluid Mech.*, Vol. 3, pp.418-436.
- Dyban, YE.P., Epik, E.YA. and Suprun, T.T. (1976), "Characteristics of the Laminar Boundary Layer in the Presence of Elevated Free-Stream Turbulence," *FLUID MECHANICS - Soviet Research*, Vol. 5, No. 4, pp. 30-36.
- Emmons, H.W. (1951), "The Laminar-Turbulent Transition in a Boundary Layer - Part I," *J. Aero. Sci.*, Vol. 18, pp.490-498.
- Gaster, M. (1974), "On the Effects of Boundary-Layer Growth on Flow Stability," *J. Fluid Mech.*, Vol. 66, pp. 465-480.
- Gaugler, R.E. (1985), "A Review and Analysis of Boundary Layer Transition Data for Turbine Application," *NASA CP-2386*, pp.81-93.
- Graham, R.W. (1979), "Fundamental Mechanisms that Influence the Estimate of Heat Transfer to Gas Turbine Blades," *NASA TM-79128*.
- Hall, D.J. and Gibbings, J.C. (1972), "Influence of Stream Turbulence and Pressure Gradient Upon Boundary Layer Transition," *J. Mech. Engr. Sci.*, Vol. 14, No. 2, pp. 134-146.

- Hedley, T.B. and Keffer, J.F. (1974), "Turbulent/Non-Turbulent Decisions in an Intermittent Flow," *J. Fluid Mech.*, Vol. 64, pp. 625-644.
- Hishida, M. and Nagano, Y. (1978), "Simultaneous Measurements of Velocity and Temperature in Nonisothermal Flows," *ASME J. Heat Transfer*, Vol. 100, pp.340-345.
- Junkhan, G.H. and Serovy, G.K. (1967), "Effect of Free-Stream Turbulence and Pressure Gradient on Flat Plate Boundary-Layer Velocity Profiles and on Heat Transfer," *ASME J. Heat Transfer*, Vol. 89, pp. 169-176.
- Kays, W.M. and Crawford, M.E. (1980), **Convective Heat and Mass Transfer**, 2nd ed., McGraw-Hill, New York.
- Kim, J., Simon, T.W. and Kestoras, M. (1989), "Fluid Mechanics and Heat Transfer Measurements in Transitional Boundary Layer Conditionally Sampled on Intermittency," *presented at the 1989 ASME National Heat Transfer Conference*, Philadelphia, PA.
- Klebanoff, P.S. (1955), "Characteristics of Turbulence in a Boundary Layer with Zero Pressure Gradient," *NACA Rep. No. 1247*.
- Klebanoff, P.S., Tidstrom, K.D. and Sargent, L.M. (1962), "The Three-Dimensional Nature of Boundary-Layer Instability," *J. Fluid Mech.*, Vol. 12, pp. 1-34.
- Kovaszny, L.S.G., Kibens, V. and Blackwelder, R.F. (1970), "Large-Scale Motion in the Intermittent Region of a Turbulent Boundary Layer," *J. Fluid Mech.*, Vol. 41, pp. 283-325.
- Kramers, H. (1946), "Heat Transfer from Spheres to Flowing Media," *Physica*, Vol. 12, pp. 61-120.
- Kuan, C.L. and Wang, T. (1988), "Some Intermittent Behavior of Transitional Boundary Layer," *submitted to Experimental Thermal and Fluid Science*.
- Ligrani, P.M. and Bradshaw, P. (1987), "Spatial Resolution and Measurement of Turbulence in the Viscous Sublayer Using Subminiature Hot-Wire Probes," *Experiments in Fluids*, Vol. 5, pp. 407-417.
- McDonald, H. and Fish, R.W. (1973), "Practical Calculations of Transitional Boundary Layers," *Int. J. Heat and Mass Transfer*, Vol. 16, pp. 1729-1744.

- Morkovin, M.V. (1979), "On the Question of Instabilities Upstream of Cylindrical Bodies," *NASA CR-3231*.
- Musker, A.J. (1979), "Explicit Expression for the Smooth Wall Velocity Distribution in a Turbulent Boundary Layer," *AIAA Journal*, Vol. 17, No. 6, pp. 655-657.
- Paik, D.K. and Reshotko, E. (1986), "Low Reynolds Number Boundary Layers in a Disturbed Environment," *NASA CR-175031* (Also, Ph.D. Thesis of D.K. Paik, Case Western Reserve University, 1985).
- Perry, A.E. (1982), *Hot-Wire Anemometry*, Clarendon Press, Oxford.
- Purtell, L.P., Klebanoff, P.S. and Buckley, F.T. (1981), "Turbulent Boundary Layer at Low Reynolds Number," *Phys. Fluids*, Vol. 24, No. 5, pp. 802-811.
- Reshotko, E. (1976), "Boundary-Layer Stability and Transition," *Ann. Rev. Fluid Mech.*, Vol. 8, pp. 311-349.
- Reshotko, E. (1986), "Stability and Transition, How Much Do We Know?," *presented at the 10th U.S. National Congress of Applied Mechanics*, Austin, Texas.
- Rued, K. and Wittig, S. (1985), "Free-Stream Turbulence and Pressure Gradient Effects on Heat Transfer and Boundary Layer Development on Highly Cooled Surfaces," *ASME J. Engr. for Gas Turbines and Power*, Vol. 107, pp. 54-59.
- Schlichting, H. (1979), *Boundary Layer Theory*, 7th ed., McGraw-Hill, New York.
- Schubauer, G.B. and Klebanoff, P.S. (1946), "Theory and Application of Hot-Wire Instruments in the Investigation of Turbulent Boundary Layers," *NACA WR-86* (Originally, *NACA Adv. Conf. Rep.*, No. 5K27).
- Schubauer, G.B. and Klebanoff, P.S. (1956), "Contributions on the Mechanics of Boundary-Layer Transition," *NACA Rep. 1289* (Also, *NACA TN-3489*, 1955).
- Schubauer, G.B. and Skramstad, H.K. (1948), "Laminar-Boundary-Layer Oscillations and Transition on a Flat Plate," *NACA Rep. No. 909*.

- Senda, M., Suzuki, K. and Sato, T. (1980), "Turbulence Structure Related to the Heat Transfer in a Turbulent Boundary Layer with Injection," *Turbulent Shear Flows*, Vol. 2, Springer-Verlag, pp. 143-157.
- Simonich, J.C. and Bradshaw, P. (1978), "Effect of Free-Stream Turbulence on Heat Transfer Through a Turbulent Boundary Layer," *ASME J. Heat Transfer*, Vol. 100, pp. 671-677.
- Sohn, K.H. and Reshotko, E. (1986), "Transition in a Disturbed Environment," *Case Western Reserve University Rep. FTAS/TR-87-189* (Also, M.S. Thesis of K.H. Sohn, C.W.R.U., 1986).
- Sohn, K.H., O'Brien, J.E. and Reshotko, E. (1989), "Some Characteristics of Bypass Transition in a Heated Boundary Layer," *NASA TM-102126*.
- Suder, K.L., O'Brien, J.E. and Reshotko, E. (1988), "Experimental Study of Bypass Transition in a Boundary Layer," *NASA TM-100913* (Also, M.S. Thesis of K.L. Suder, C.W.R.U., 1988).
- Tani, I. (1969), "Boundary-Layer Transition," *Ann. Rev. Fluid Mech.*, Vol. 1, pp. 169-196.
- Tennekes, H. and Lumley, J.L. (1972), *A First Course in Turbulence*, 2nd ed., MIT Press, Massachusetts.
- Turner, A.B. (1971), "Local Heat Transfer Measurements on a Gas Turbine Blade," *J. Mech. Engr. Sci.*, Vol. 13, No. 1, pp. 1-12.
- van Driest, E.R. and Blumer, C.B. (1963), "Boundary Layer Transition: Freestream Turbulence and Pressure Gradient Effects," *AIAA Journal*, Vol. 1, No. 6, pp. 1303-1306.
- Wang, T., Simon, T.W. and Buddhavarapu, J. (1985), "Heat Transfer and Fluid Mechanics Measurements in Transitional Boundary Layer Flows," *NASA CP-2386*, pp. 69-79.
- White, F.M. (1974), *Viscous Fluid Flow*, McGraw-Hill, New York.
- Wynanski, I.J. and Champagne, F.H. (1973), "On Transition in a Pipe. Part 1. The Origin of Puffs and Slugs and the Flow in a Turbulent Slug," *J. Fluid Mech.*, Vol. 59, pp.281-335.
- Wynanski, I., Sokolov, M. and Friedman, D. (1975), "On Transition in a Pipe.

Part 2. The Equilibrium Puff," *J. Fluid Mech.*, Vol. 69, pp. 283-304.

Wynanski, I., Sokolov, M. and Friedman, D. (1976), "On a Turbulent 'Spot' in a Laminar Boundary Layer," *J. Fluid Mech.*, Vol. 78, pp. 785-819.

TABLE I

Characteristics of Momentum and Thermal Boundary Layer Profiles

Grid 0

$X$ (in)	$\theta$ (in)	$H$	$Re_x$	$Re_\theta$	$U_e$ (ft/s)	$u_e$ (ft/s)	$U_e/u_e$	$C_f$	$St$	$2 St/C_f$
5.0	0.006338	2.597	231379	293	101.7	2.778	36.607	0.0014924	0.0014988	2.0085
10.0	0.009469	2.620	460957	437	102.2	2.293	44.566	0.0010070	0.0009419	1.8707
15.0	0.012435	2.590	693143	575	103.2	2.063	50.015	0.0007995	0.0007327	1.8329
17.5	0.013639	2.574	811066	632	103.6	2.020	51.286	0.0007604	0.0006830	1.7964
20.0	0.017917	2.295	932113	835	103.8	2.225	46.665	0.0009184	0.0008011	1.7446

TABLE II

Characteristics of Momentum and Thermal Boundary Layer Profiles

Grid 0.5

$X$ (in)	$\theta$ (in)	$H$	$Re_x$	$Re_\theta$	$U_x$ (ft/s)	$u_x$ (ft/s)	$U/\mu_x$	$C_f$	$St$	$2 St/C_f$
5.0	0.006583	2.610	229423	302	100.5	2.712	37.604	0.0014559	0.0014559	2.0000
7.0	0.008411	2.596	323591	389	101.9	2.429	41.958	0.0011361	0.0010998	1.9362
10.0	0.010168	2.375	467347	475	102.6	2.450	41.863	0.0011412	0.0010699	1.8749
12.0	0.014080	2.031	552797	649	100.7	2.726	36.938	0.0014658	0.0012701	1.7330
15.0	0.019830	1.664	699612	925	101.6	3.365	30.202	0.0021926	0.0016284	1.4854
17.5	0.024665	1.535	837366	1180	102.8	4.050	25.373	0.0031065	0.0019766	1.2726
20.0	0.029302	1.493	944446	1384	101.5	4.265	23.792	0.0035331	0.0021665	1.2264

TABLE III

Characteristics of Momentum and Thermal Boundary Layer Profiles

Grid 1

$X$ (in)	$\theta$ (in)	$H$	$Re_x$	$Re_\theta$	$U_x$ (ft/s)	$u_x$ (ft/s)	$U/u_x$	$C_f$	$St$	$2 St/C_f$
5.0	0.007013	2.611	231596	325	102.2	2.670	38.265	0.0013659	0.0013662	2.0004
7.0	0.008436	2.598	318461	384	101.0	2.416	41.787	0.0011454	0.0011087	1.9360
9.0	0.010176	2.327	415391	470	102.2	2.527	40.448	0.0012225	0.0011377	1.8613
11.0	0.013579	2.014	490950	606	98.6	2.832	34.937	0.0016386	0.0014204	1.7337
13.0	0.018067	1.720	594165	826	100.4	3.385	29.669	0.0022721	0.0017334	1.5258
15.0	0.024144	1.515	714169	1150	103.9	4.190	24.809	0.0032494	0.0020368	1.2536
17.5	0.029058	1.503	828953	1377	103.3	4.348	23.746	0.0035470	0.0021210	1.1960
20.0	0.033445	1.457	944818	1580	102.9	4.352	23.645	0.0035771	0.0021817	1.2198

TABLE IV

## Characteristics of Momentum and Thermal Boundary Layer Profiles

Grid 2

$X$ (in)	$\theta$ (in)	$H$	$Re_x$	$Re_\theta$	$U_x$ (ft/s)	$u_x$ (ft/s)	$U/u_x$	$C_T$	$St$	$2 St/C_T$
5.0	0.007070	2.476	227817	322	99.5	2.805	35.475	0.0015893	0.0015460	1.9455
7.0	0.010950	1.958	318010	498	99.0	3.200	30.938	0.0020896	0.0017824	1.7060
9.0	0.015697	1.626	414706	723	99.9	3.958	25.232	0.0031414	0.0021505	1.3691
11.0	0.019658	1.514	508672	909	101.7	4.320	23.533	0.0036114	0.0023458	1.2991
13.0	0.024597	1.465	597328	1130	101.0	4.457	22.652	0.0038979	0.0023460	1.2037
15.0	0.028763	1.475	692943	1329	101.6	4.500	22.584	0.0039212	0.0024144	1.2315
17.5	0.034578	1.439	804876	1590	101.3	4.383	23.104	0.0037467	0.0023085	1.2323
20.0	0.039928	1.431	916101	1829	100.8	4.276	23.577	0.0035979	0.0022515	1.2515

TABLE V

Characteristics of Momentum and Thermal Boundary Layer Profiles

Grid 3

$X$ (in)	$\theta$ (in)	$H$	$Re_s$	$Re_t$	$U_s$ (ft/s)	$u_s$ (ft/s)	$U/u_s$	$C_f$	$St$	$2 St/C_f$
5.0	0.010939	1.652	229626	502	100.8	4.423	22.796	0.0038487	0.0026087	1.3556
7.0	0.016846	1.528	326099	785	102.0	4.620	22.086	0.0041002	0.0027235	1.3284
10.0	0.022443	1.450	462990	1039	101.1	4.658	21.710	0.0042435	0.0026876	1.2667
12.0	0.027966	1.431	556091	1296	101.4	4.560	22.236	0.0040448	0.0025387	1.2553
15.0	0.032784	1.409	662811	1449	98.2	4.350	22.569	0.0039265	0.0023795	1.2120
17.5	0.039886	1.392	803639	1832	101.9	4.415	23.071	0.0037574	0.0023960	1.2754
20.0	0.045199	1.376	910554	2058	101.0	4.339	23.283	0.0036894	0.0023792	1.2898

TABLE VI

Characteristics of Momentum and Thermal Boundary Layer Profiles

Grid 4

$X$ (in)	$\theta$ (in)	$H$	$Re_x$	$Re_s$	$U_x$ (ft/s)	$u_s$ (ft/s)	$U/\mu_s$	$C_r$	$St$	$2 St/C_r$
5.0	0.012924	1.562	227855	589	100.9	4.812	20.974	0.0045466	0.0028813	1.2675
8.0	0.022073	1.435	369666	1020	102.3	4.773	21.433	0.0043537	0.0027542	1.2652
12.0	0.029993	1.434	545349	1363	100.7	4.525	22.255	0.0040380	0.0025605	1.2682
15.0	0.038524	1.405	684130	1757	100.6	4.443	22.651	0.0038981	0.0024408	1.2523
17.5	0.047480	1.383	814967	2211	102.0	4.403	23.174	0.0037241	0.0023056	1.2382
20.0	0.049412	1.349	924971	2285	101.3	4.350	23.286	0.0036881	0.0023368	1.2672

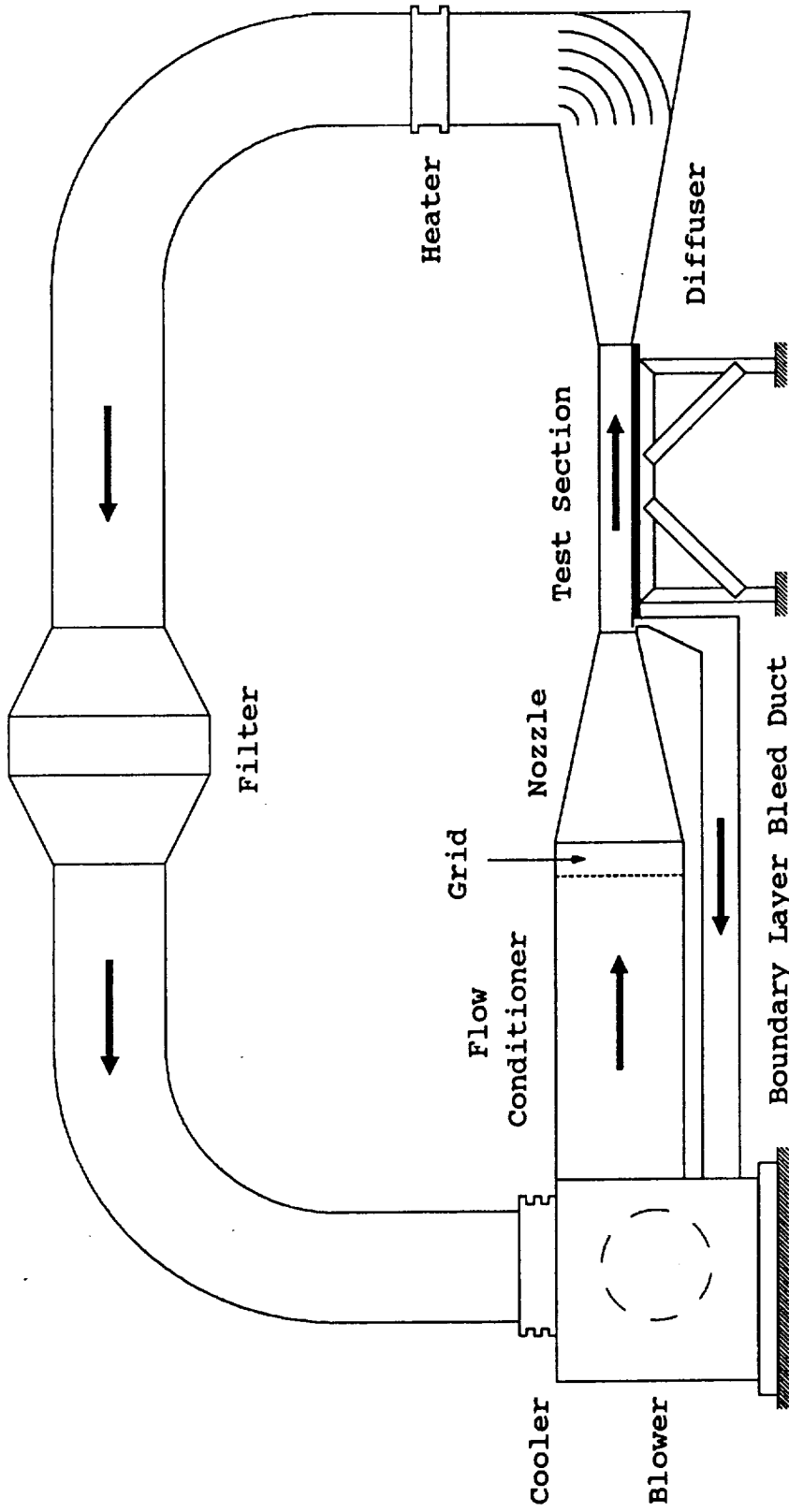


Fig. 1 Schematic diagram of the wind tunnel

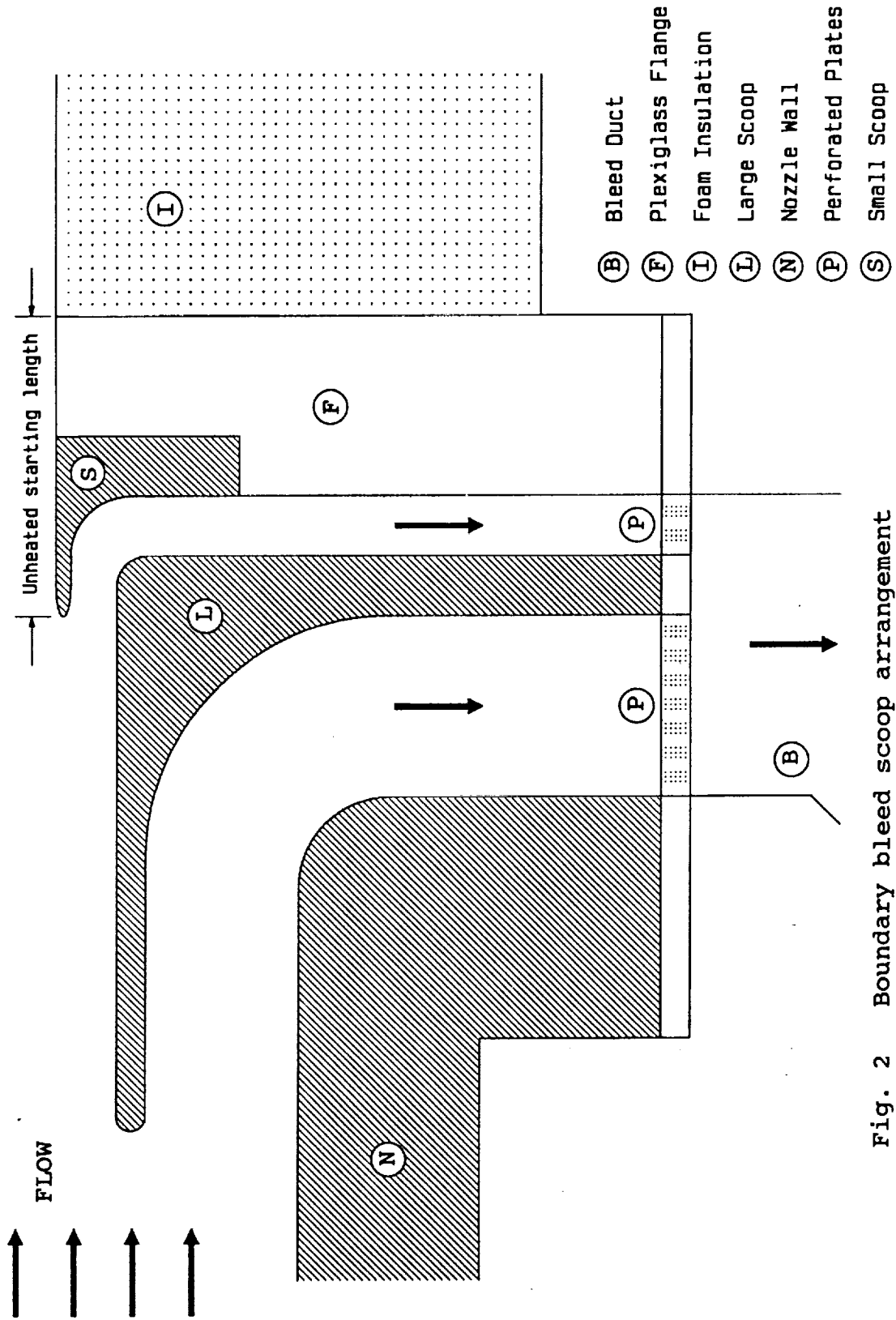


Fig. 2 Boundary bleed scoop arrangement

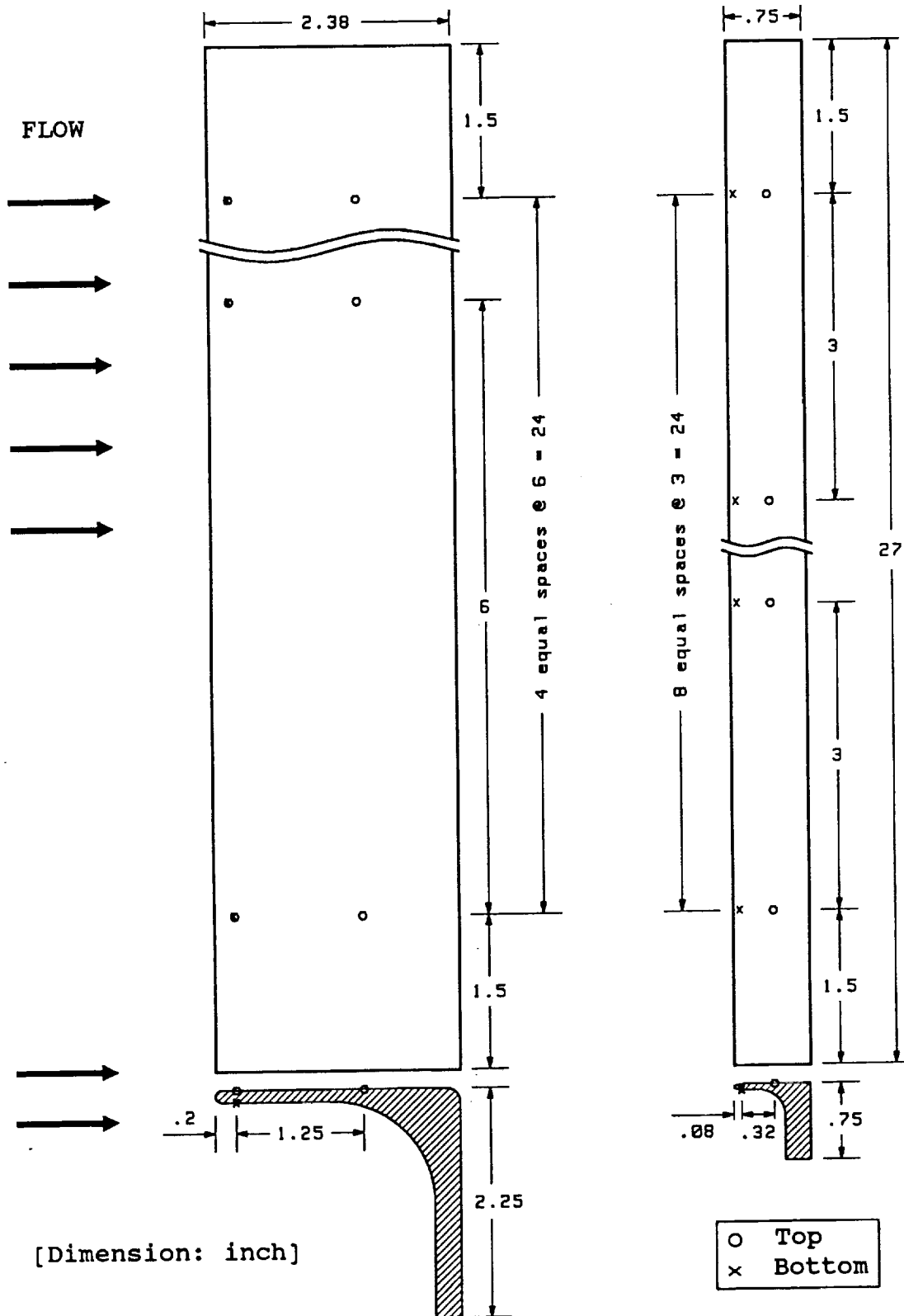


Fig. 3 Boundary bleed large and small scoop statics





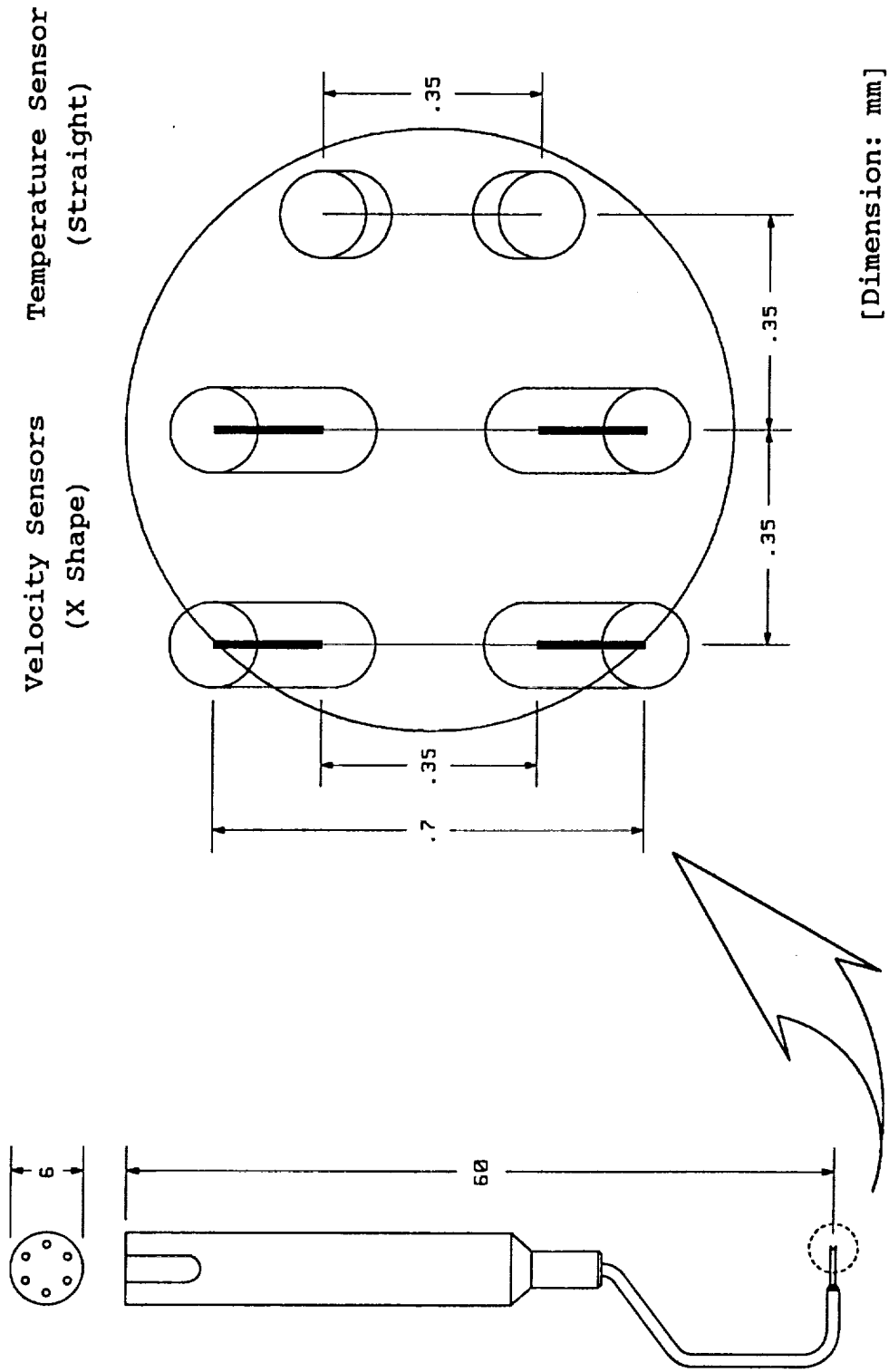


Fig. 6 Schematic of the 3-wire probe

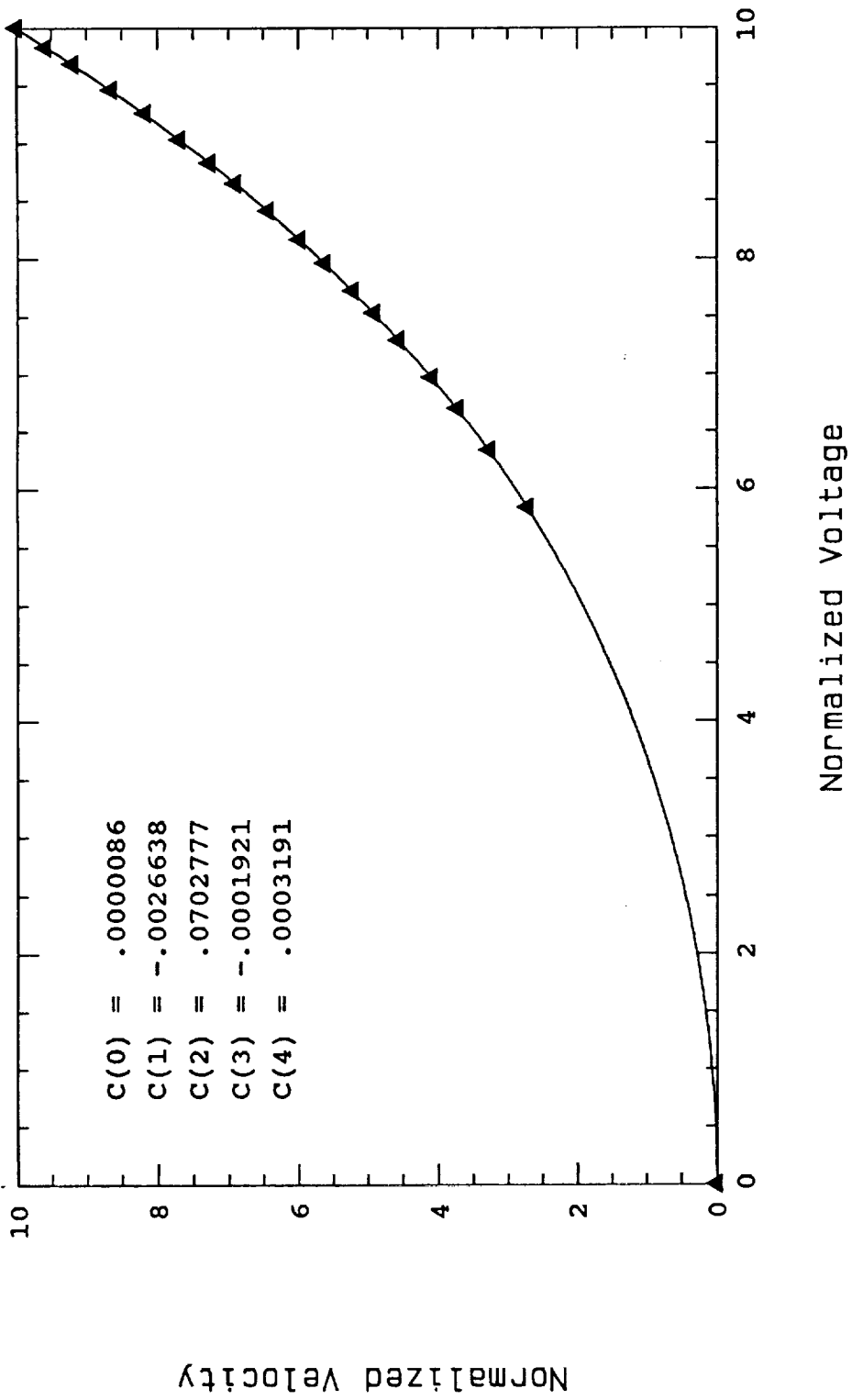


Fig. 7 Normalized voltage-velocity calibration for hot-wire

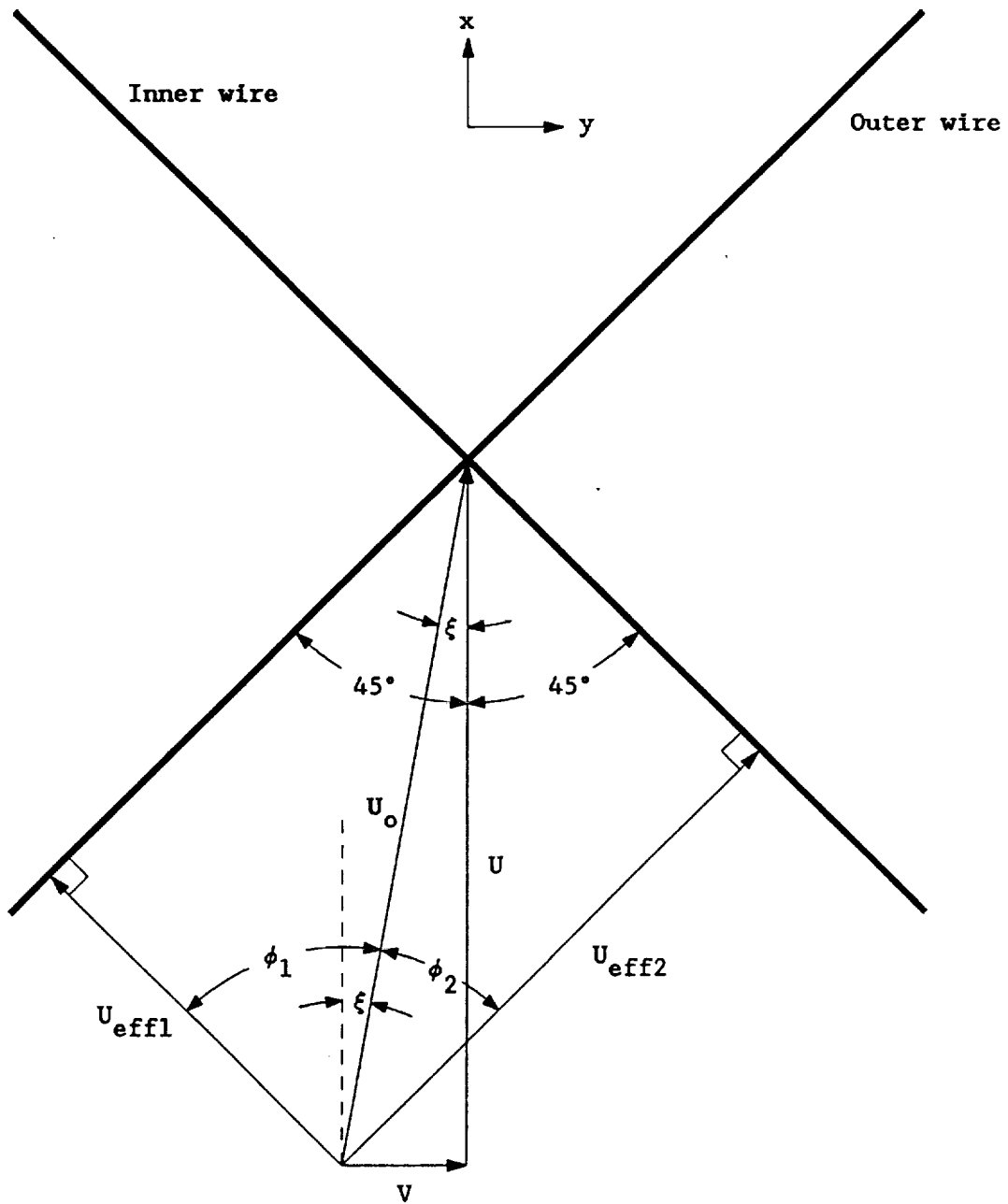


Fig. 8 Details of velocity components for X wire

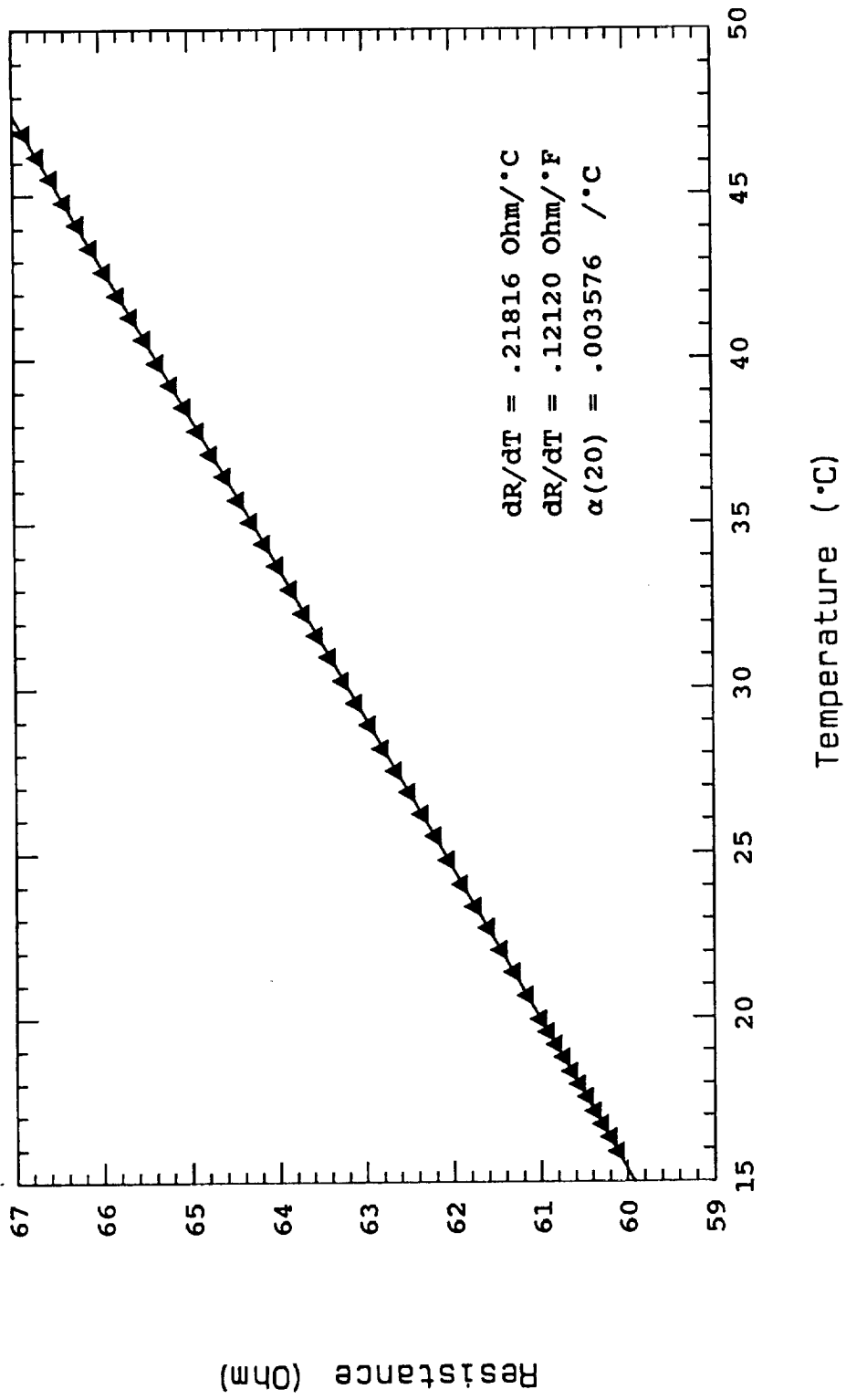


Fig. 9 Temperature-resistance calibration for temperature wire

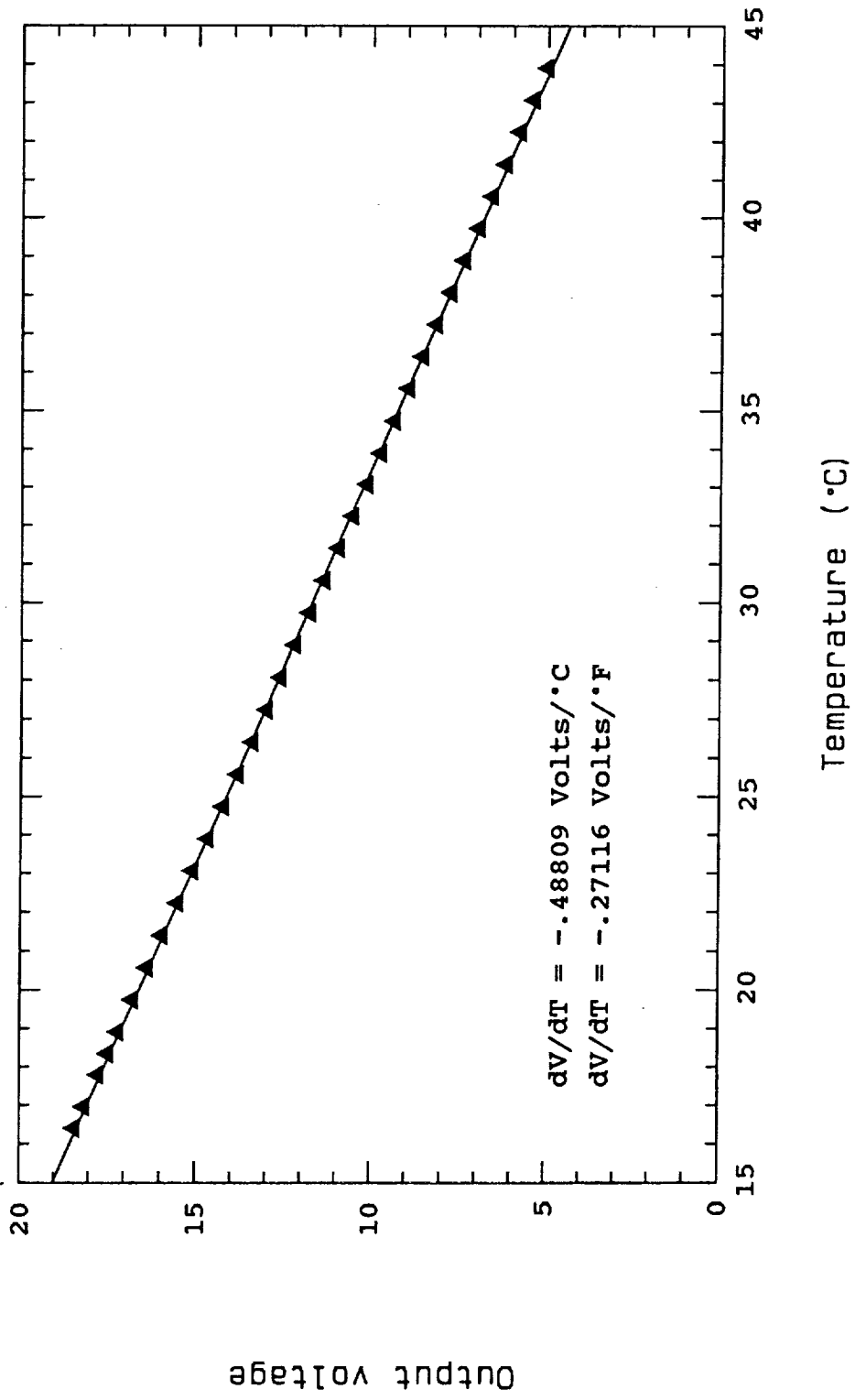


Fig. 10 Voltage-temperature calibration for temperature wire

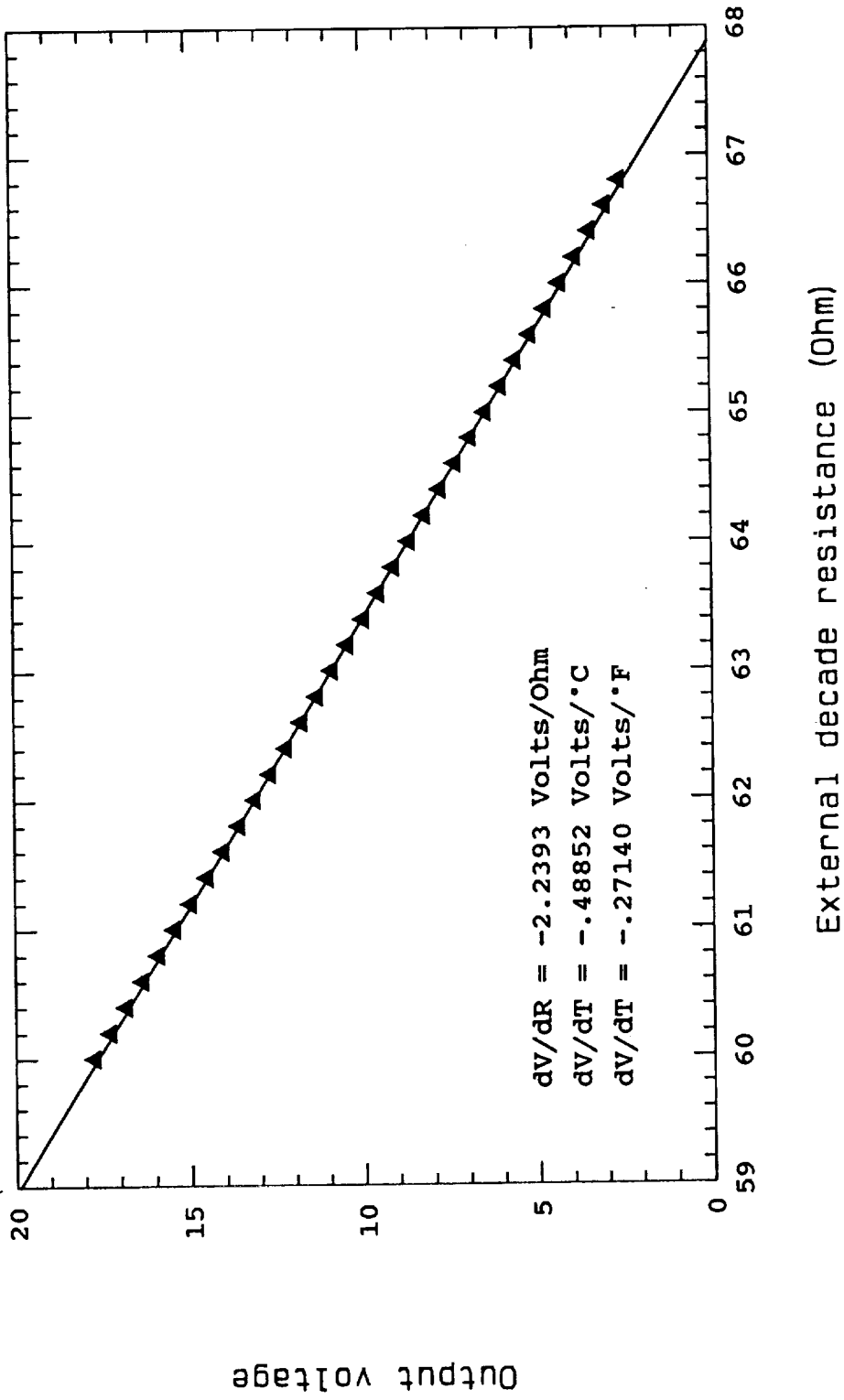


Fig. 11 Voltage-resistance calibration for temperature wire

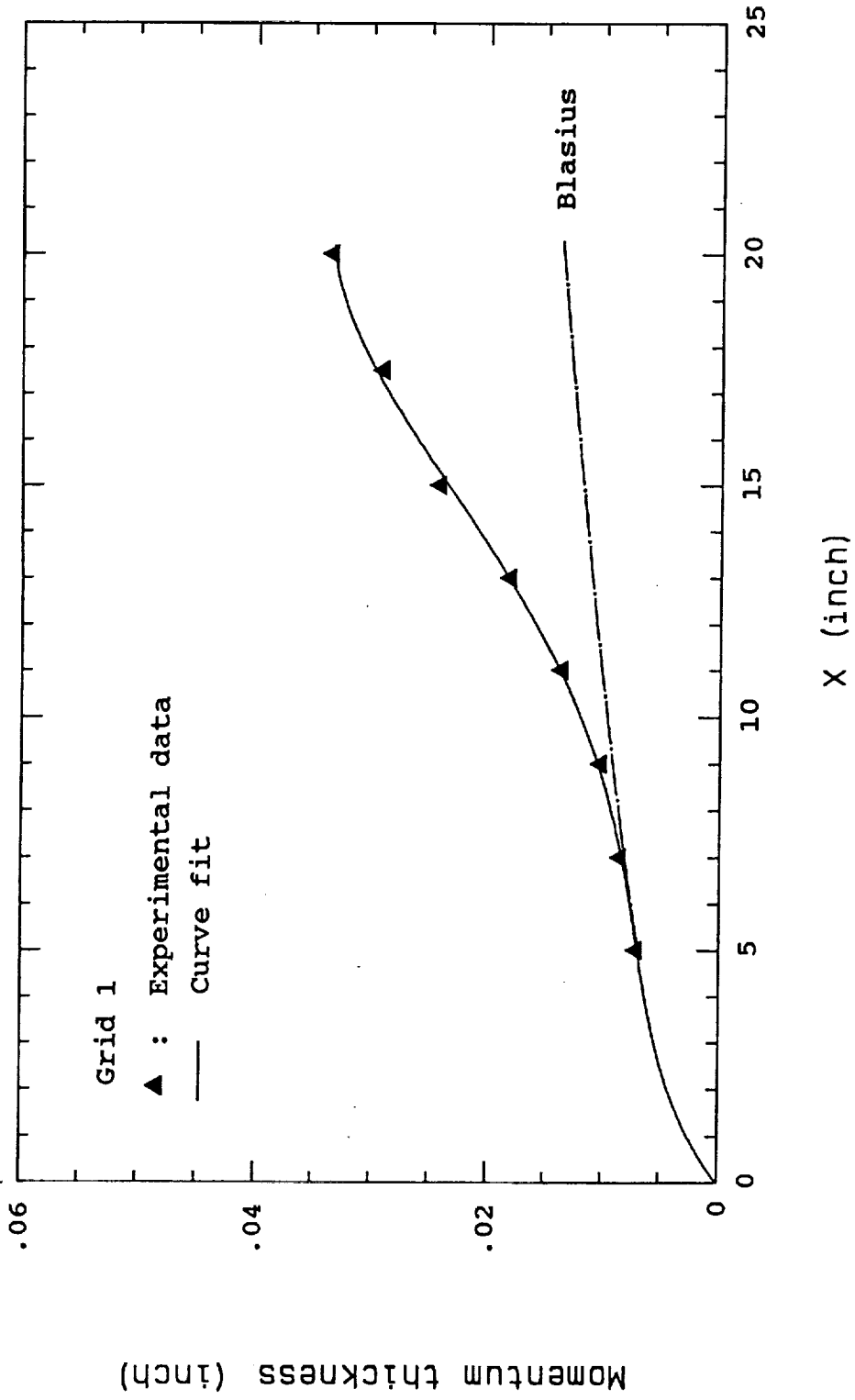


Fig. 12 Variation of momentum thickness with streamwise distance

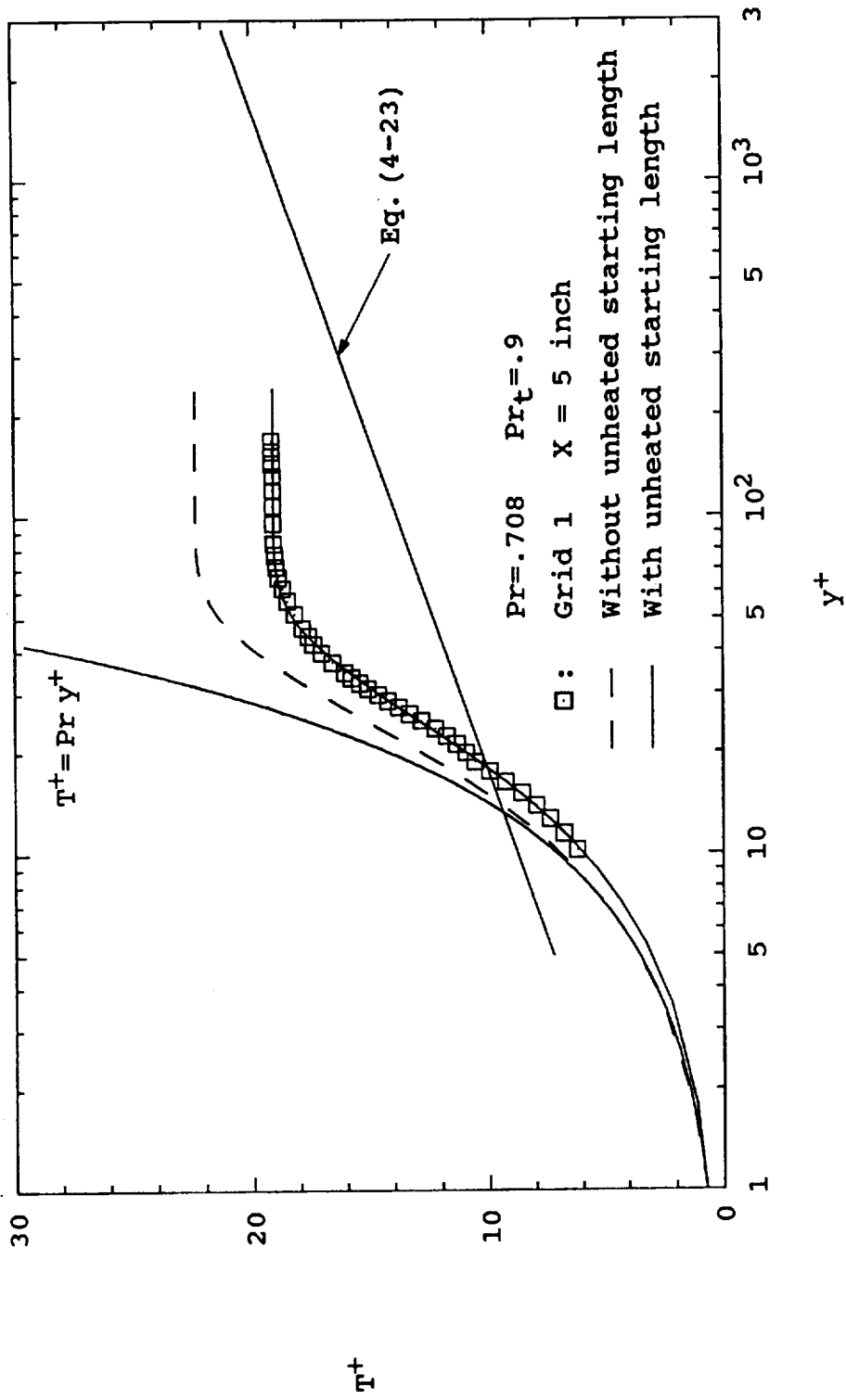


Fig. 13 Effect of unheated starting length on the laminar temperature

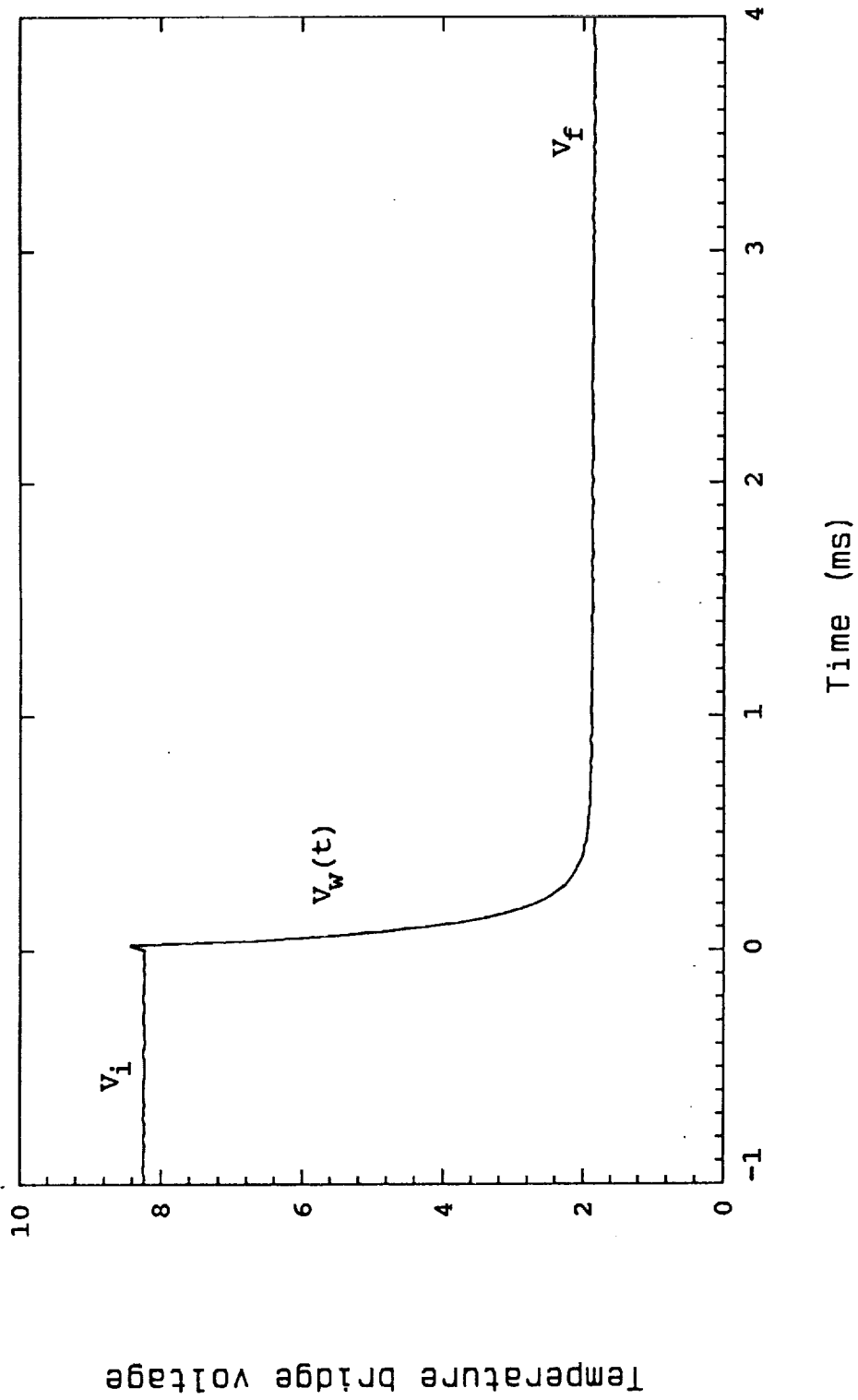


Fig. 14 Response of temperature wire on step-change of air temperature

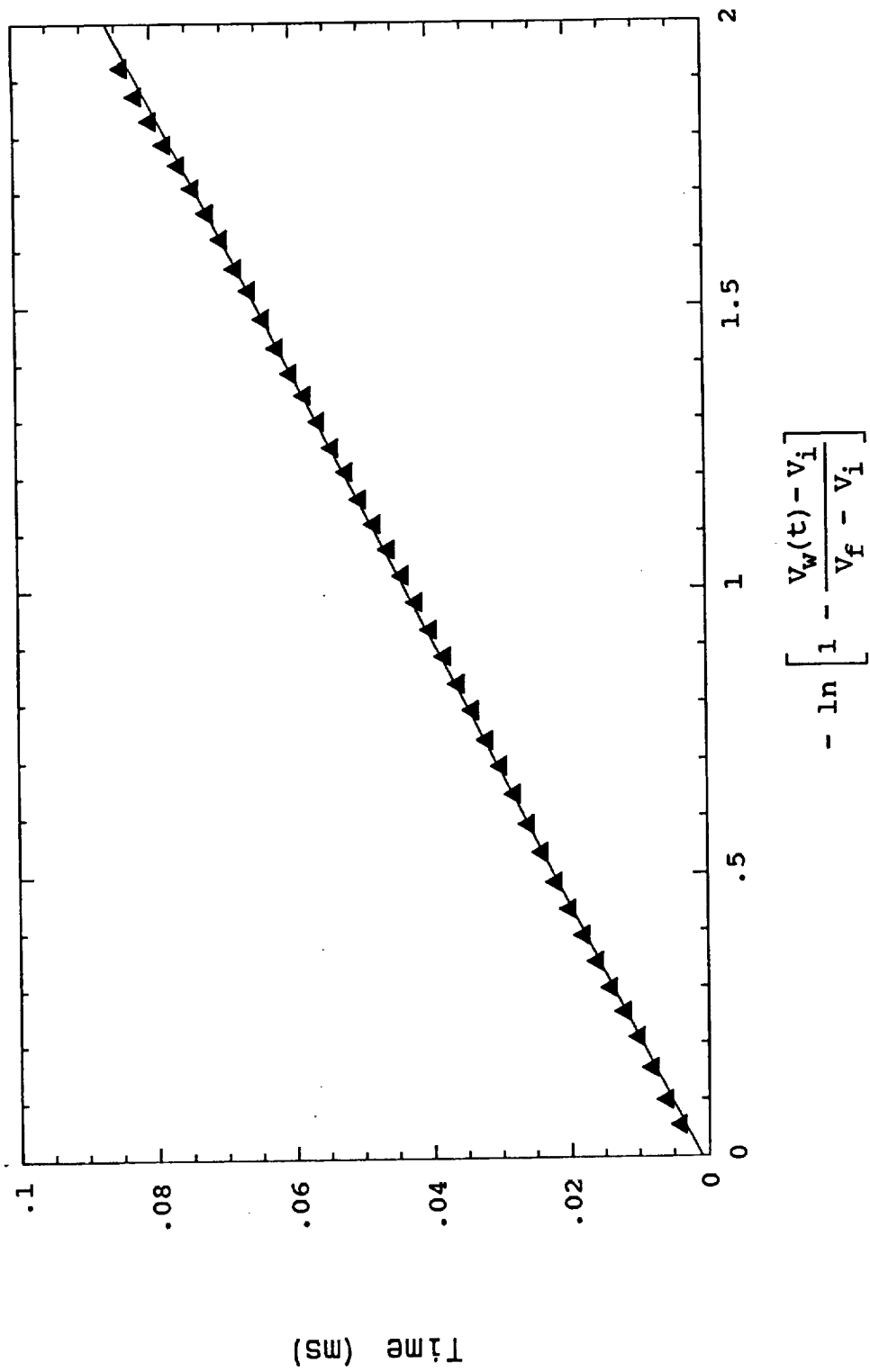


Fig. 15 Determination of time constant for cold-wire at certain velocity

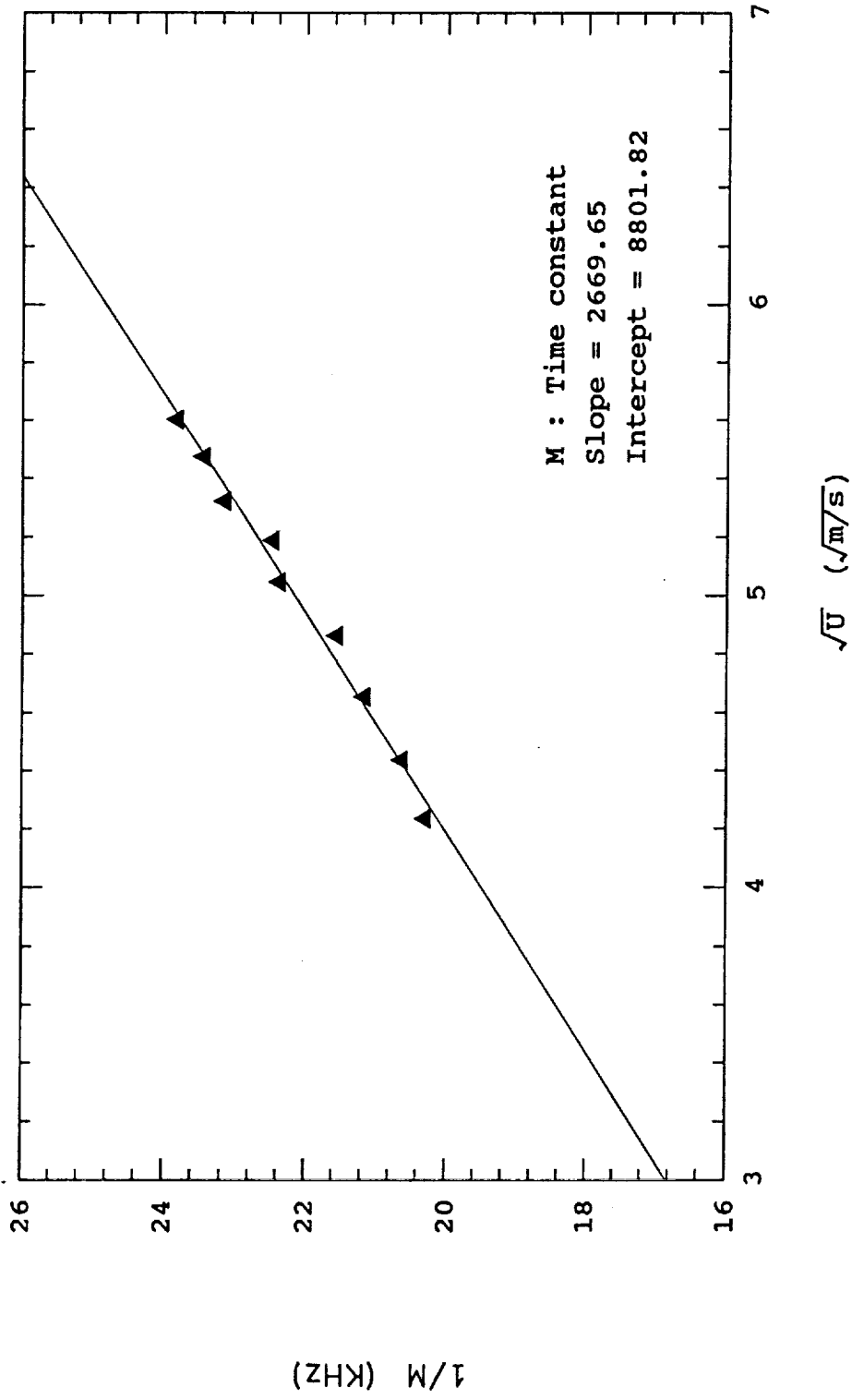


Fig. 16 Time constant-velocity calibration for temperature wire

Grid 2 X = 20 inch Y = .12 inch

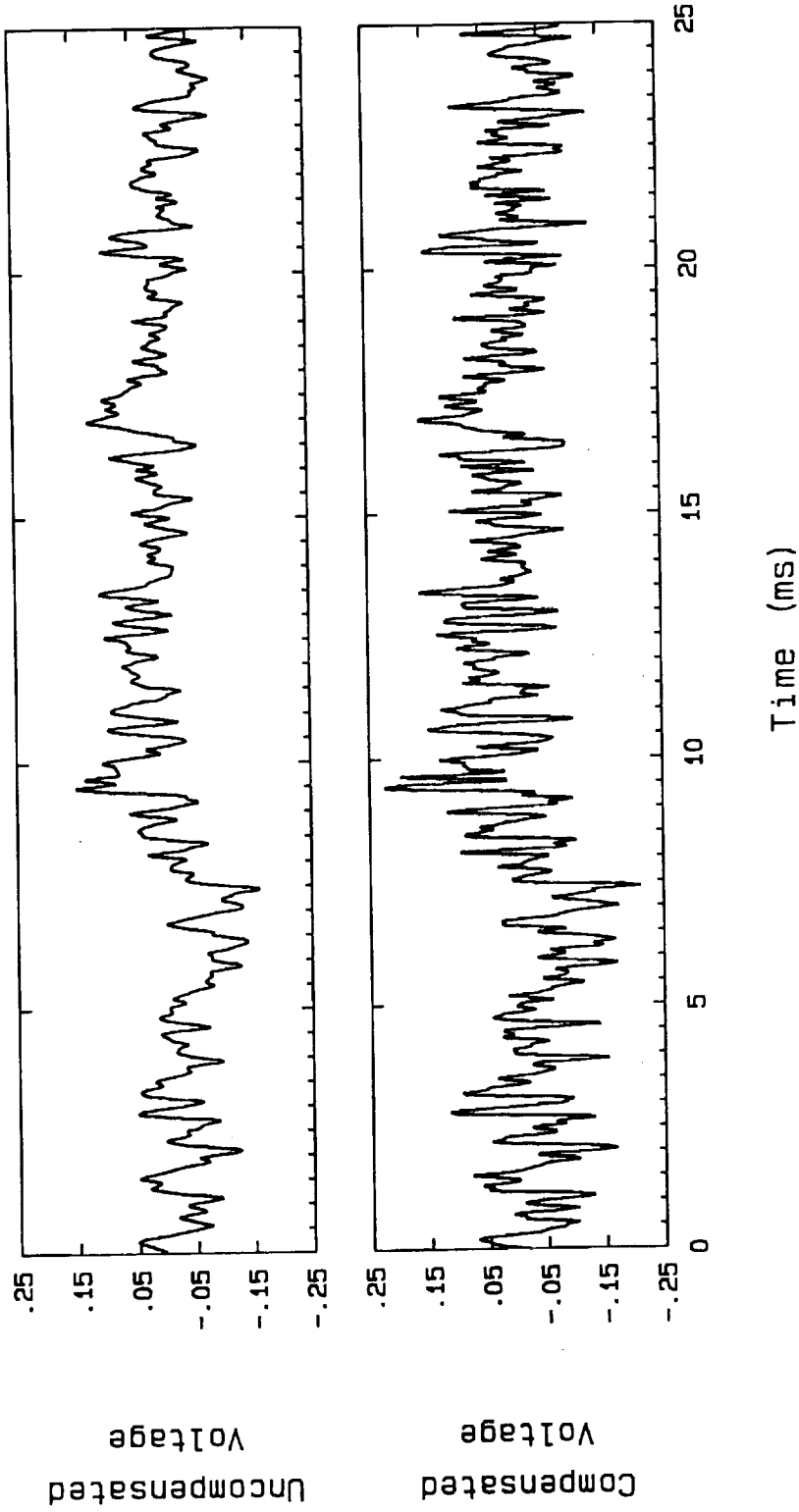


Fig. 17(a) Effect of compensation for instantaneous temperature signal measured within the boundary layer

Grid 2 X = 20 inch Y = .82 inch

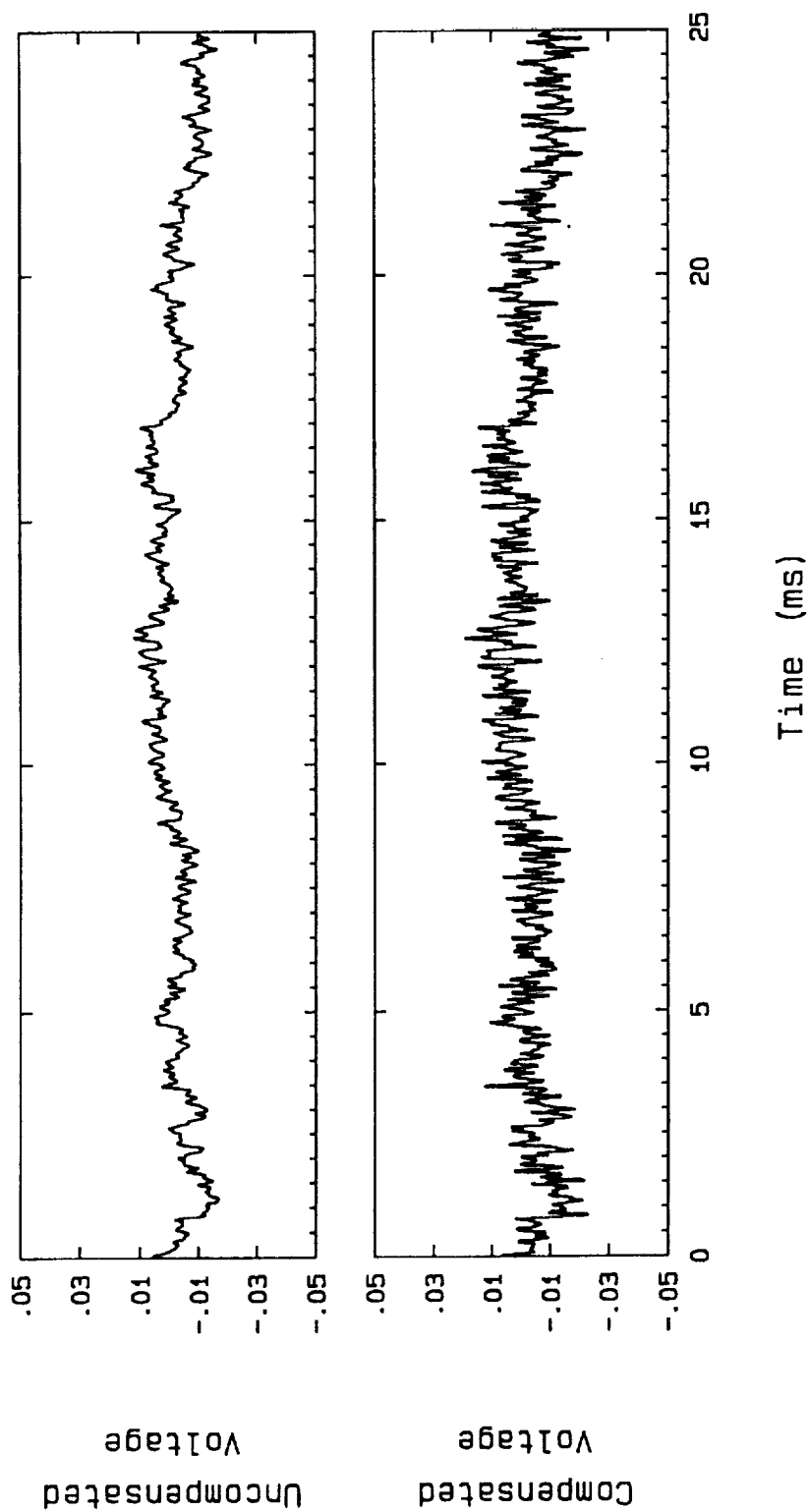


Fig. 17(b) Effect of compensation for instantaneous temperature signal measured farther out to the edge of the boundary layer

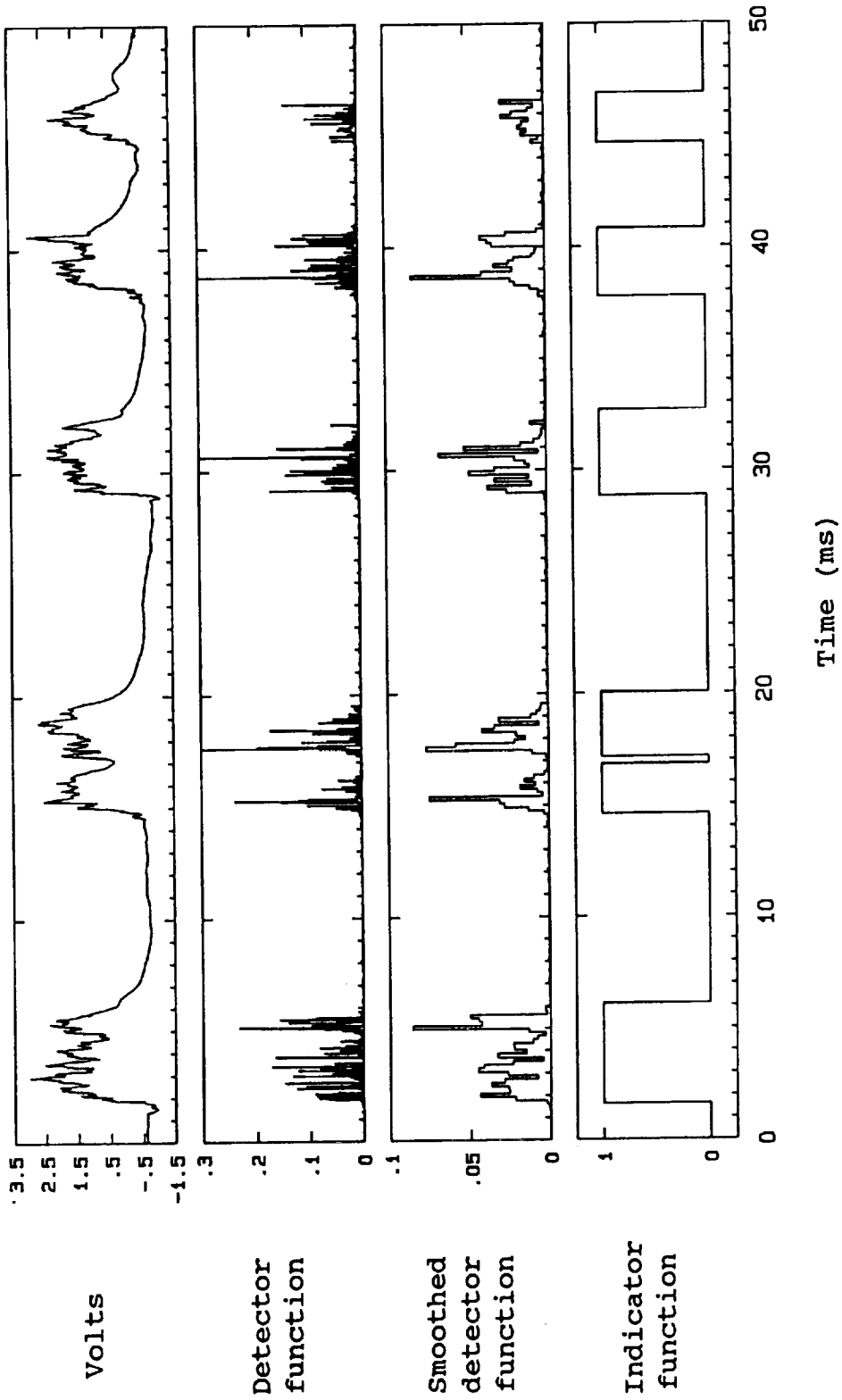


Fig. 18(a) Illustration of indicator function determination technique for single-wire probe

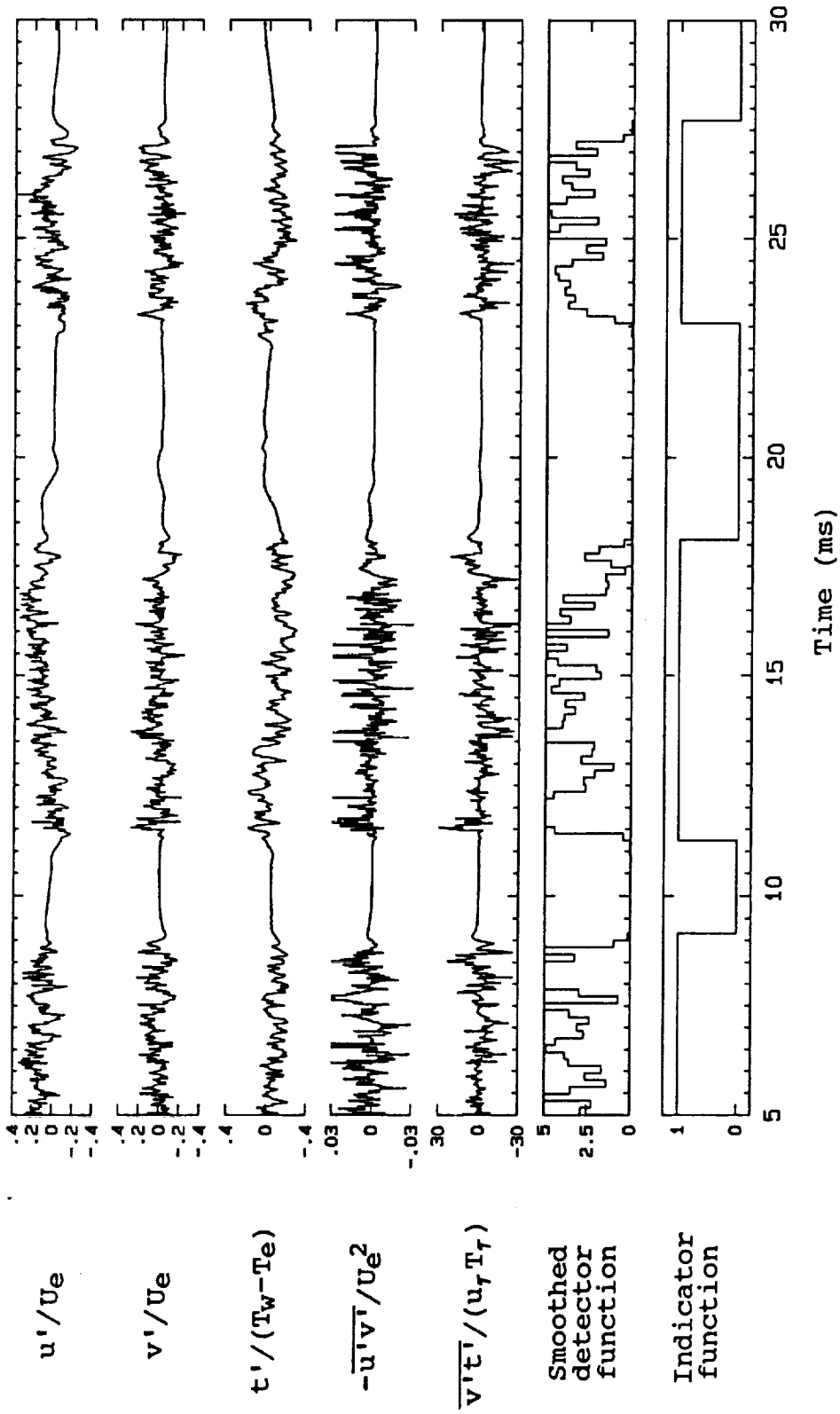


Fig. 18(b) Illustration of indicator function determination technique for 3-wire probe

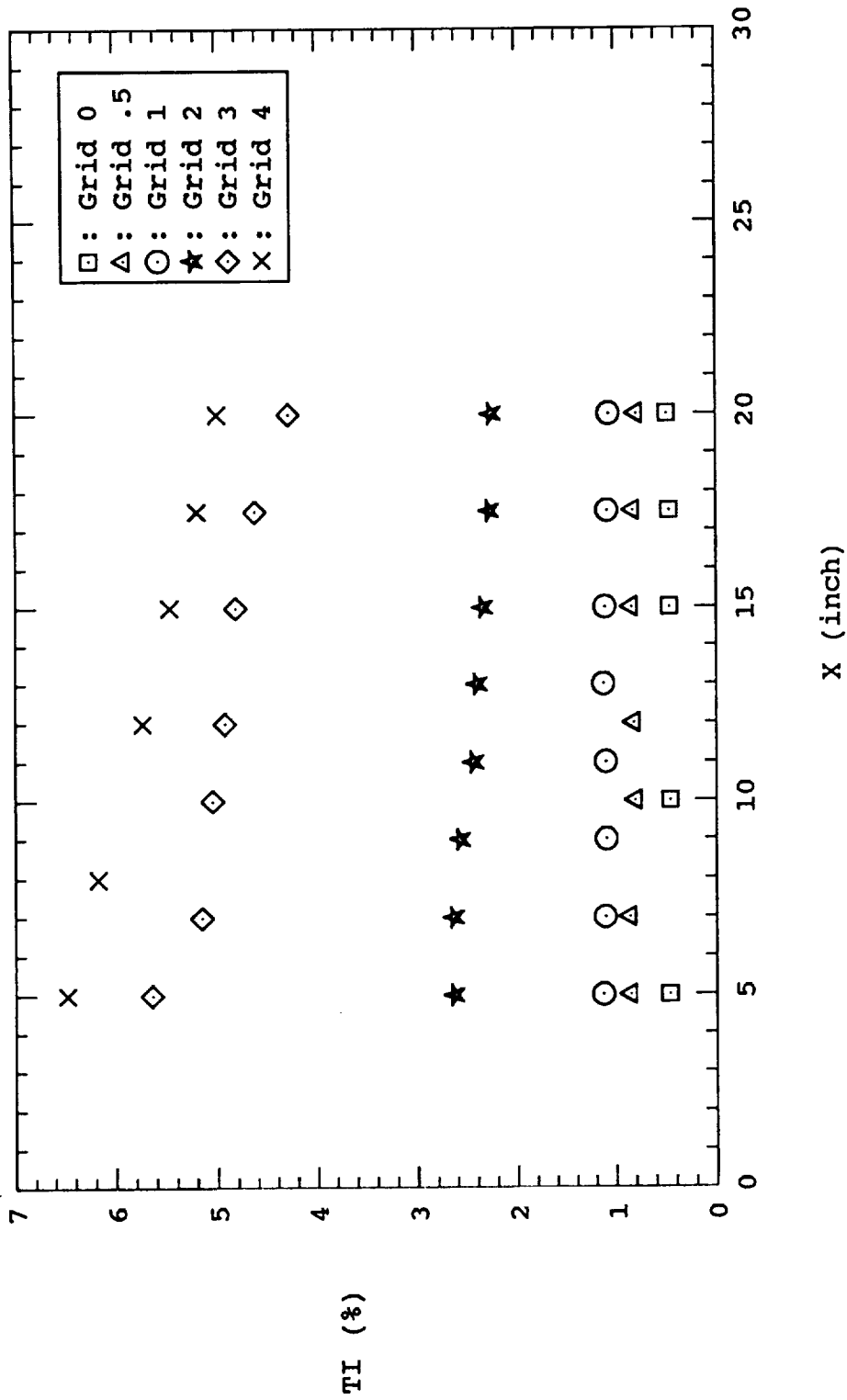


Fig. 19 Streamwise freestream turbulence intensity through the test section

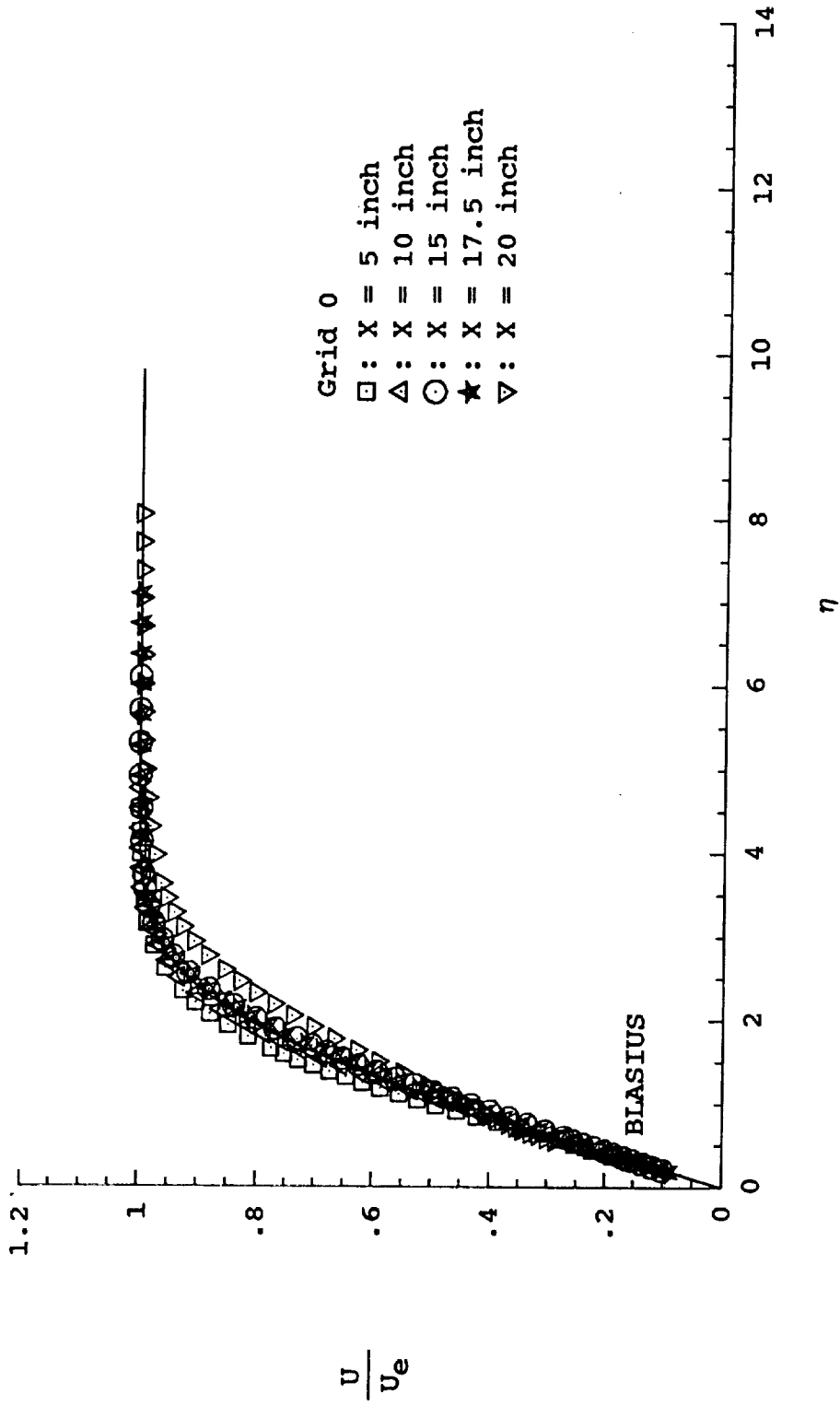


Fig. 20(a) Streamwise mean velocity profiles in Blasius coordinates for grid 0

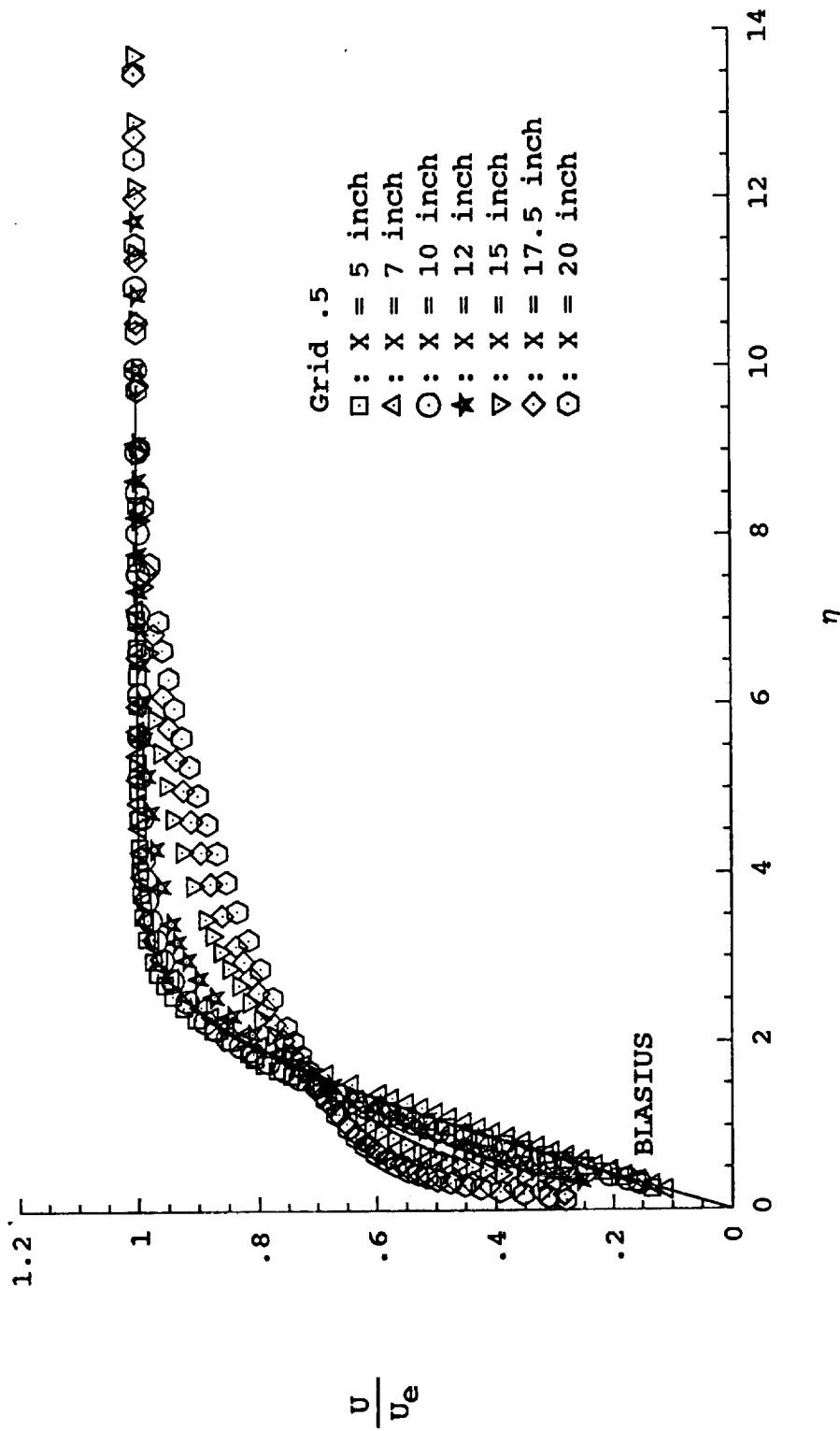


Fig. 20(b) Streamwise mean velocity profiles in Blasius coordinates for grid .5

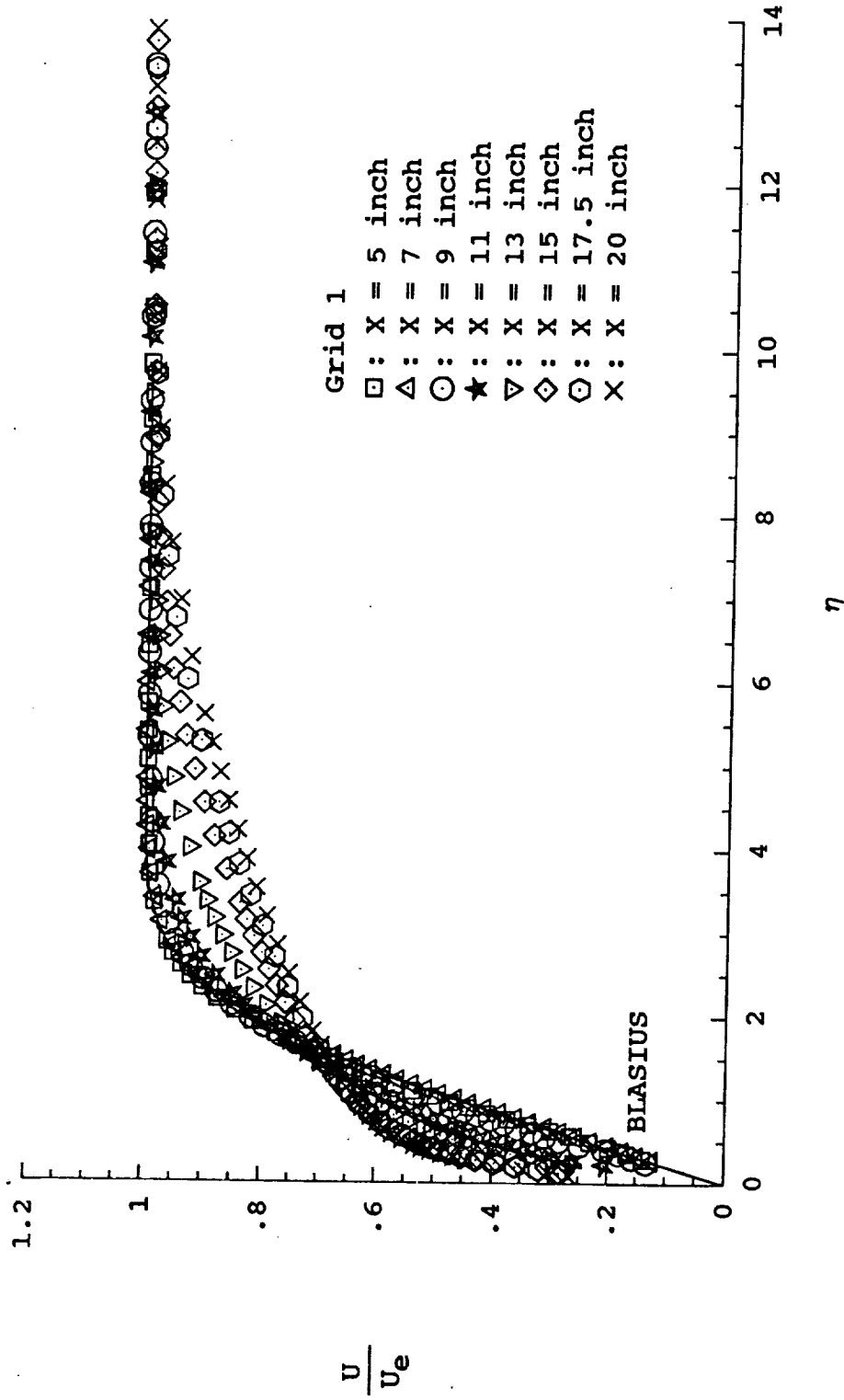


Fig. 20(c) Streamwise mean velocity profiles in Blasius coordinates for grid 1

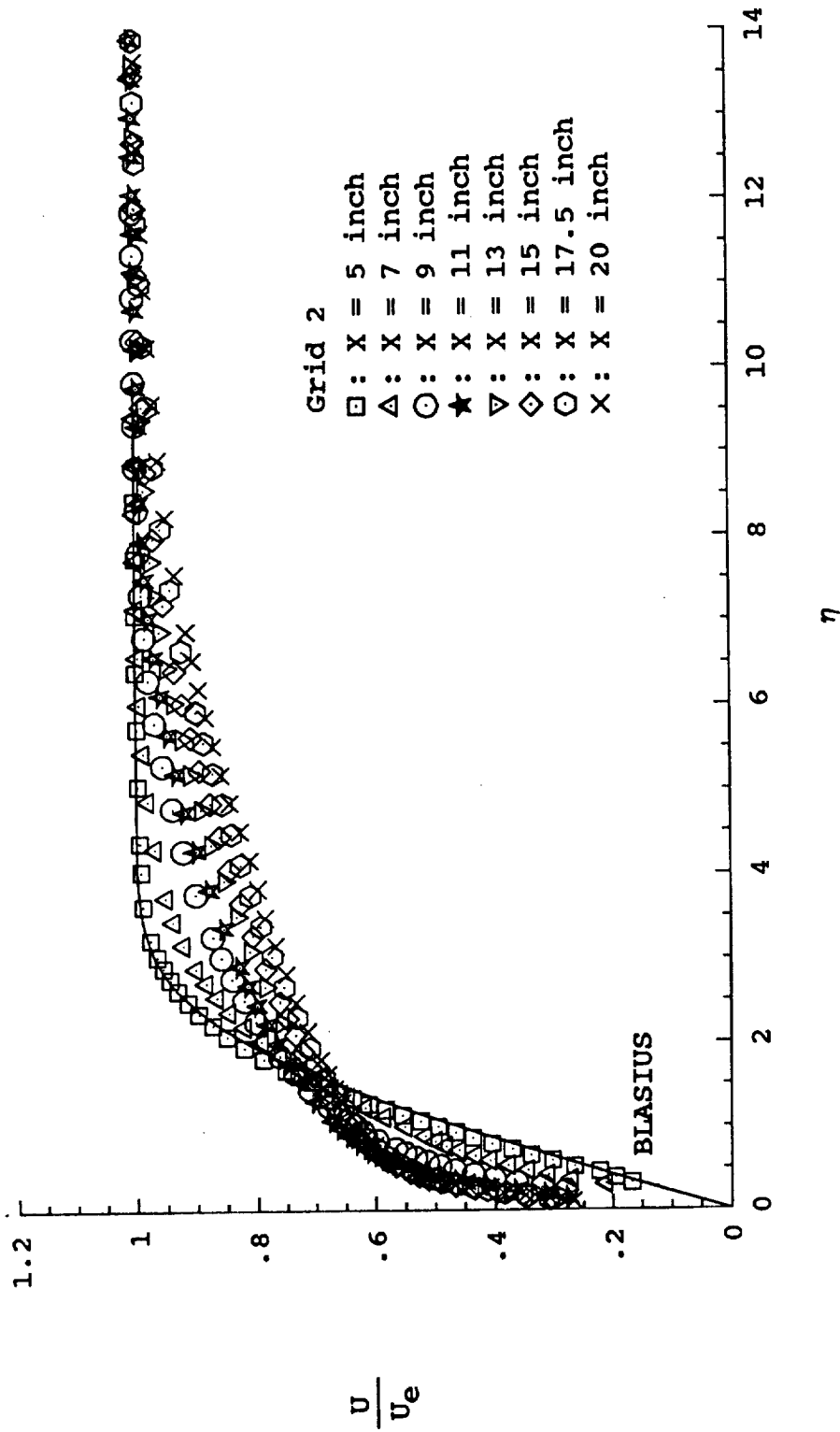


Fig. 20(d) Streamwise mean velocity profiles in Blasius coordinates for grid 2

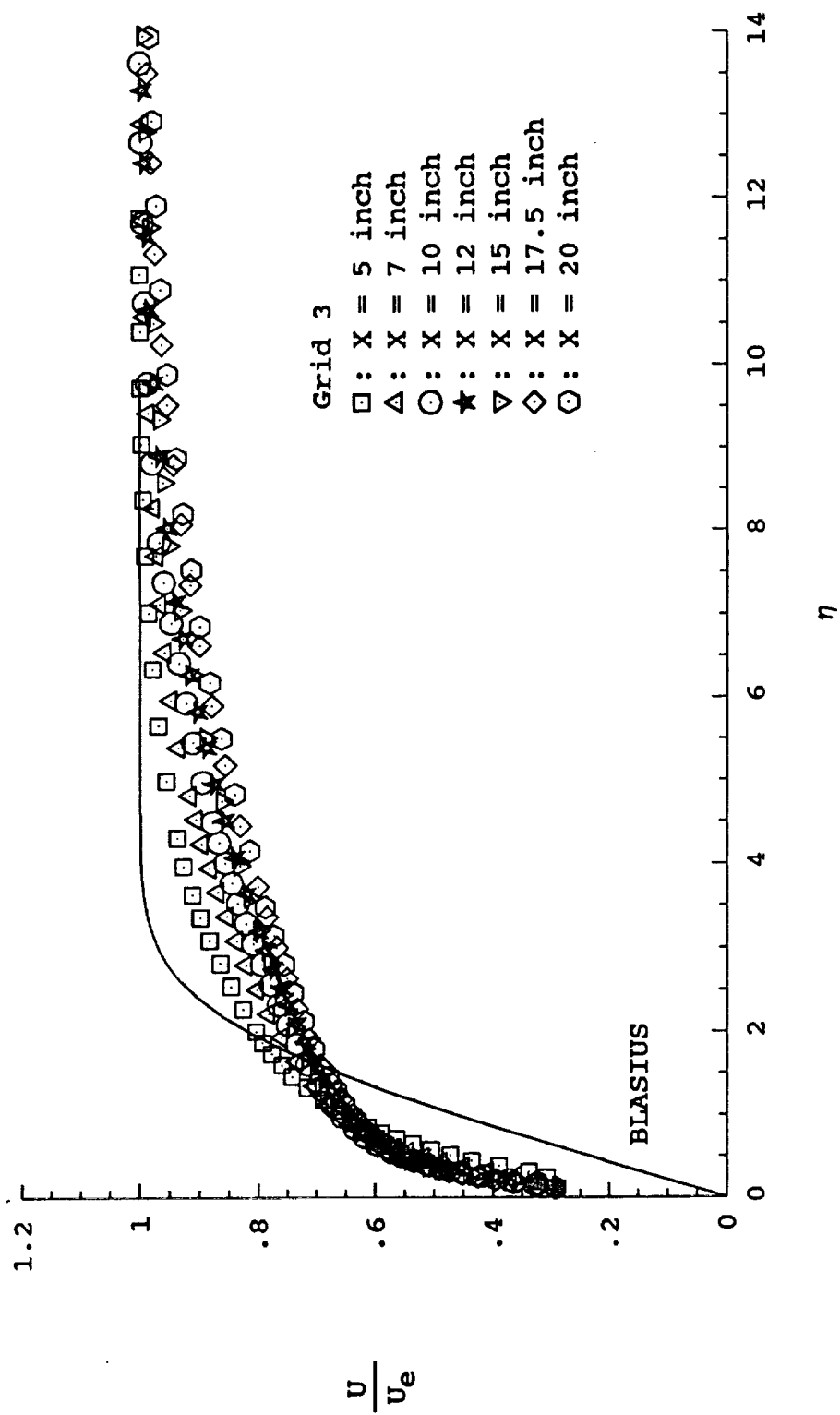


Fig. 20(e) Streamwise mean velocity profiles in Blasius coordinates for grid 3

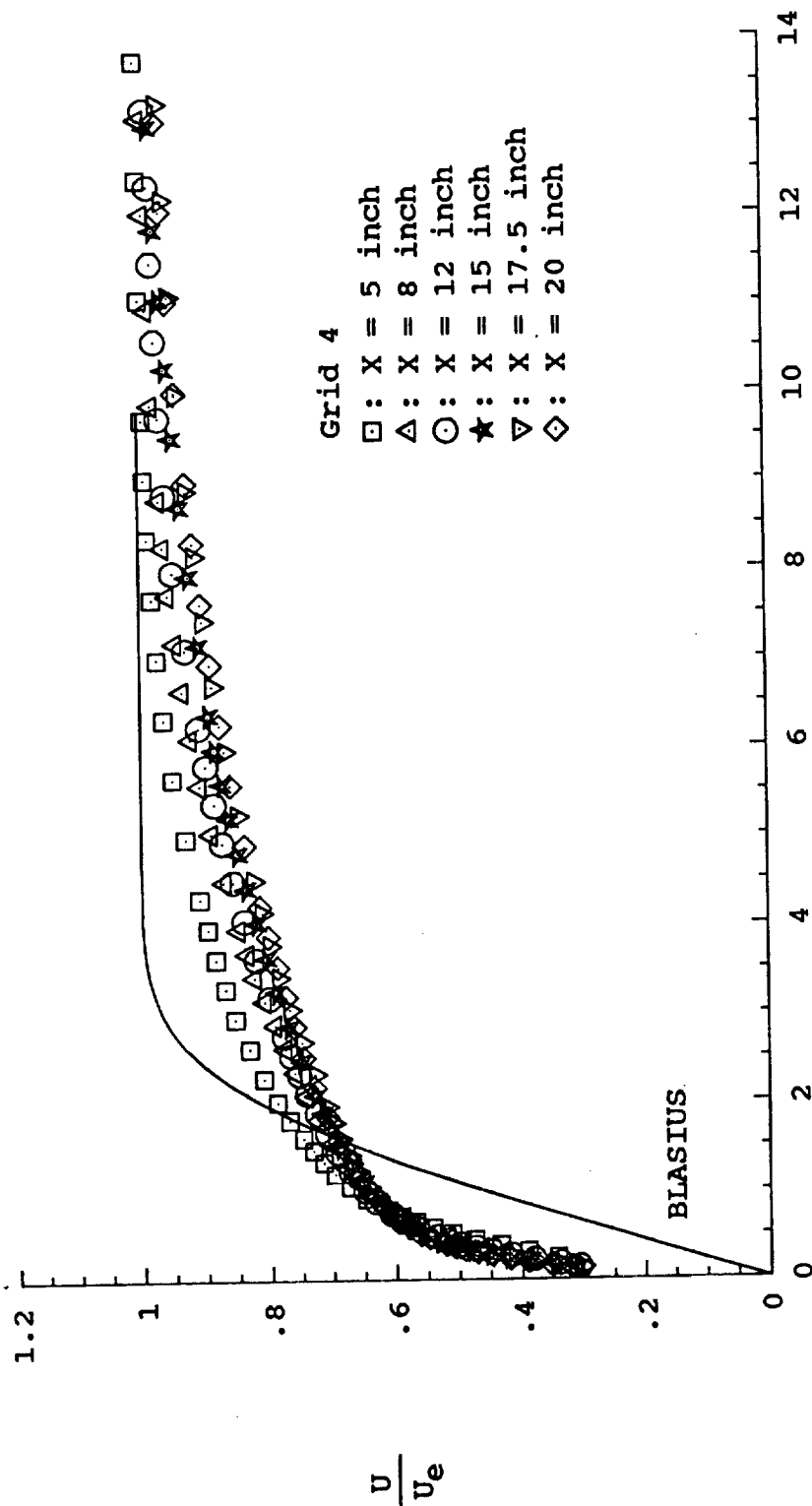


Fig. 20(f) Streamwise mean velocity profiles in Blasius coordinates for grid 4

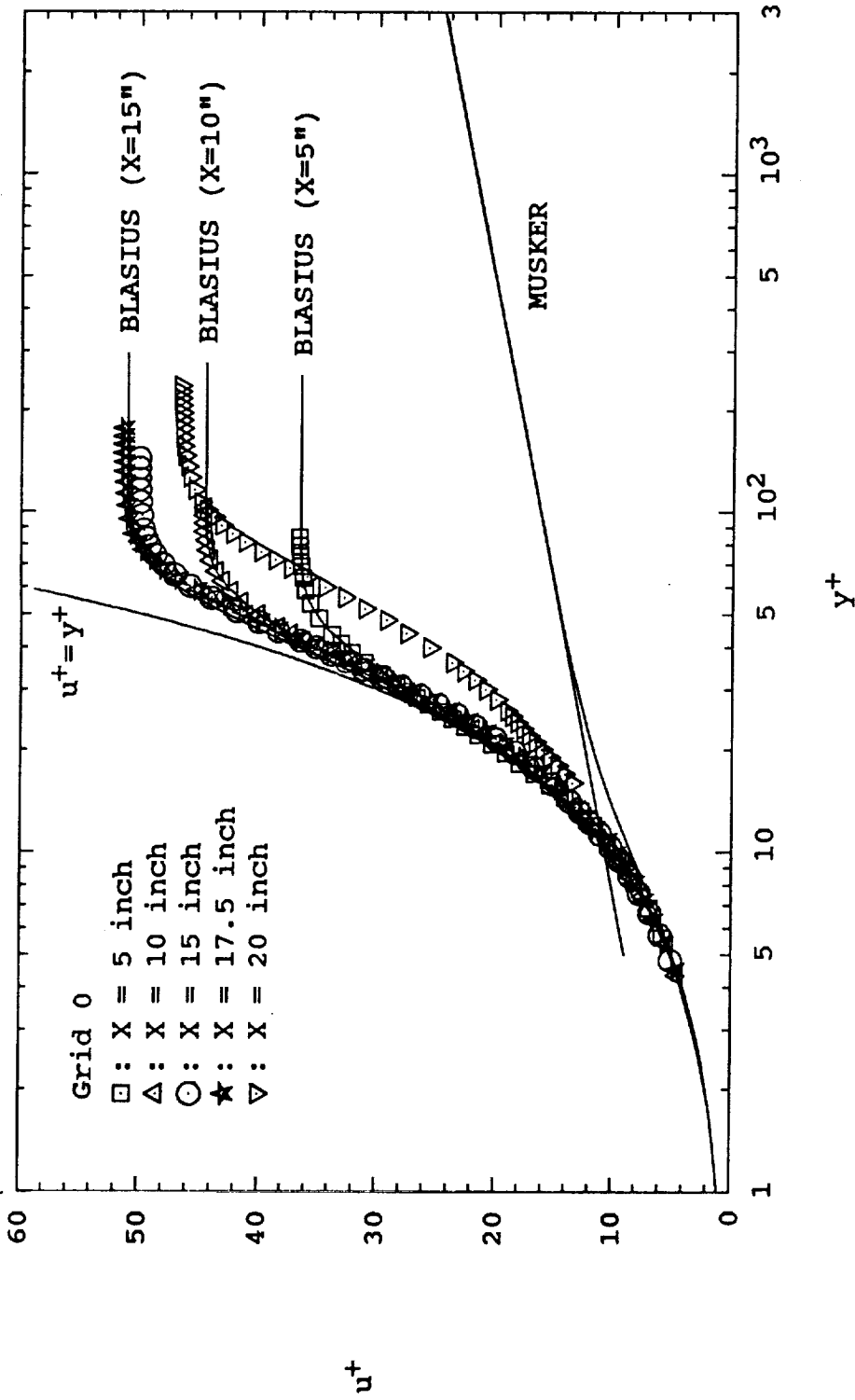


Fig. 21(a) Streamwise mean velocity profiles in wall units for grid 0

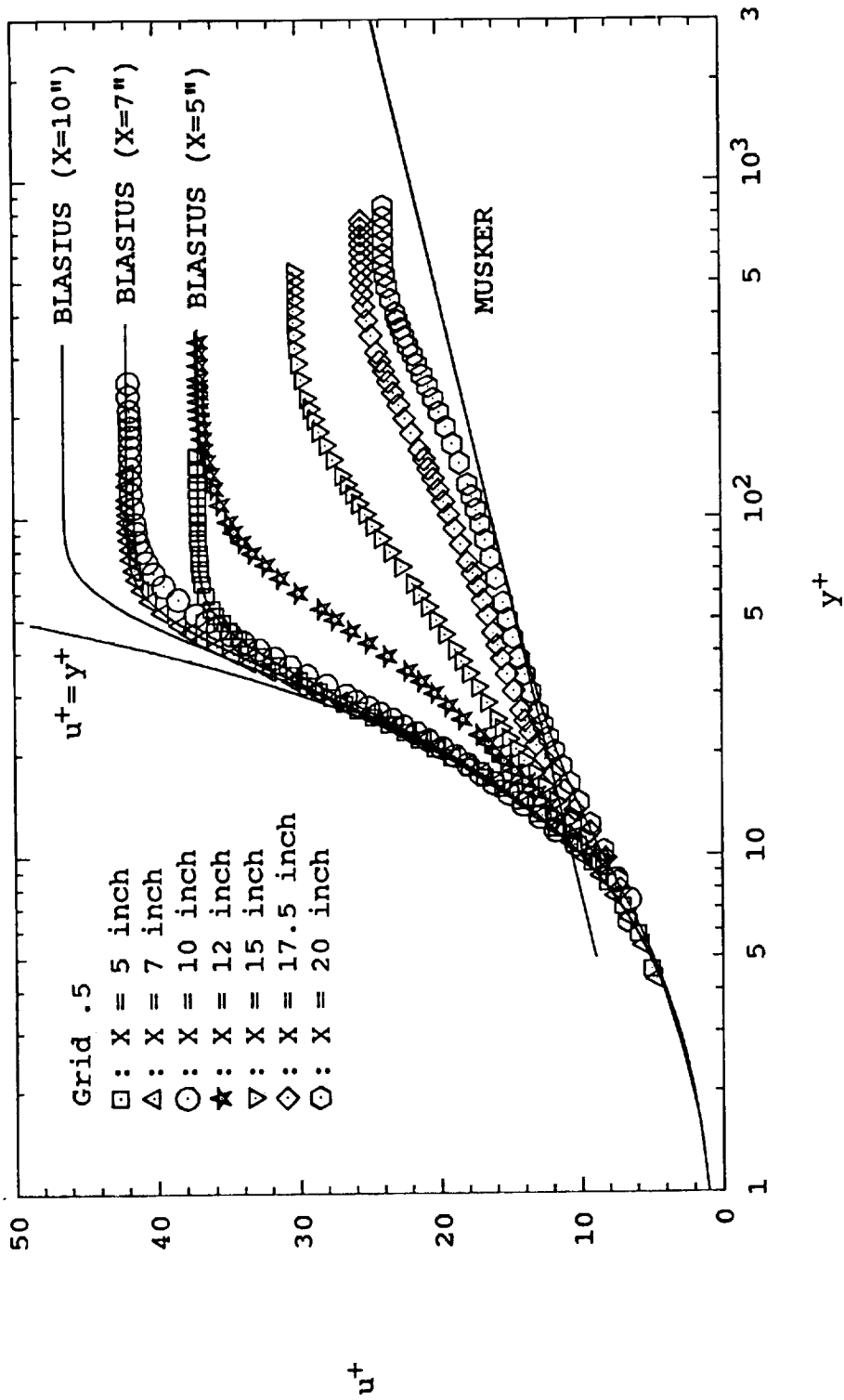


Fig. 21(b) Streamwise mean velocity profiles in wall units for grid .5

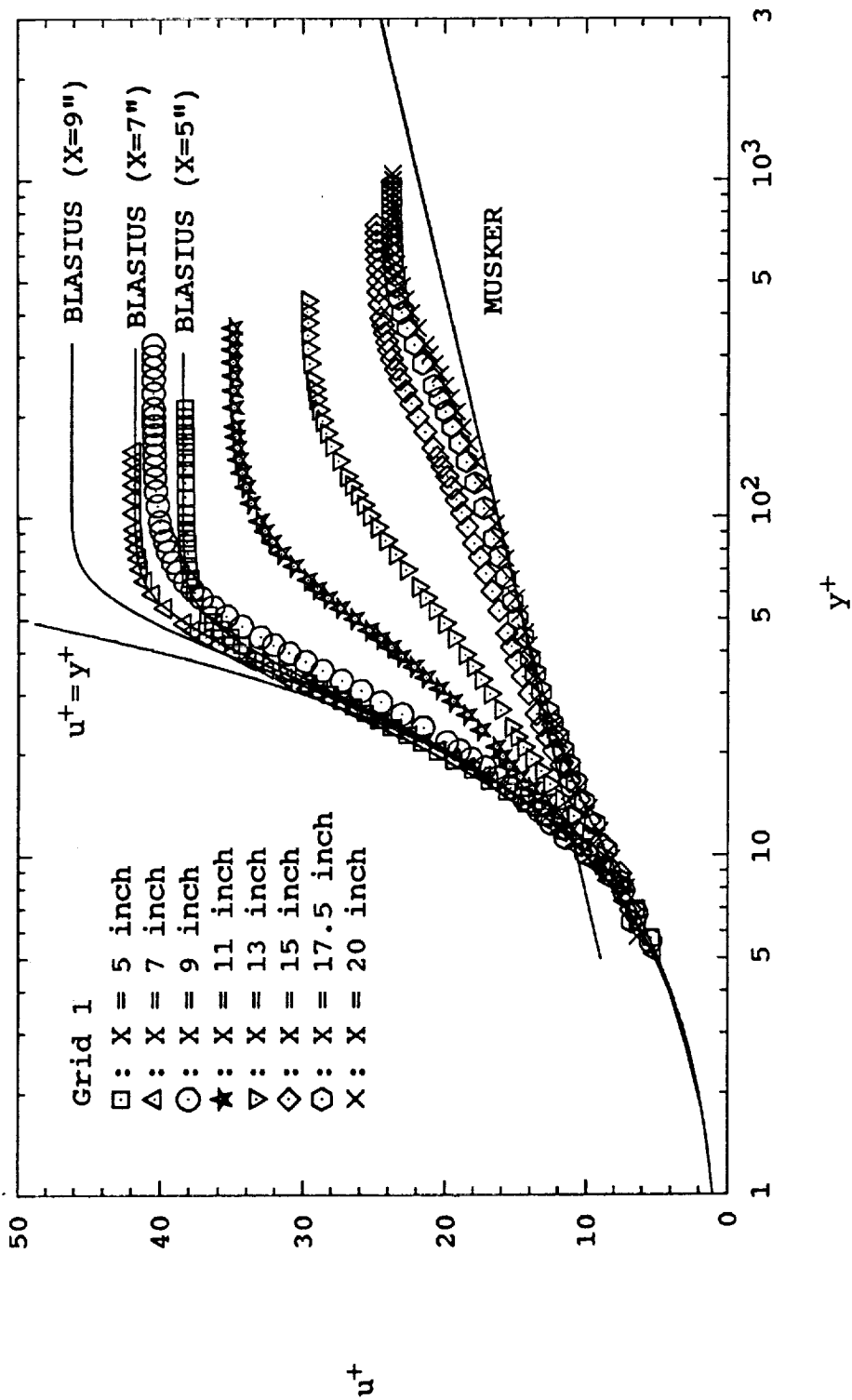


Fig. 21(c) Streamwise mean velocity profiles in wall units for grid 1

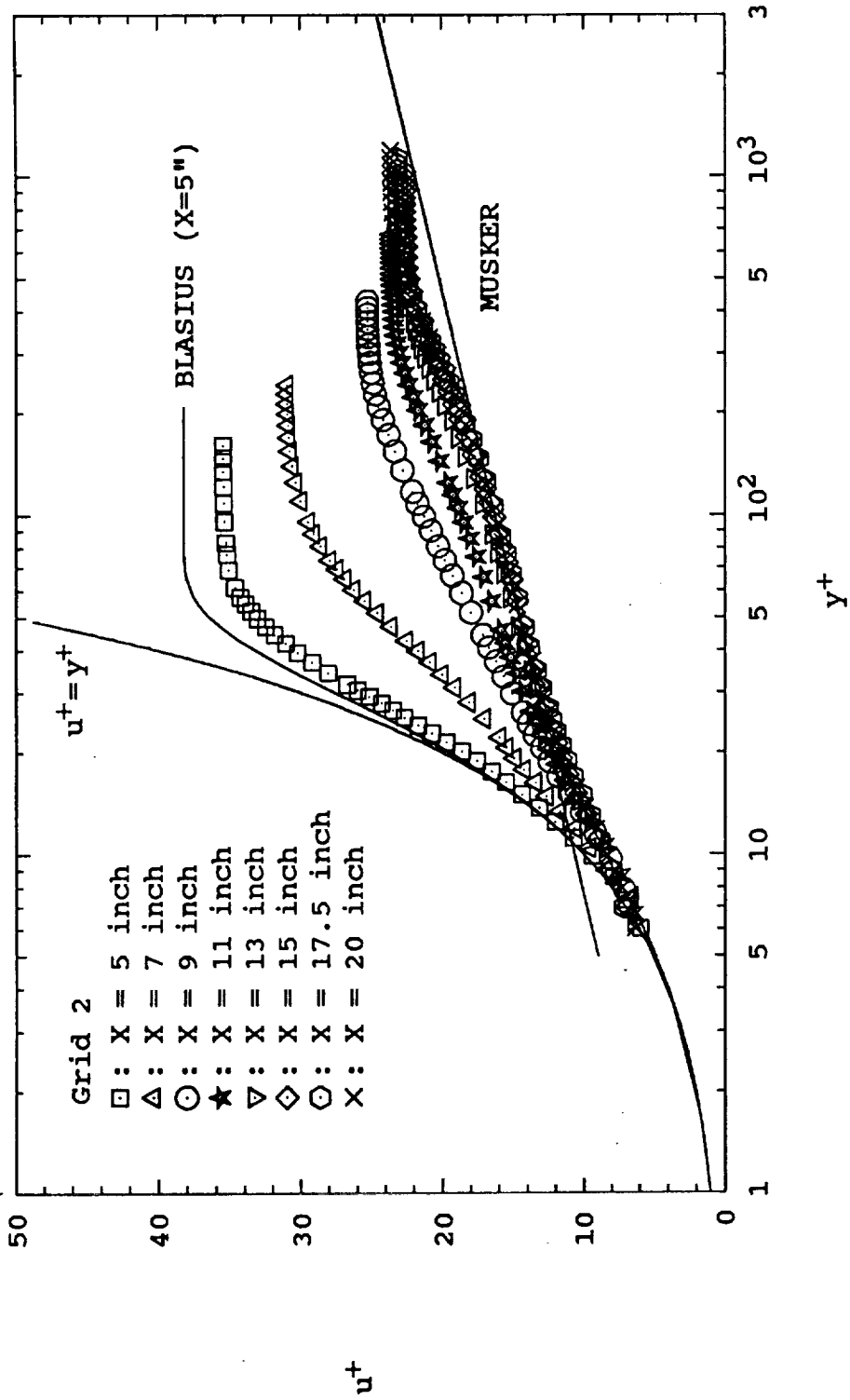


Fig. 21(d) Streamwise mean velocity profiles in wall units for grid 2

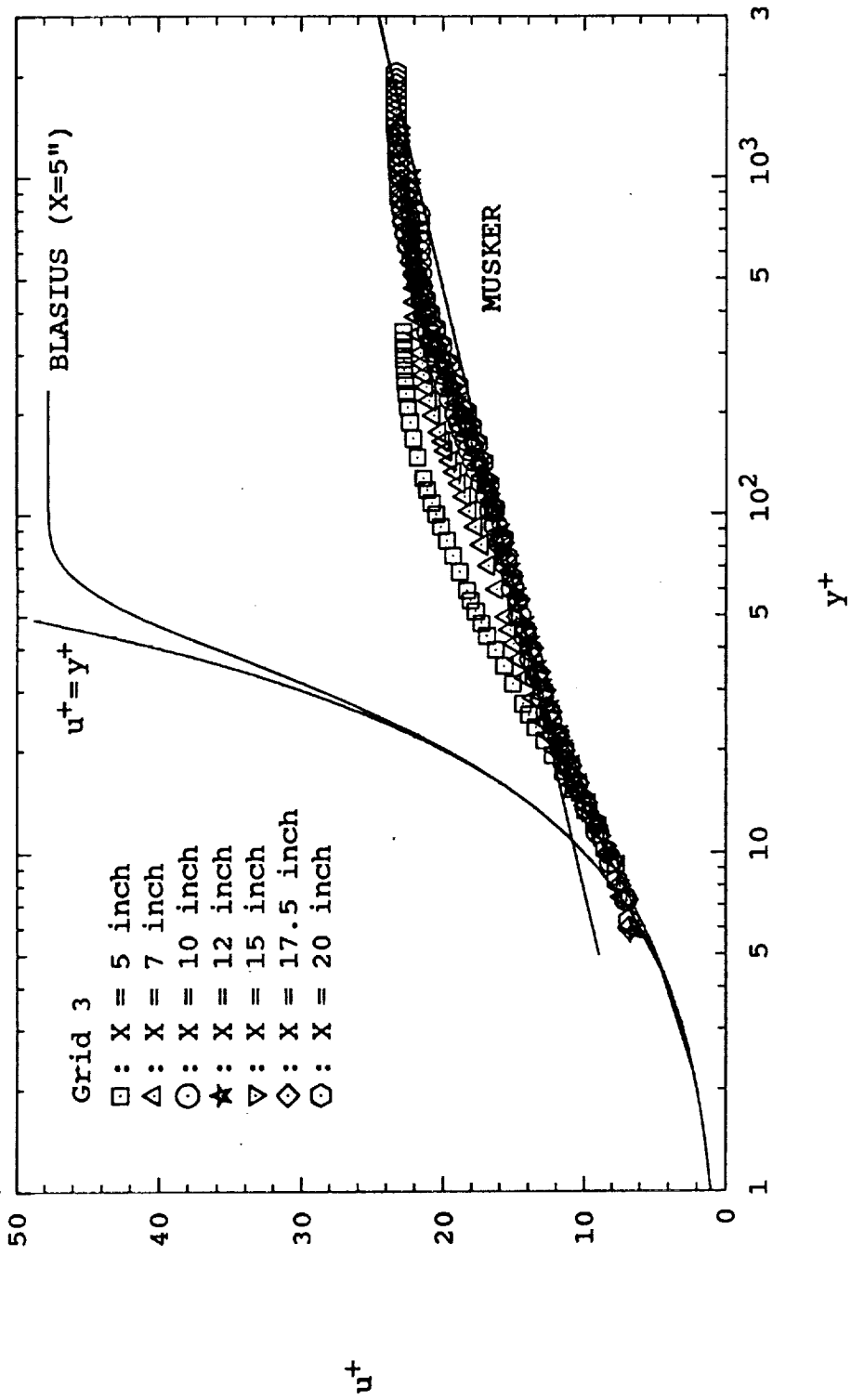


Fig. 21(e) Streamwise mean velocity profiles in wall units for grid 3

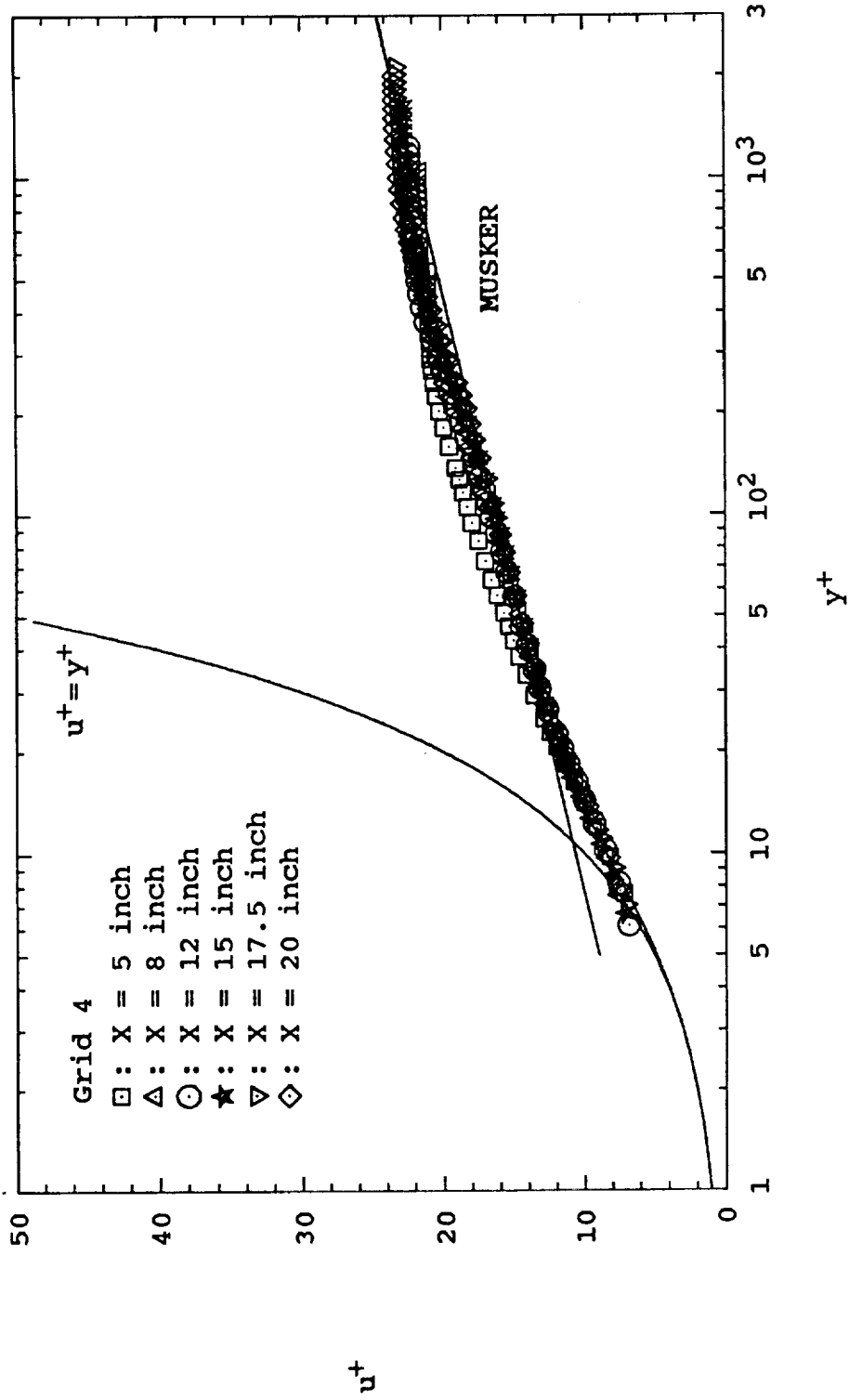


Fig. 21(f) Streamwise mean velocity profiles in wall units for grid 4

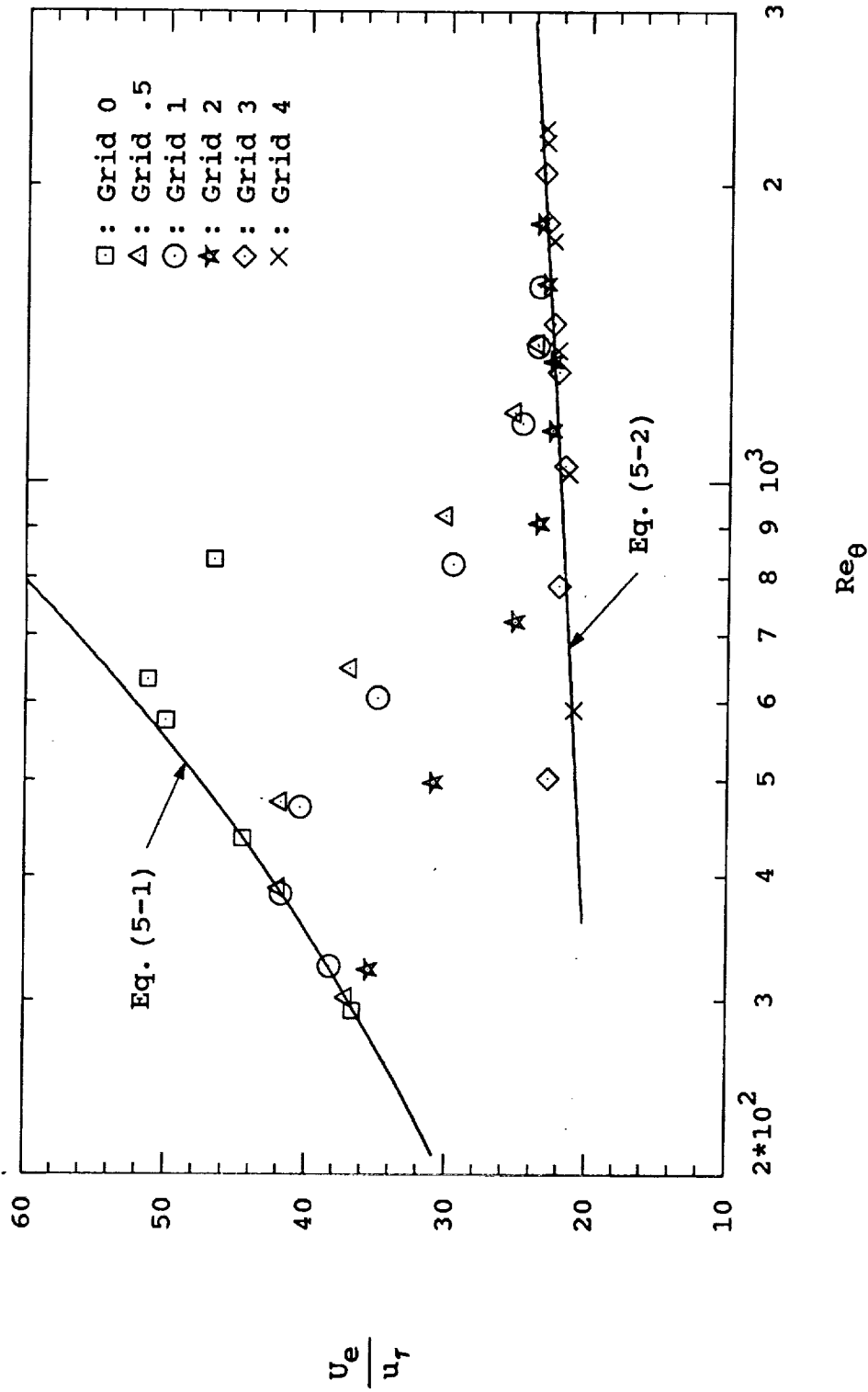


Fig. 22(a)  $u_e^+$  dependence on  $Re_\theta$  and freestream turbulence

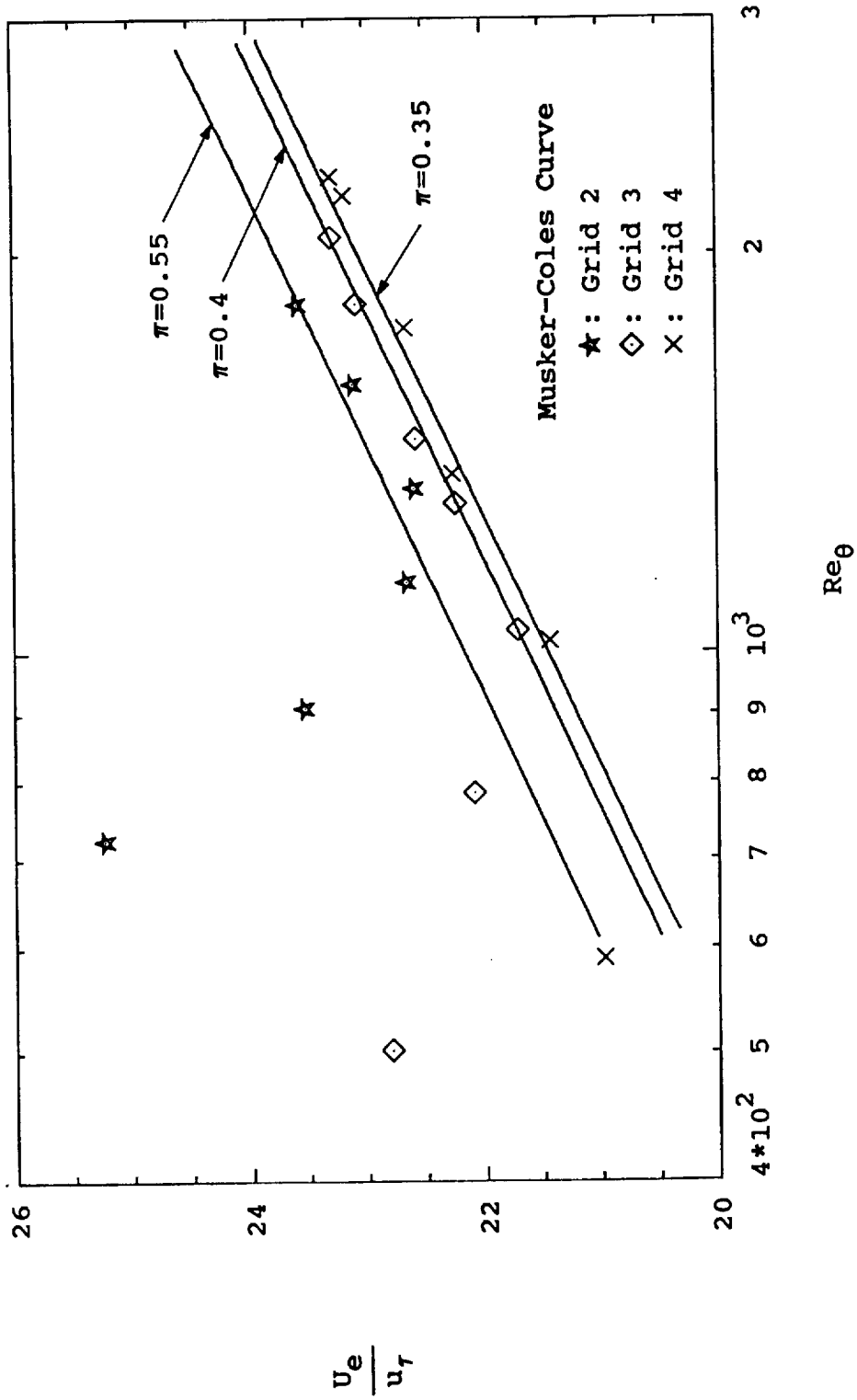


Fig. 22(b) Detailed comparison of  $u_e^+$  in turbulent boundary layer with Musker-Coles curves

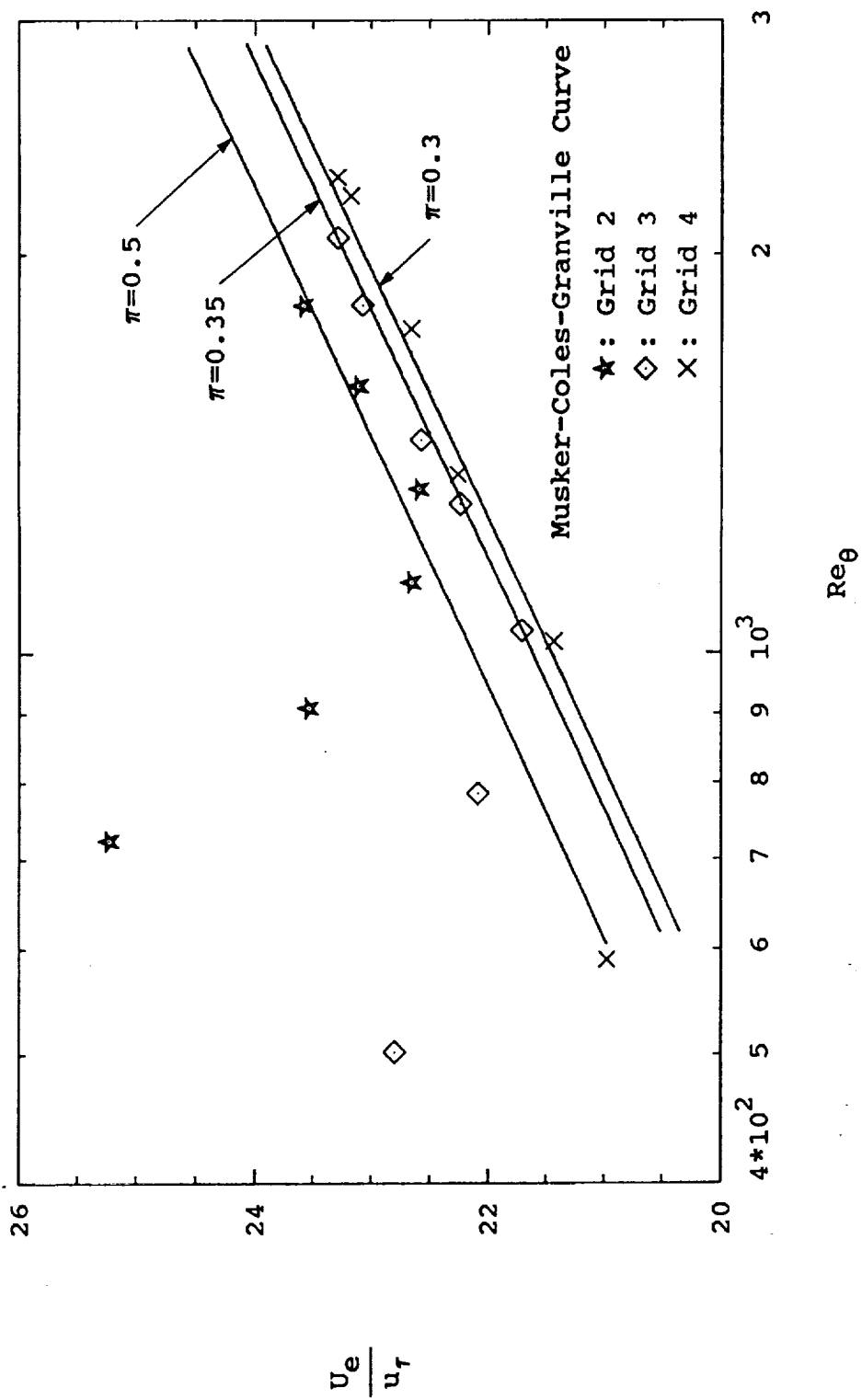


Fig. 22(c) Detailed comparison of  $u_e^+$  in turbulent boundary layer with Musker-Coles-Granville curves

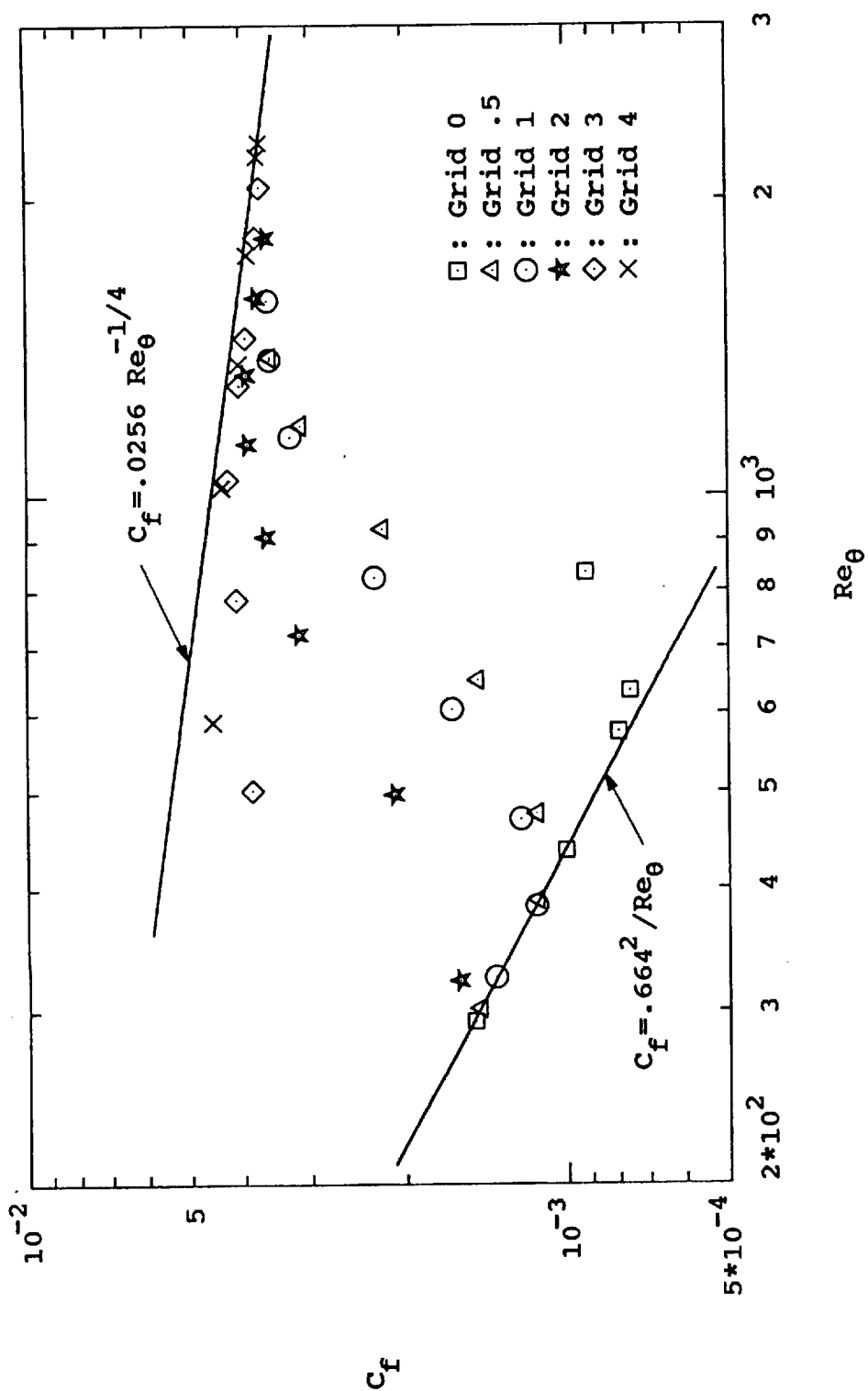


Fig. 23(a) Skin friction coefficient dependence on  $Re_\theta$  and freestream turbulence

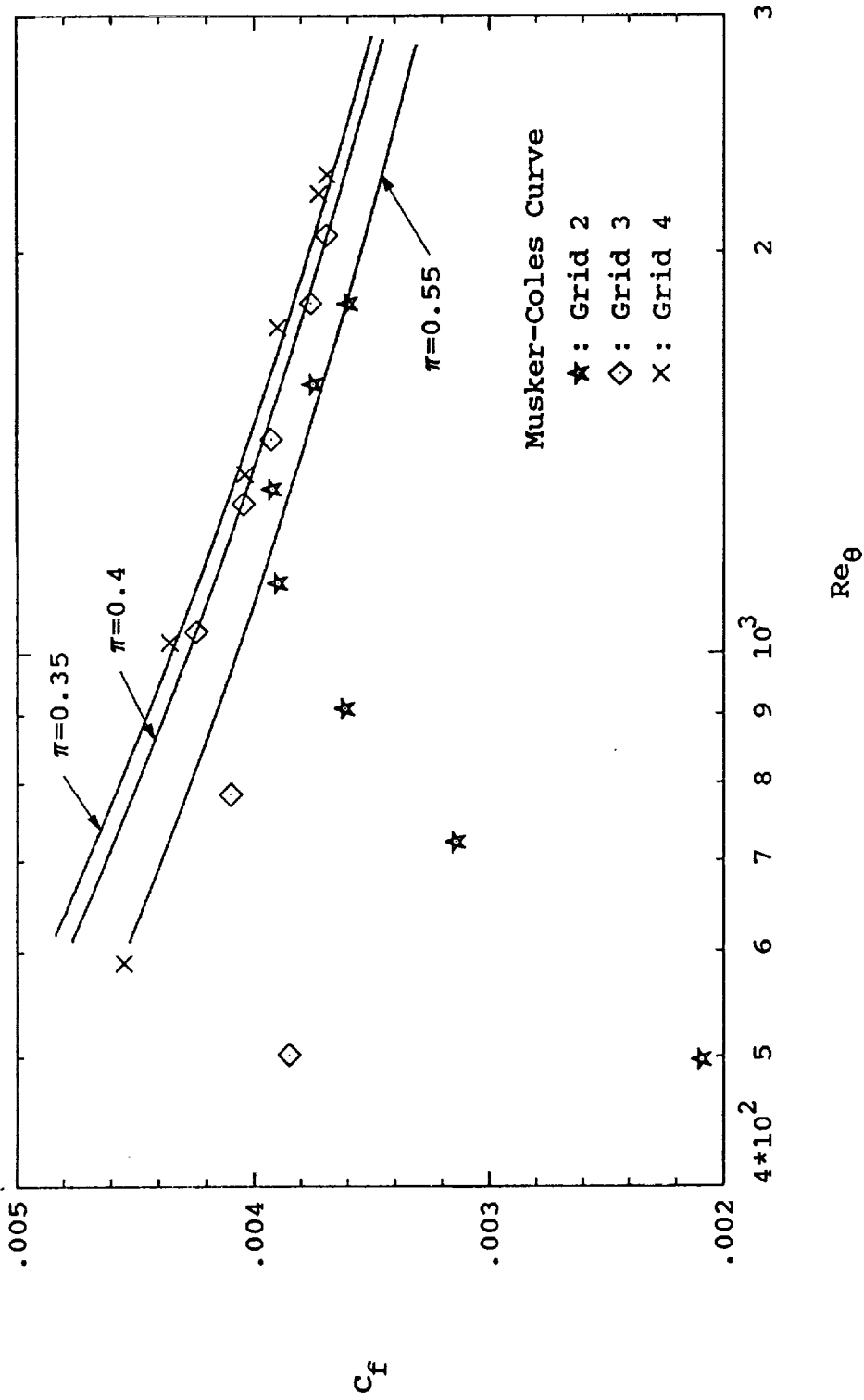


Fig. 23(b) Detailed comparison of  $C_f$  in turbulent boundary layer with Musker-Coles curves

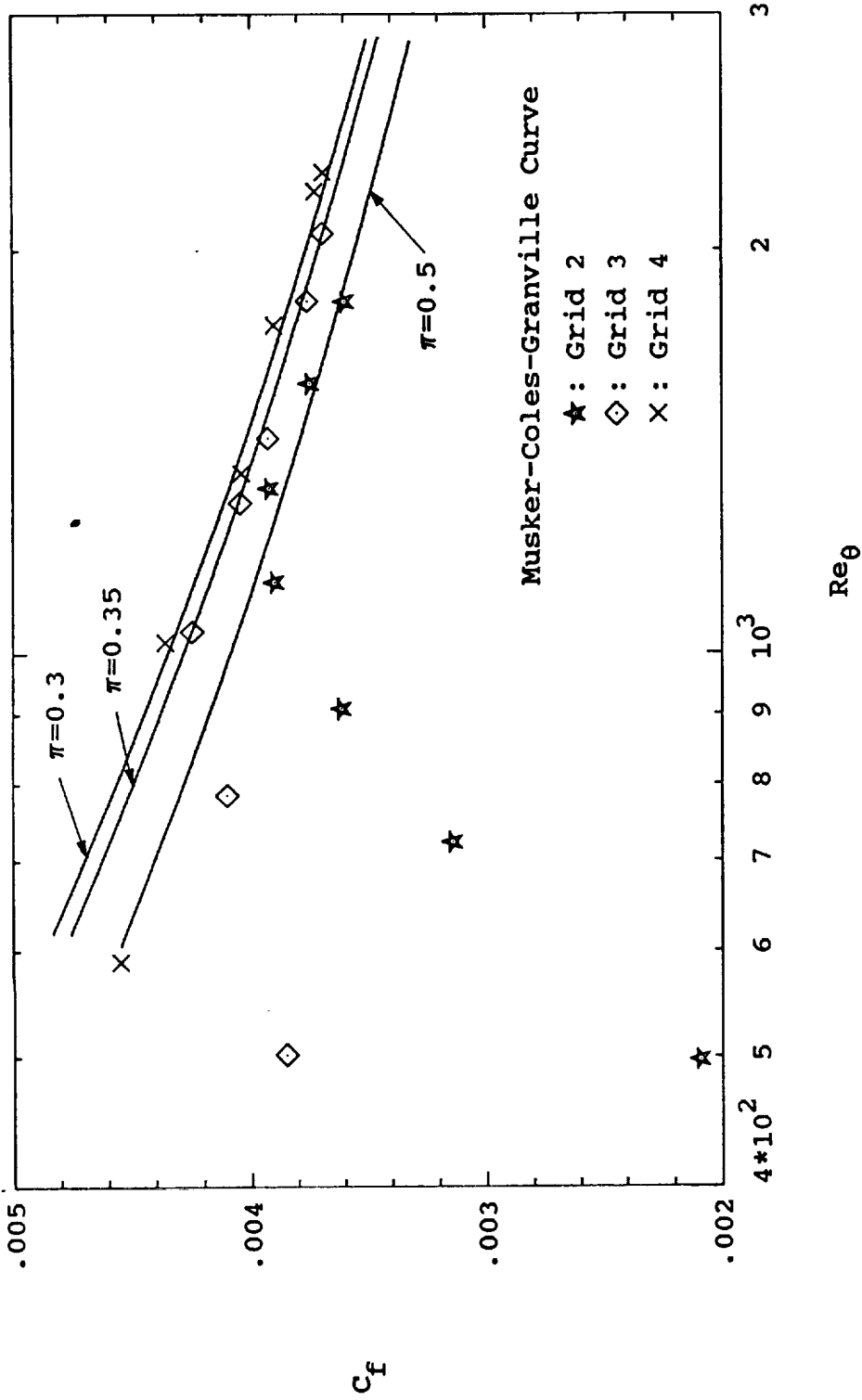


Fig. 23(c) Detailed comparison of  $C_f$  in turbulent boundary layer with Musker-Coles-Granville curves

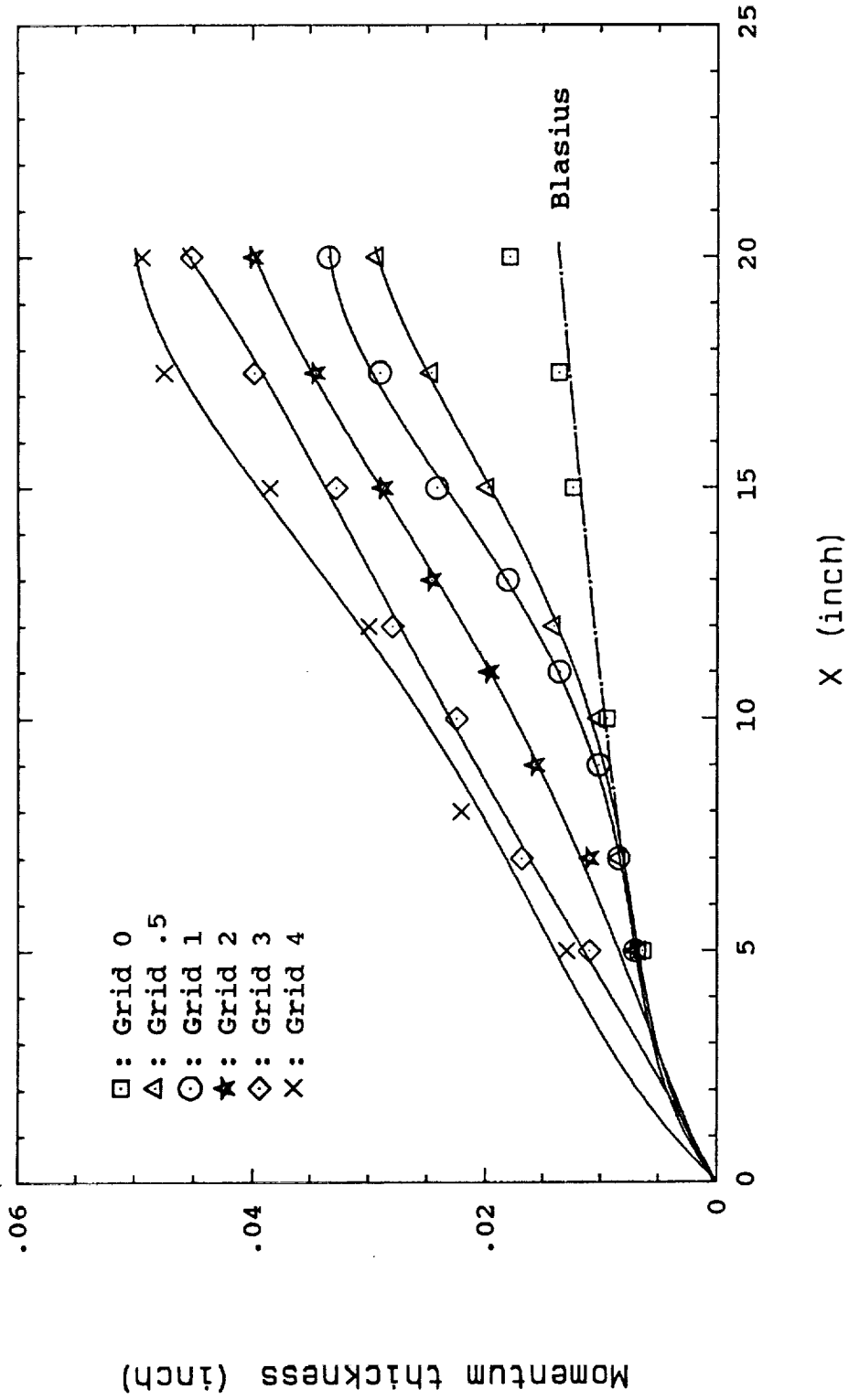


Fig. 24 Variation of integral momentum thickness with streamwise distance for all grids

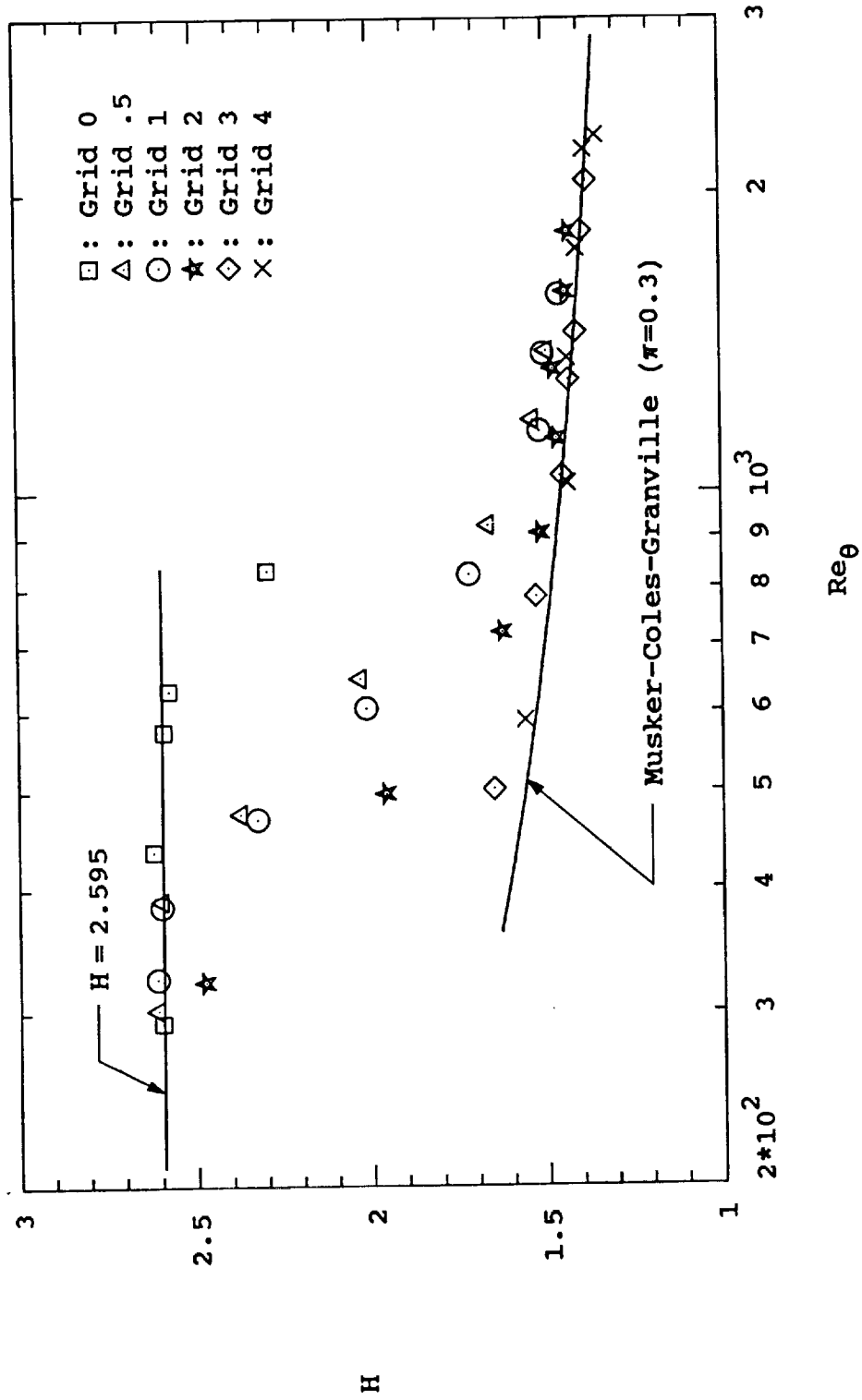


Fig. 25 Distribution of shape factor with  $Re_\theta$  for all grids

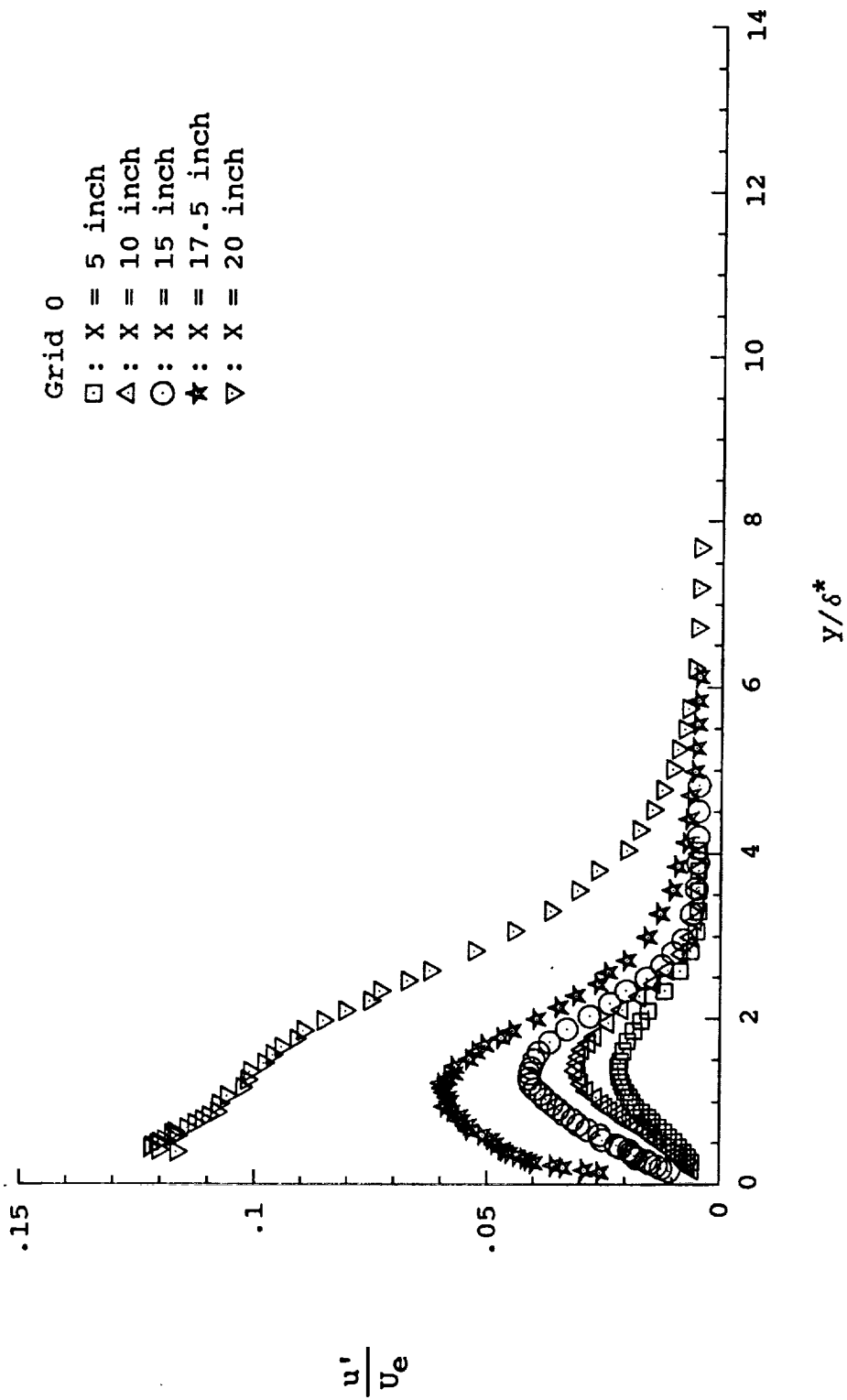


Fig. 26(a) Overall streamwise rms velocity profiles in outer coordinates for grid 0

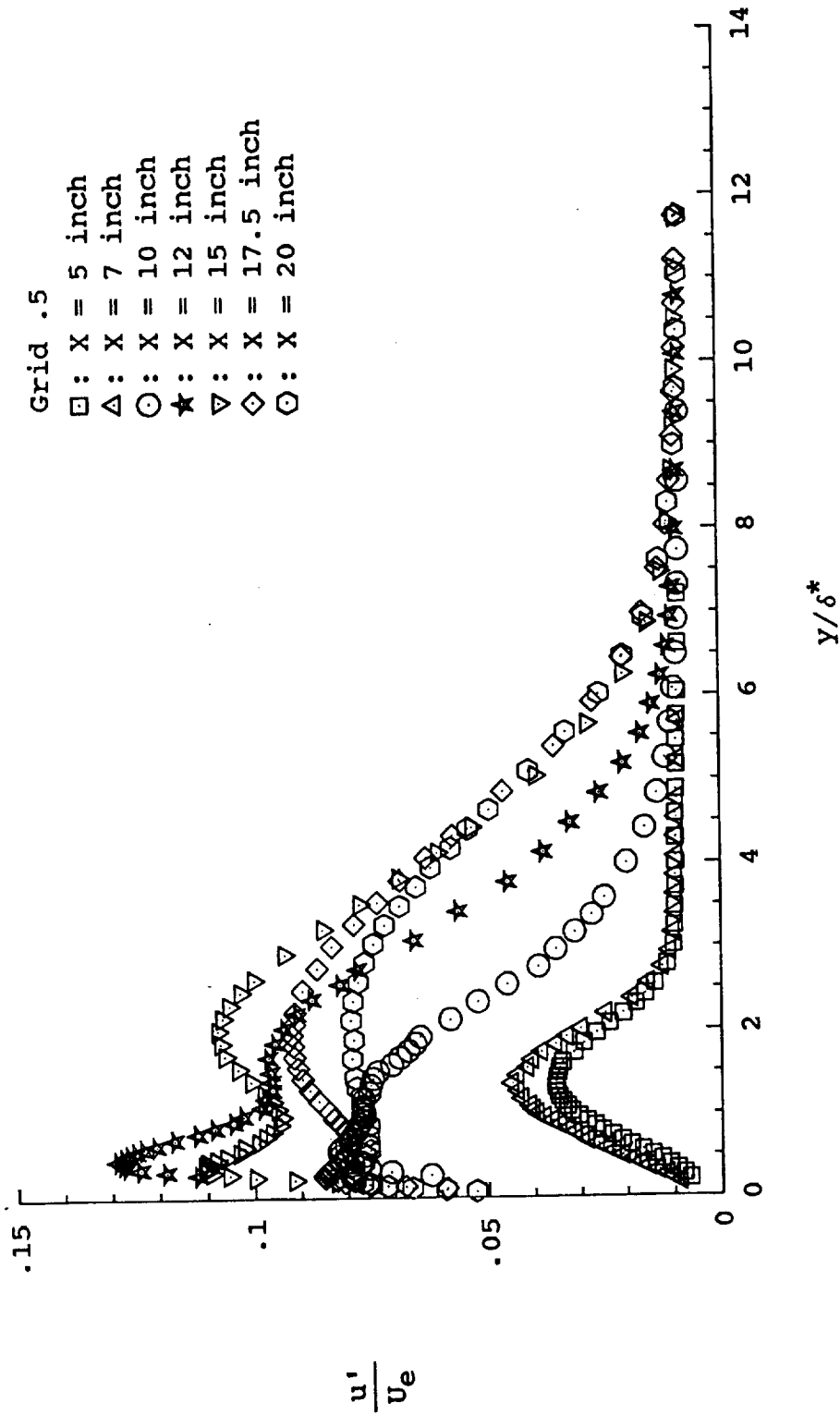


Fig. 26(b) Overall streamwise rms velocity profiles in outer coordinates for grid .5

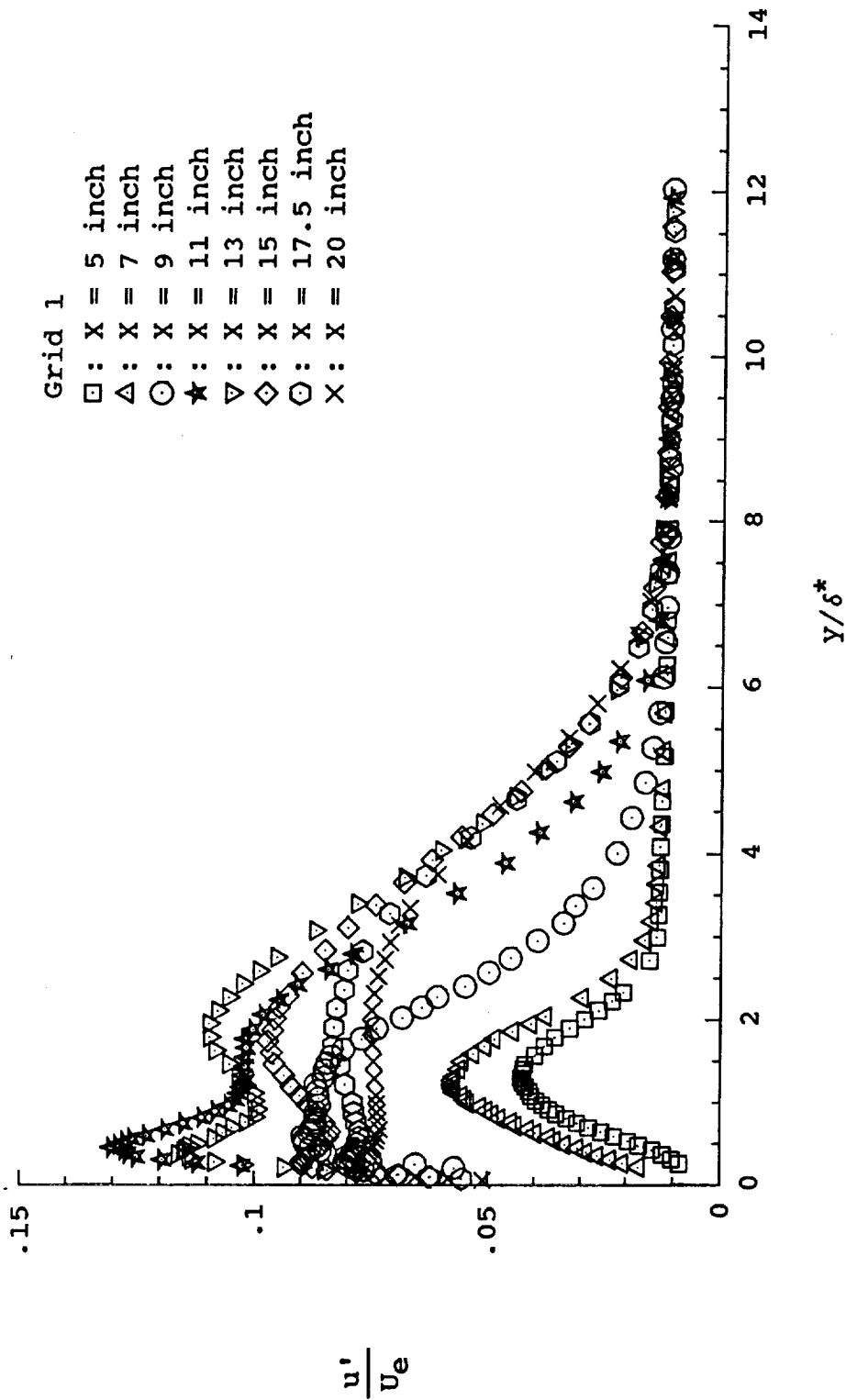


Fig. 26(c) Overall streamwise rms velocity profiles in outer coordinates for grid 1

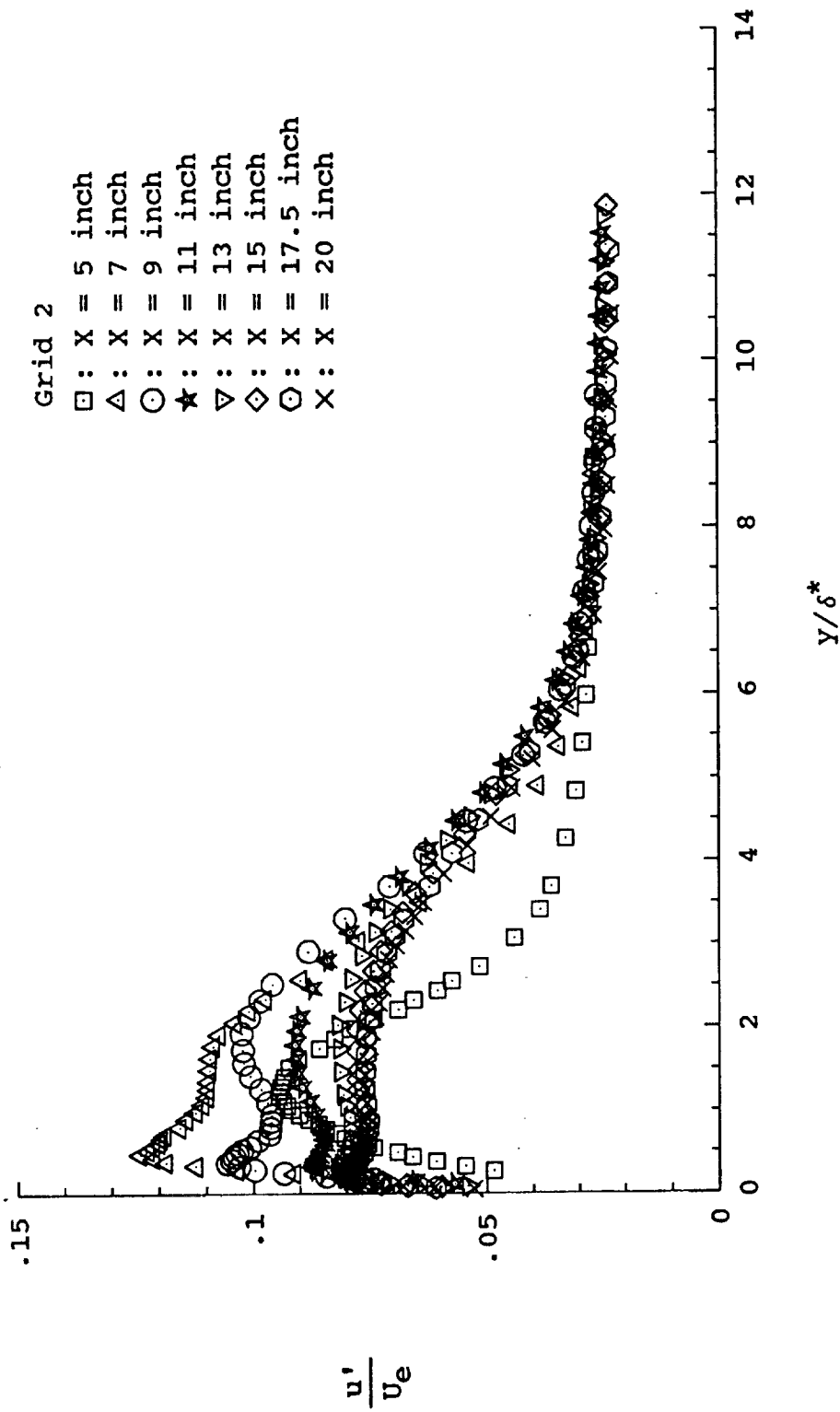


Fig. 26(d) Overall streamwise rms velocity profiles in outer coordinates for grid 2

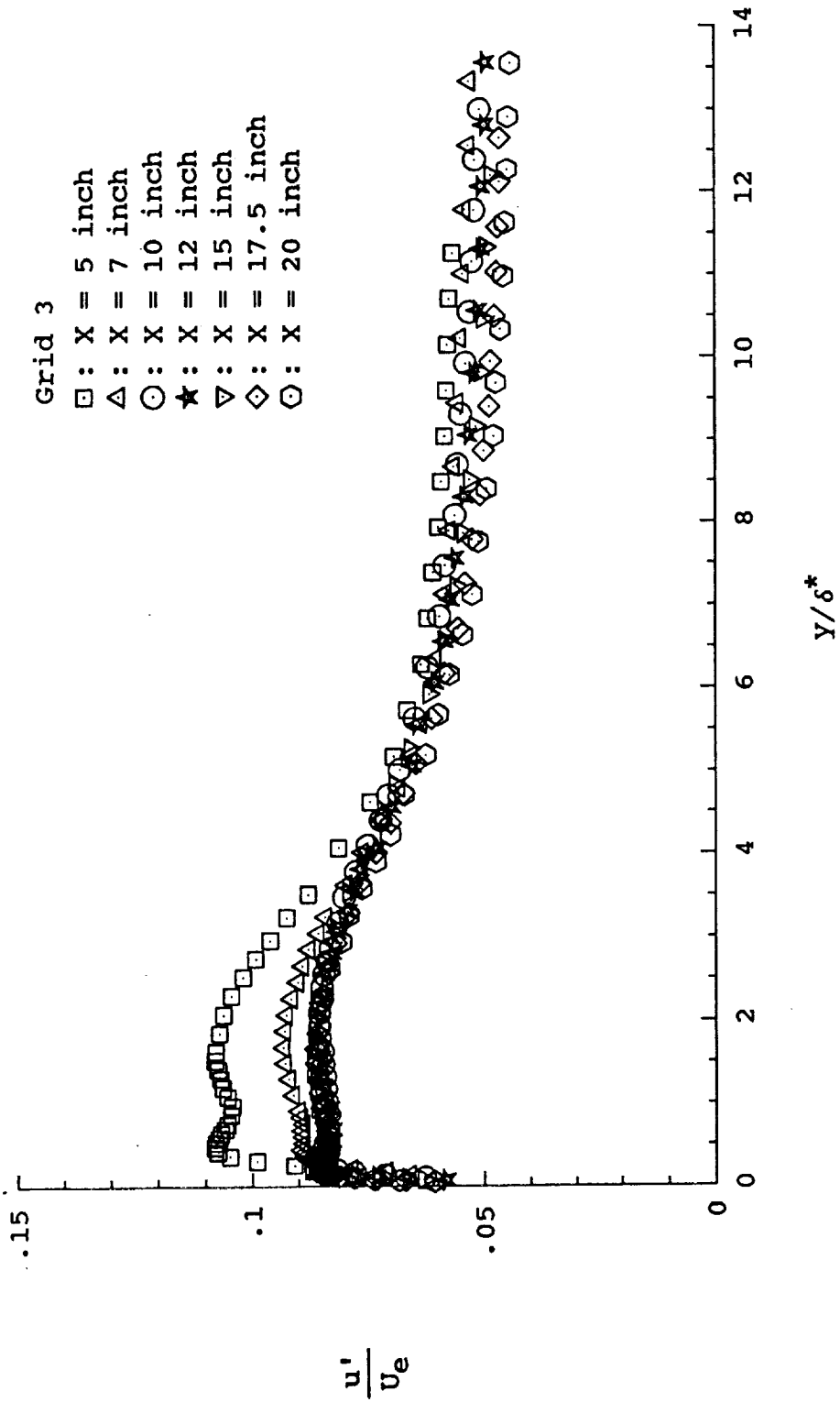


Fig. 26(e) Overall streamwise rms velocity profiles in outer coordinates  
for grid 3

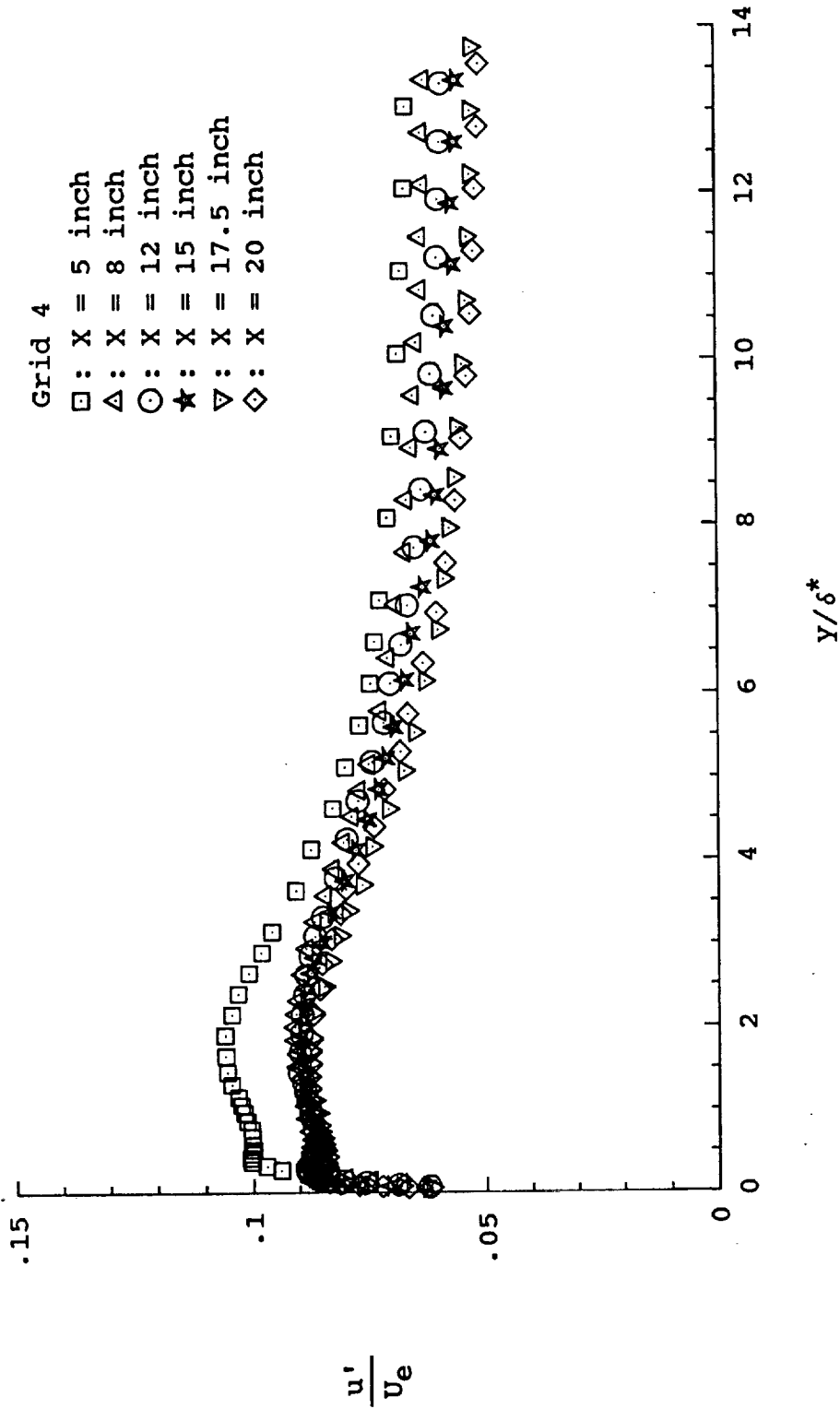


Fig. 26(f) Overall streamwise rms velocity profiles in outer coordinates for grid 4

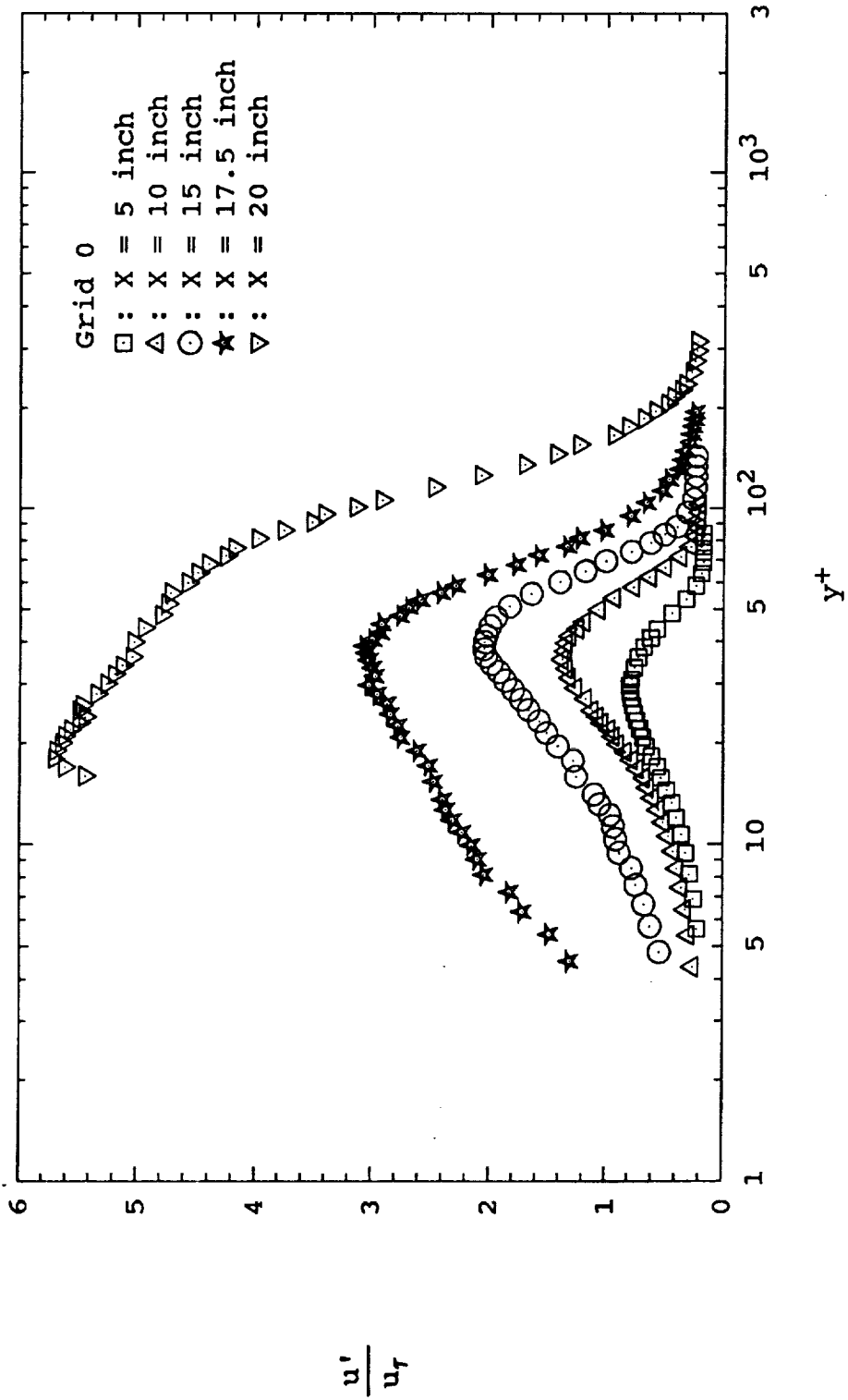


Fig. 27(a) Overall streamwise rms velocity profiles in wall units for grid 0

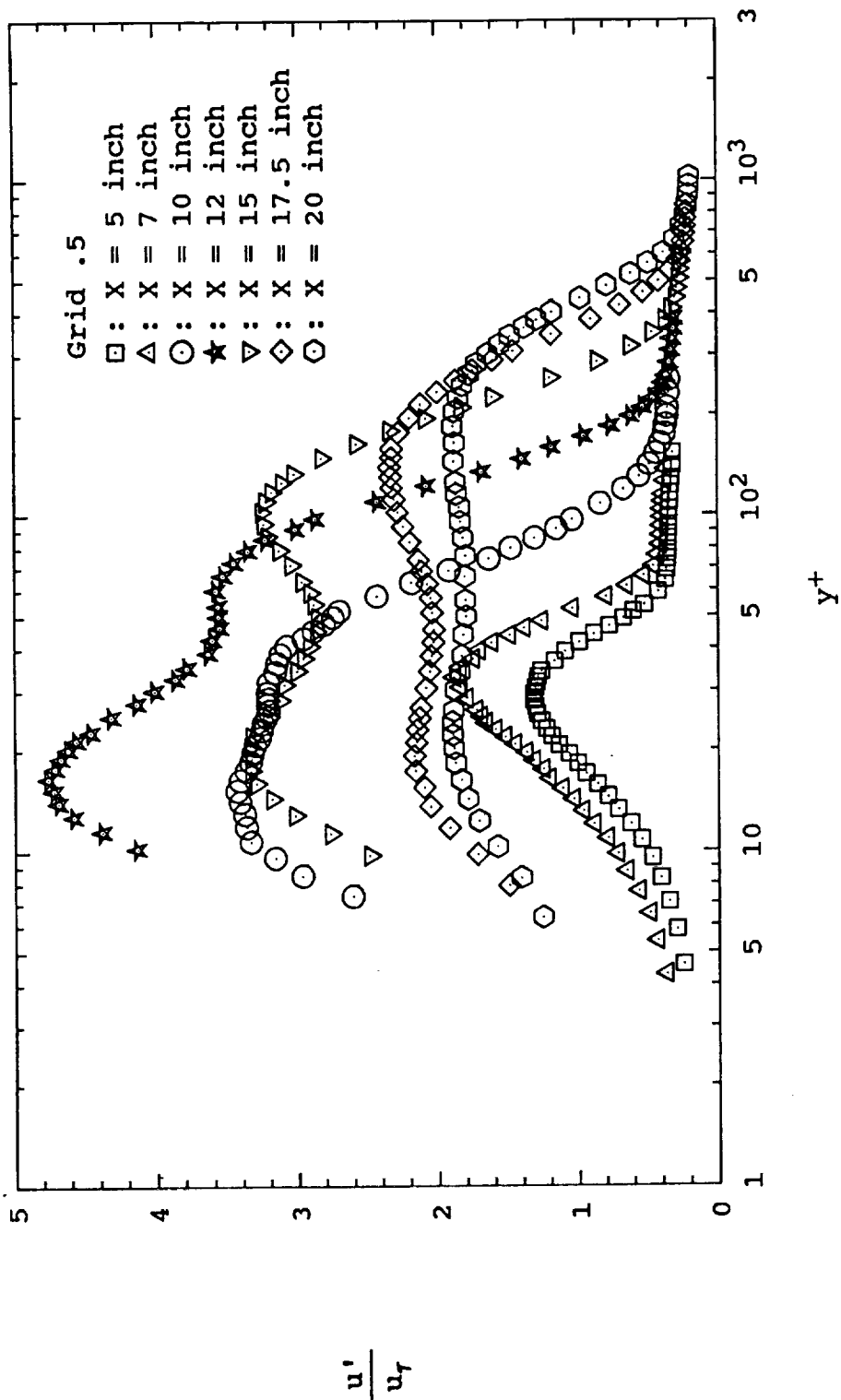


Fig. 27(b) Overall streamwise rms velocity profiles in wall units for grid .5

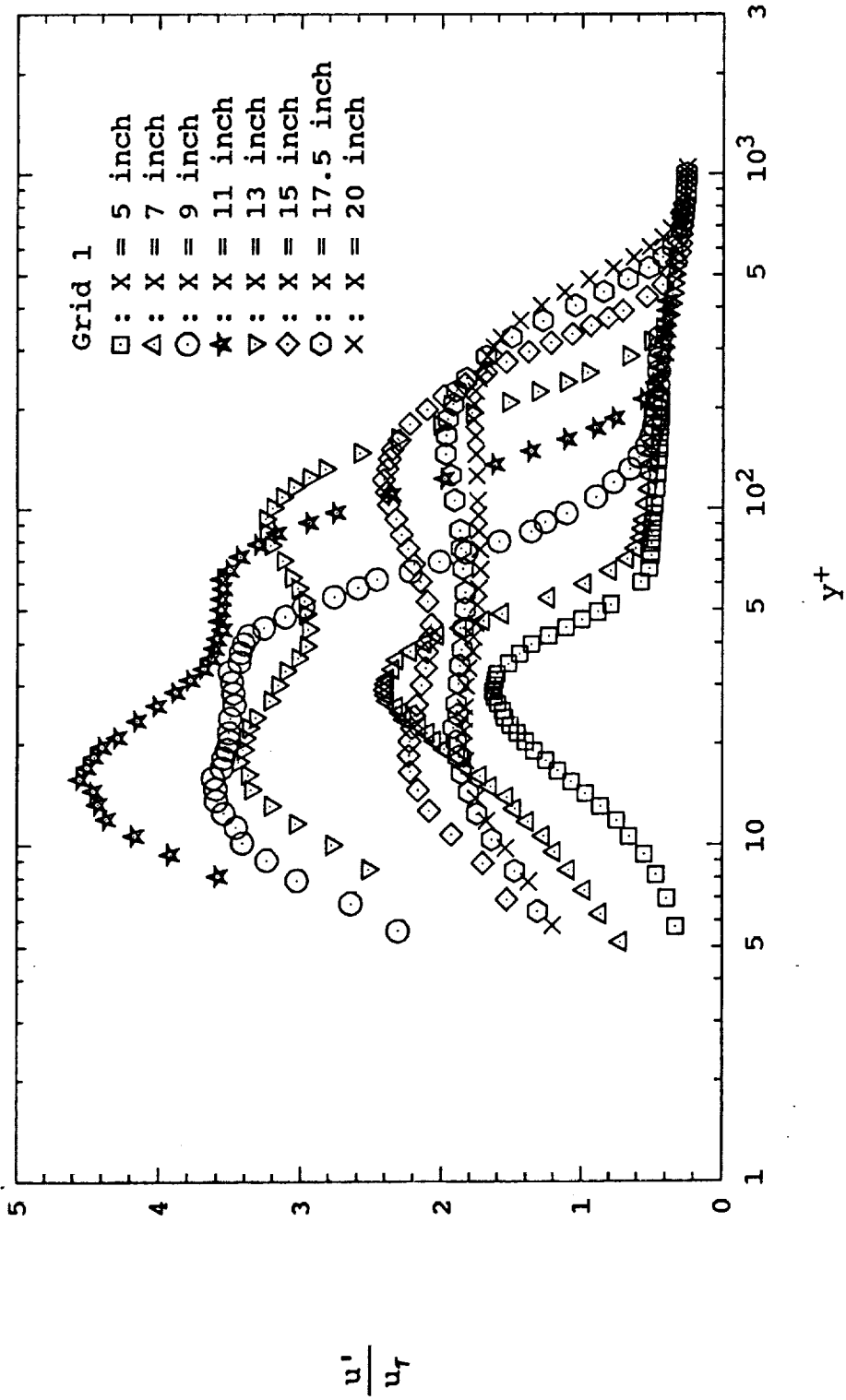


Fig. 27(c) Overall streamwise rms velocity profiles in wall units for grid 1

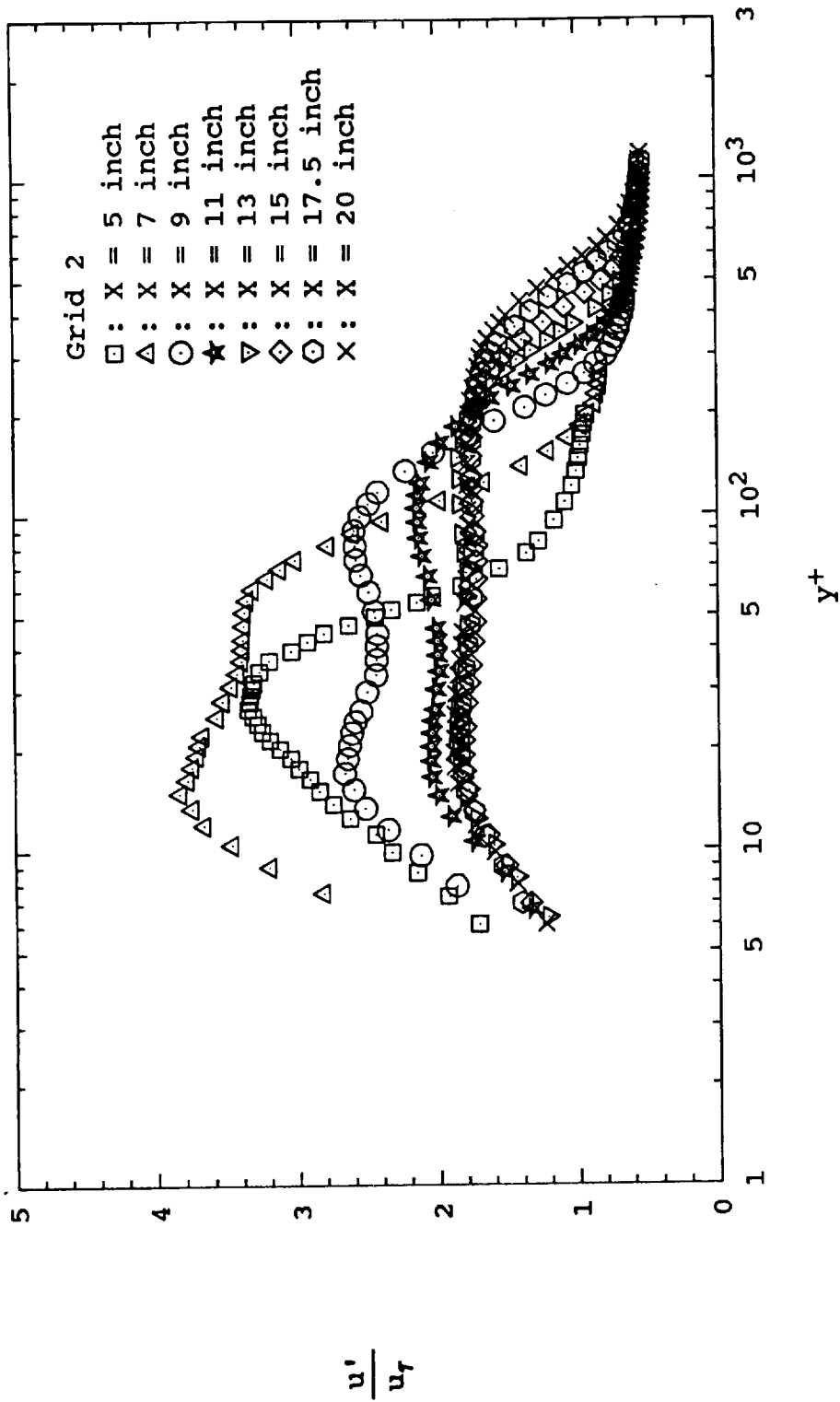


Fig. 27(d) Overall streamwise rms velocity profiles in wall units for grid 2

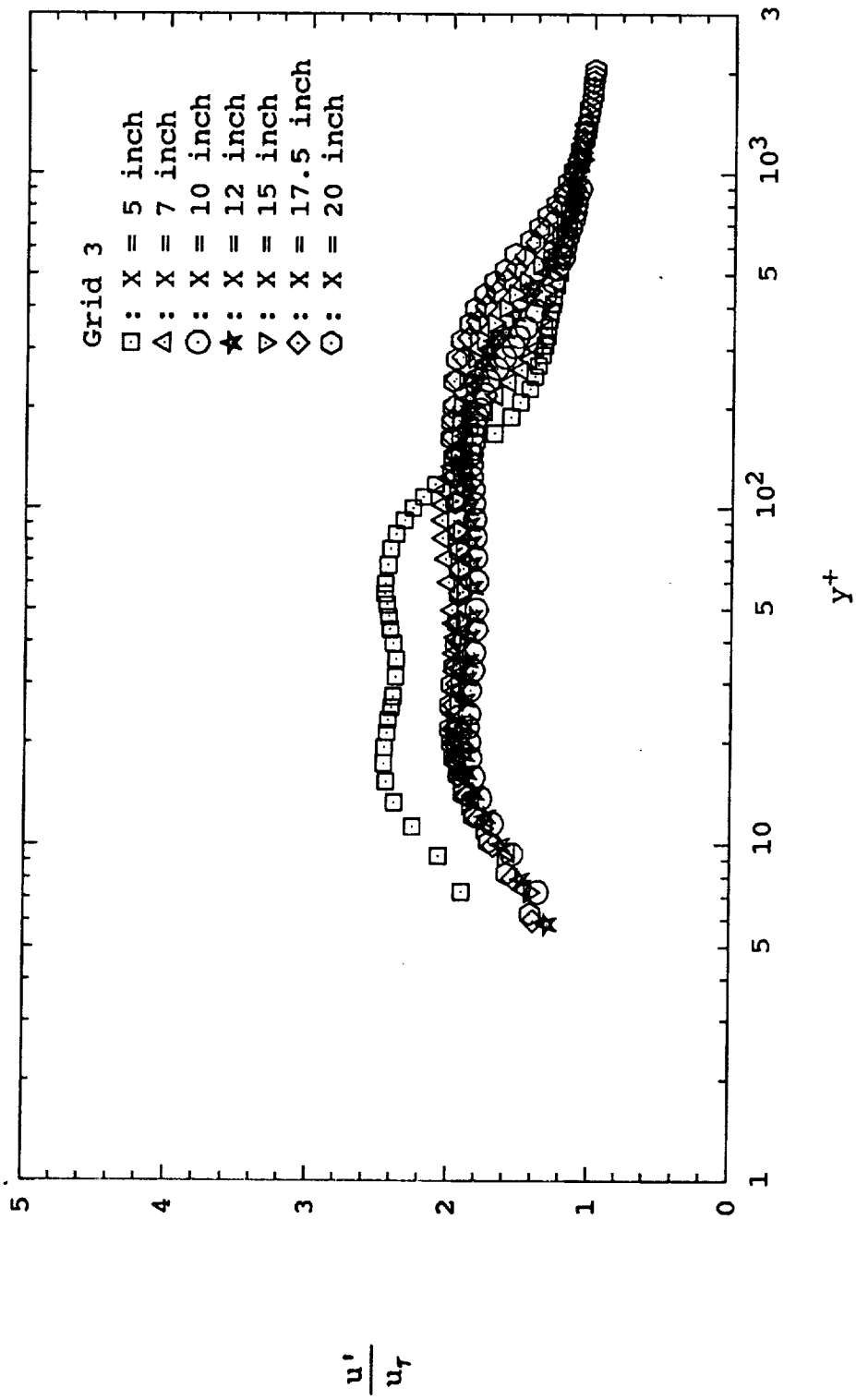


Fig. 27(e) Overall streamwise rms velocity profiles in wall units for grid 3

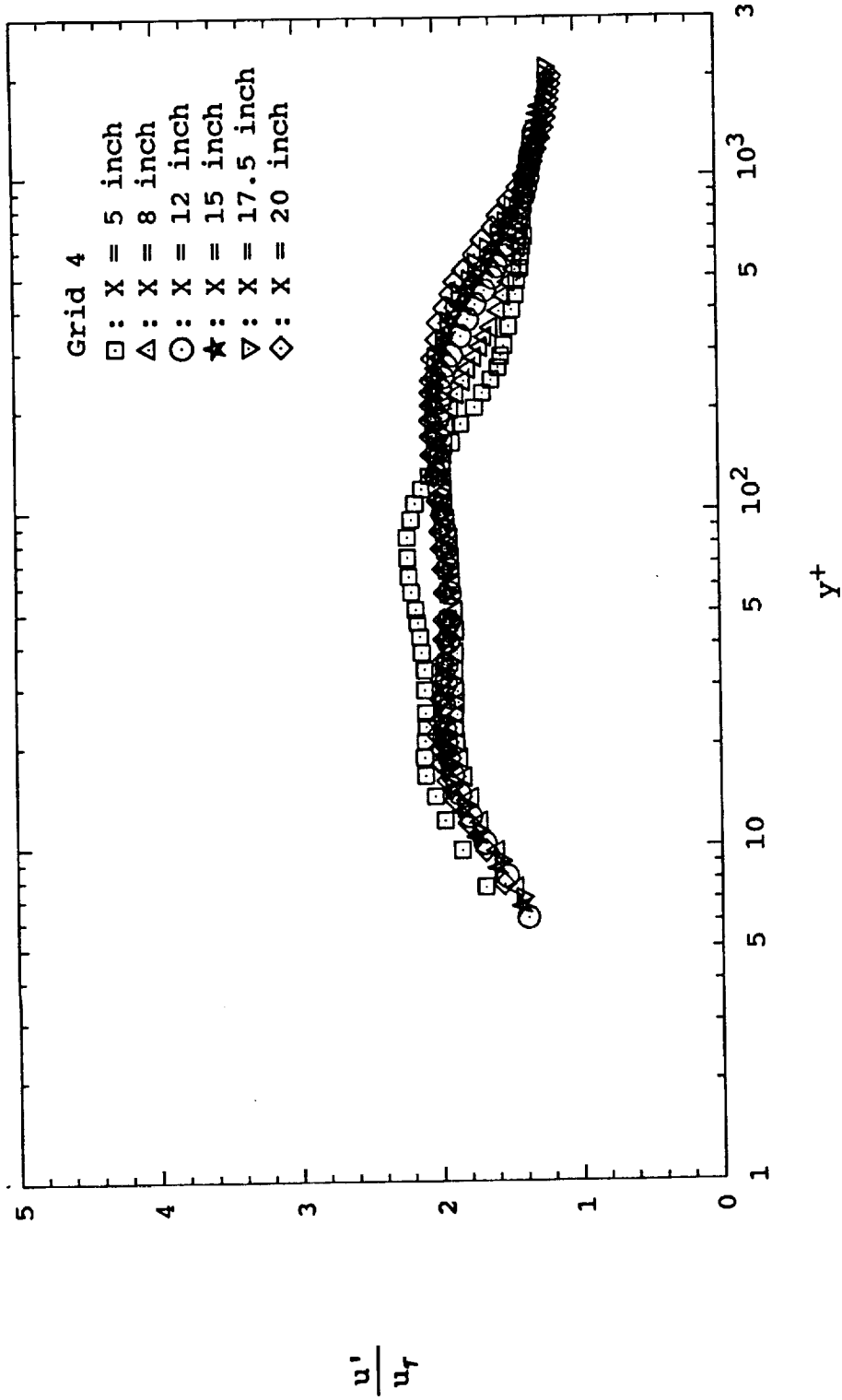


Fig. 27(f) Overall streamwise rms velocity profiles in wall units  
for grid 4

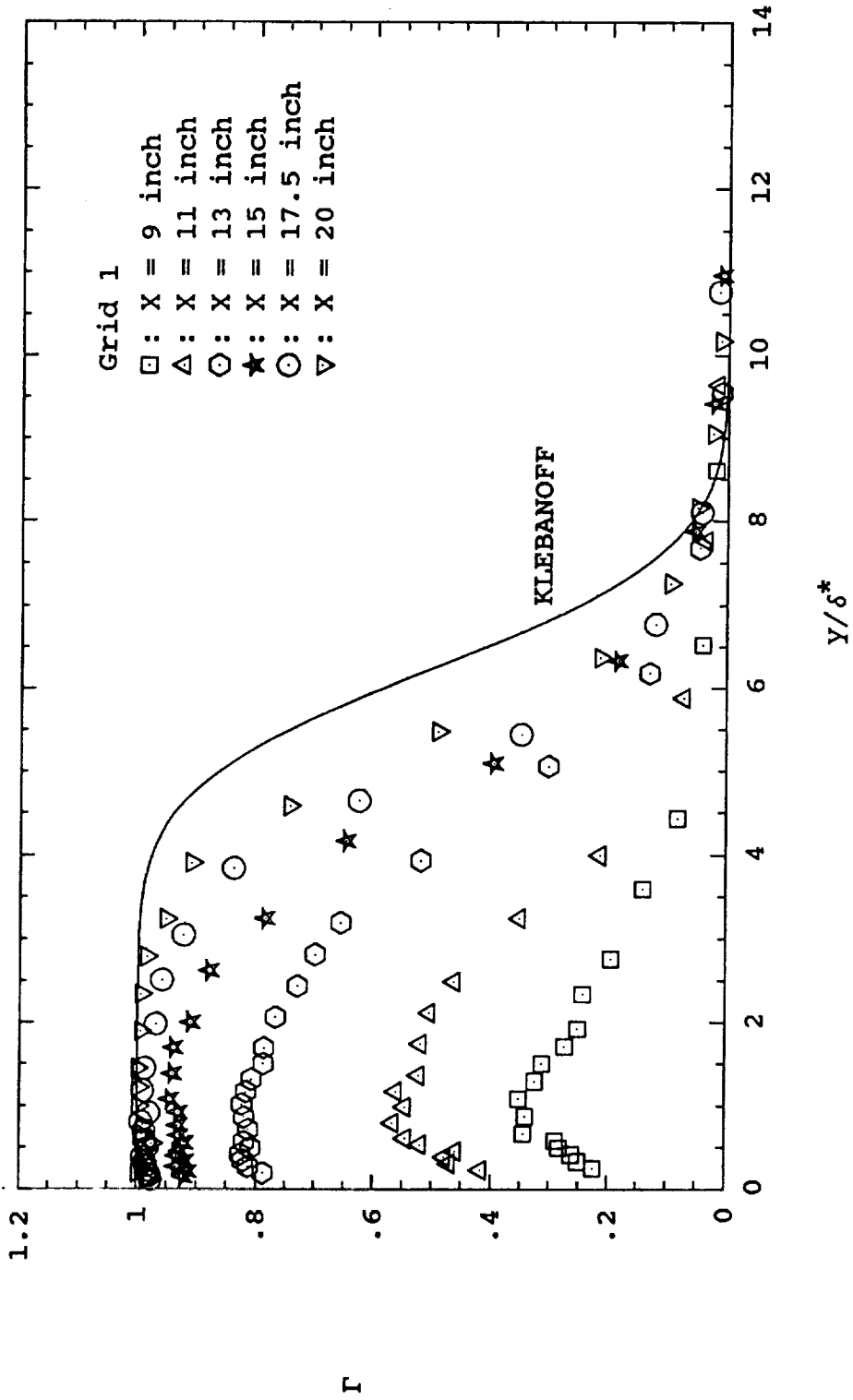


Fig. 28(a) Intermittency profiles across the boundary layer for grid 1

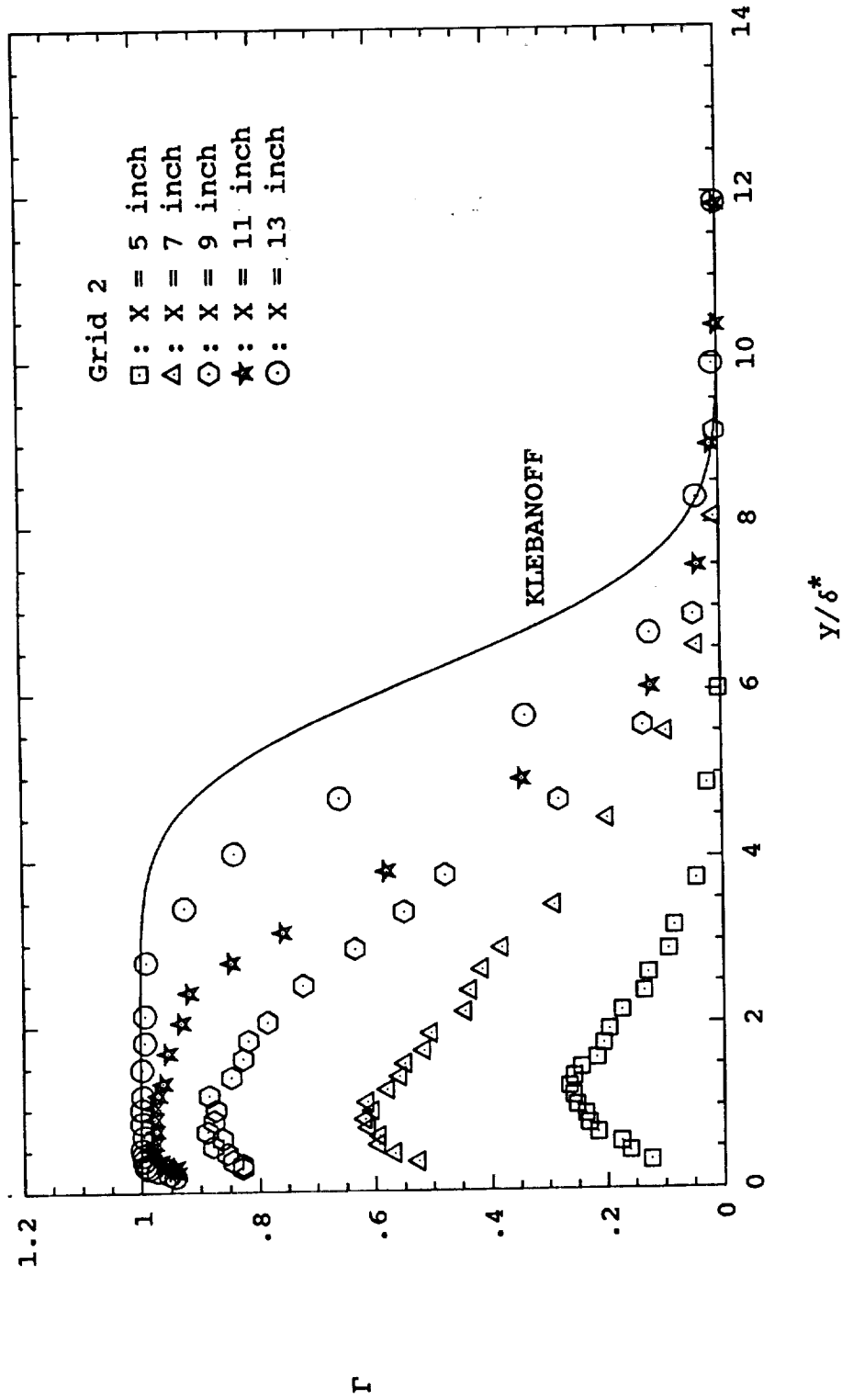


Fig. 28(b) Intermittency profiles across the boundary layer for grid 2

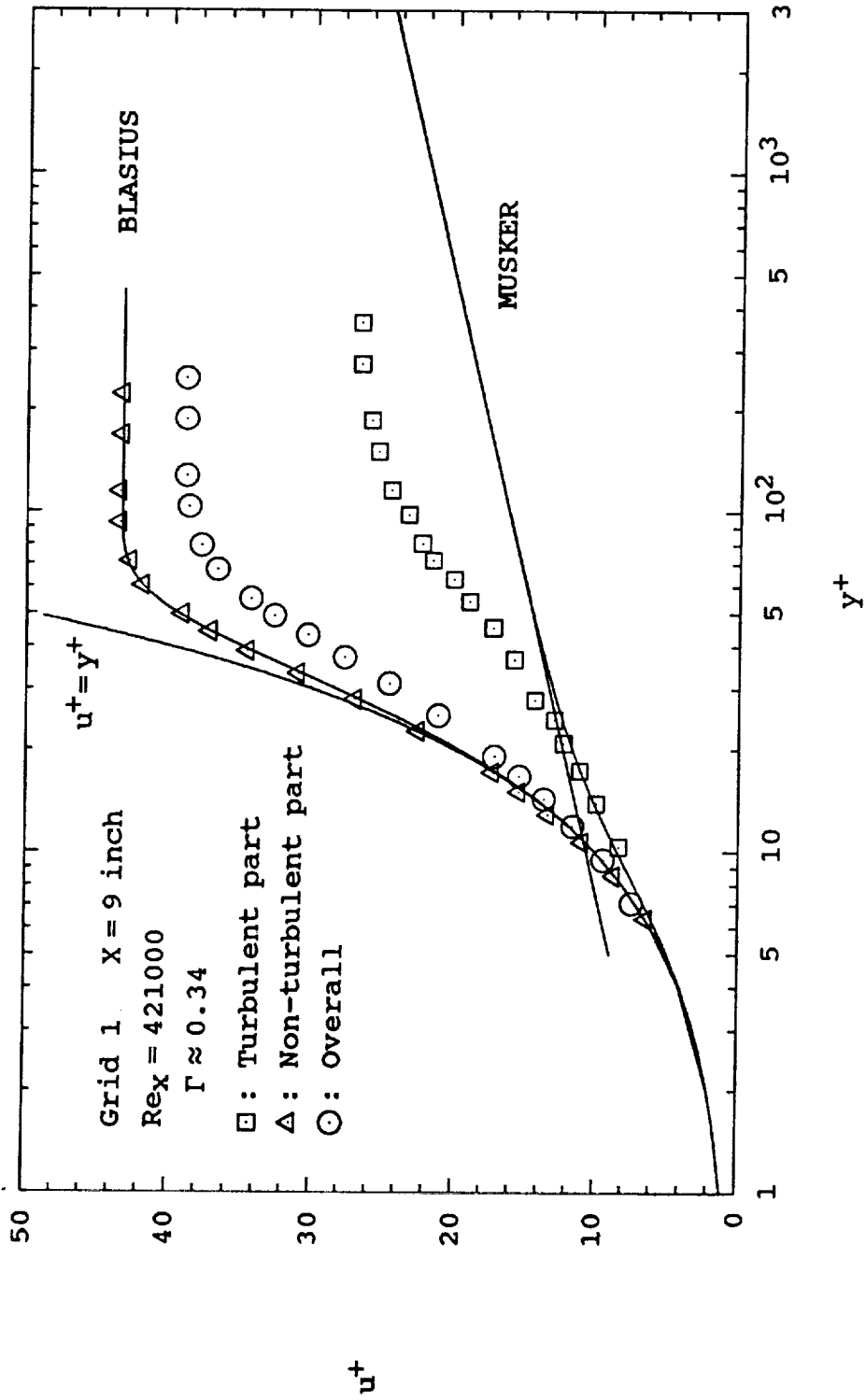


Fig. 29(a) Conditionally sampled mean velocity profiles in wall units at X=9 inches for grid 1

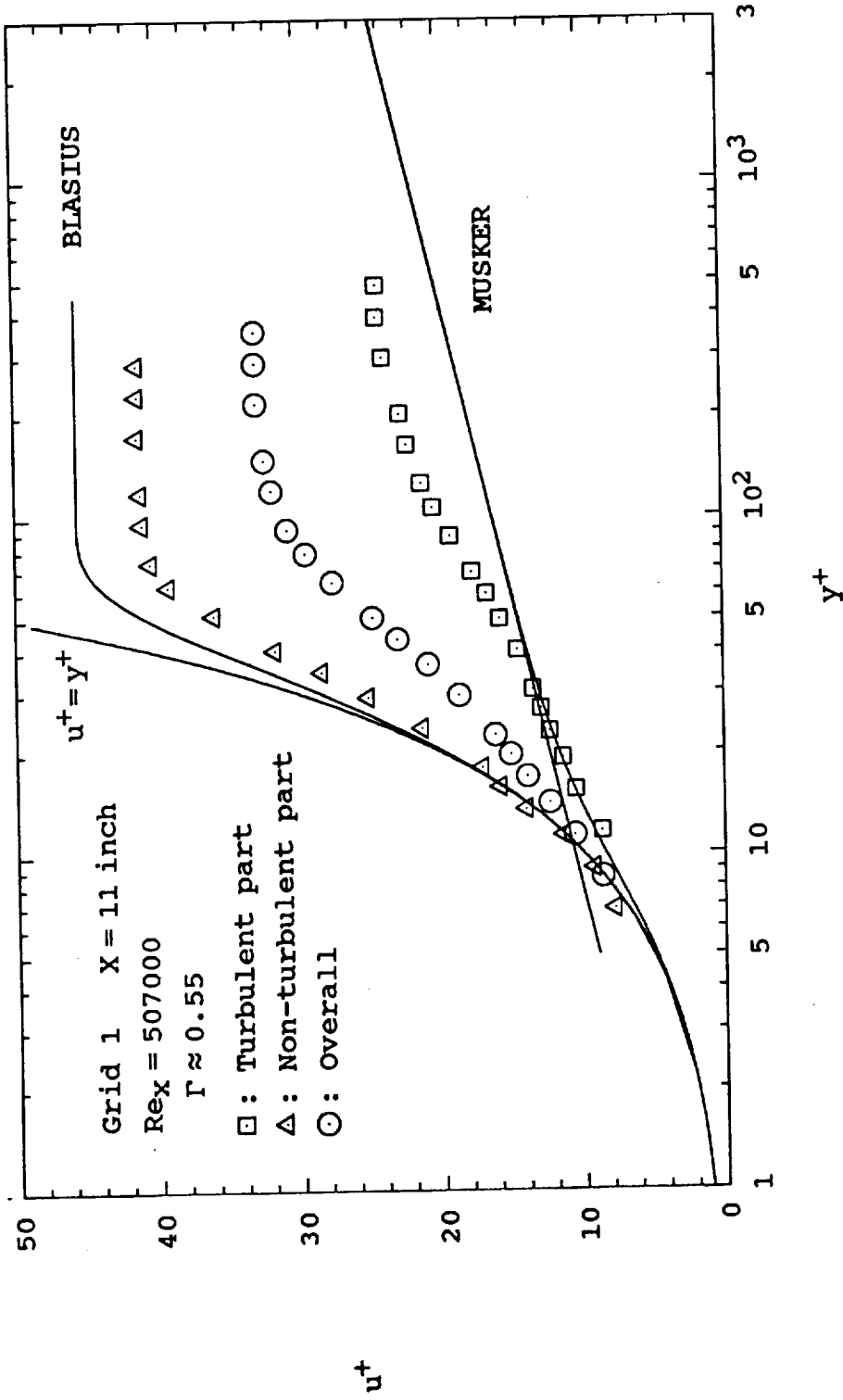


Fig. 29(b) Conditionally sampled mean velocity profiles in wall units at X=11 inches for grid 1

C-3

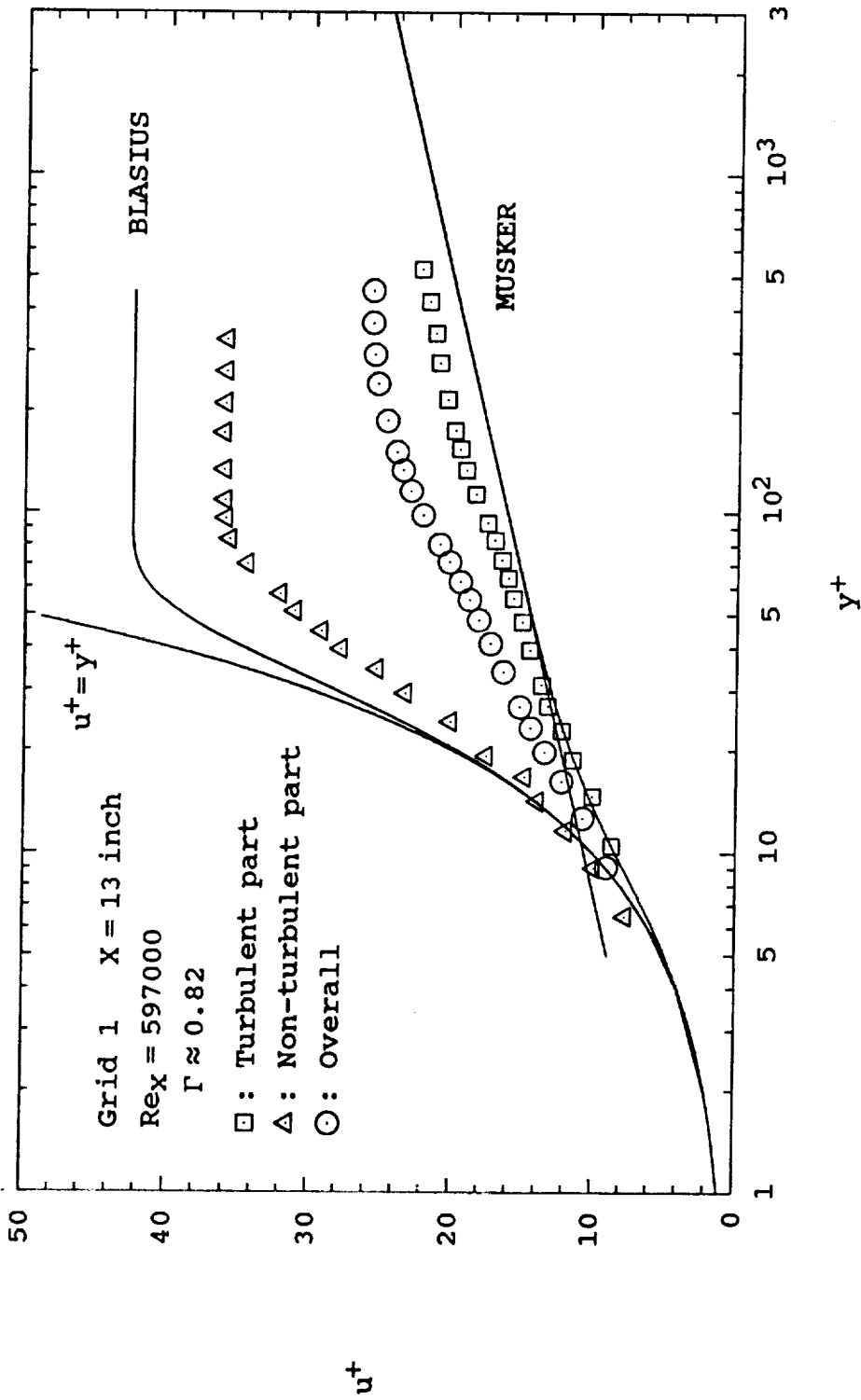


Fig. 29(c) Conditionally sampled mean velocity profiles in wall units at X=13 inches for grid 1

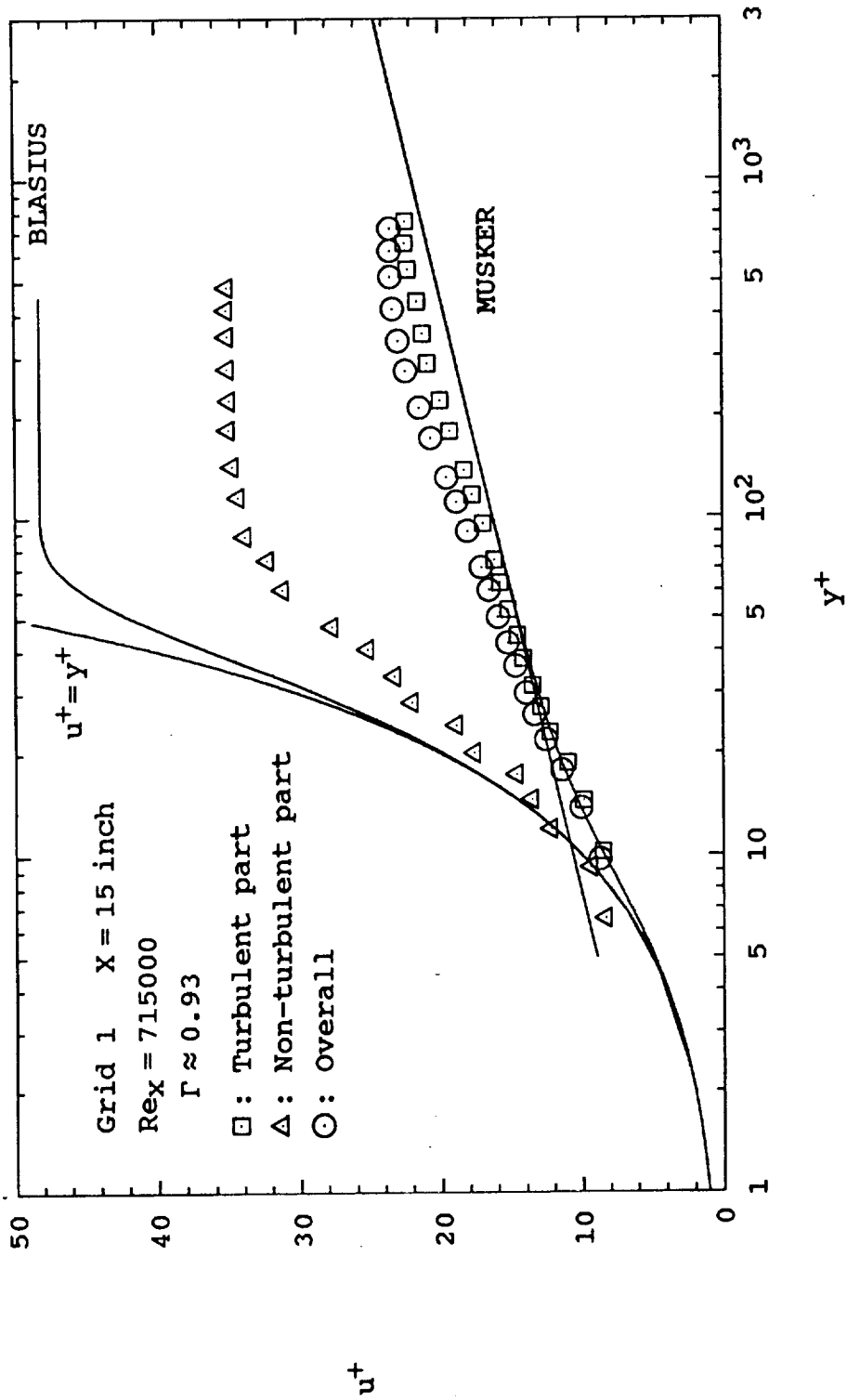


Fig. 29(d) Conditionally sampled mean velocity profiles in wall units at  $X=15$  inches for grid 1

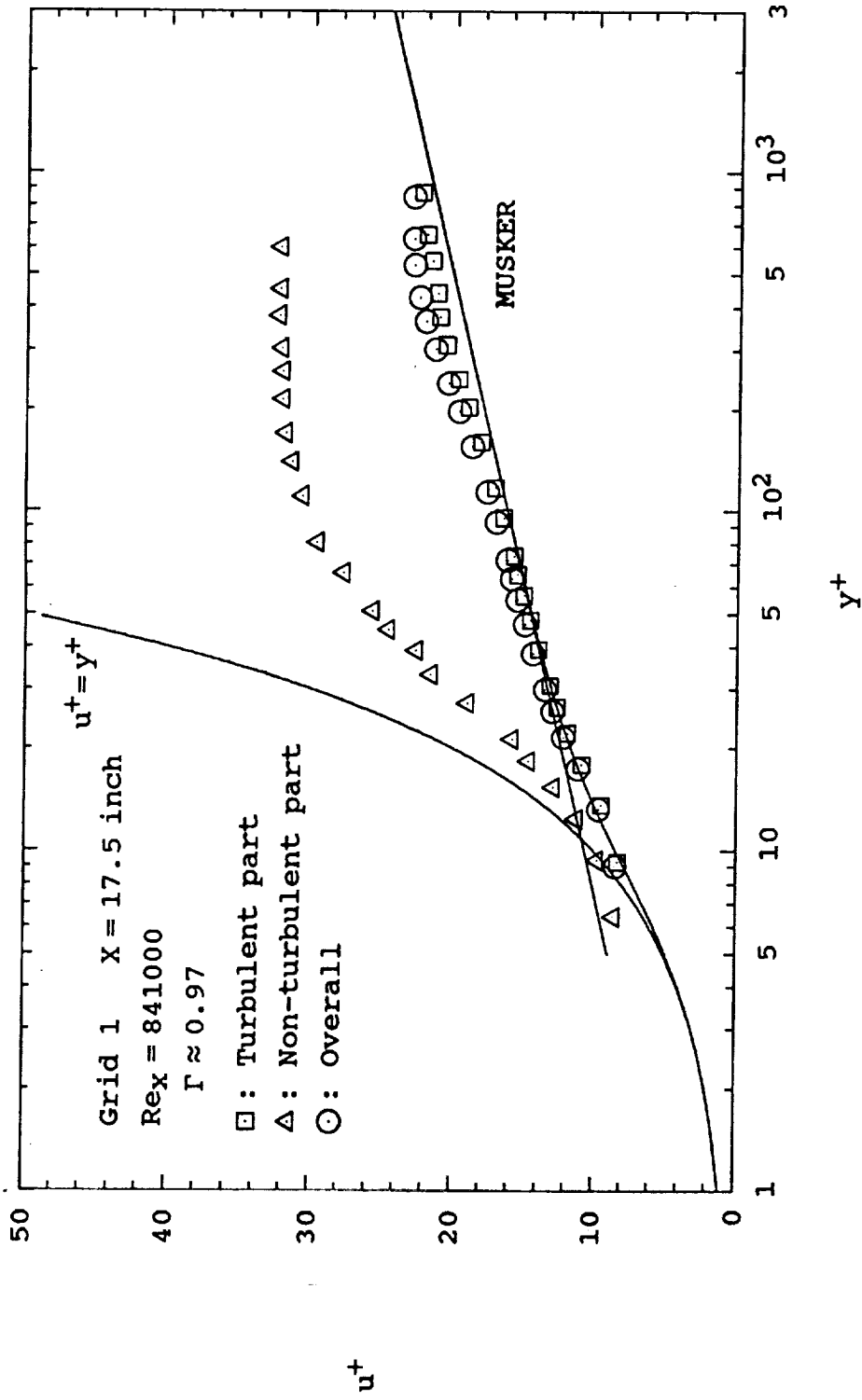


Fig. 29(e) Conditionally sampled mean velocity profiles in wall units at X=17.5 inches for grid 1

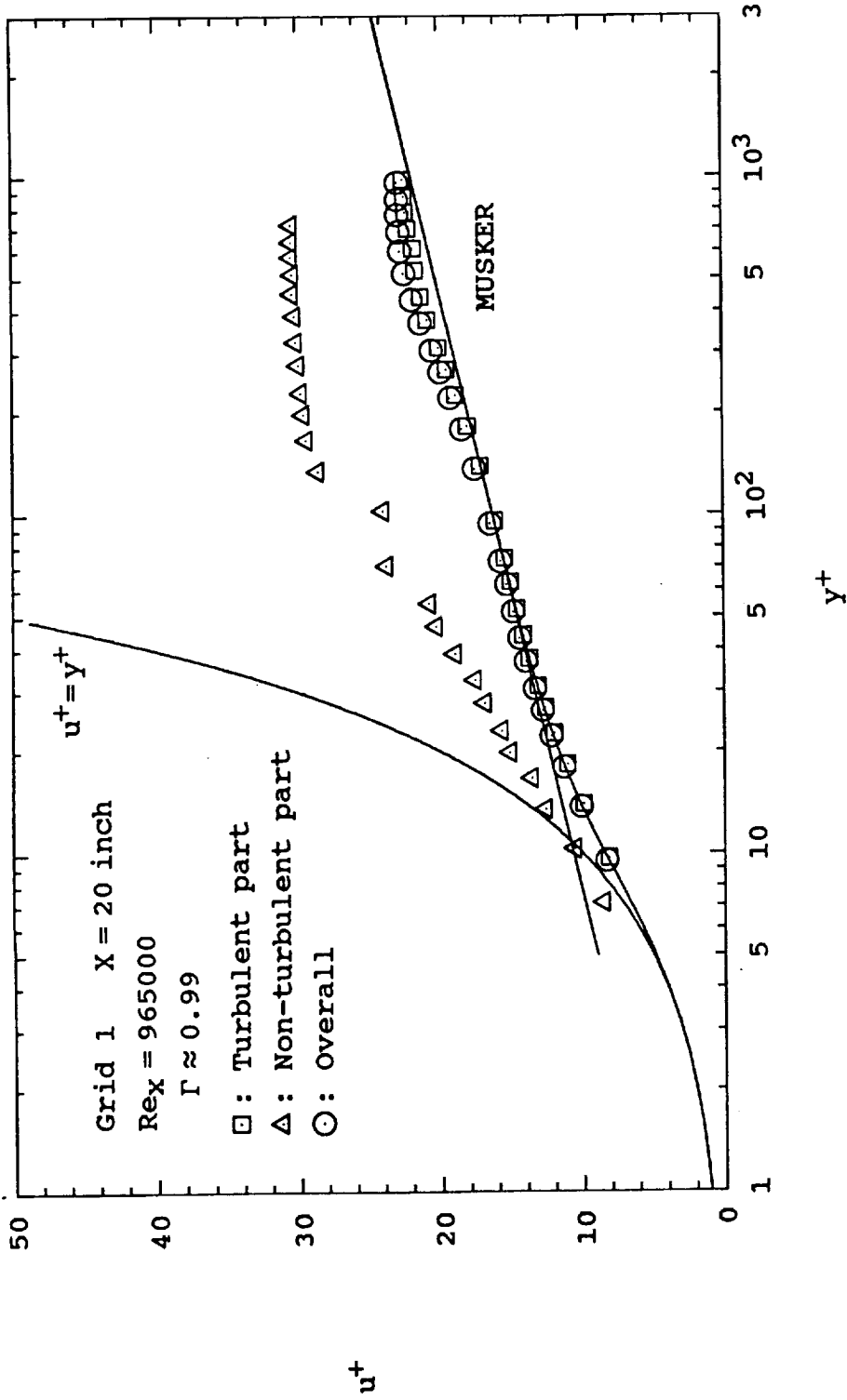


Fig. 29(f) Conditionally sampled mean velocity profiles in wall units at X=20 inches for grid 1

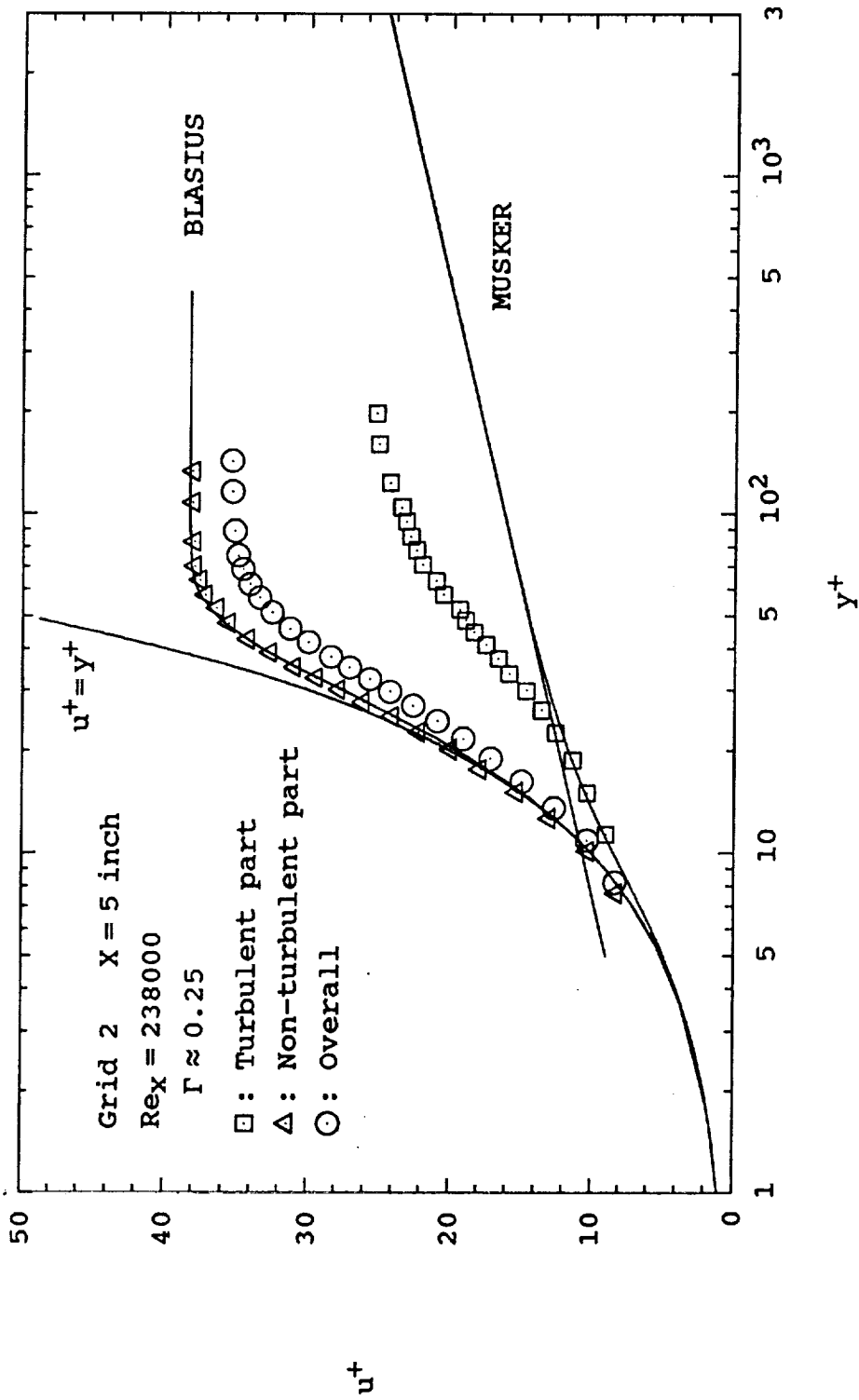


Fig. 30(a) Conditionally sampled mean velocity profiles in wall units at X=5 inches for grid 2

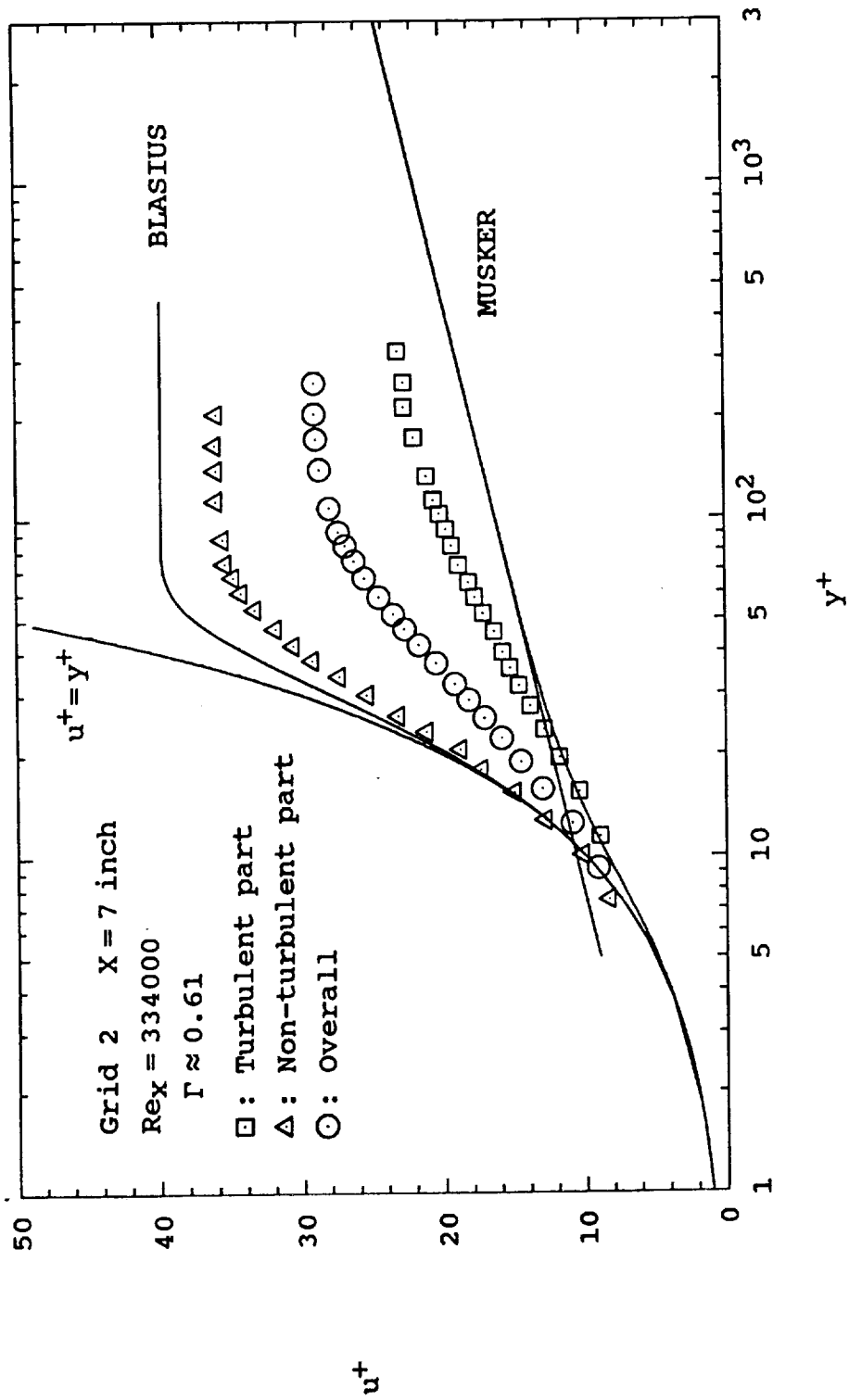


Fig. 30(b) Conditionally sampled mean velocity profiles in wall units at X=7 inches for grid 2

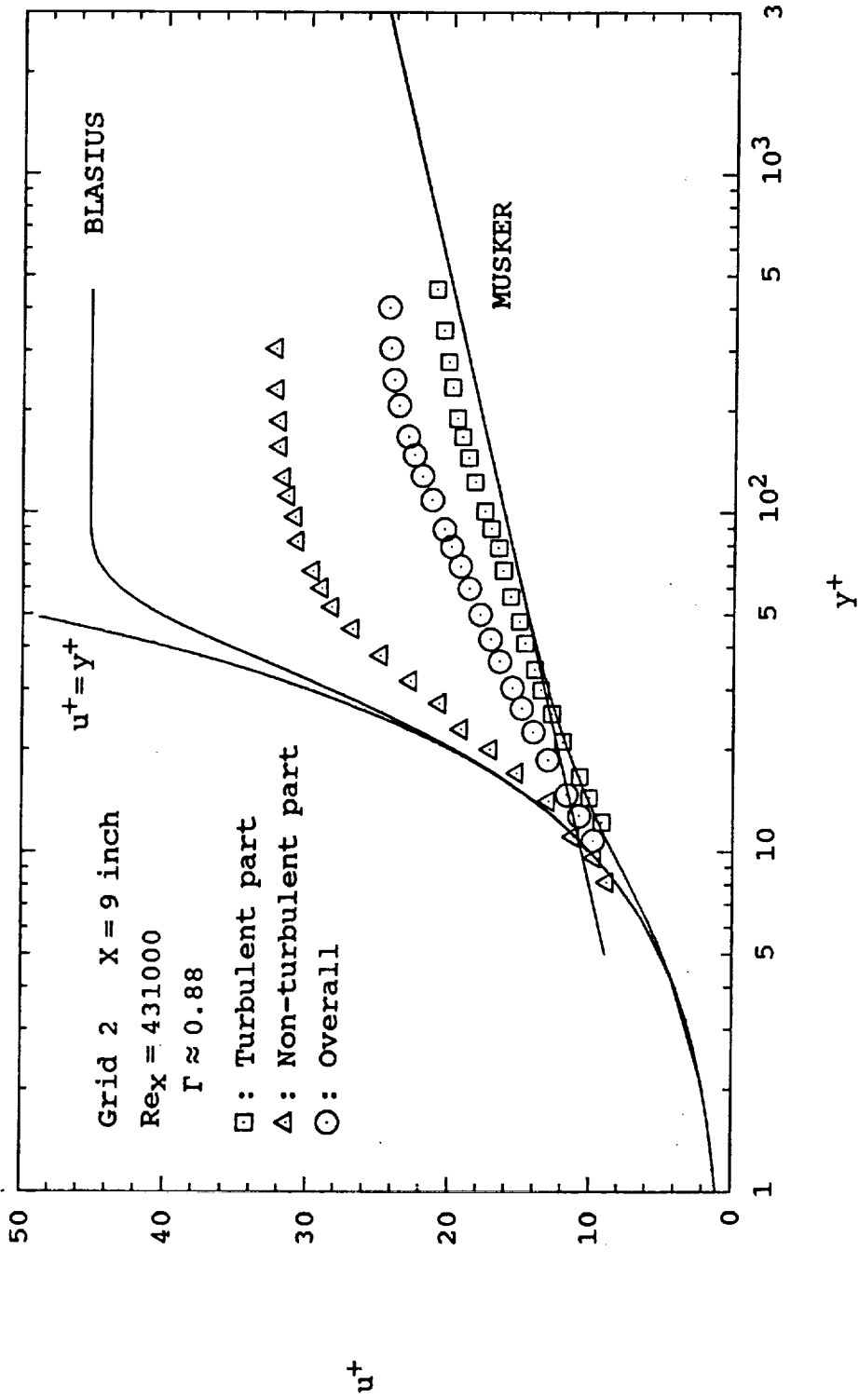


Fig. 30(c) Conditionally sampled mean velocity profiles in wall units at X=9 inches for grid 2

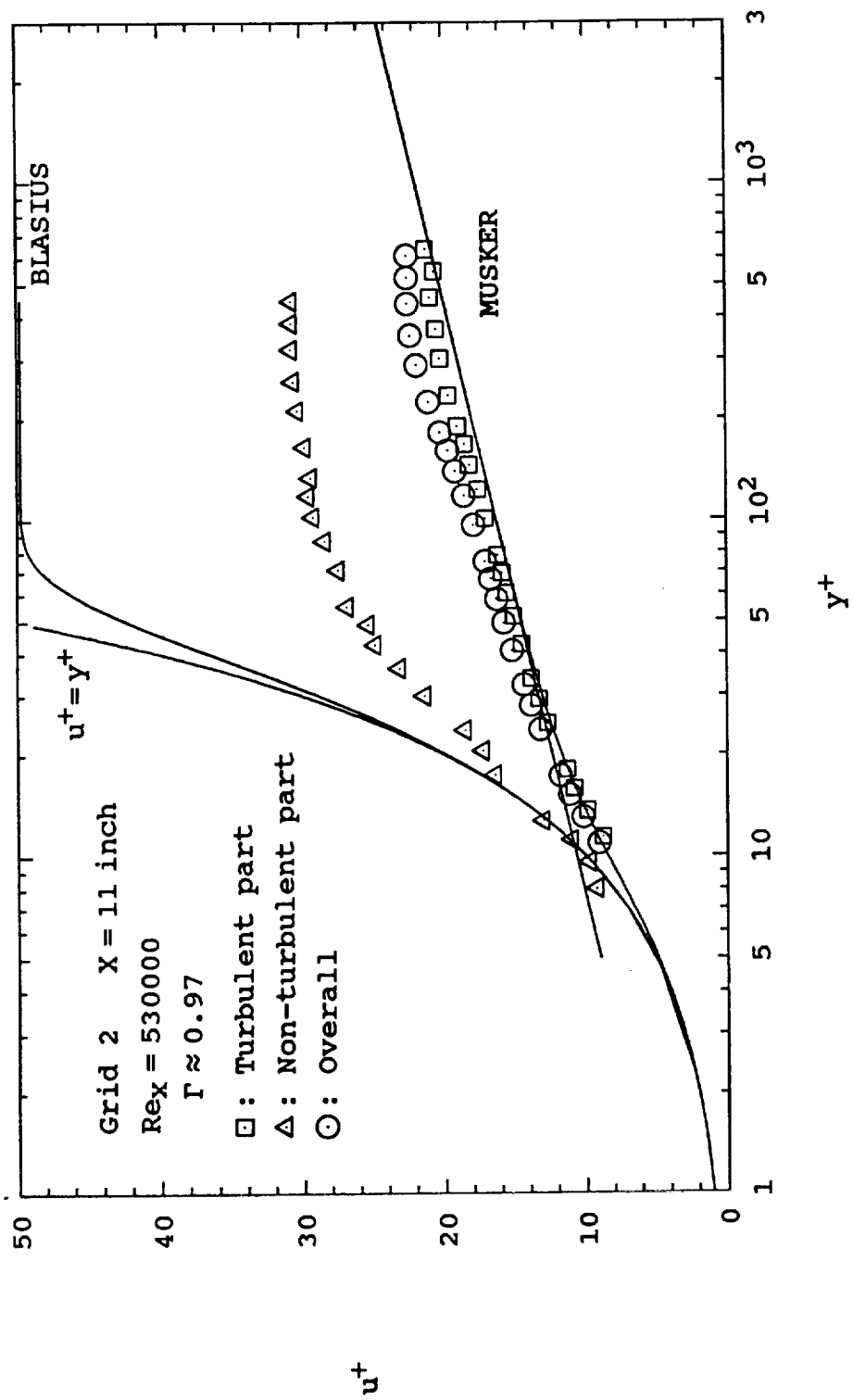


Fig. 30(d) Conditionally sampled mean velocity profiles in wall units at X=11 inches for grid 2

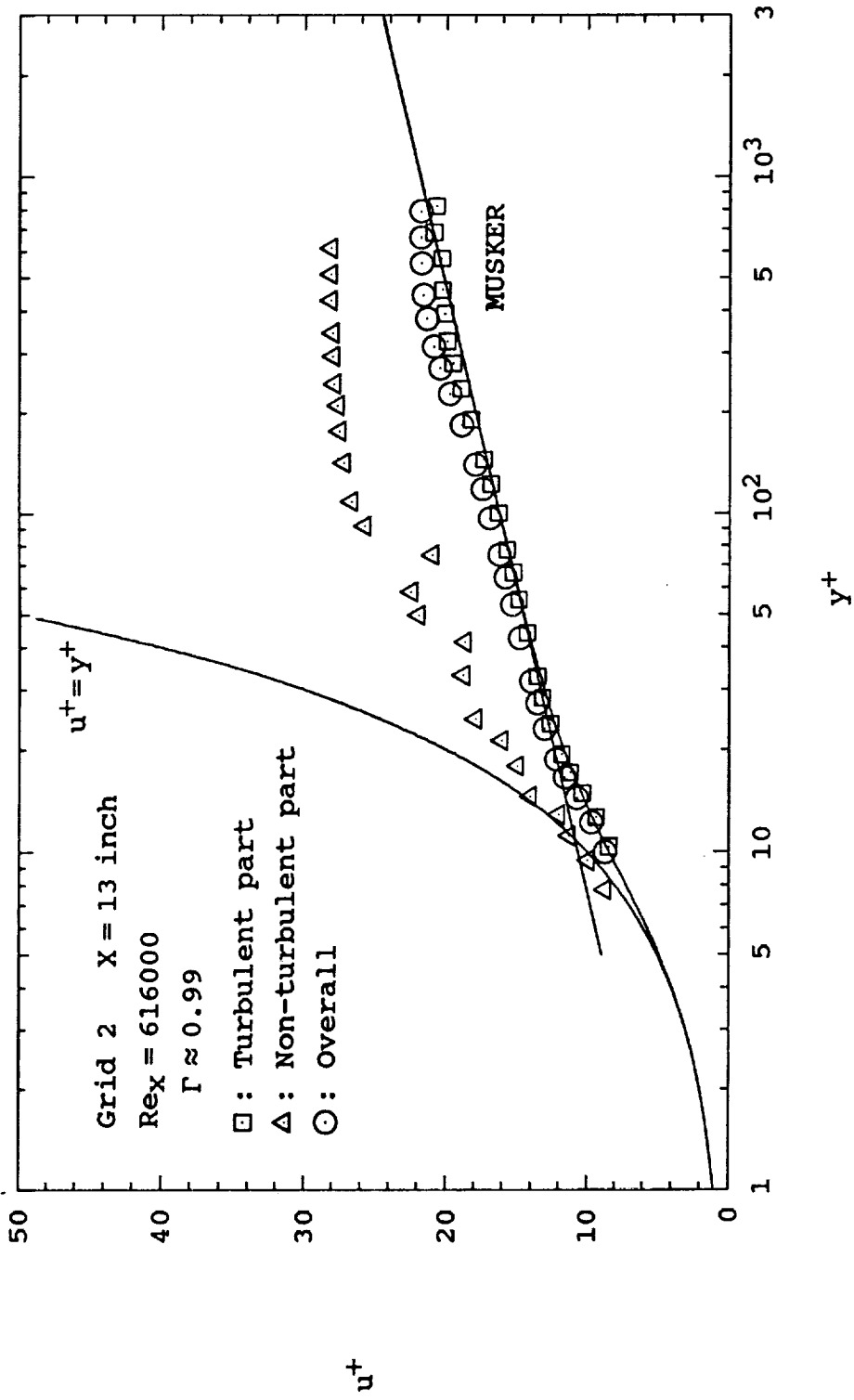


Fig. 30(e) Conditionally sampled mean velocity profiles in wall units at X=13 inches for grid 2

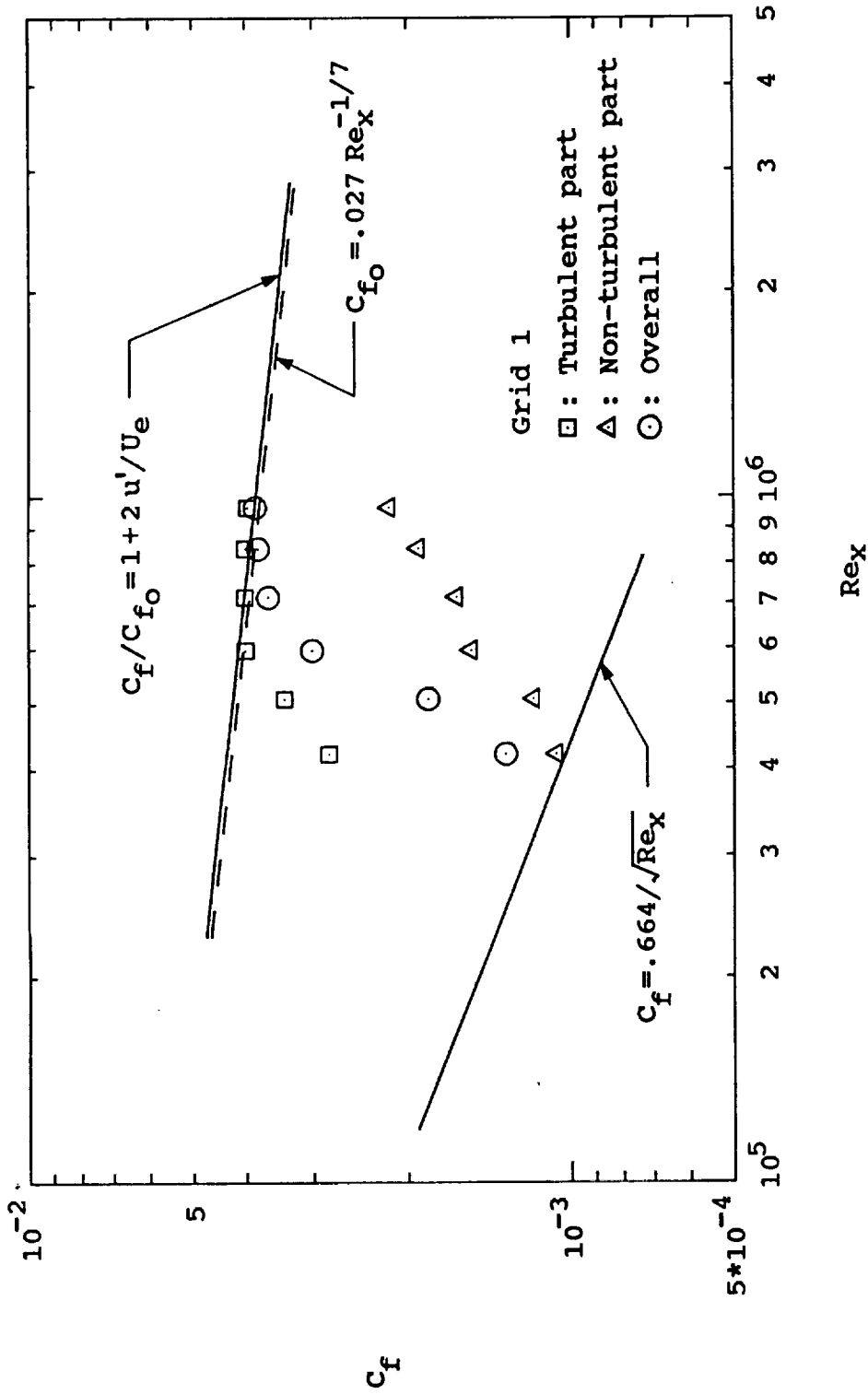


Fig. 31(a) Conditionally sampled skin friction coefficient profiles for grid 1

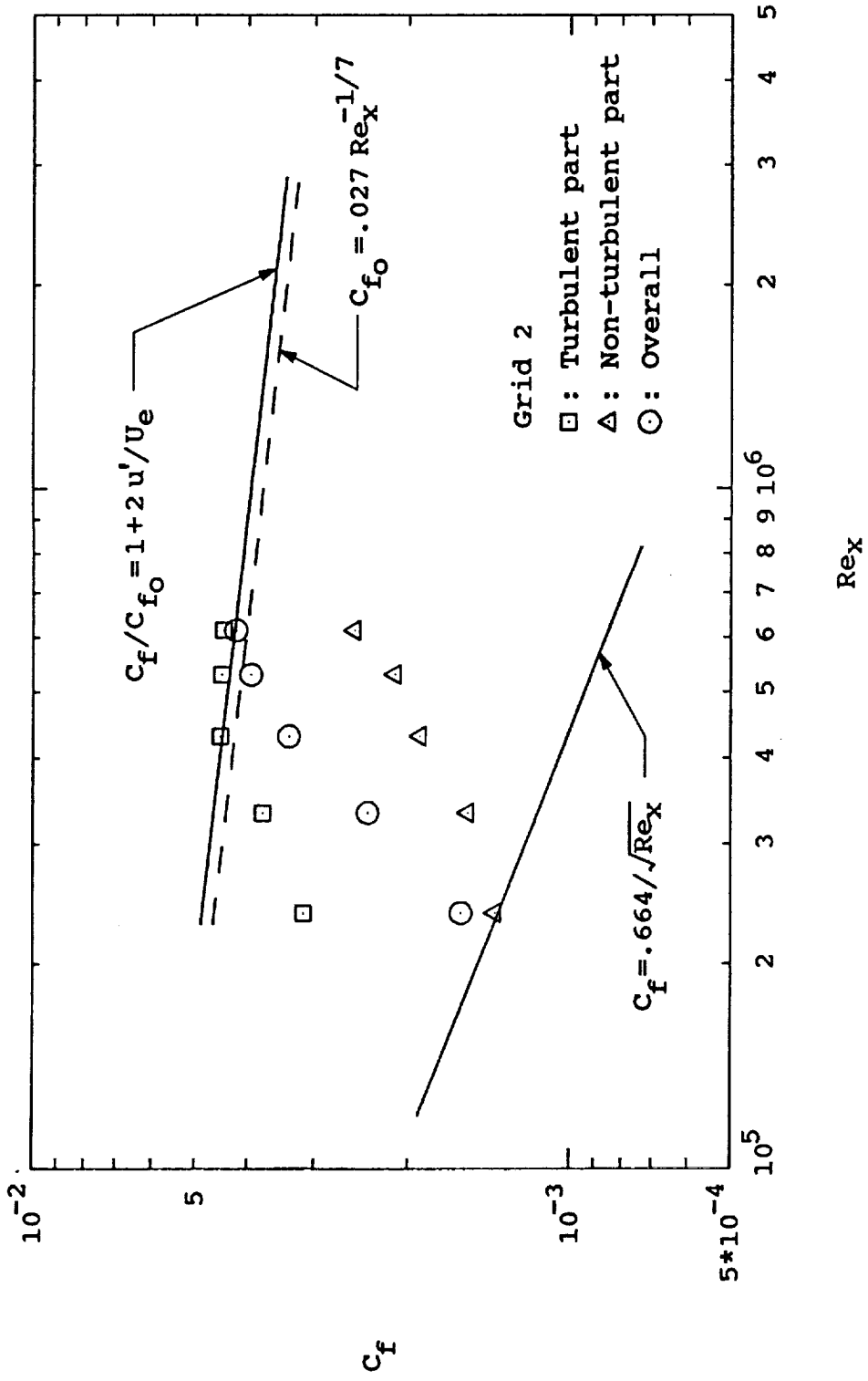


Fig. 31(b) Conditionally sampled skin friction coefficient profiles for grid 2

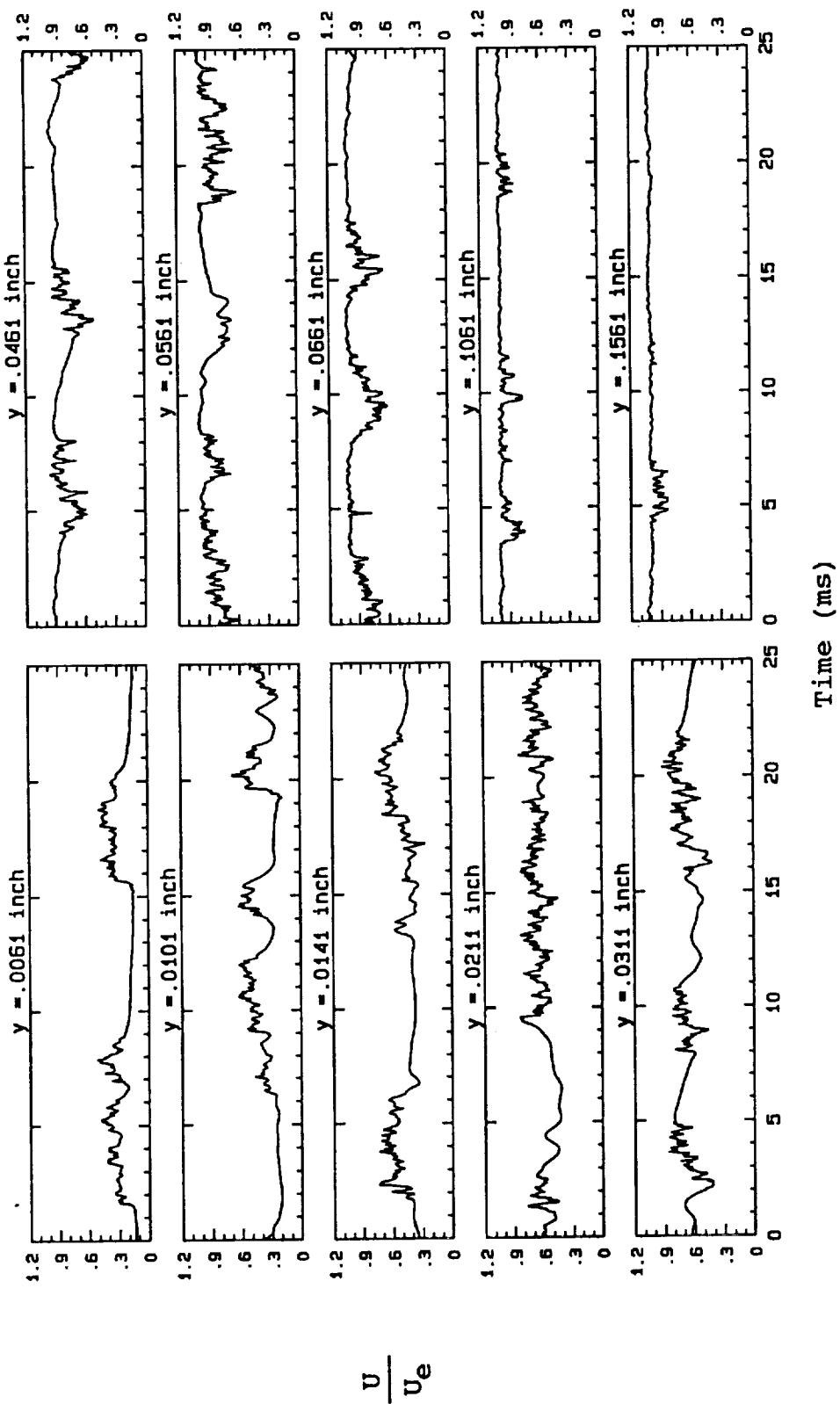


Fig. 32(a) Hot-wire velocity traces throughout the boundary layer at X=11 inches for grid 1

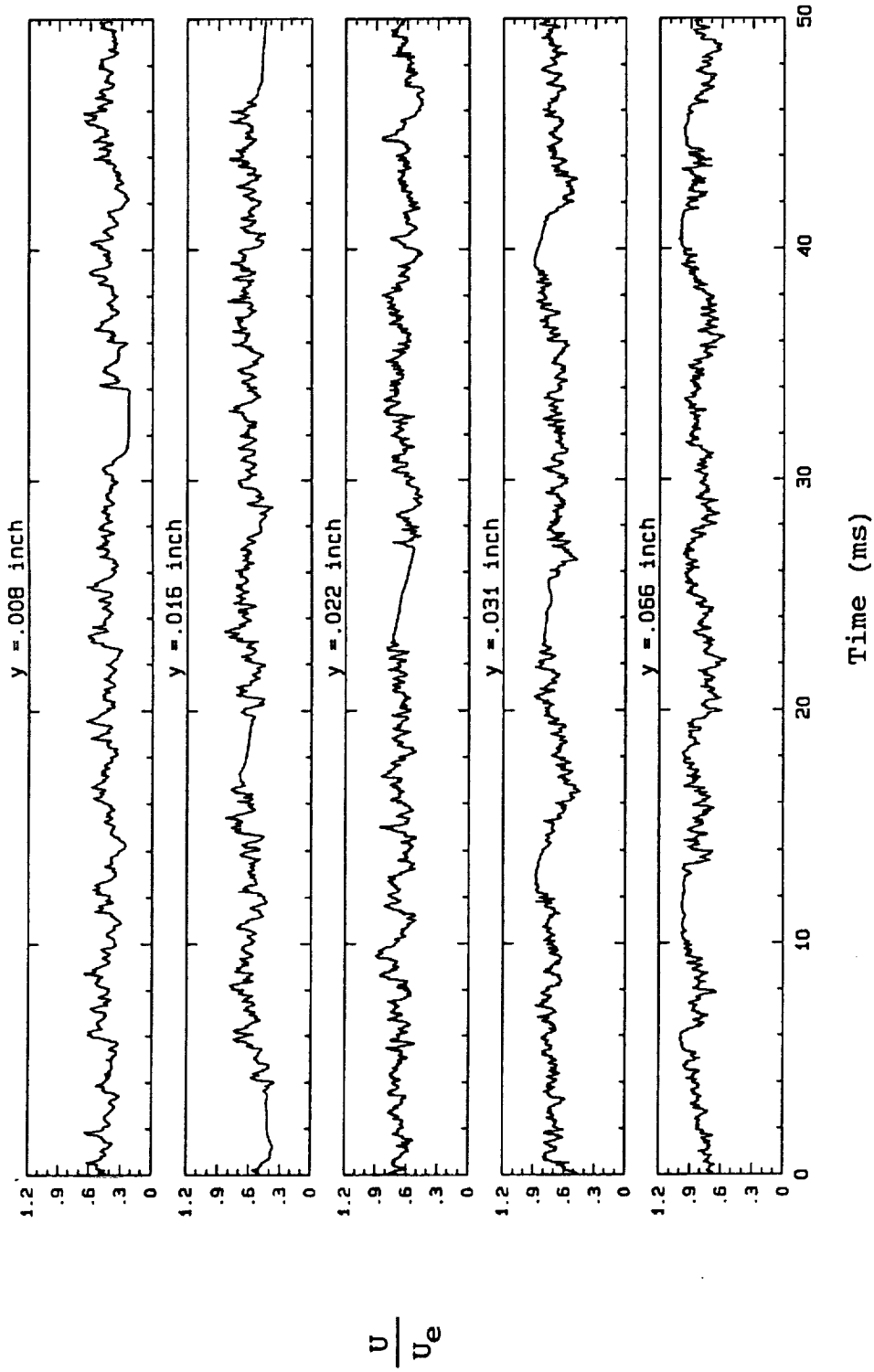


Fig. 32(b) Hot-wire velocity traces throughout the boundary layer at X=15 inches for grid 1

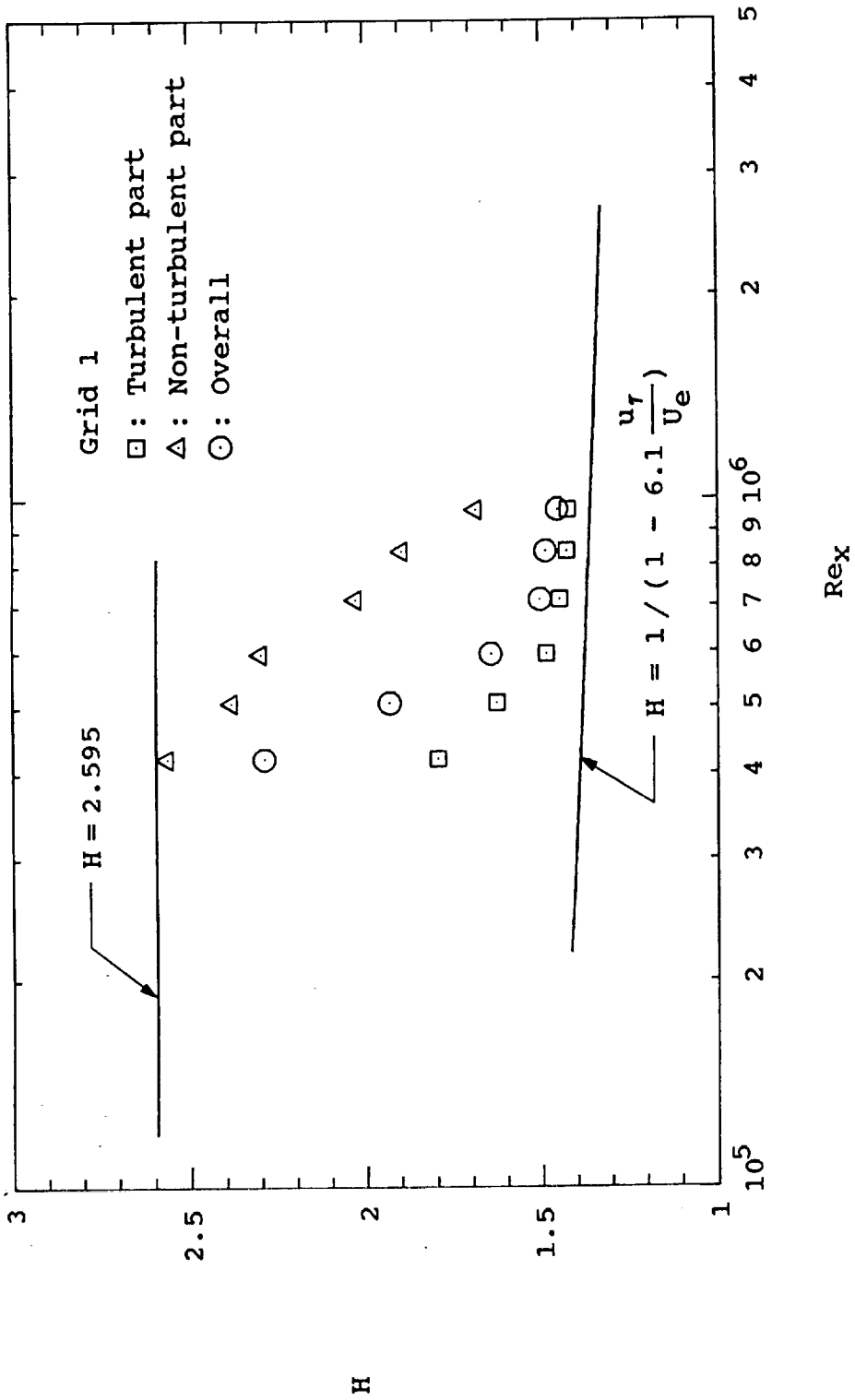


Fig. 33(a) Conditionally sampled shape factor profiles for grid 1

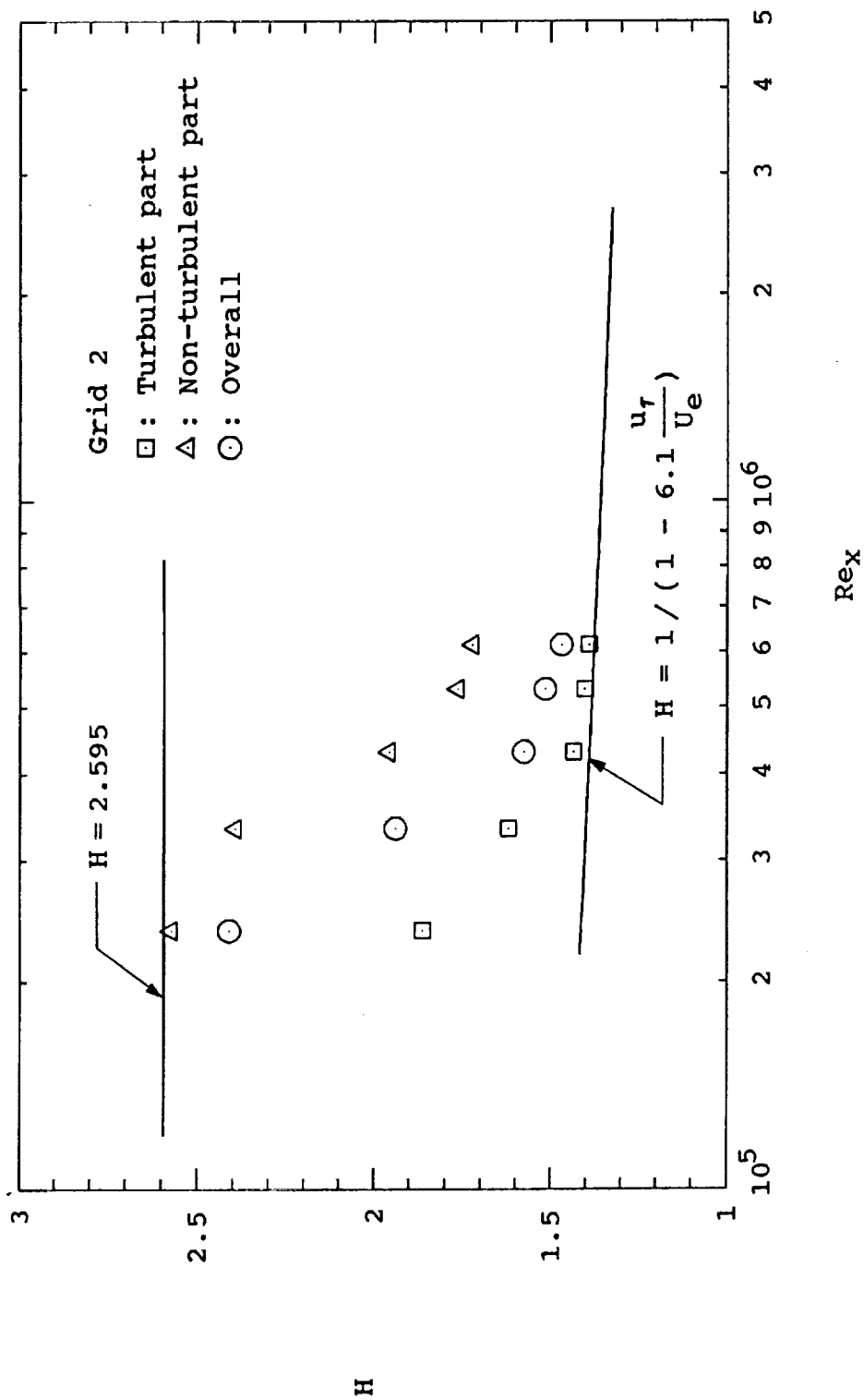


Fig. 33(b) Conditionally sampled shape factor profiles for grid 2

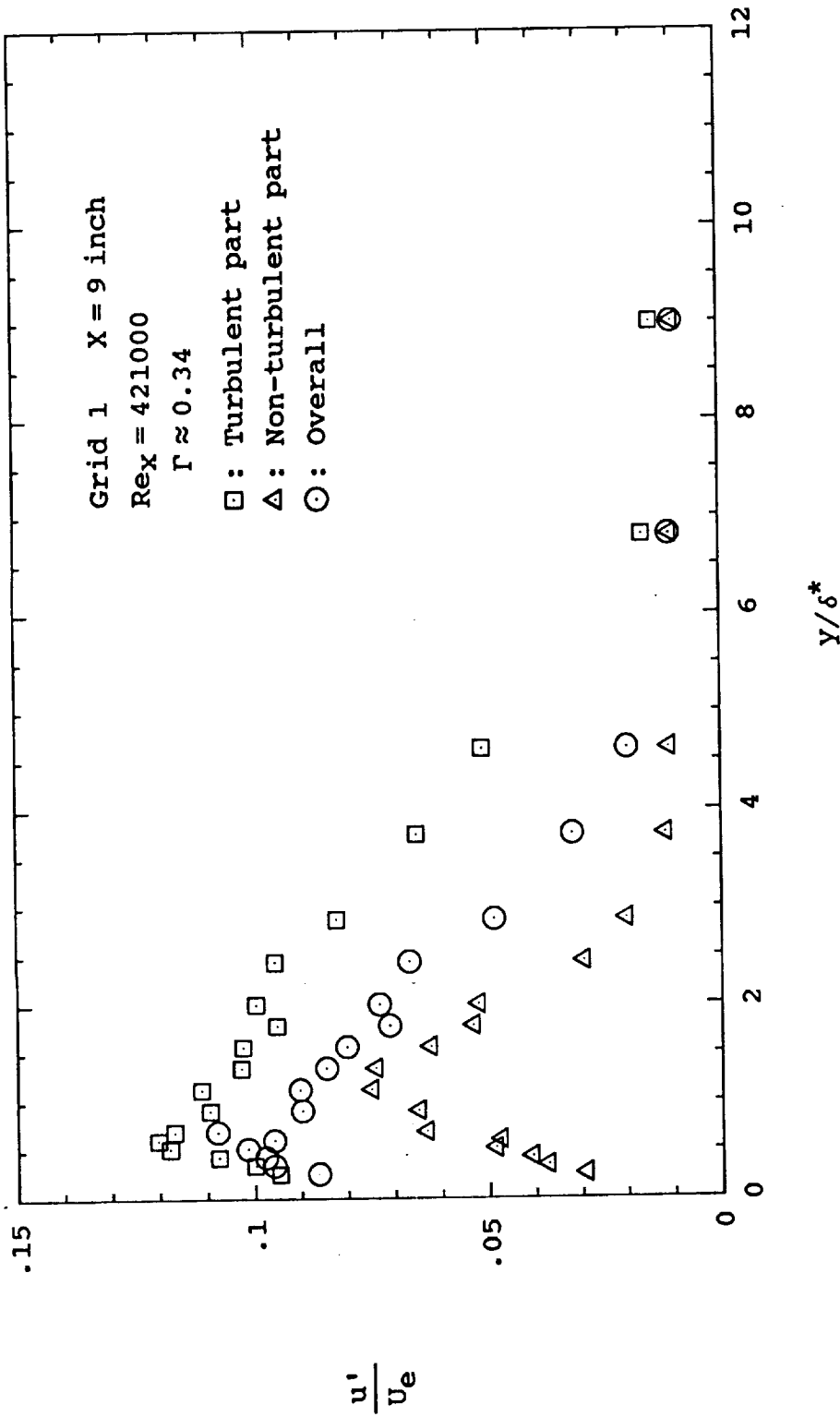


Fig. 34(a) Conditionally sampled rms velocity profiles at X=9 inches for grid 1

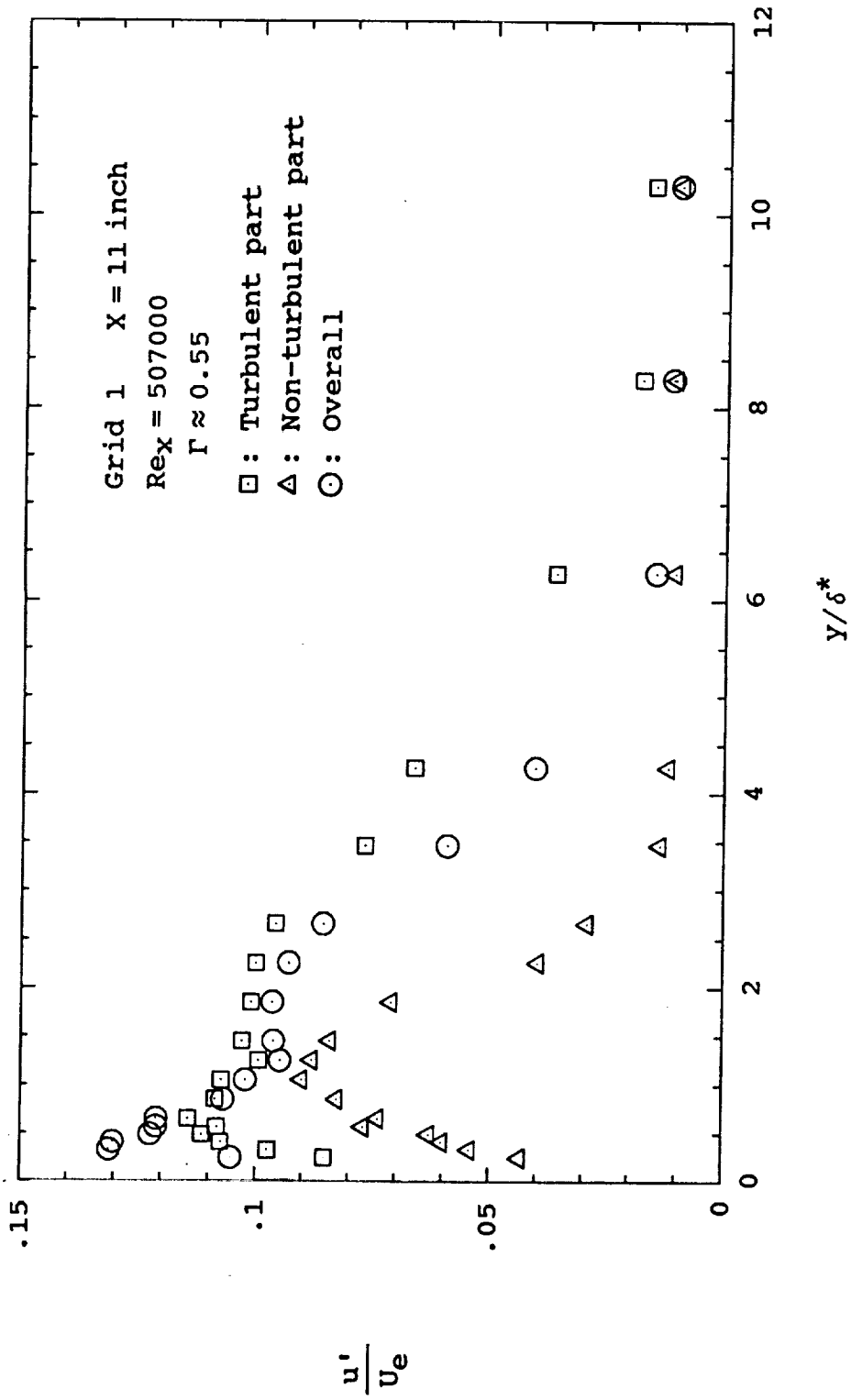


Fig. 34(b) Conditionally sampled rms velocity profiles at X=11 inches for grid 1

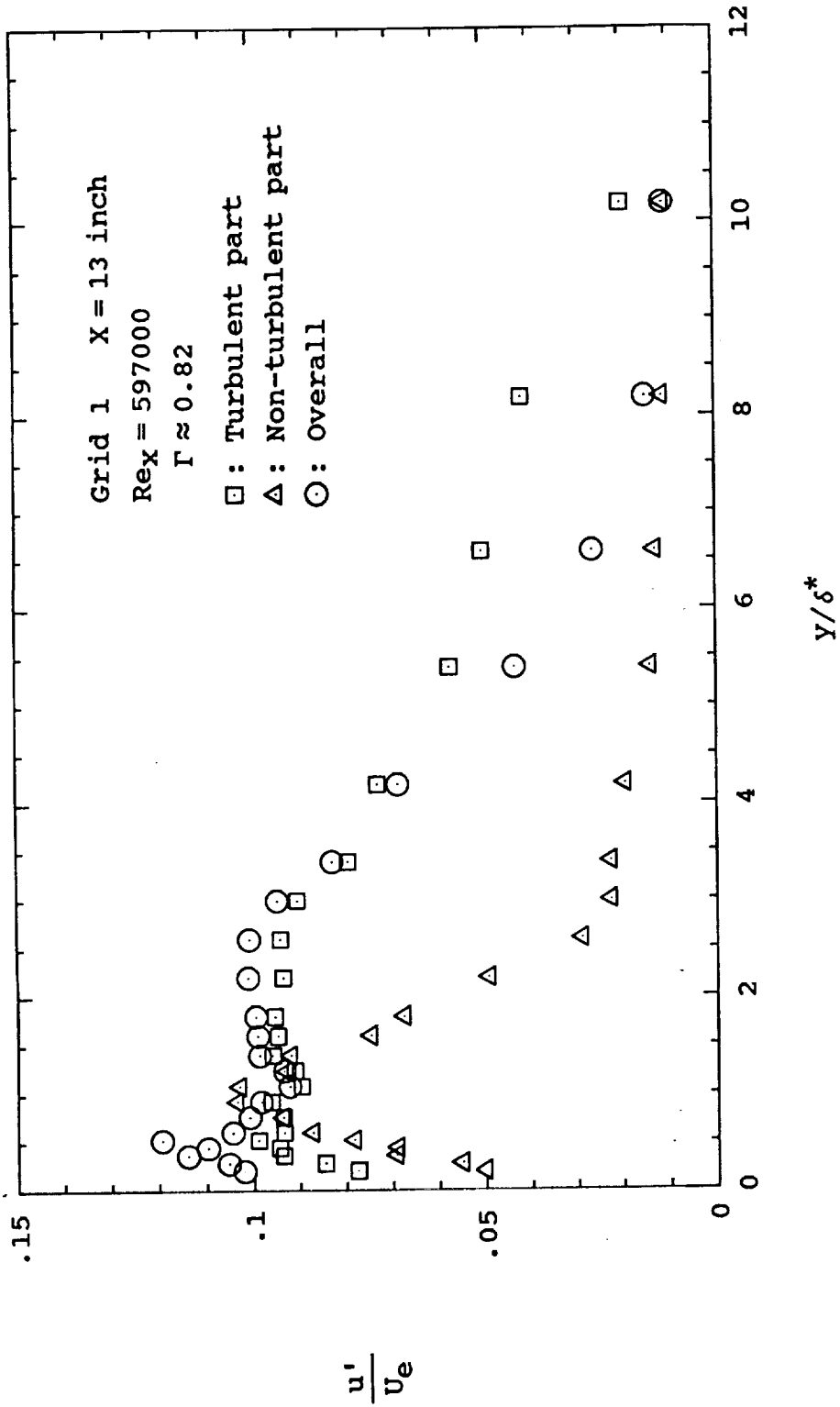


Fig. 34(c) Conditionally sampled rms velocity profiles at X=13 inches for grid 1

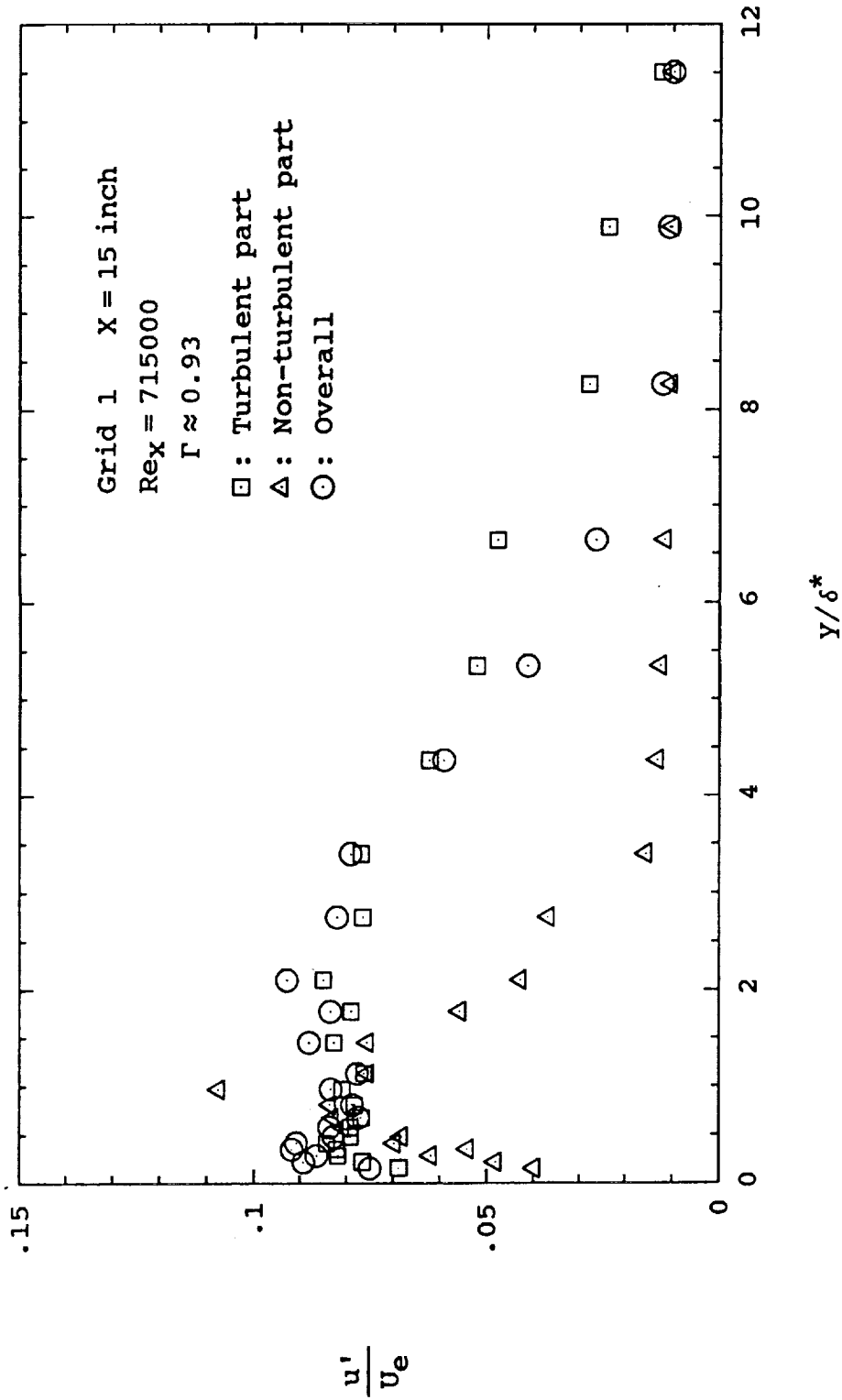


Fig. 34(d) Conditionally sampled rms velocity profiles at X=15 inches for grid 1

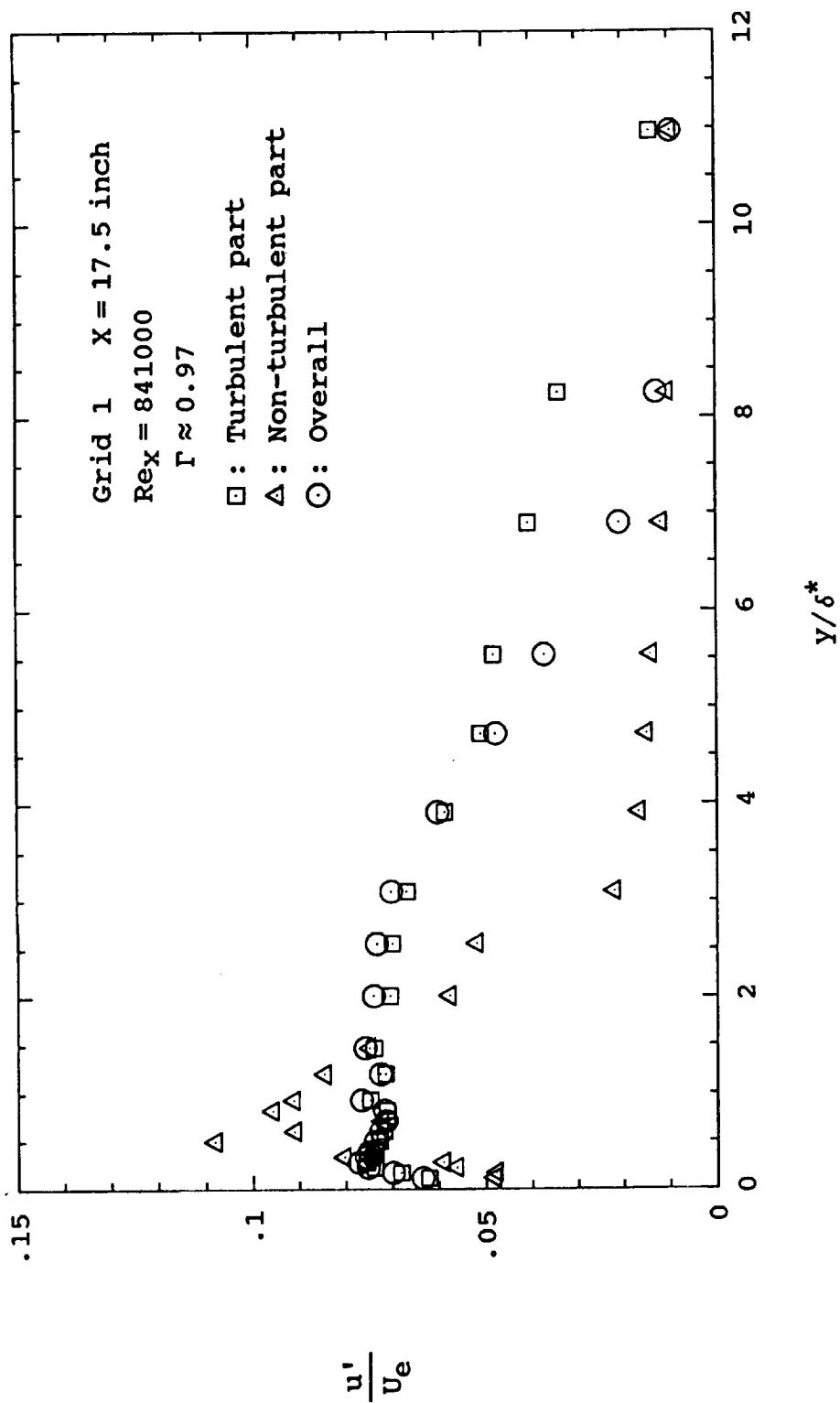


Fig. 34(e) Conditionally sampled rms velocity profiles at X=17.5 inches for grid 1

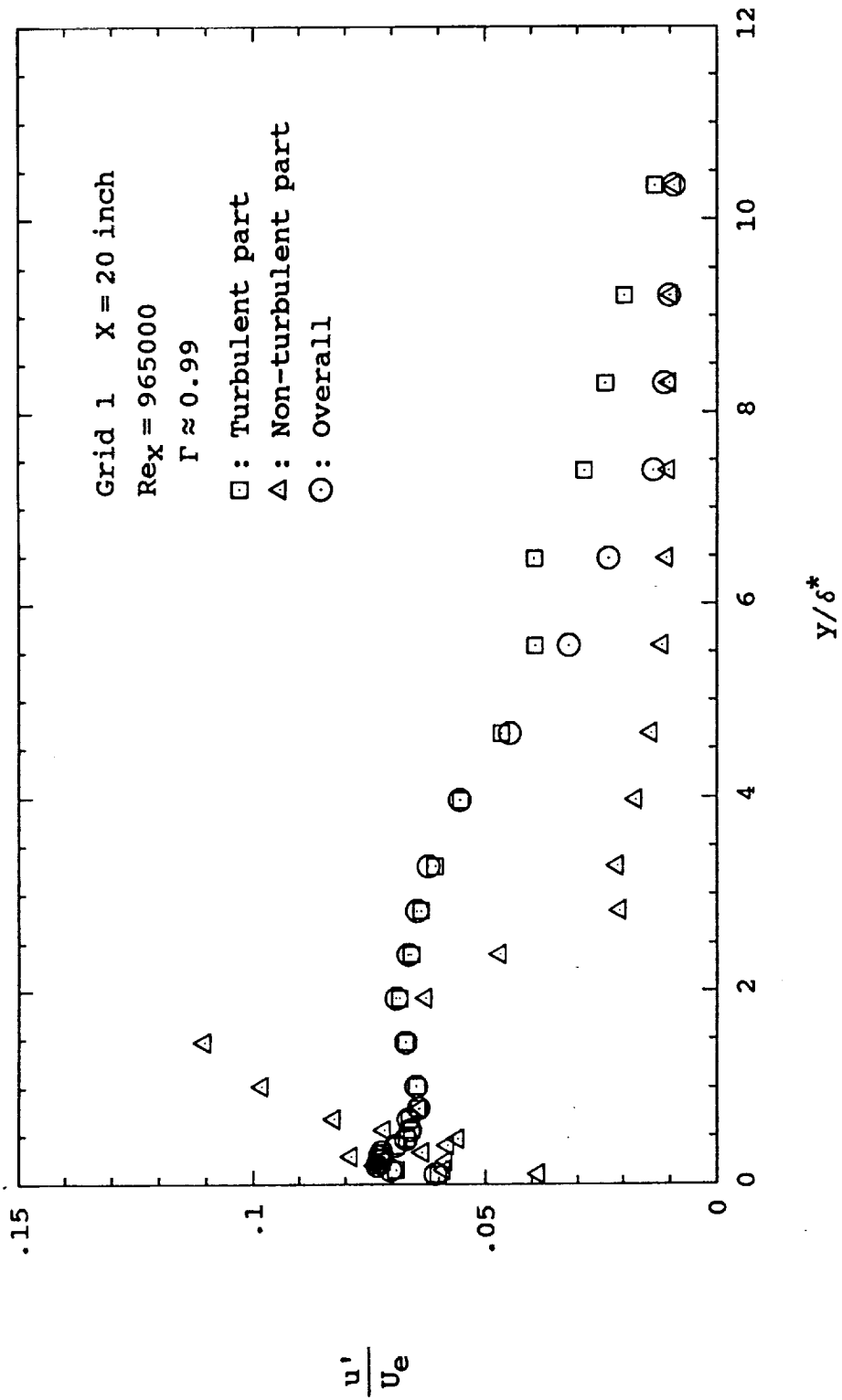


Fig. 34(f) Conditionally sampled rms velocity profiles at X=20 inches for grid 1

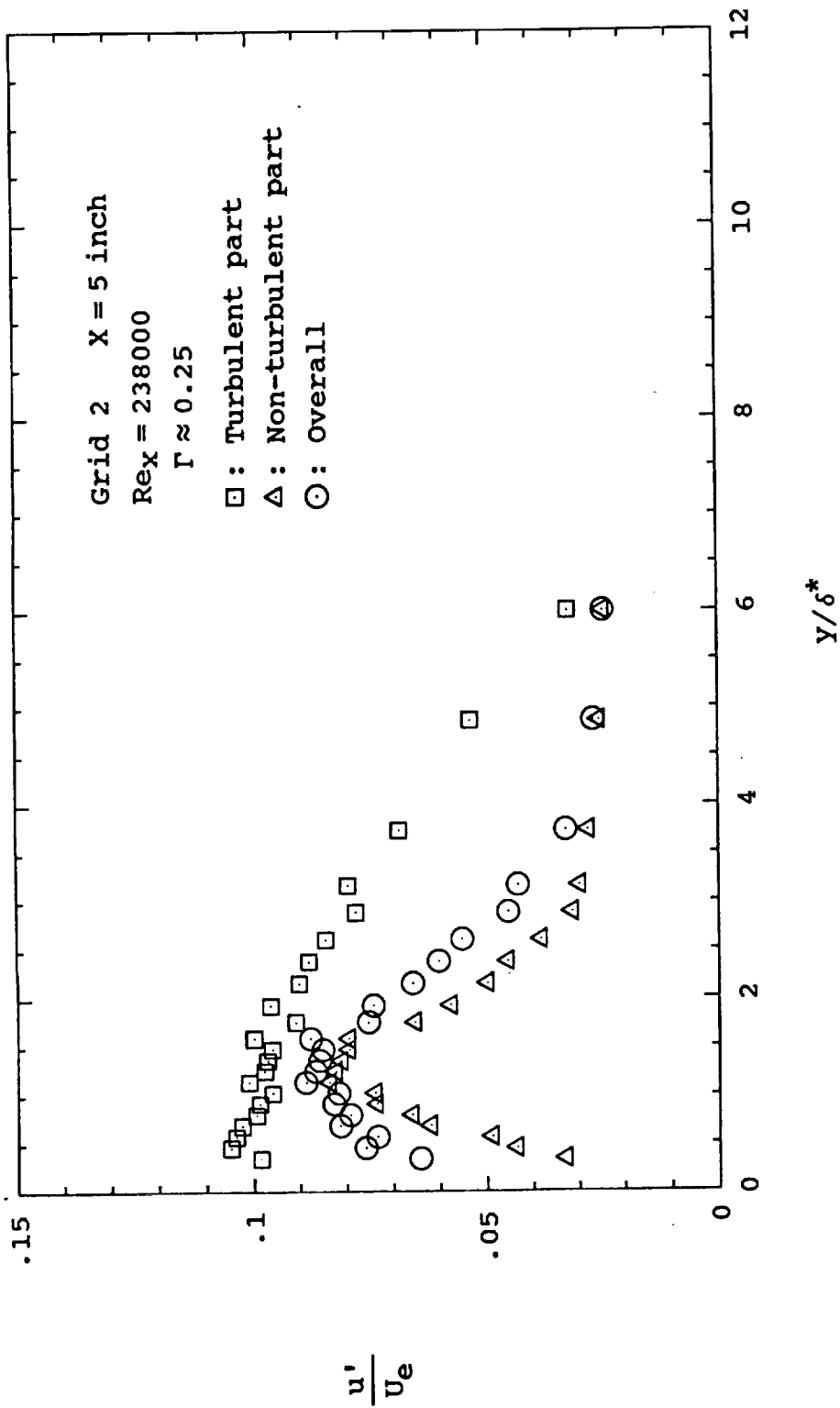


Fig. 35(a) Conditionally sampled rms velocity profiles at X=5 inches for grid 2

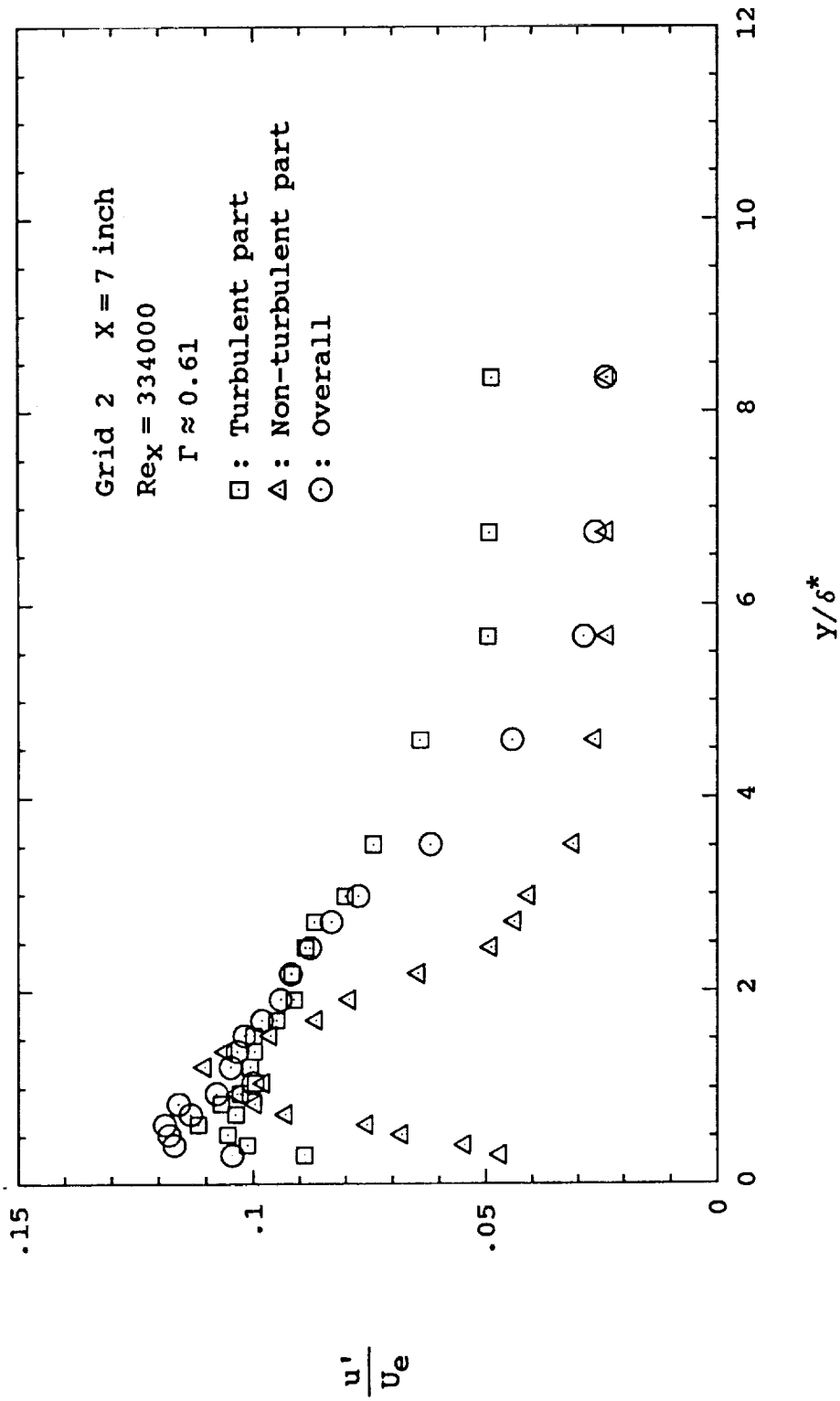


Fig. 35(b) Conditionally sampled rms velocity profiles at X=7 inches for grid 2

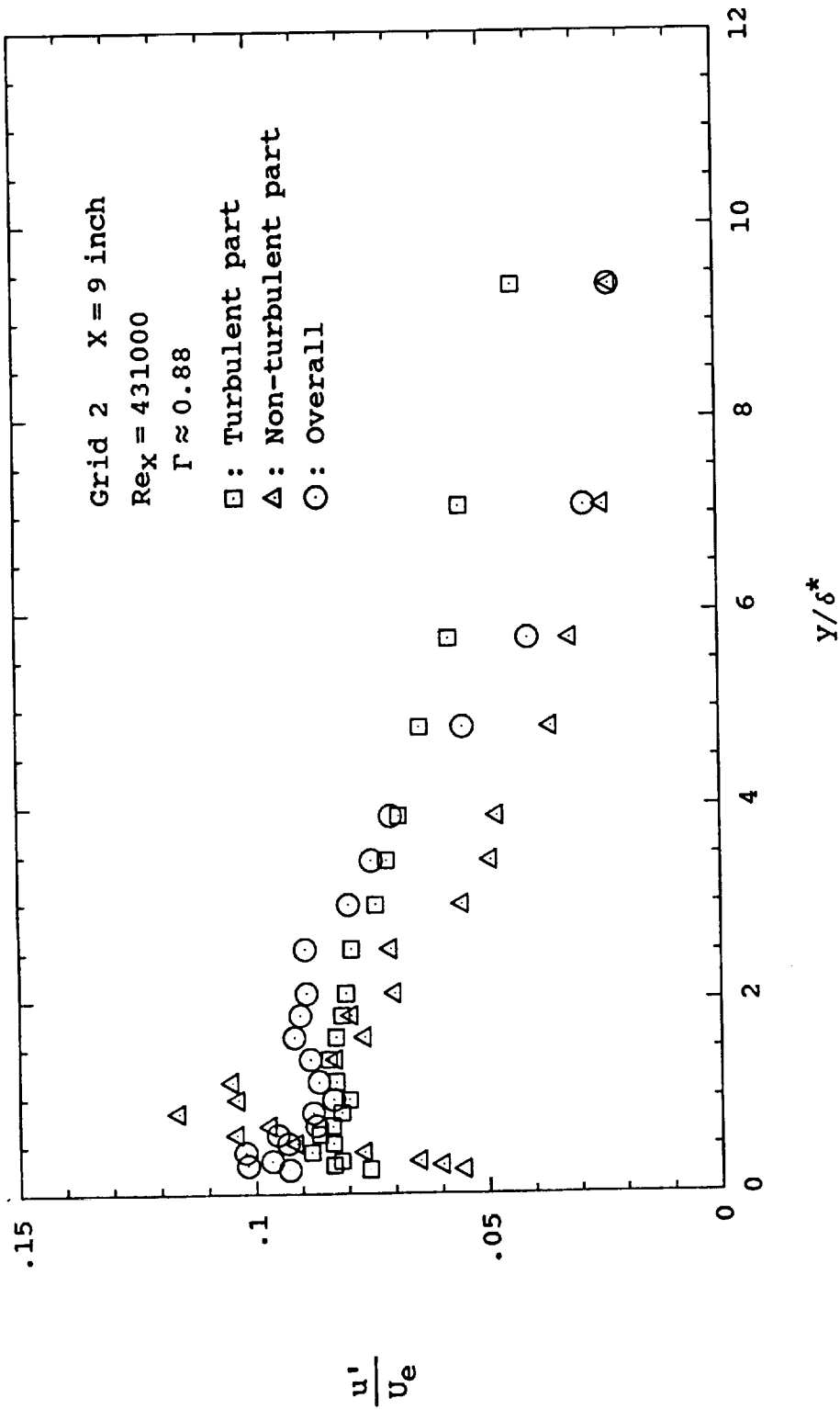


Fig. 35(c) Conditionally sampled rms velocity profiles at X=9 inches for grid 2

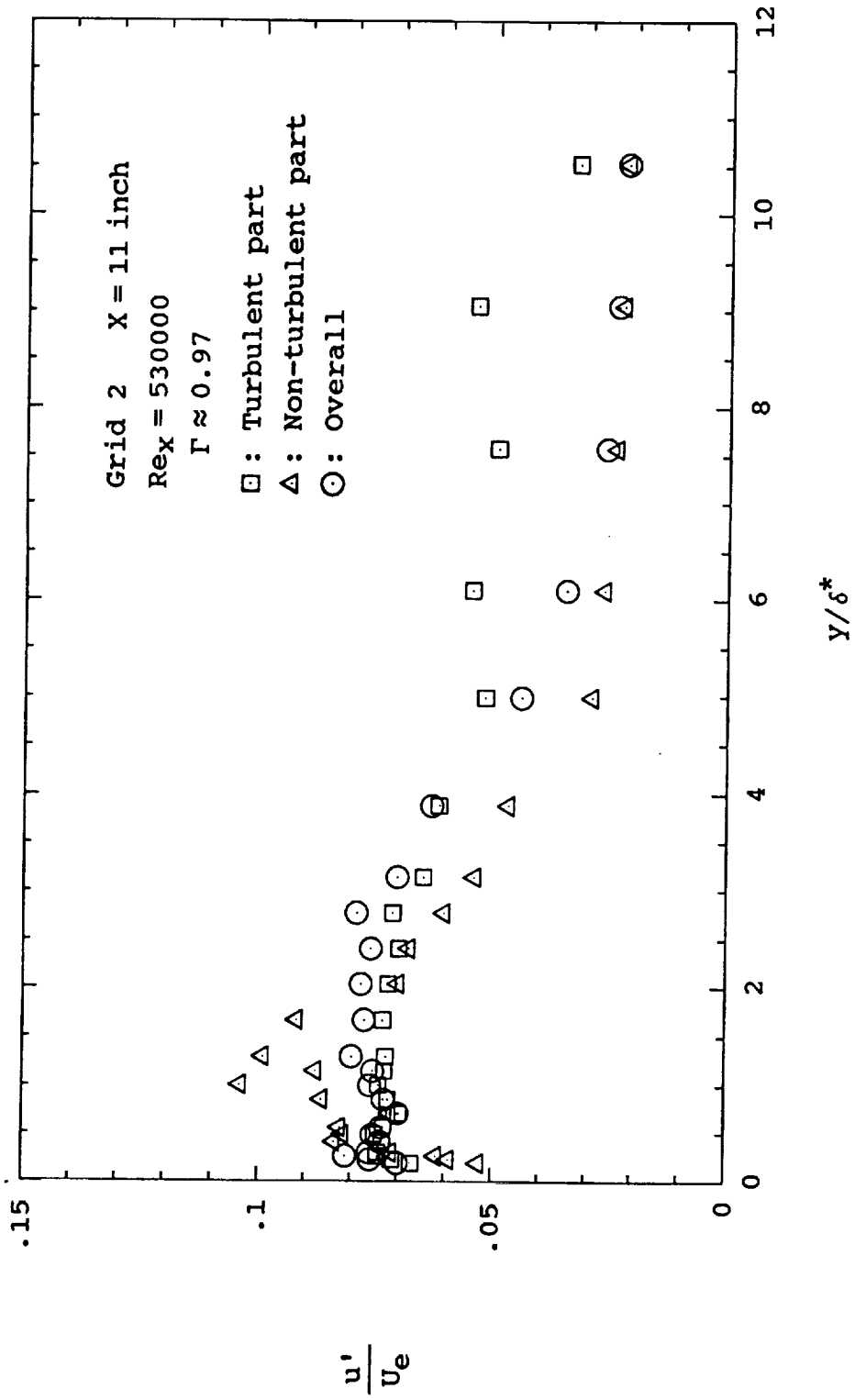


Fig. 35(d) Conditionally sampled rms velocity profiles at X=11 inches for grid 2

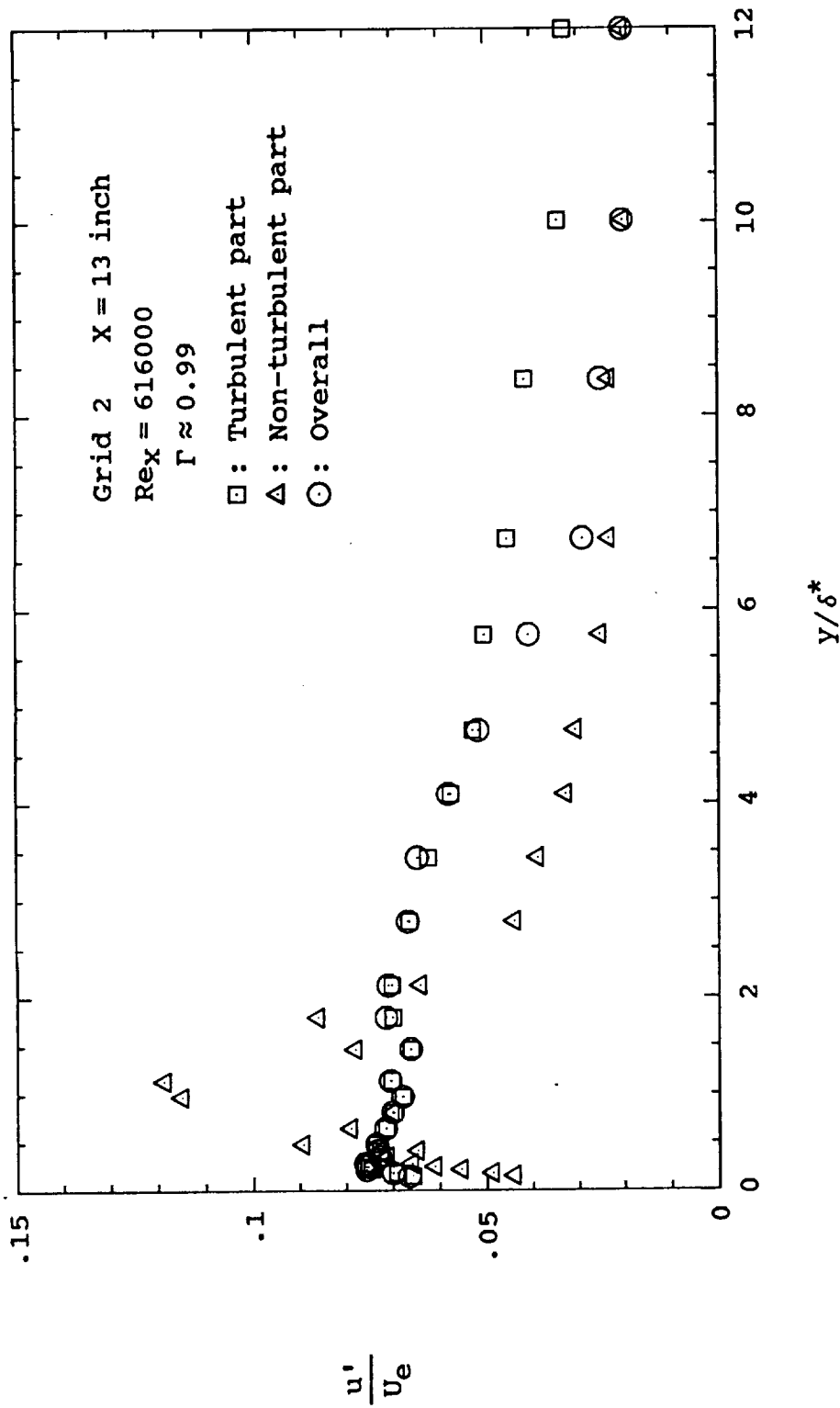


Fig. 35(e) Conditionally sampled rms velocity profiles at X=13 inches for grid 2

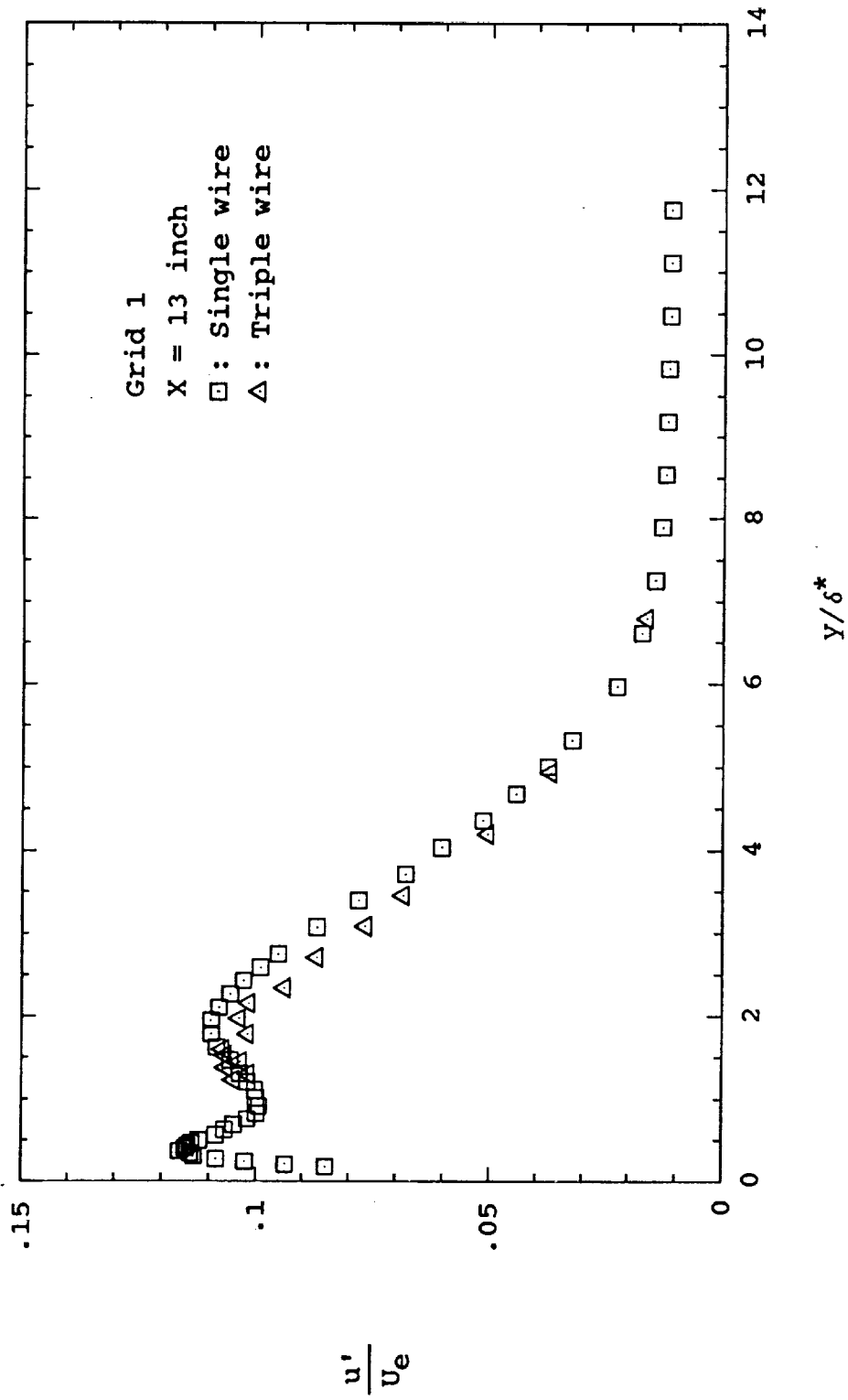


Fig. 36 Comparison of streamwise rms velocity profiles in the boundary layer measured with single and 3-wire probes at X=13 inches for grid 1

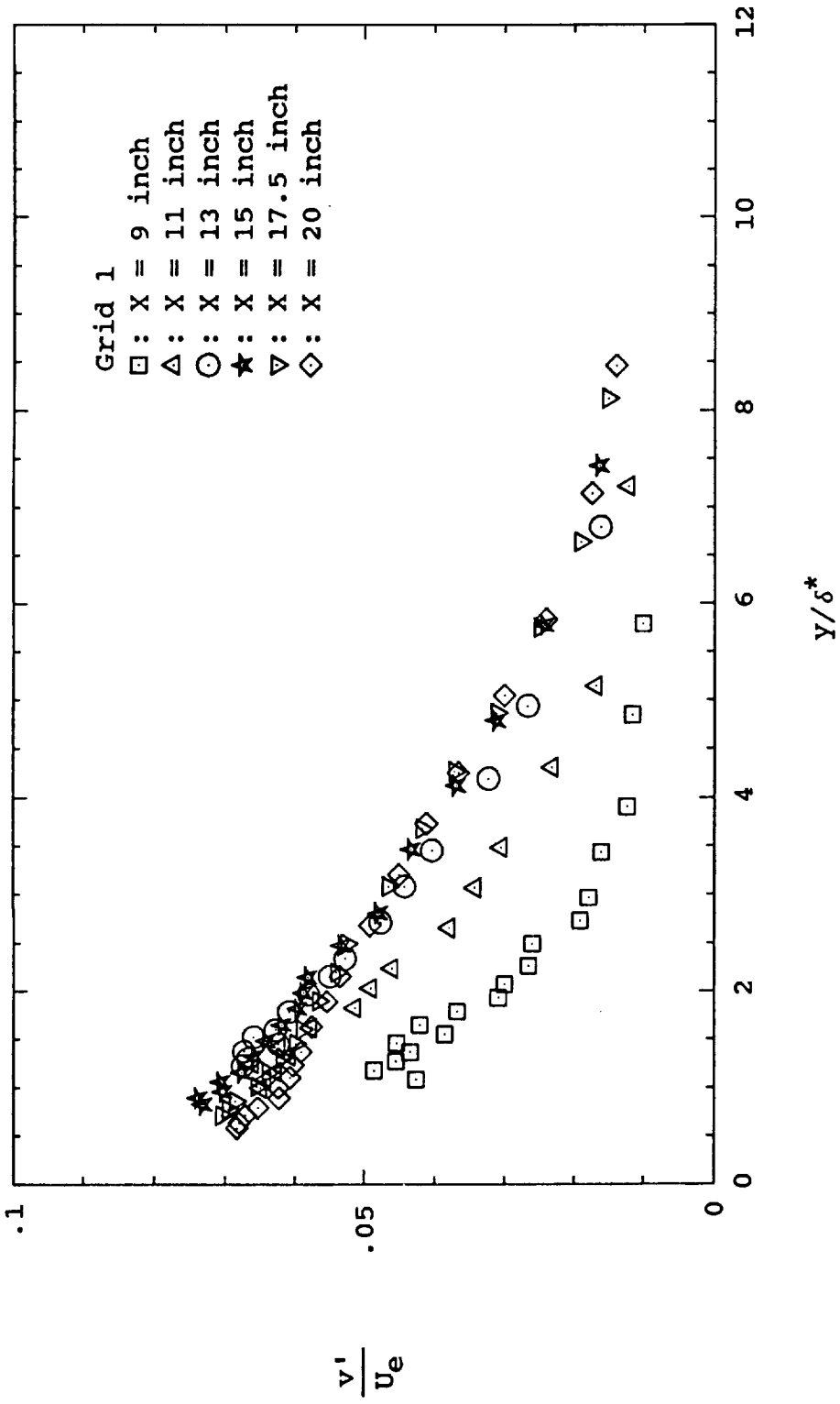


Fig. 37 Vertical component of rms velocity profiles for grid 1

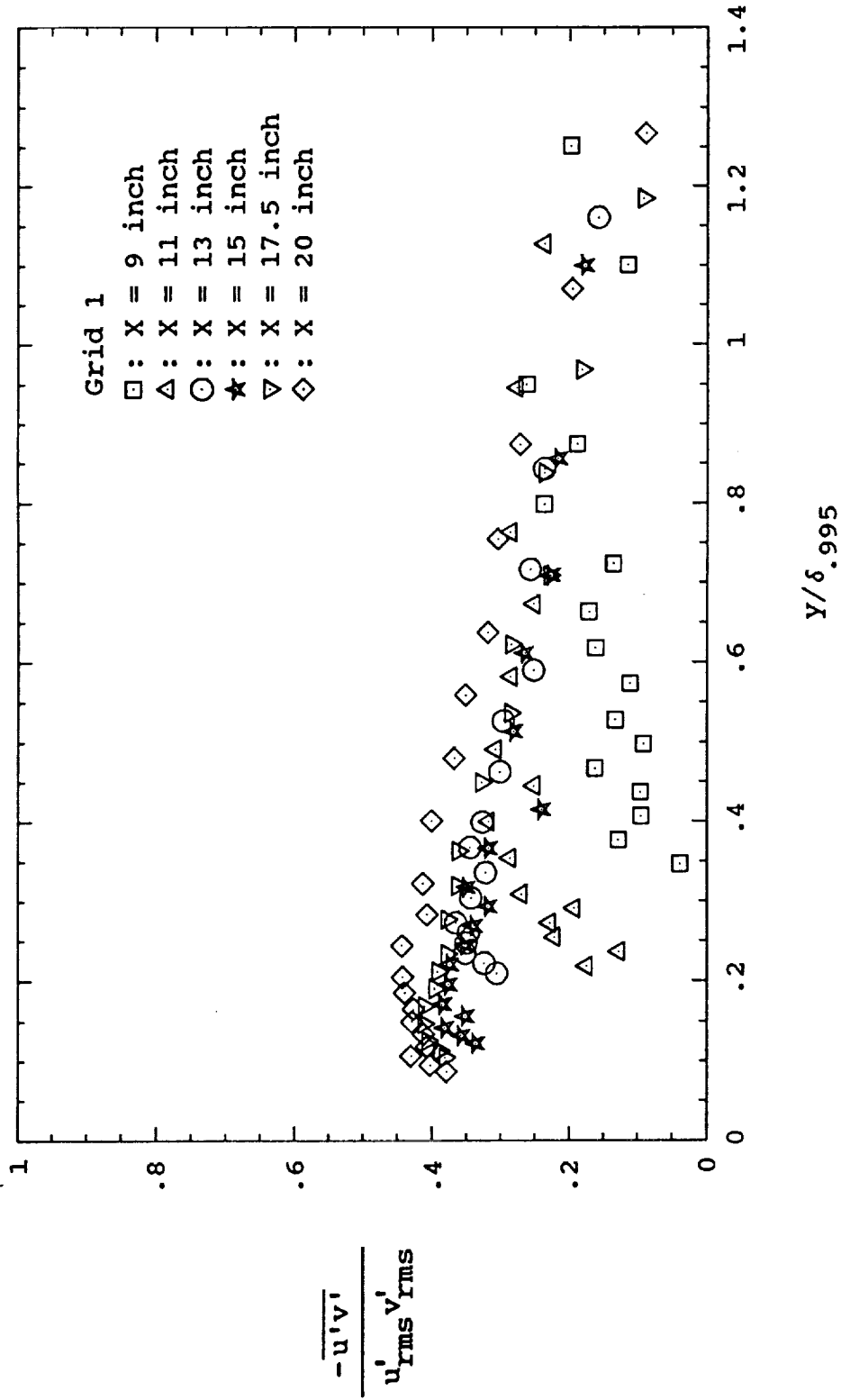


Fig. 38(a) Correlation coefficient profiles of u' and v' for grid 1

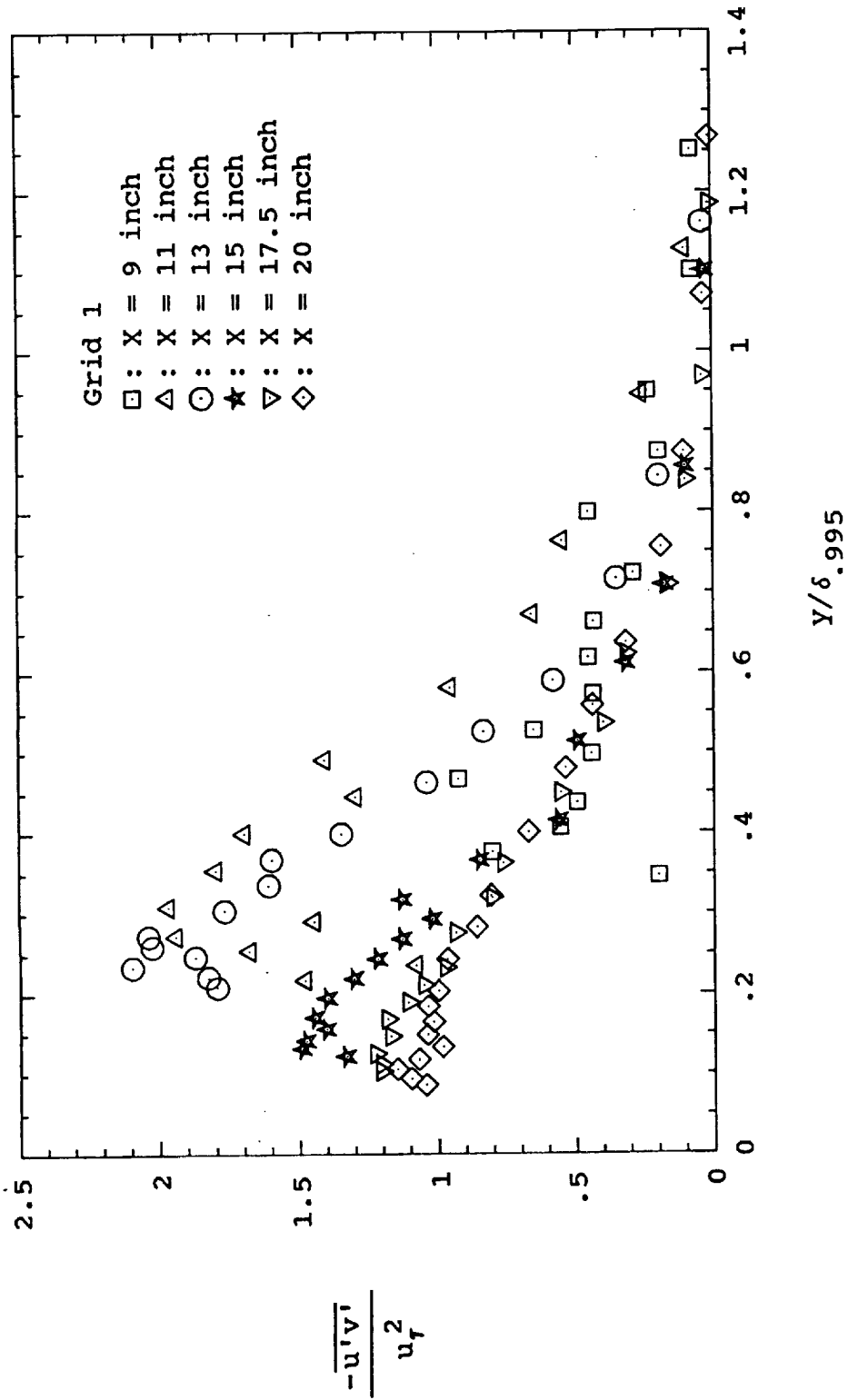


Fig. 38(b) Reynolds shear stress profiles for grid 1

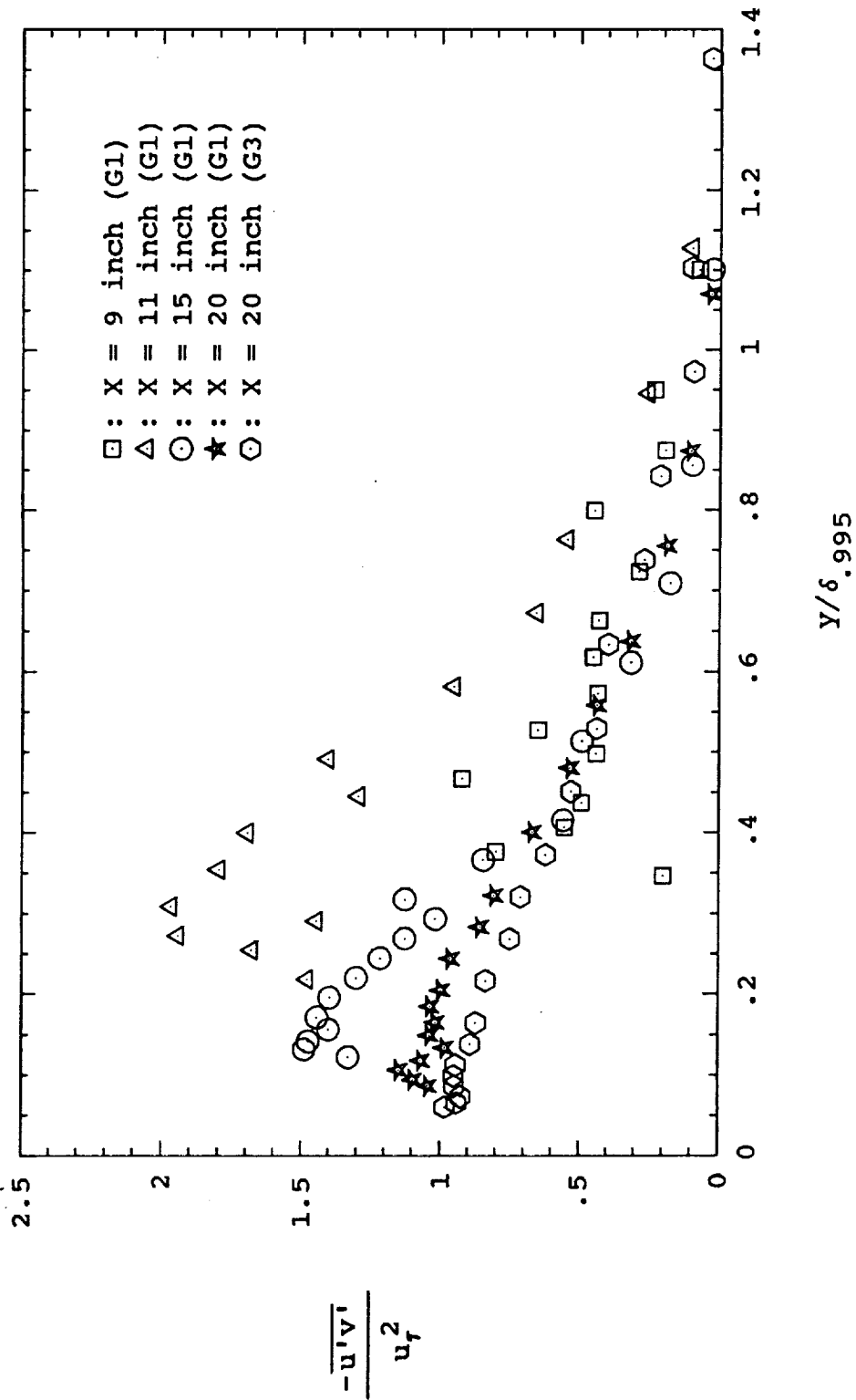


Fig. 39 Reynolds shear stress profile of fully turbulent boundary layer for grid 3 along with profiles of transitional boundary layer for grid 1

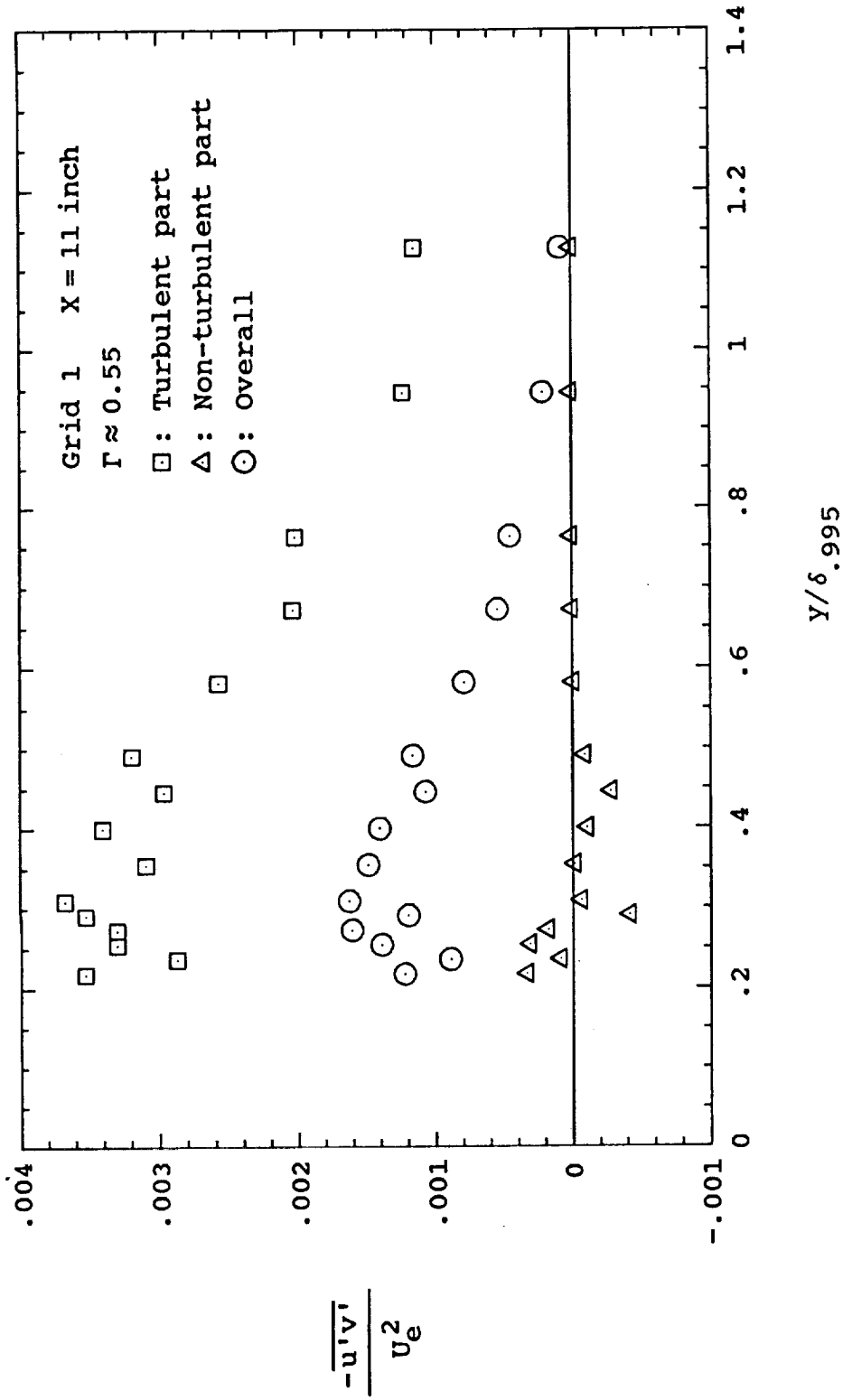


Fig. 40(a) Conditionally sampled Reynolds shear stress profiles for grid 1 at X=11 inches

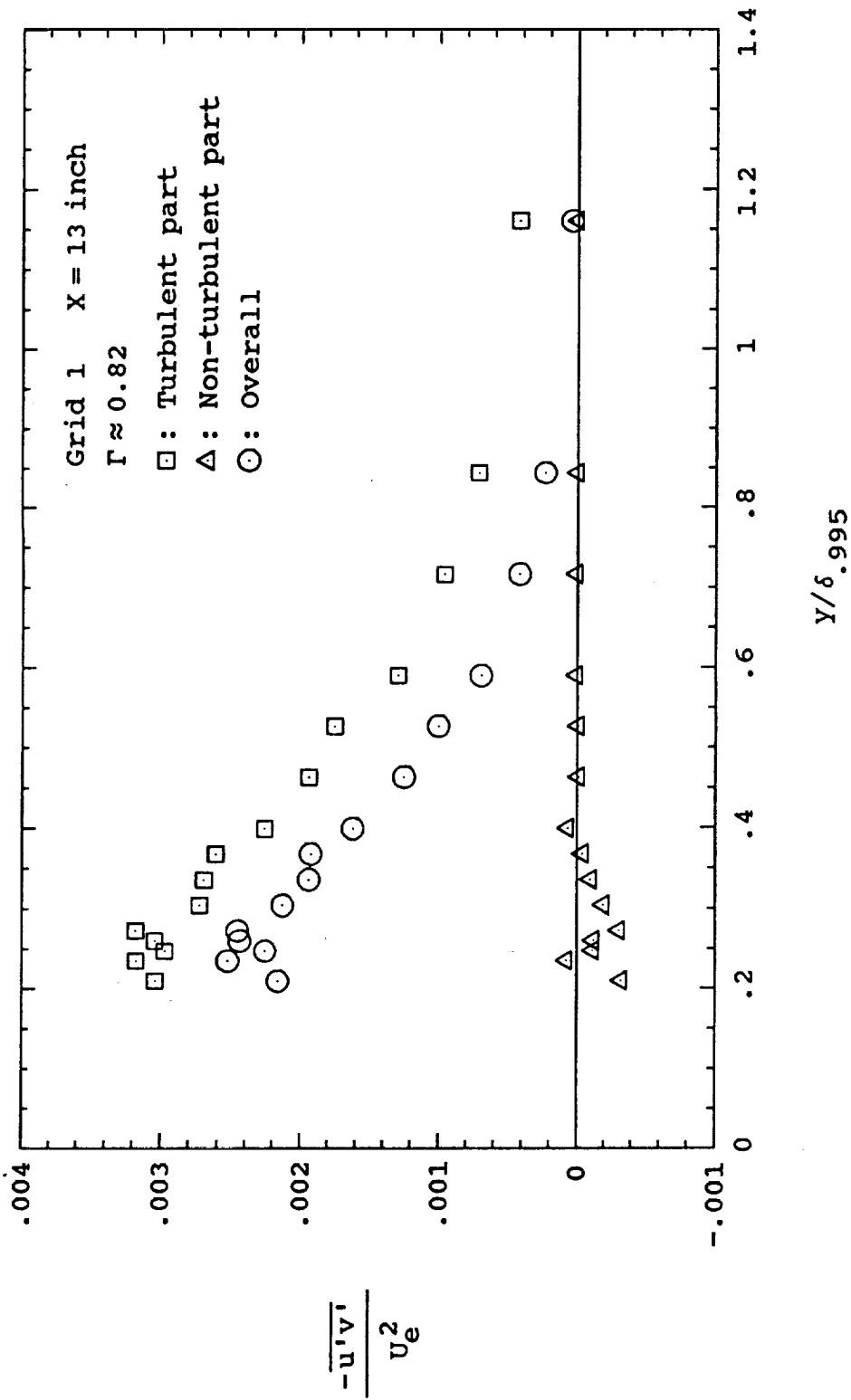


Fig. 40(b) Conditionally sampled Reynolds shear stress profiles for grid 1 at X=13 inches

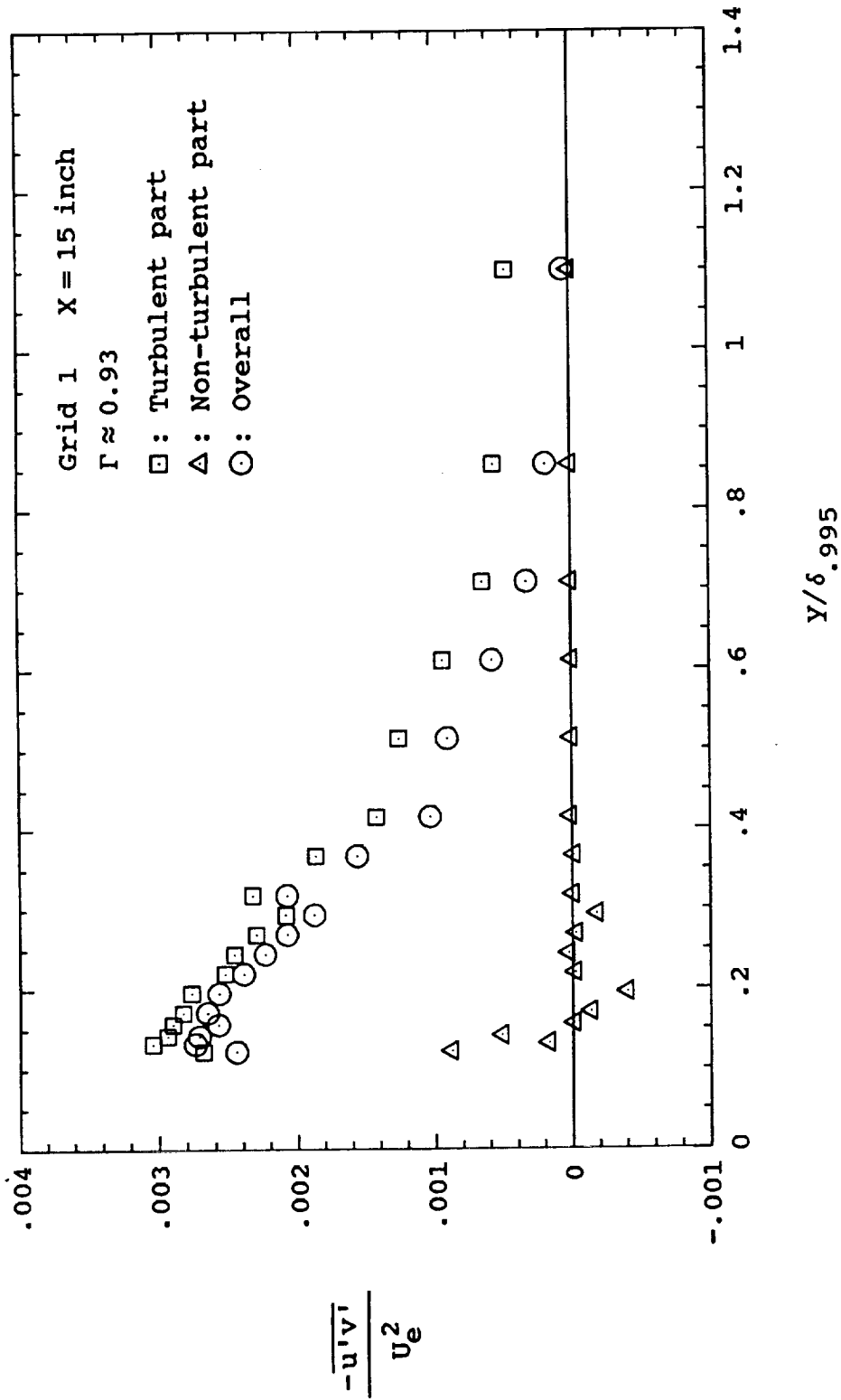


Fig. 40(c) Conditionally sampled Reynolds shear stress profiles for grid 1 at X=15 inches

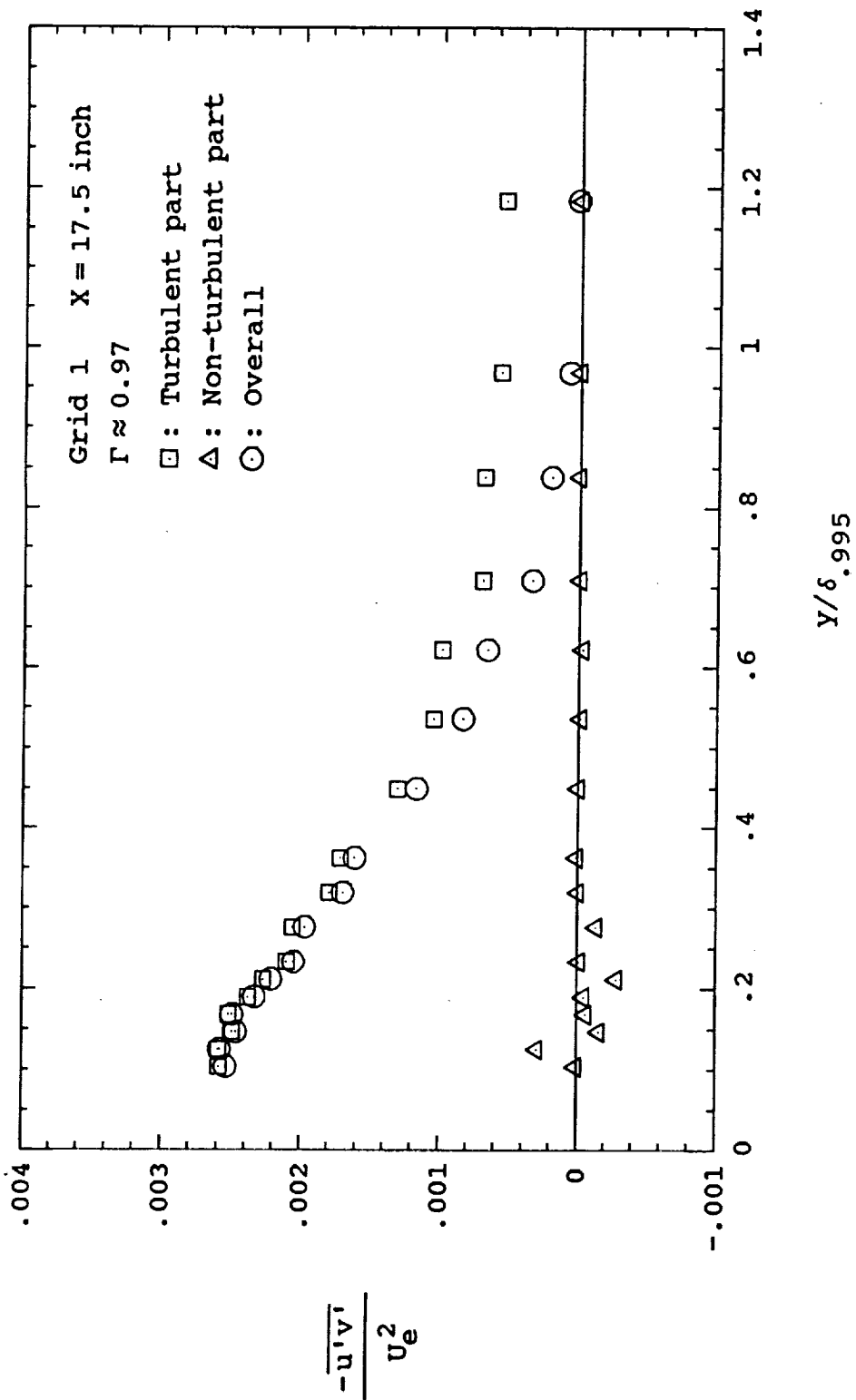


Fig. 40(d) Conditionally sampled Reynolds shear stress profiles for grid 1 at X=17.5 inches

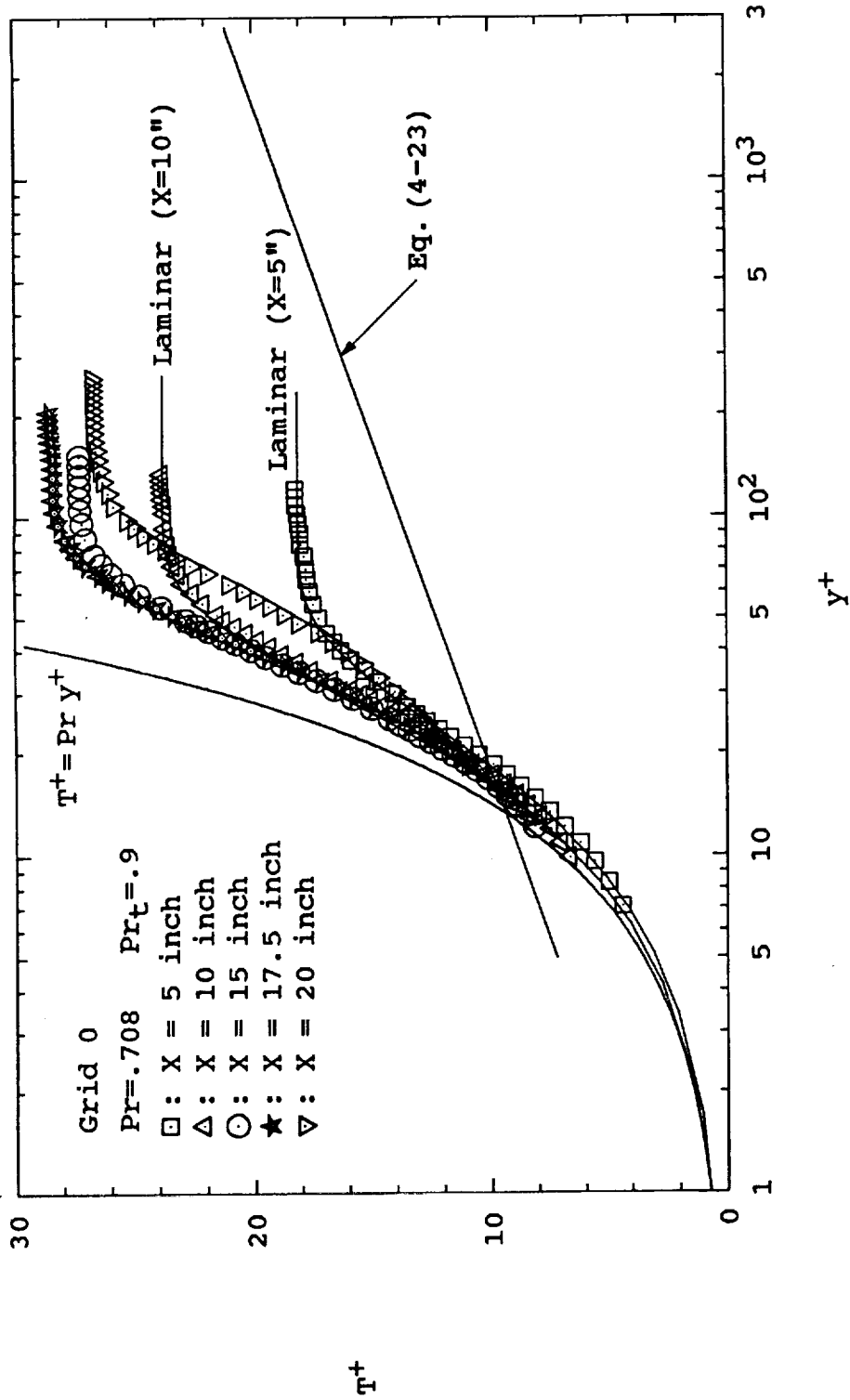


Fig. 41(a) Mean temperature profiles in wall units for grid 0

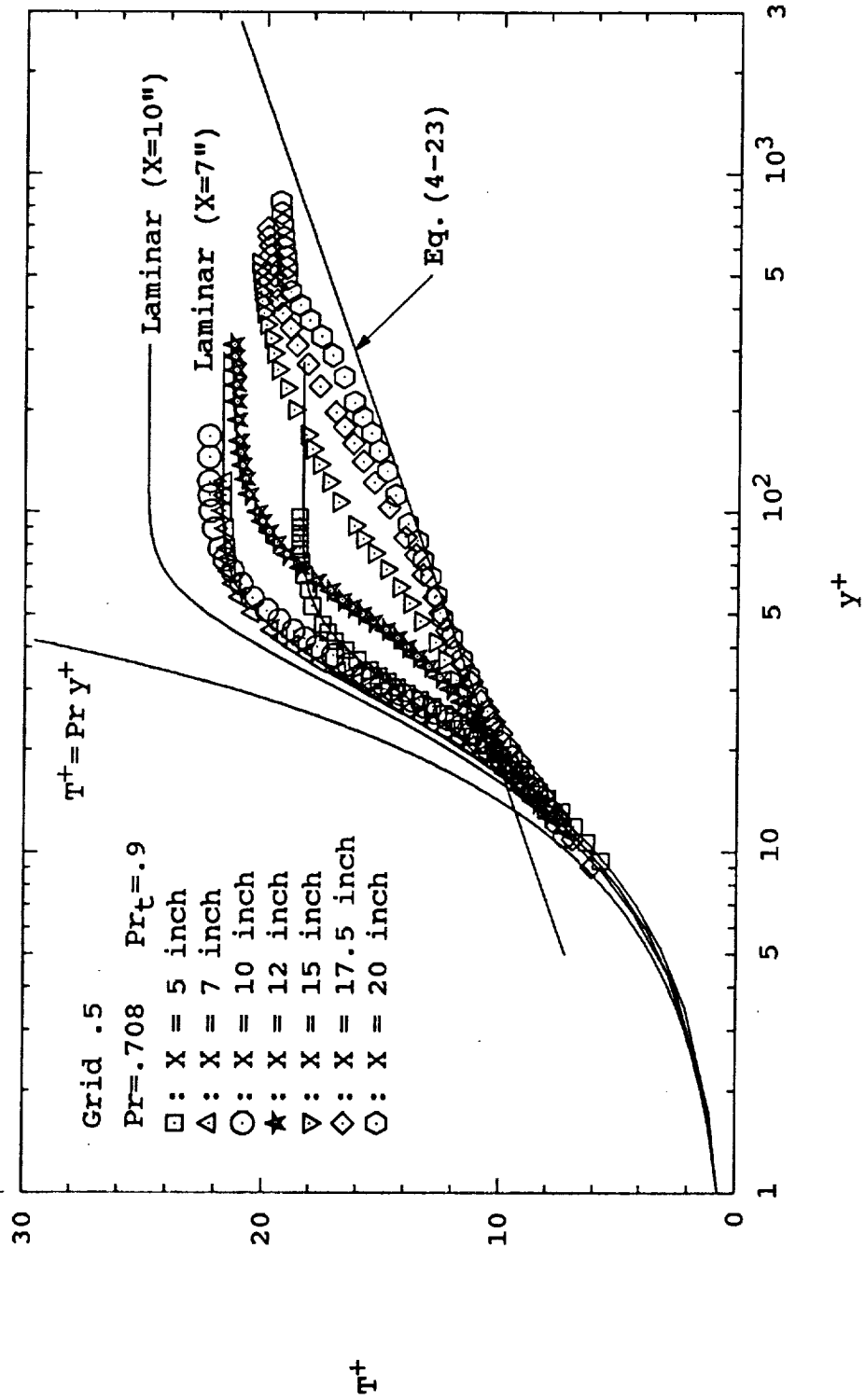


Fig. 41(b) Mean temperature profiles in wall units for grid .5

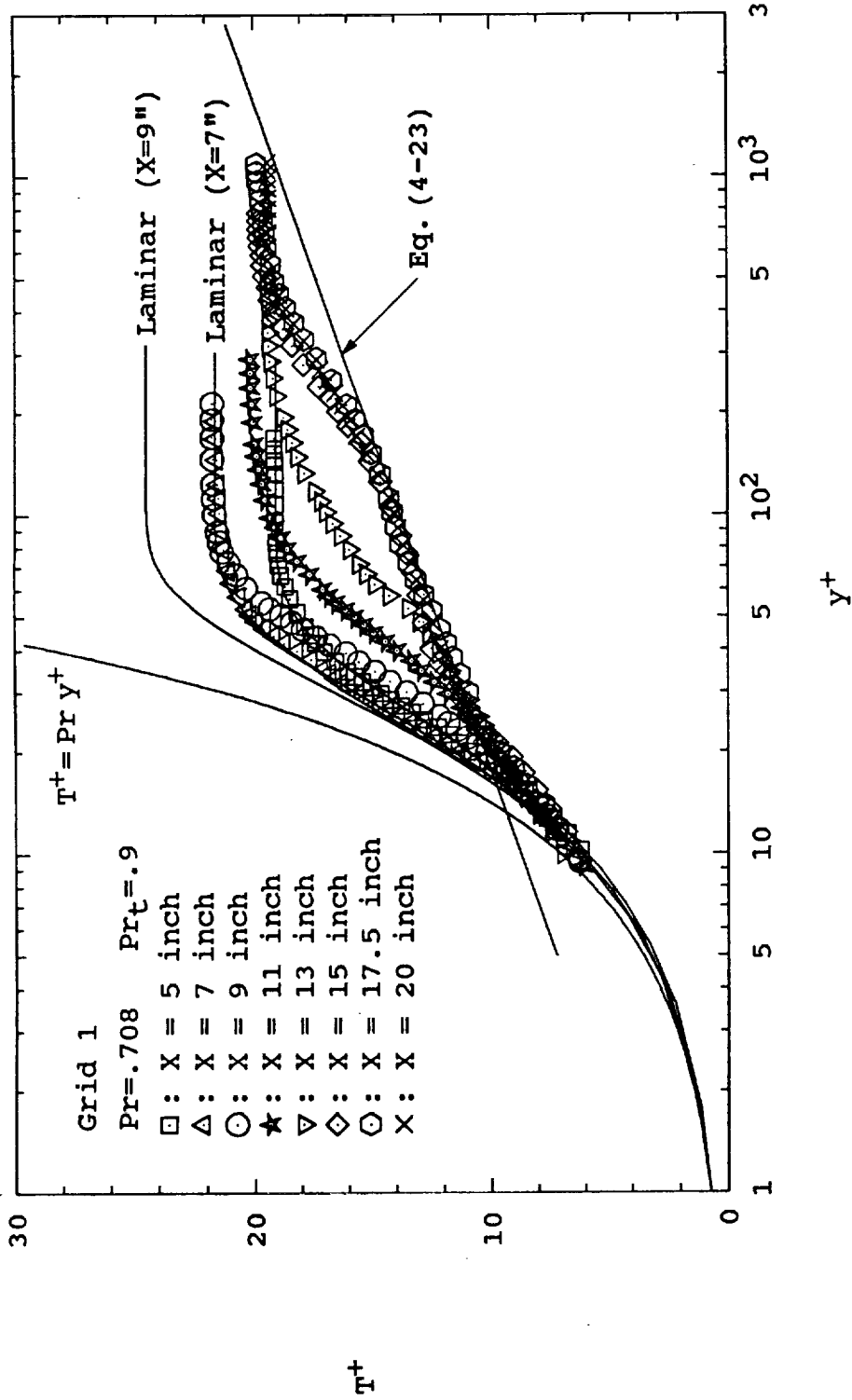


Fig. 41(c) Mean temperature profiles in wall units for grid 1

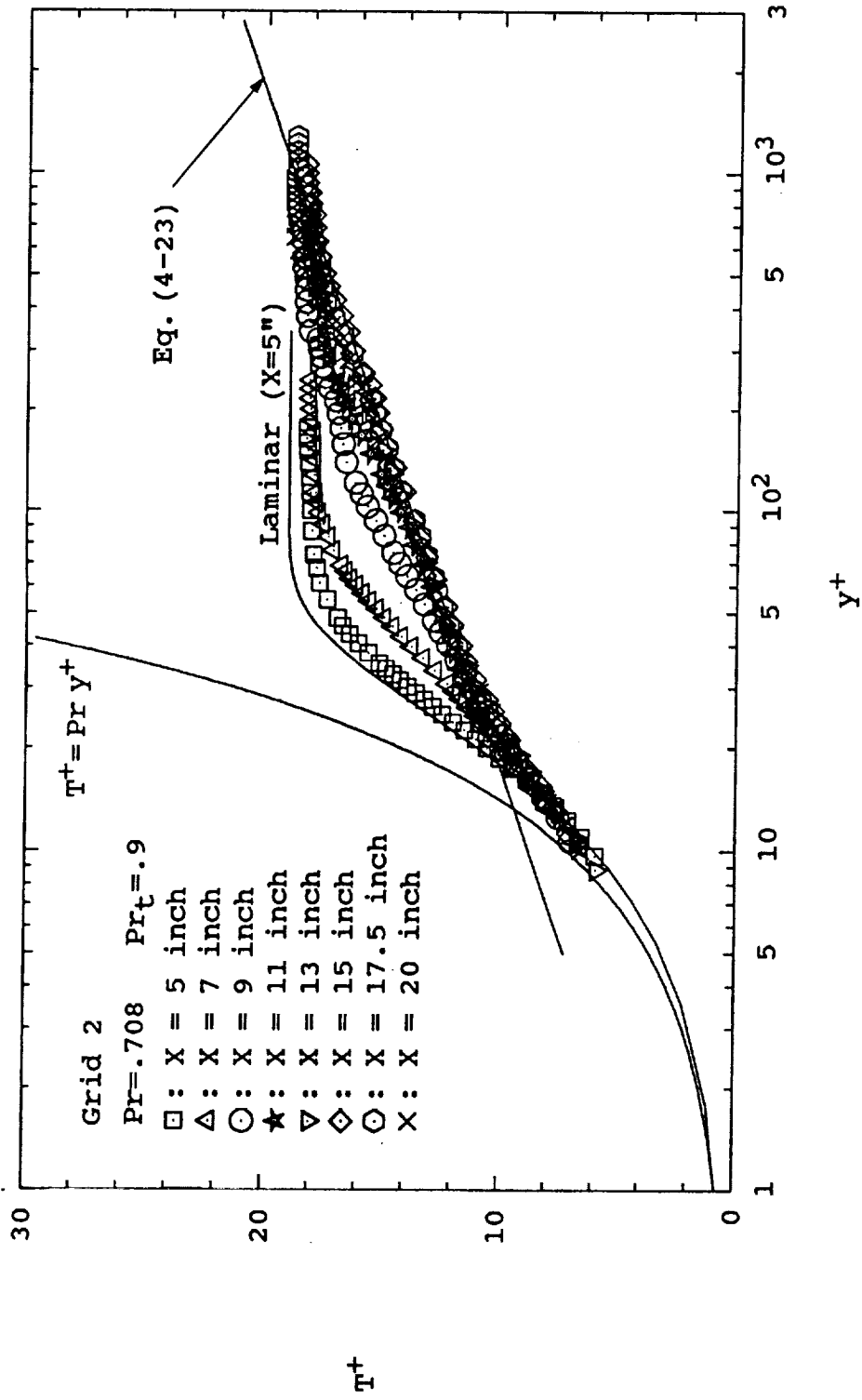


Fig. 41(d) Mean temperature profiles in wall units for grid 2

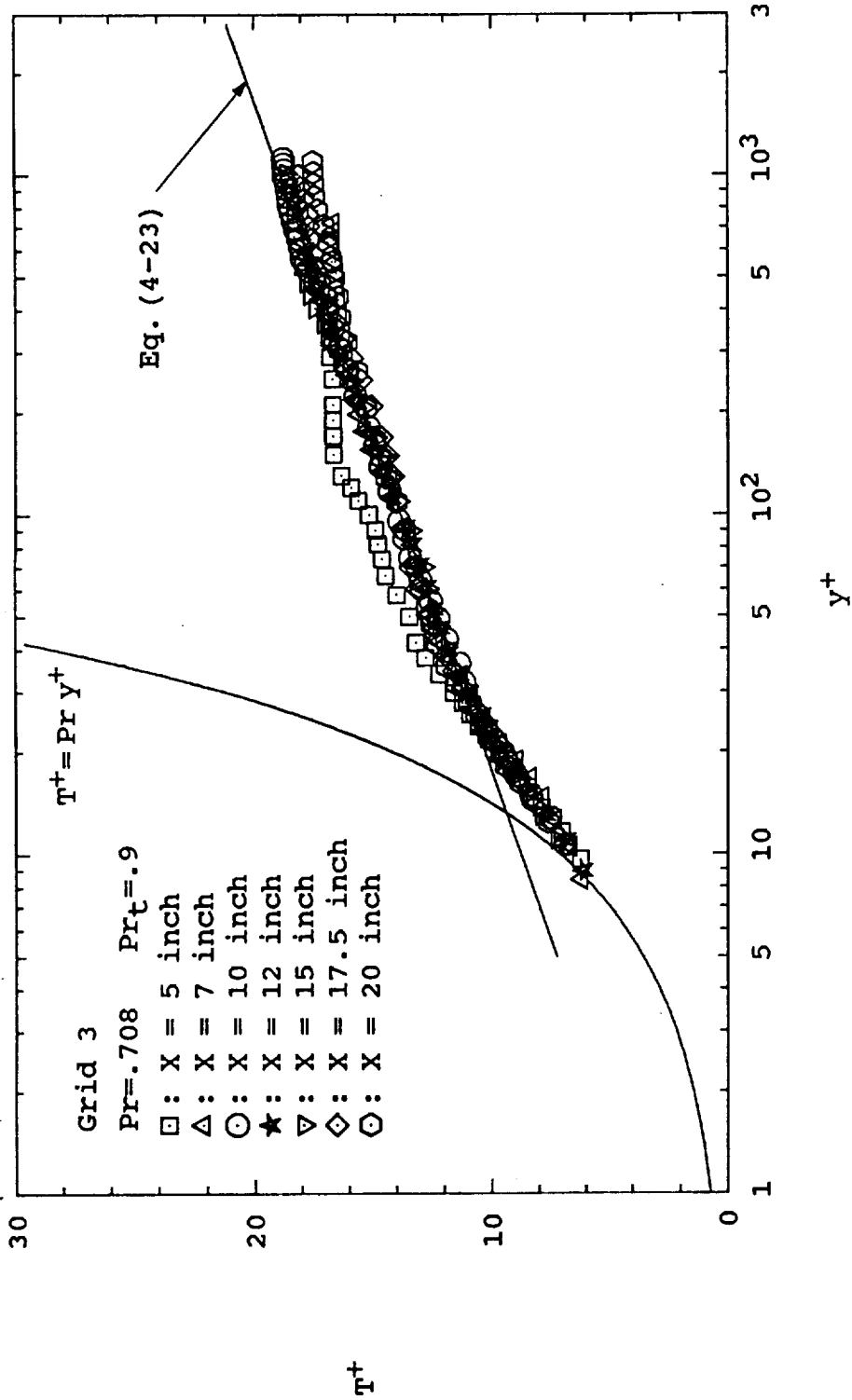


Fig. 41(e) Mean temperature profiles in wall units for grid 3

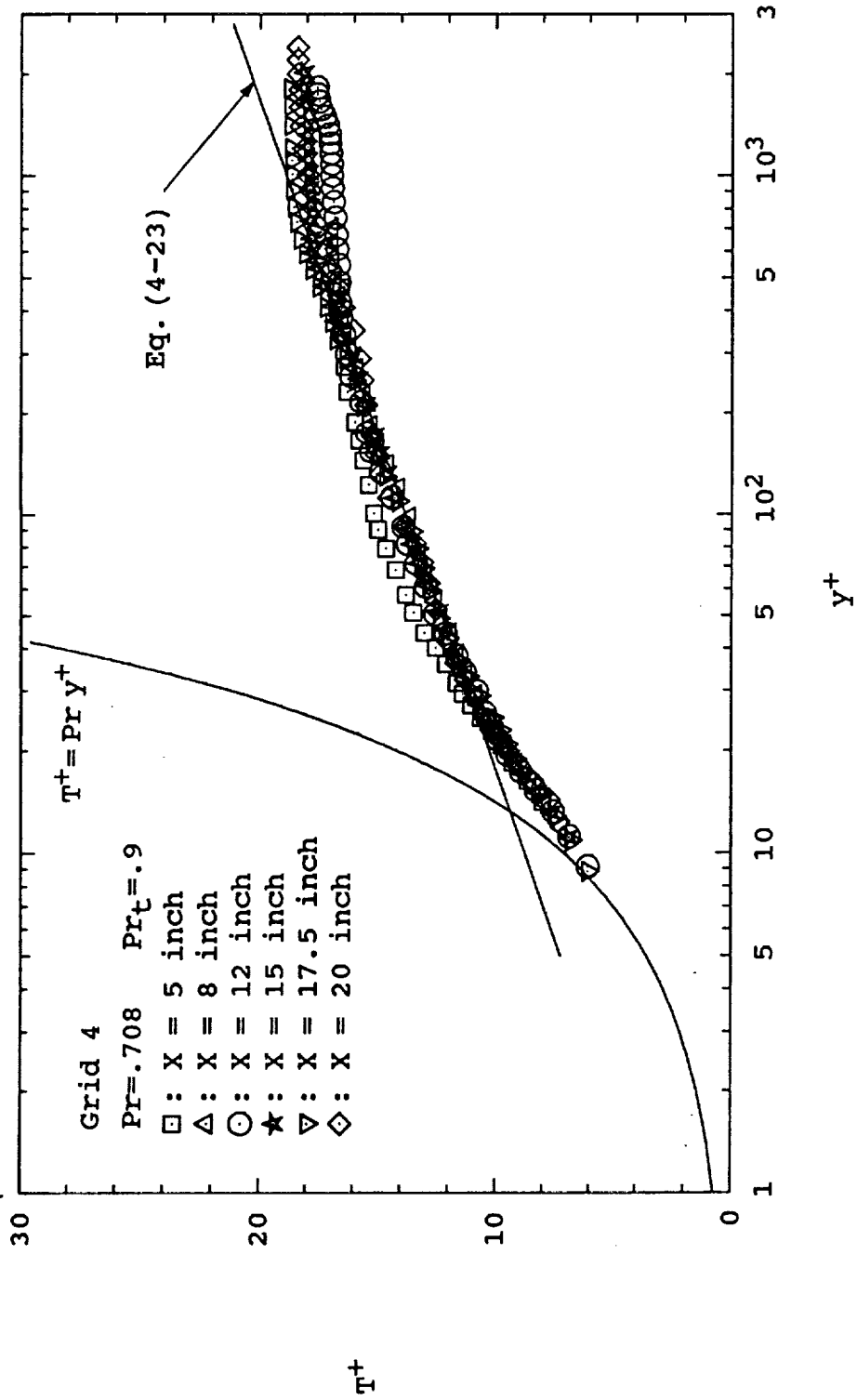


Fig. 41(f) Mean temperature profiles in wall units for grid 4

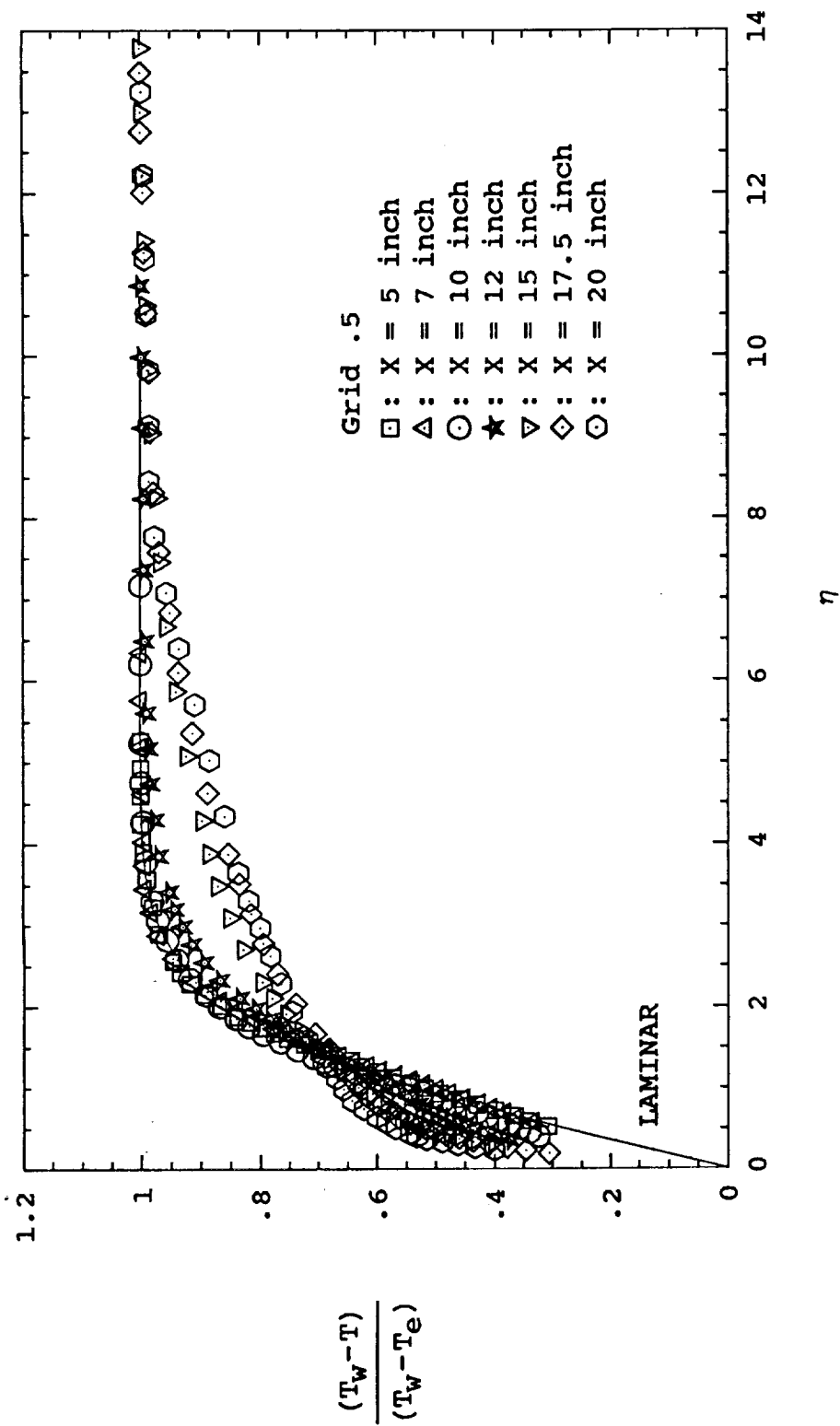


Fig. 42 Mean temperature profiles in outer coordinates for grid 0.5

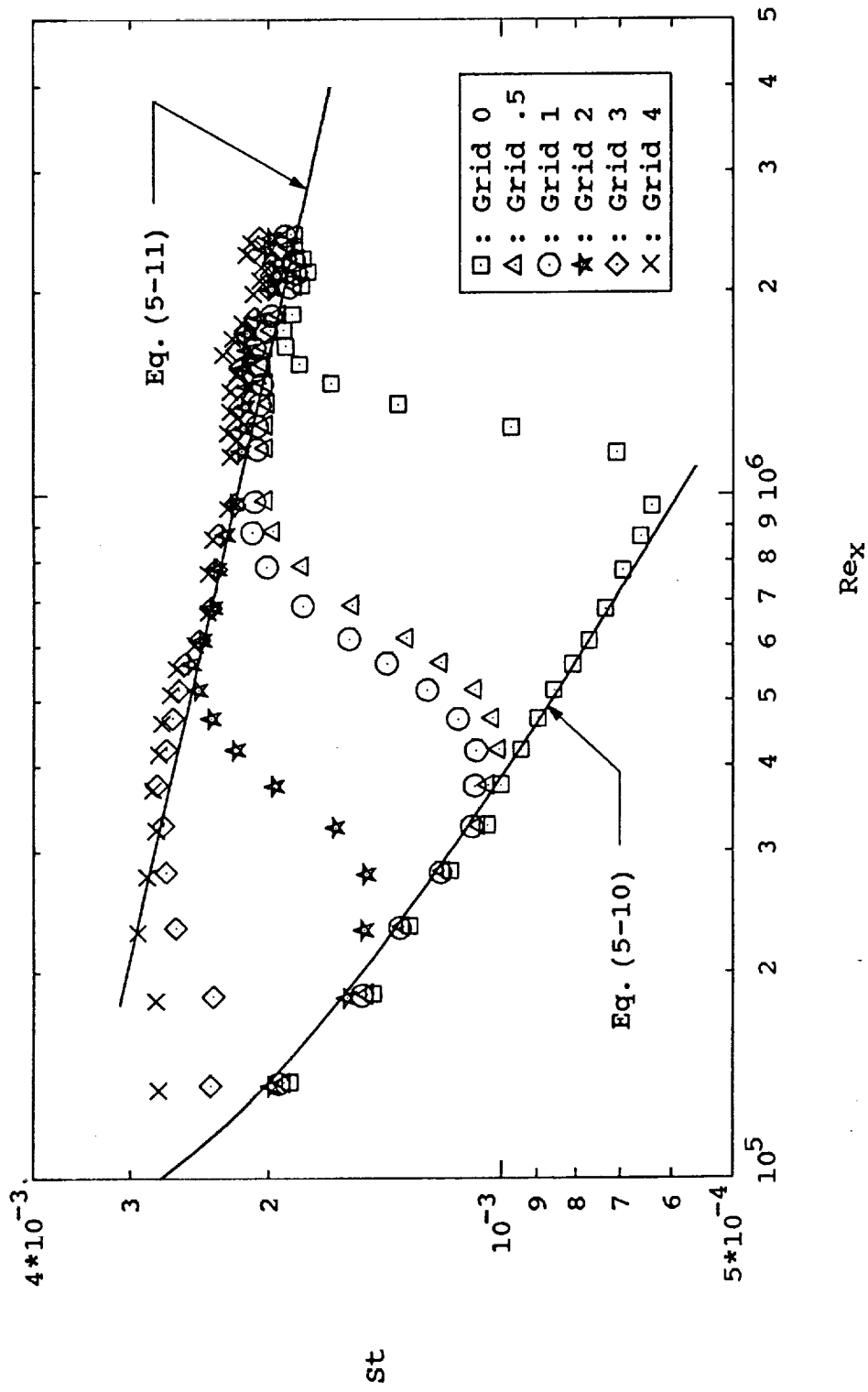


Fig. 43 Stanton number dependence on  $Re_x$  and freestream turbulence

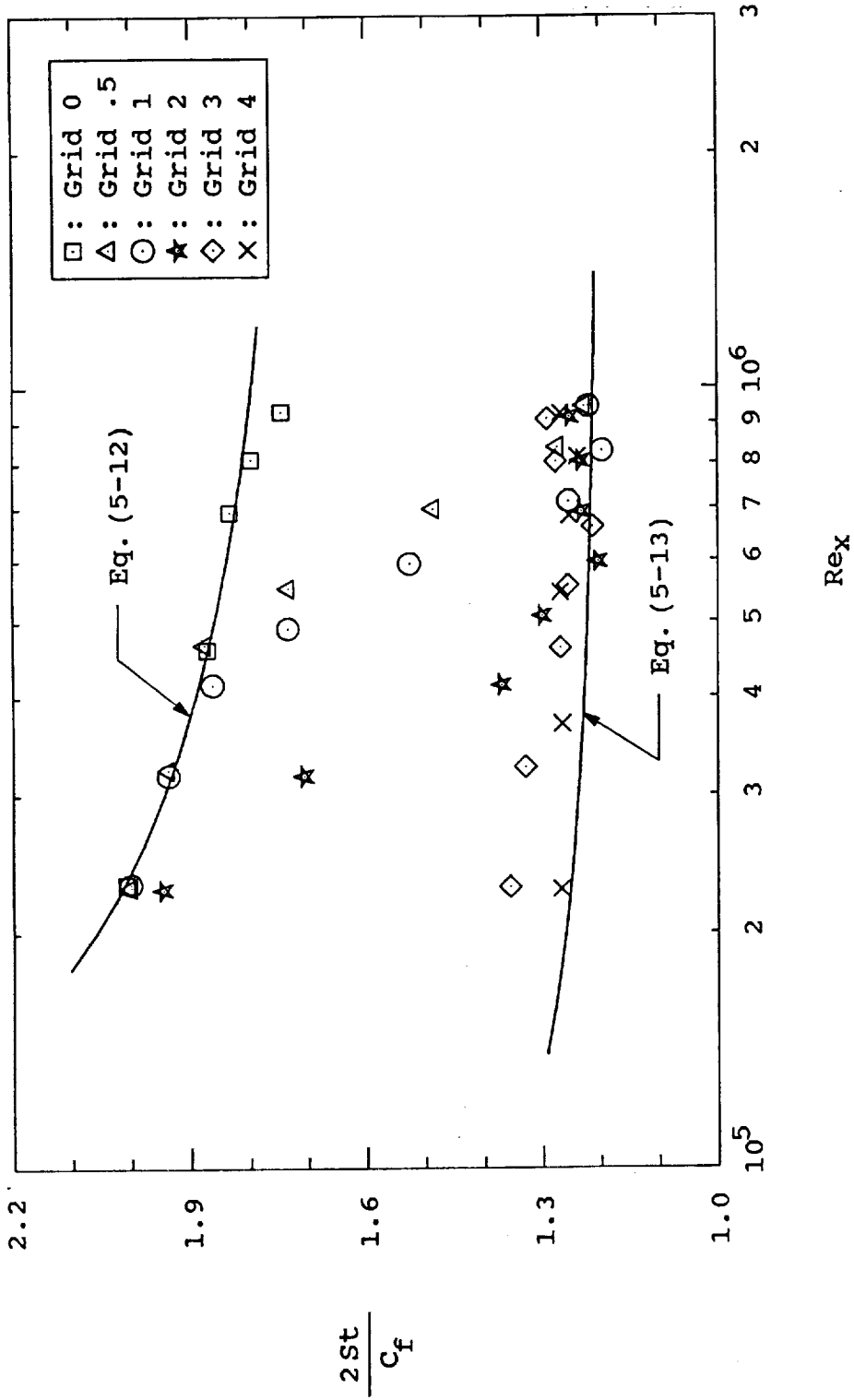


Fig. 44 Distribution of Reynolds analogy factor

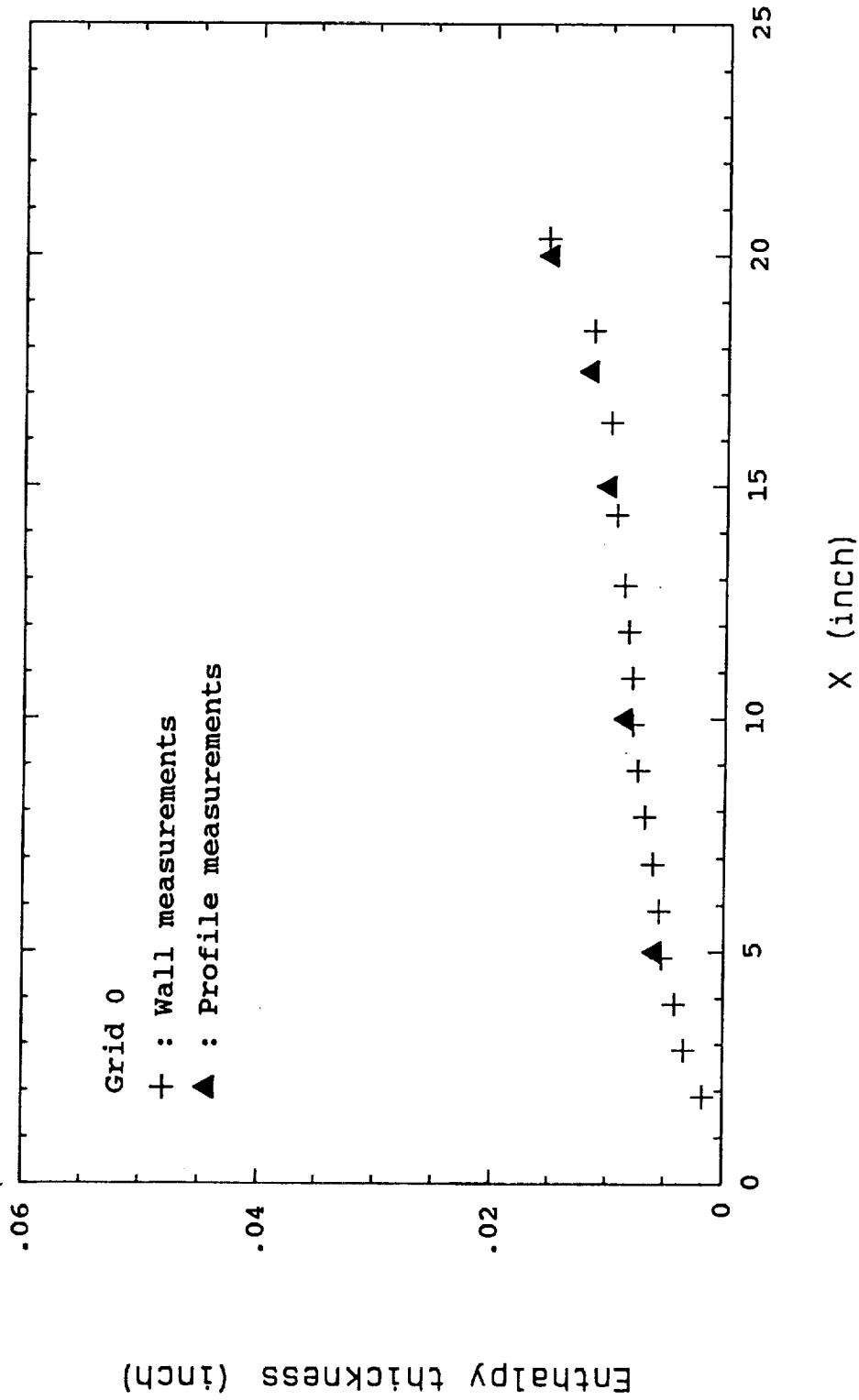


Fig. 45(a) Development of enthalpy thickness and energy closure verification for grid 0

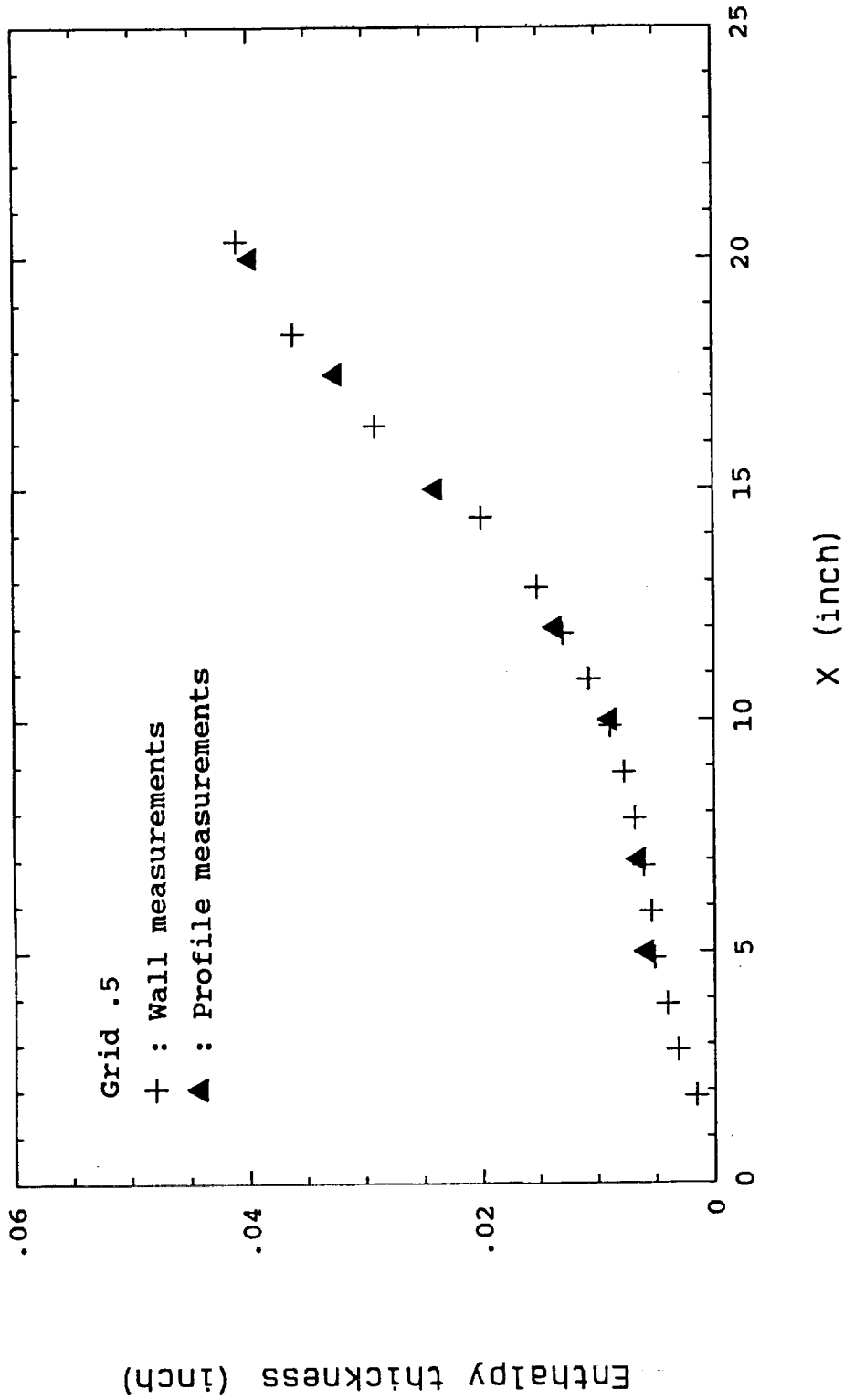


Fig. 45(b) Development of enthalpy thickness and energy closure verification for grid .5

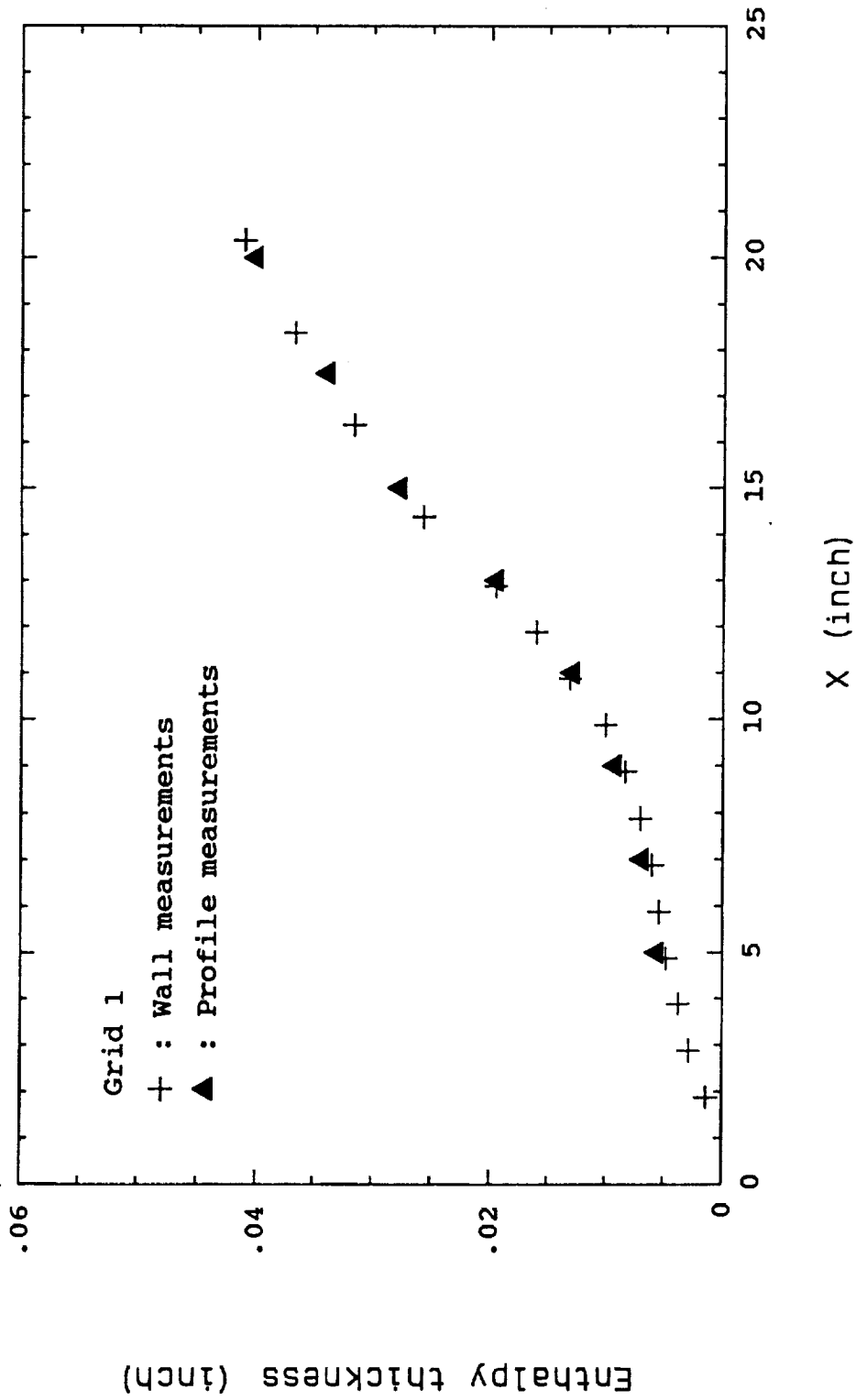


Fig. 45(c) Development of enthalpy thickness and energy closure verification for grid 1

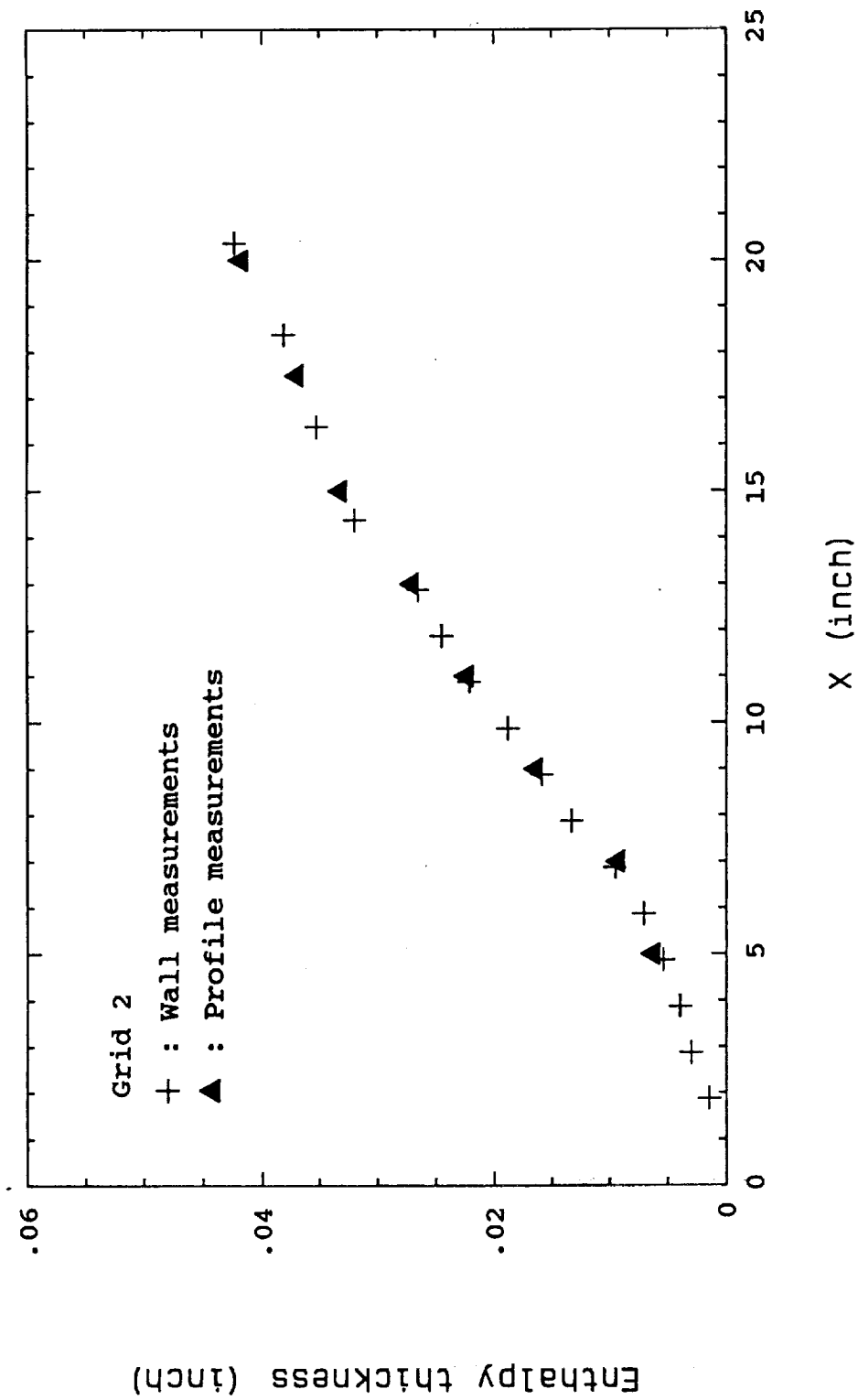


Fig. 45(d) Development of enthalpy thickness and energy closure verification for grid 2

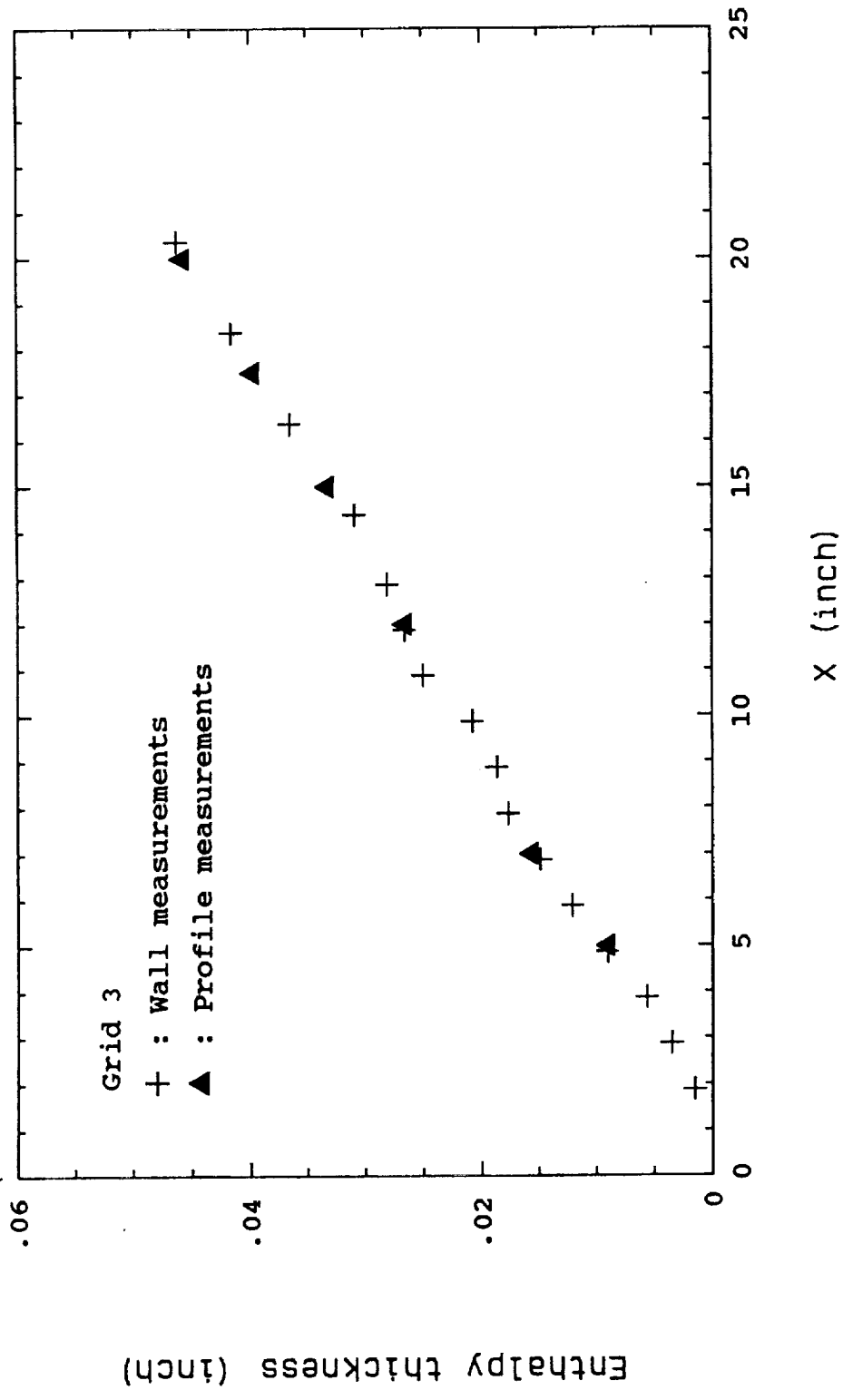


Fig. 45(e) Development of enthalpy thickness and energy closure verification for grid 3

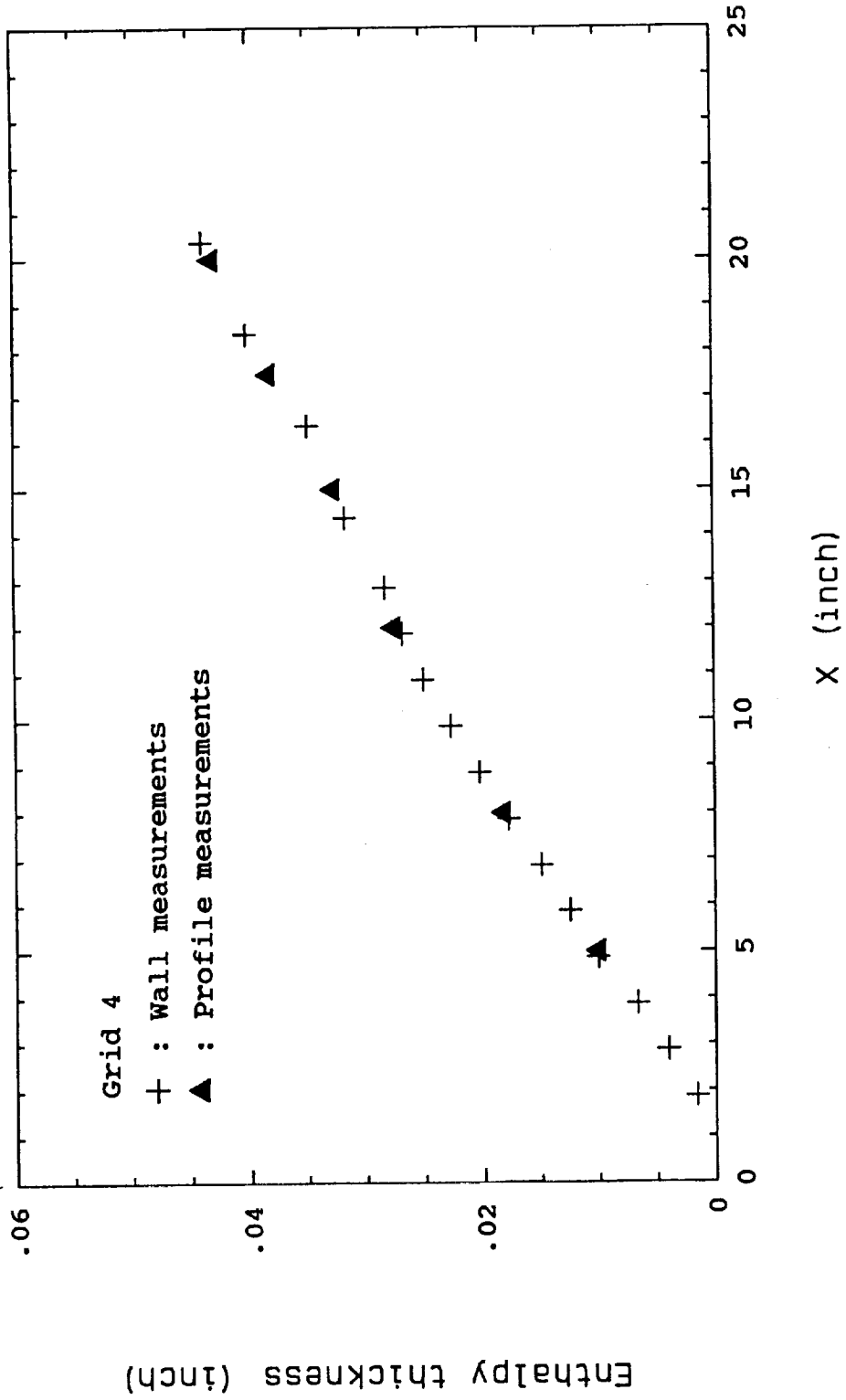


Fig. 45(f) Development of enthalpy thickness and energy closure verification for grid 4

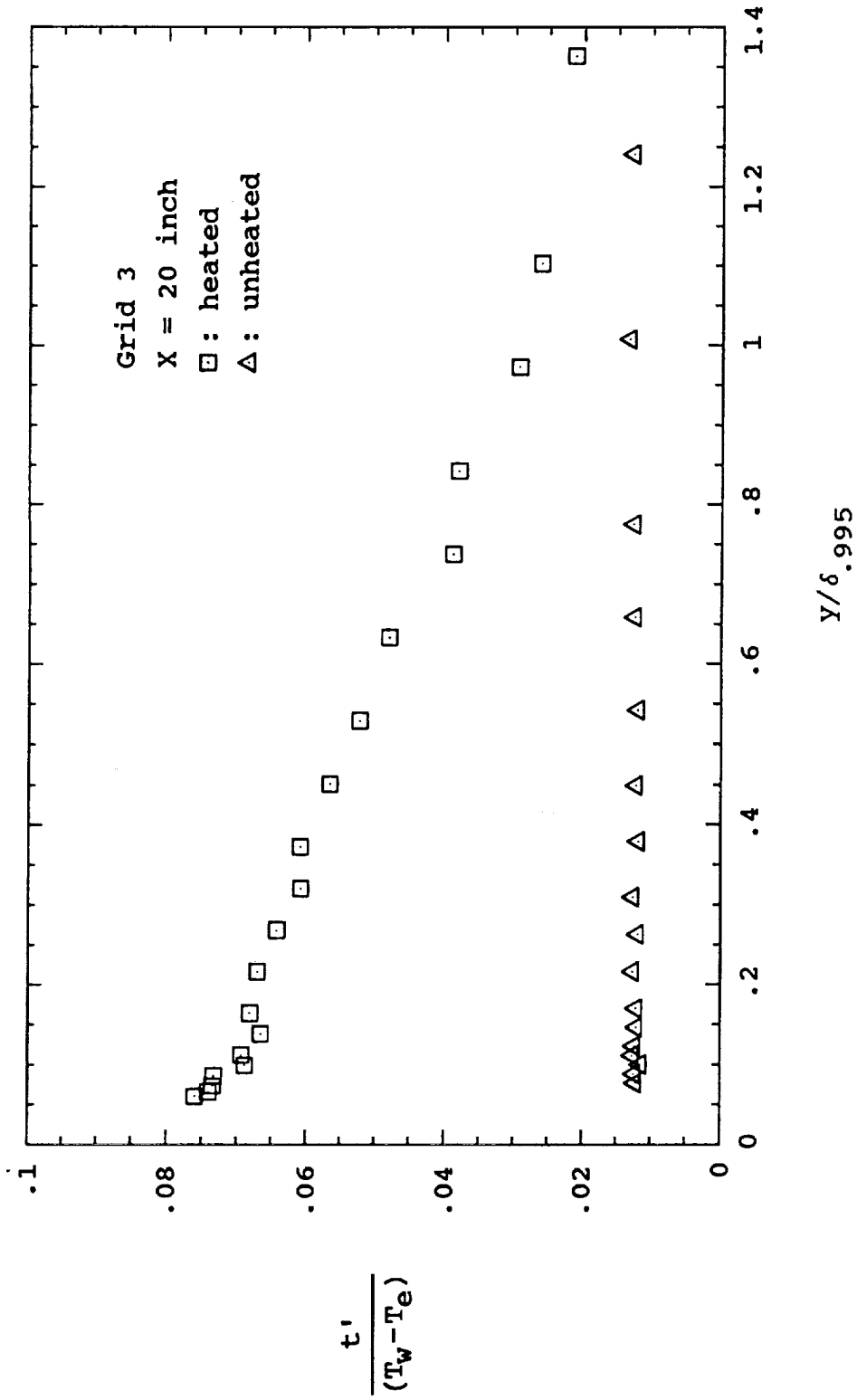


Fig. 46 Apparent temperature fluctuation

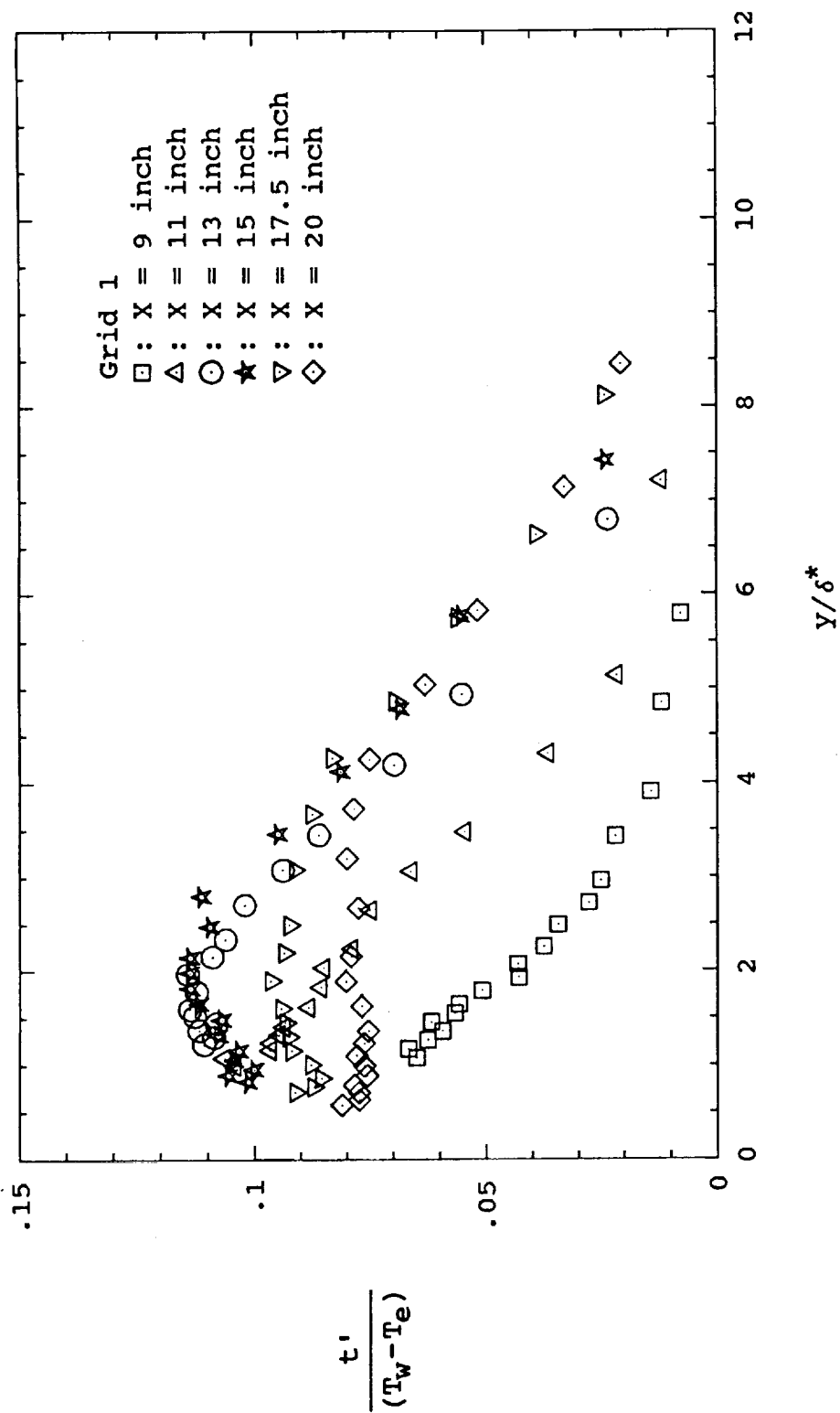


Fig. 47 RMS temperature fluctuation profiles for grid 1

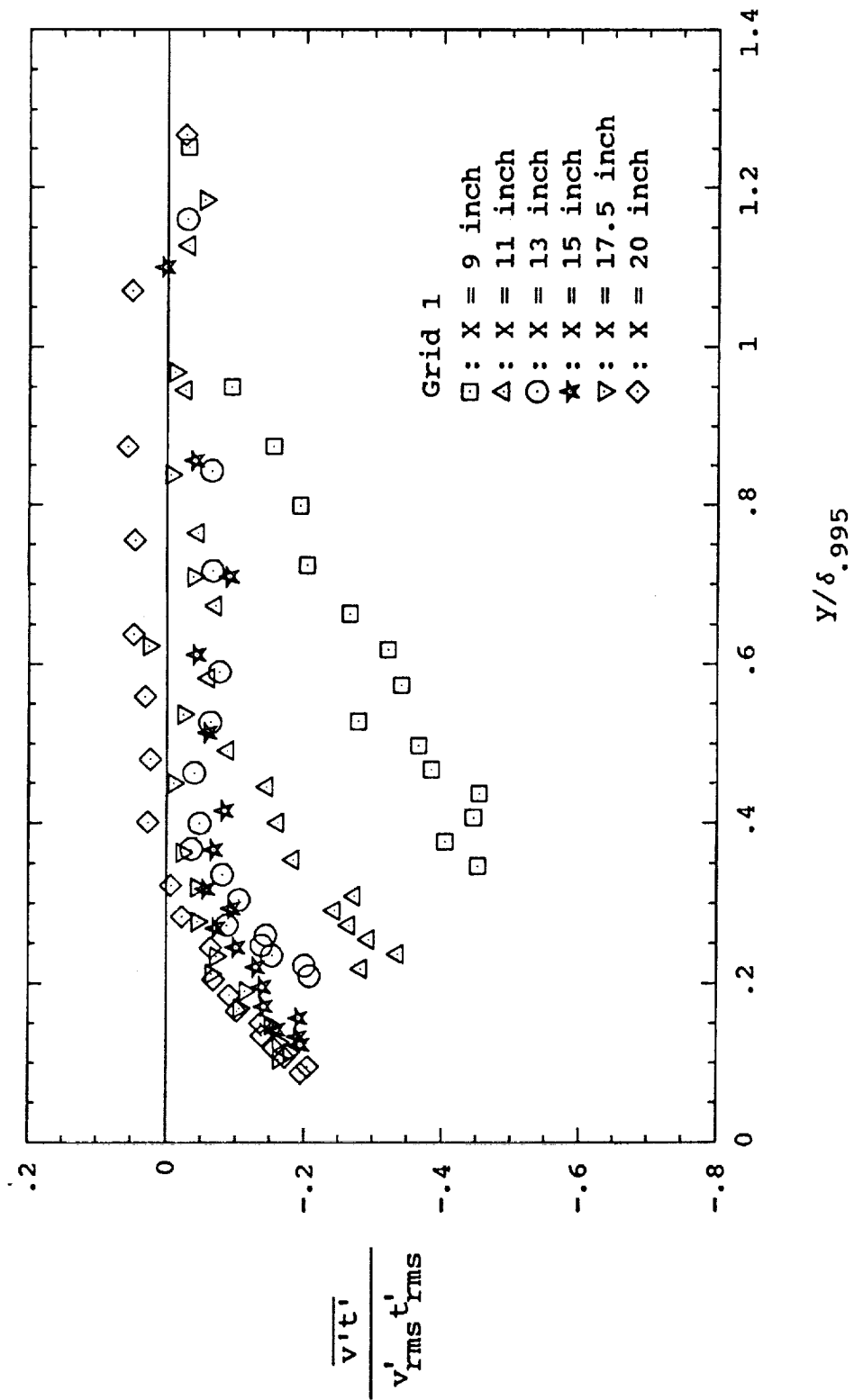


Fig. 48(a) Correlation coefficient profiles of  $v'$  and  $t'$  for grid 1

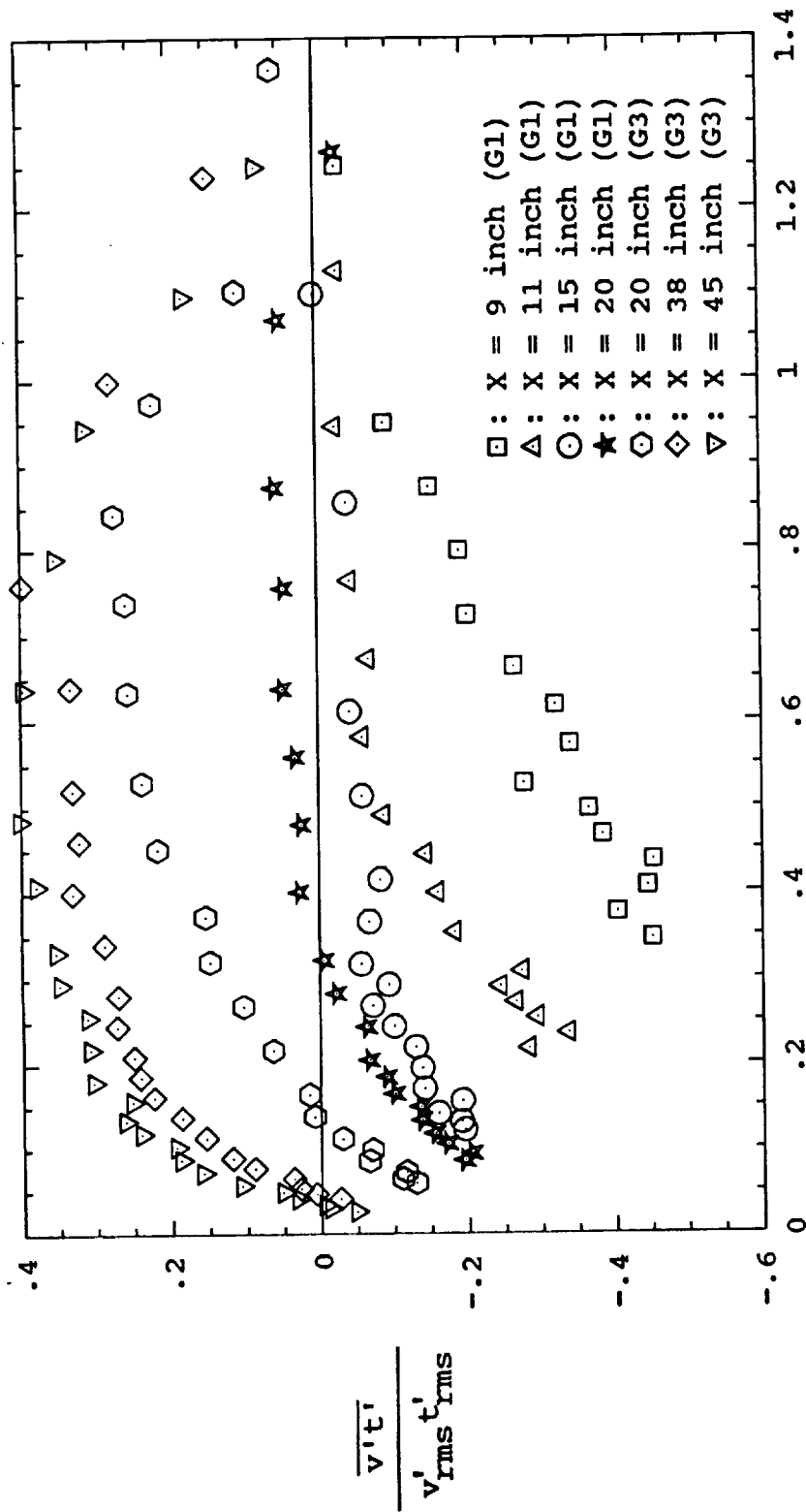


Fig. 48(b) Correlation coefficient profiles of  $v'$  and  $t'$  for fully turbulent boundary layer

Y/δ.995

Grid 3 X = 20 inch Y = 0.03 inch

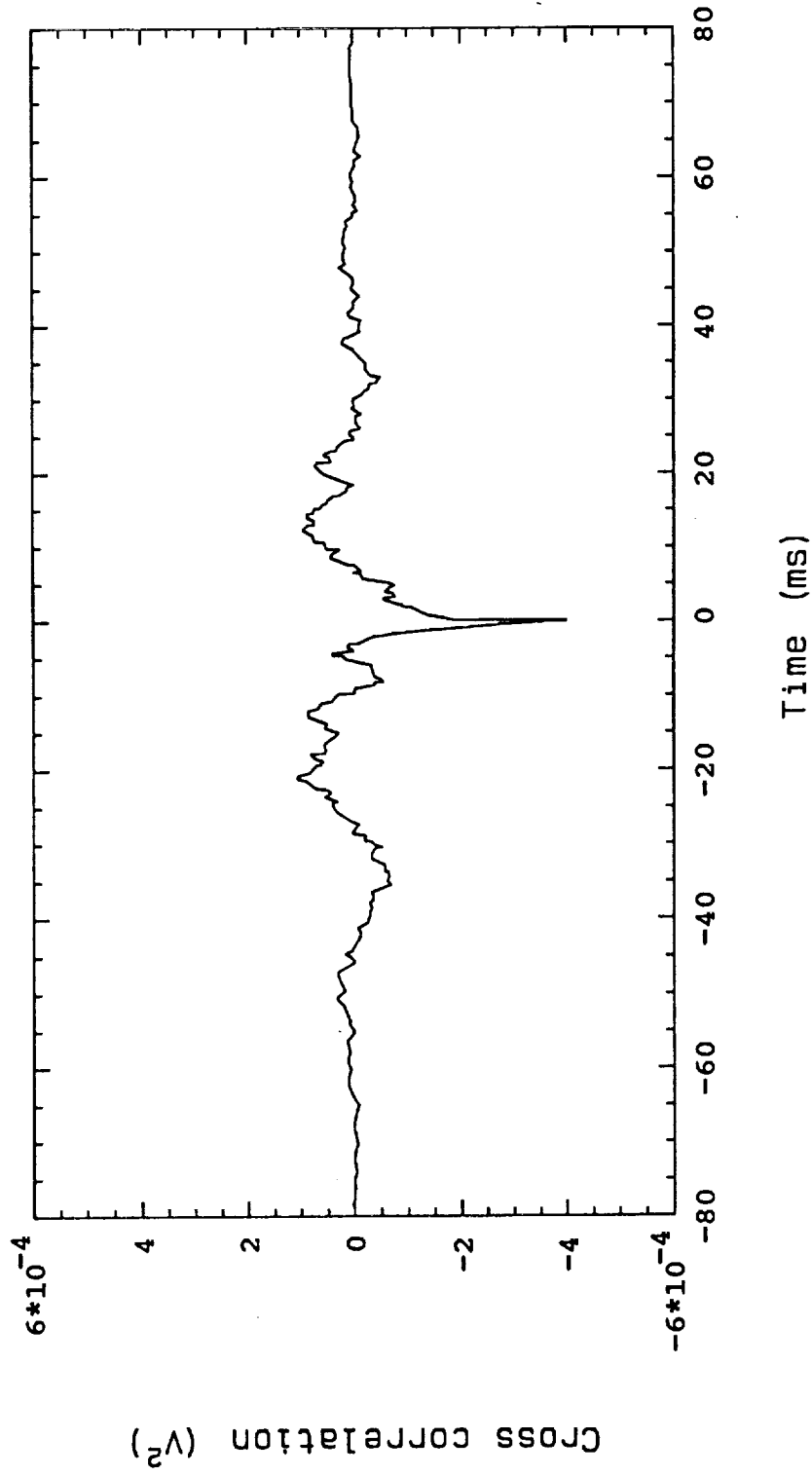


Fig. 49(a) Sign check of turbulent heat flux at near-wall location for grid 3

Grid 3 X = 20 inch Y = 0.18 inch

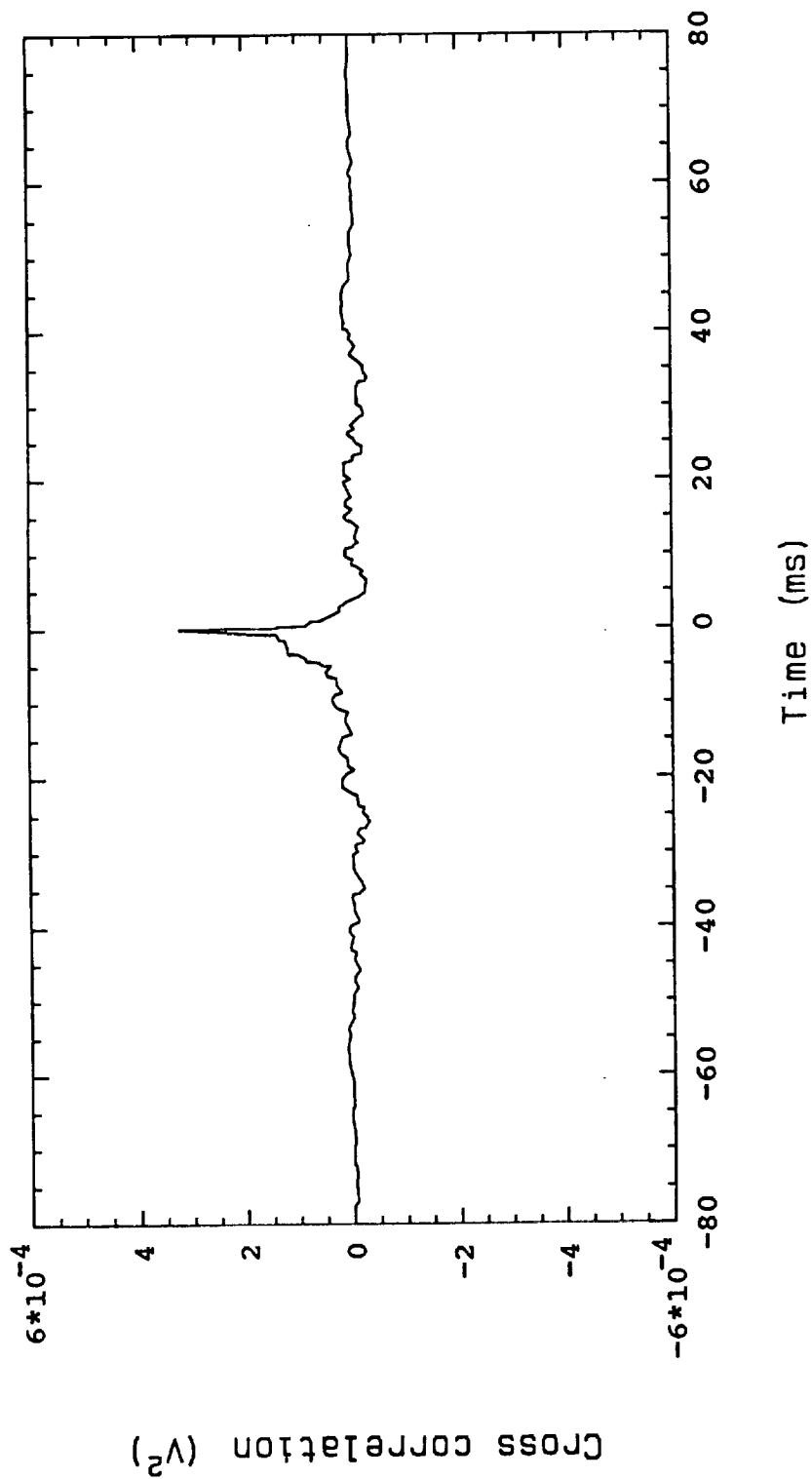


Fig. 49(b) Sign check of turbulent heat flux farther out in the boundary layer for grid 3

Grid 1 X = 11 inch Y = 0.049 inch

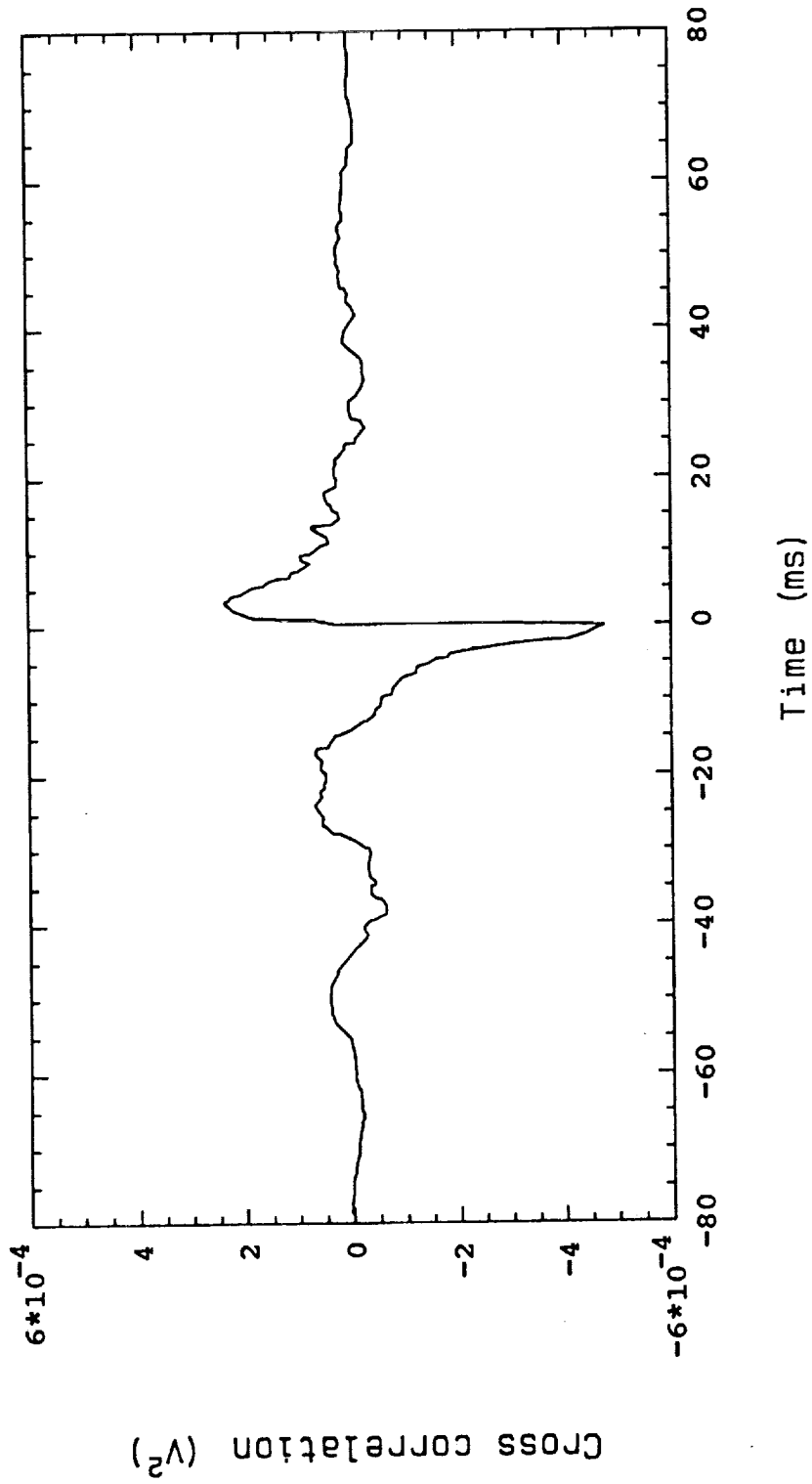


Fig. 49(c) Sign check of turbulent heat flux at mid span for grid 1

Grid 1 X = 11 inch Y = 0.049 inch

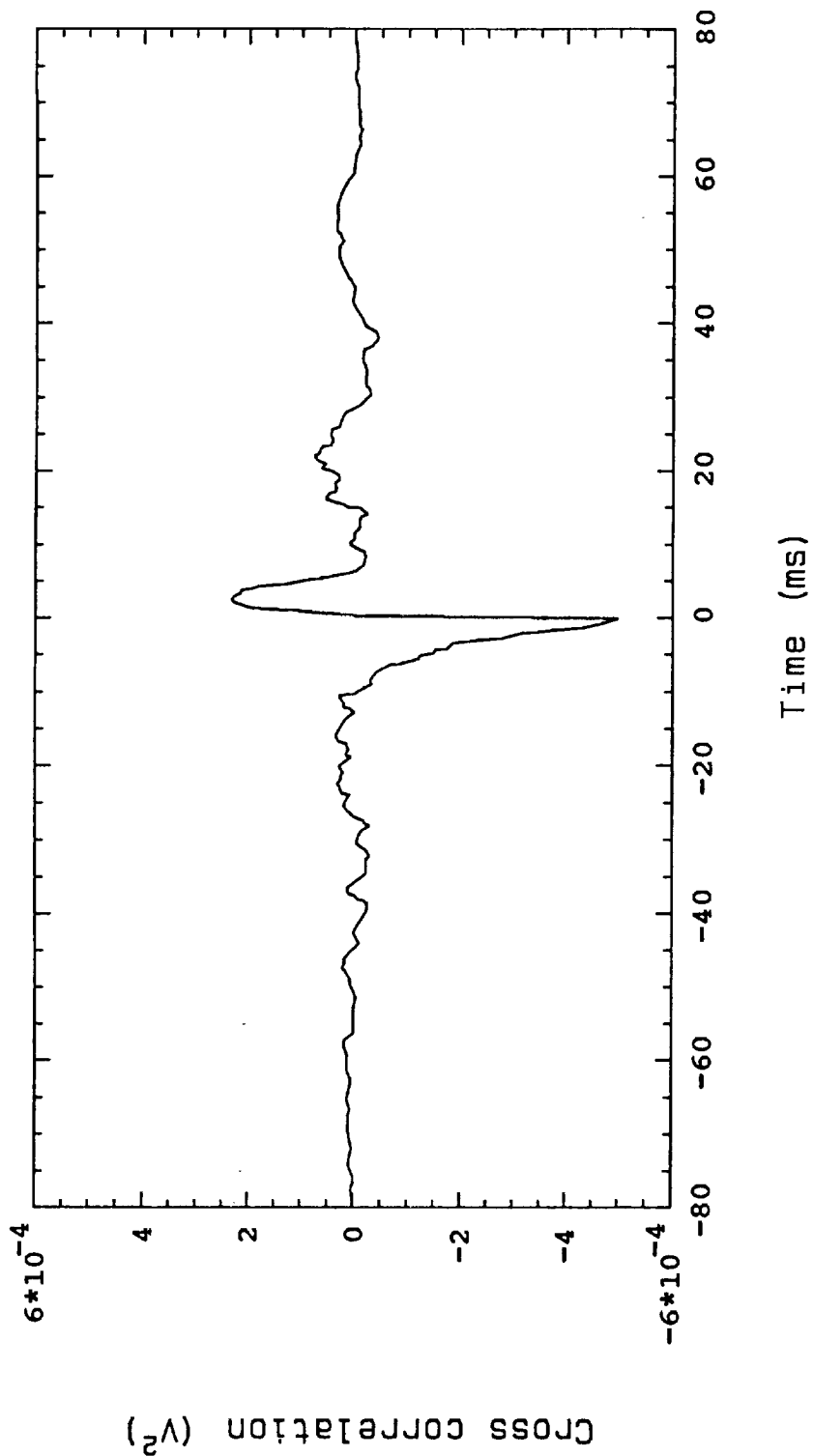


Fig. 49(d) Sign check of turbulent heat flux at 1 inch off center span for grid 1

Grid 1 X = 11 inch Y = .03 inch Heated

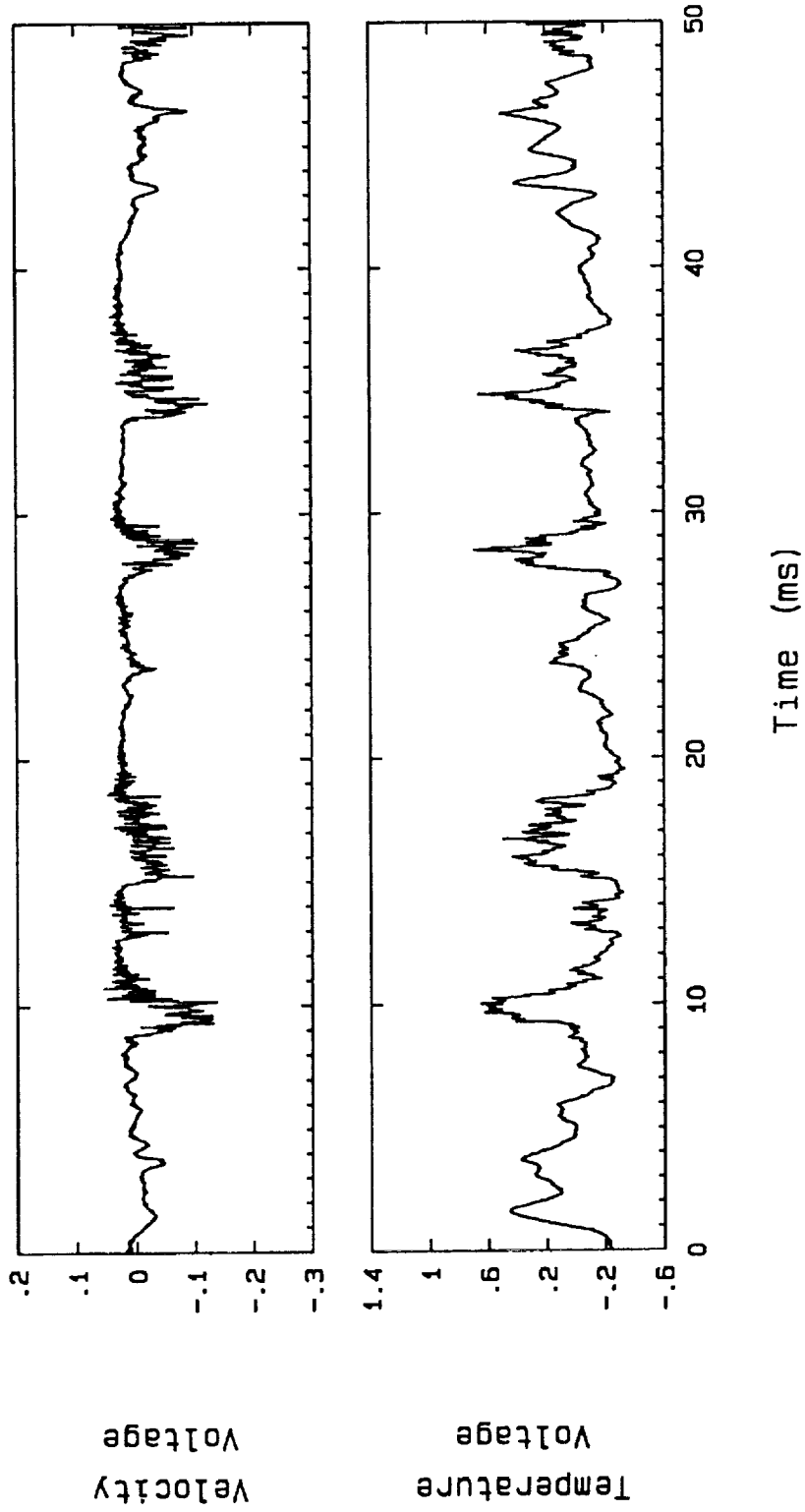


Fig. 50(a) Phase shift check in correlation of v' and t' for low frequency range

Grid 1 X = 20 inch Y = .08 inch Heated

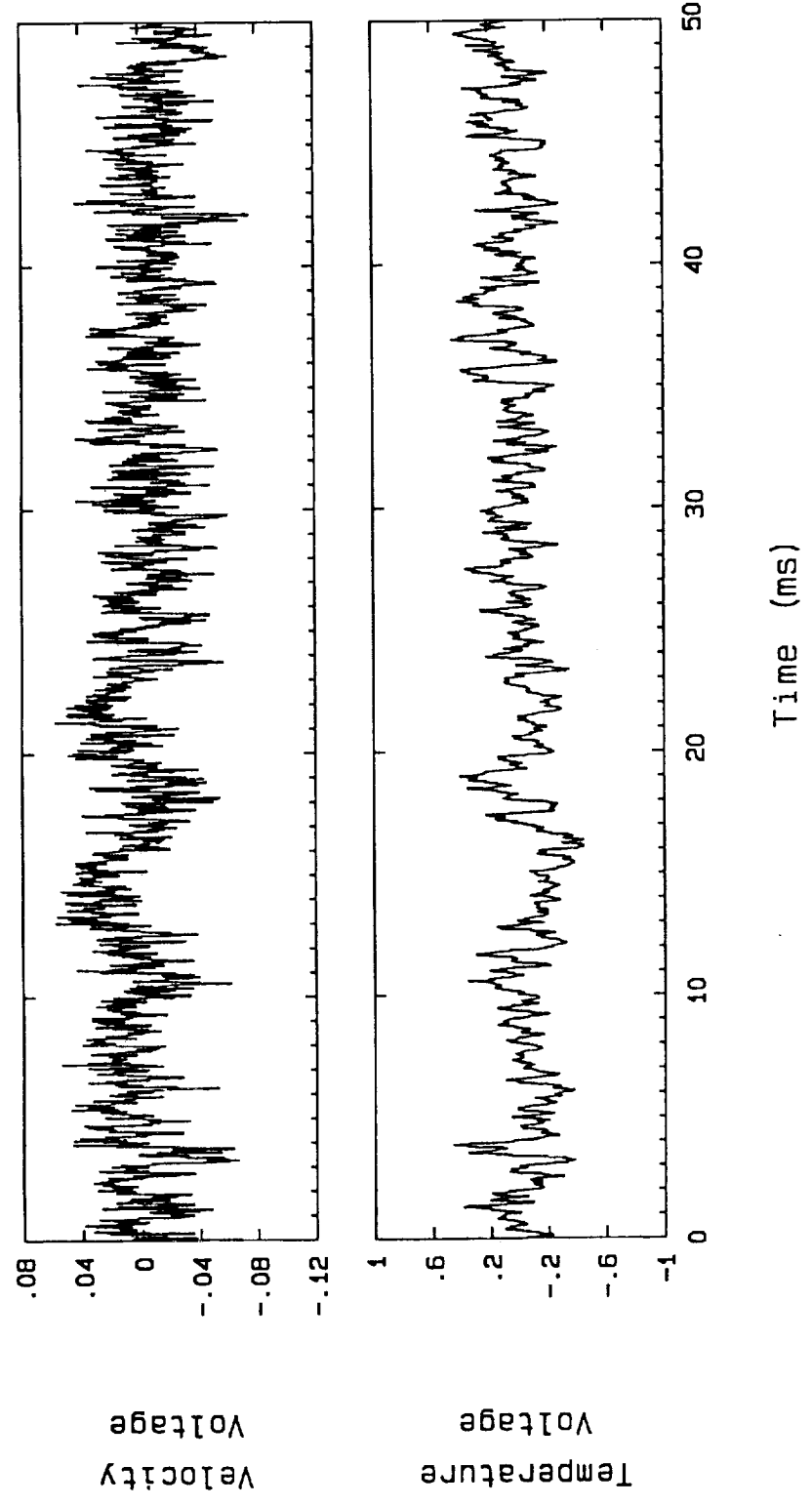


Fig. 50(b) Phase shift check in correlation of v' and t' for high frequency range

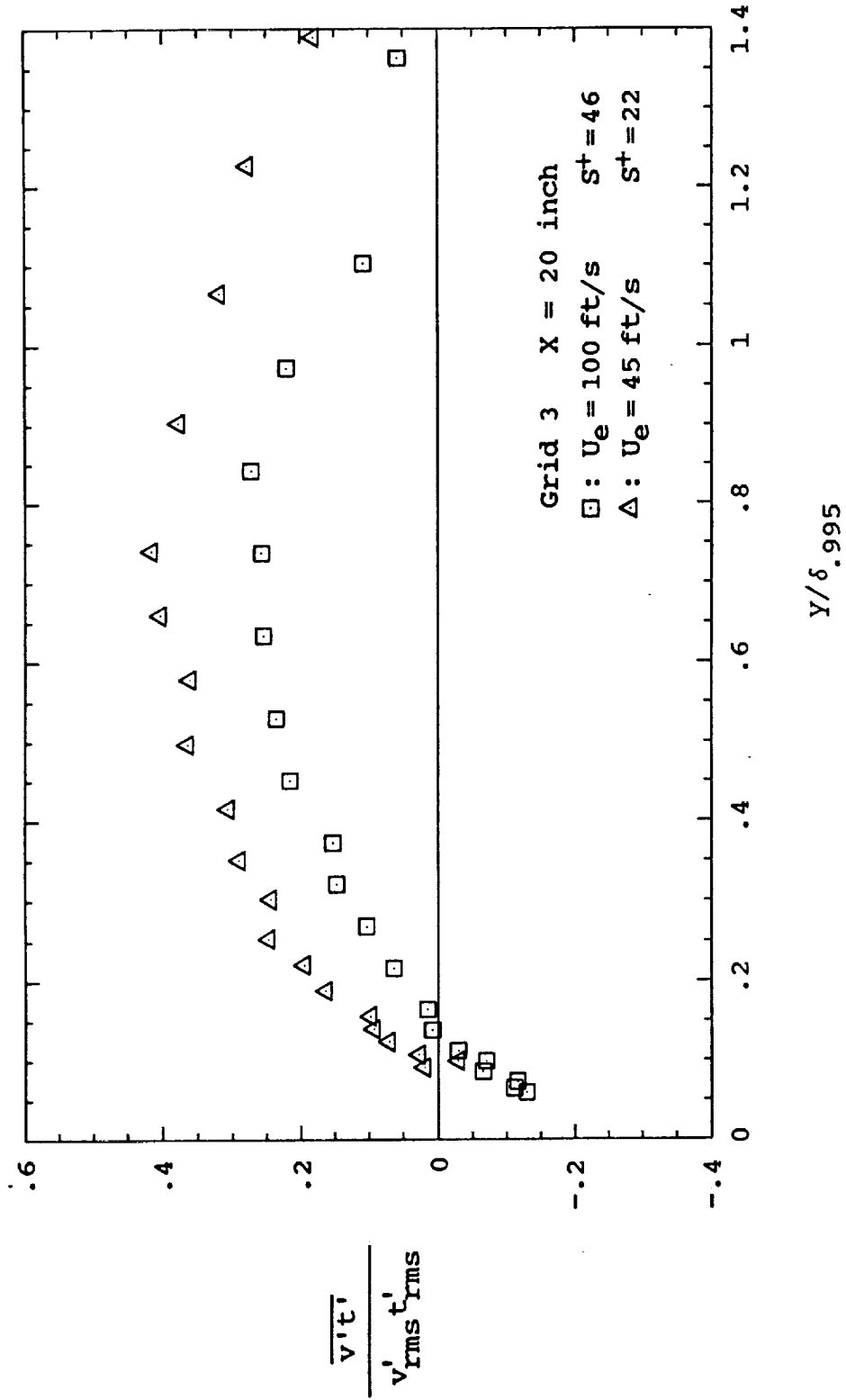


Fig. 51 Correlation coefficient profiles of  $v'$  and  $t'$  with different  $S^+$

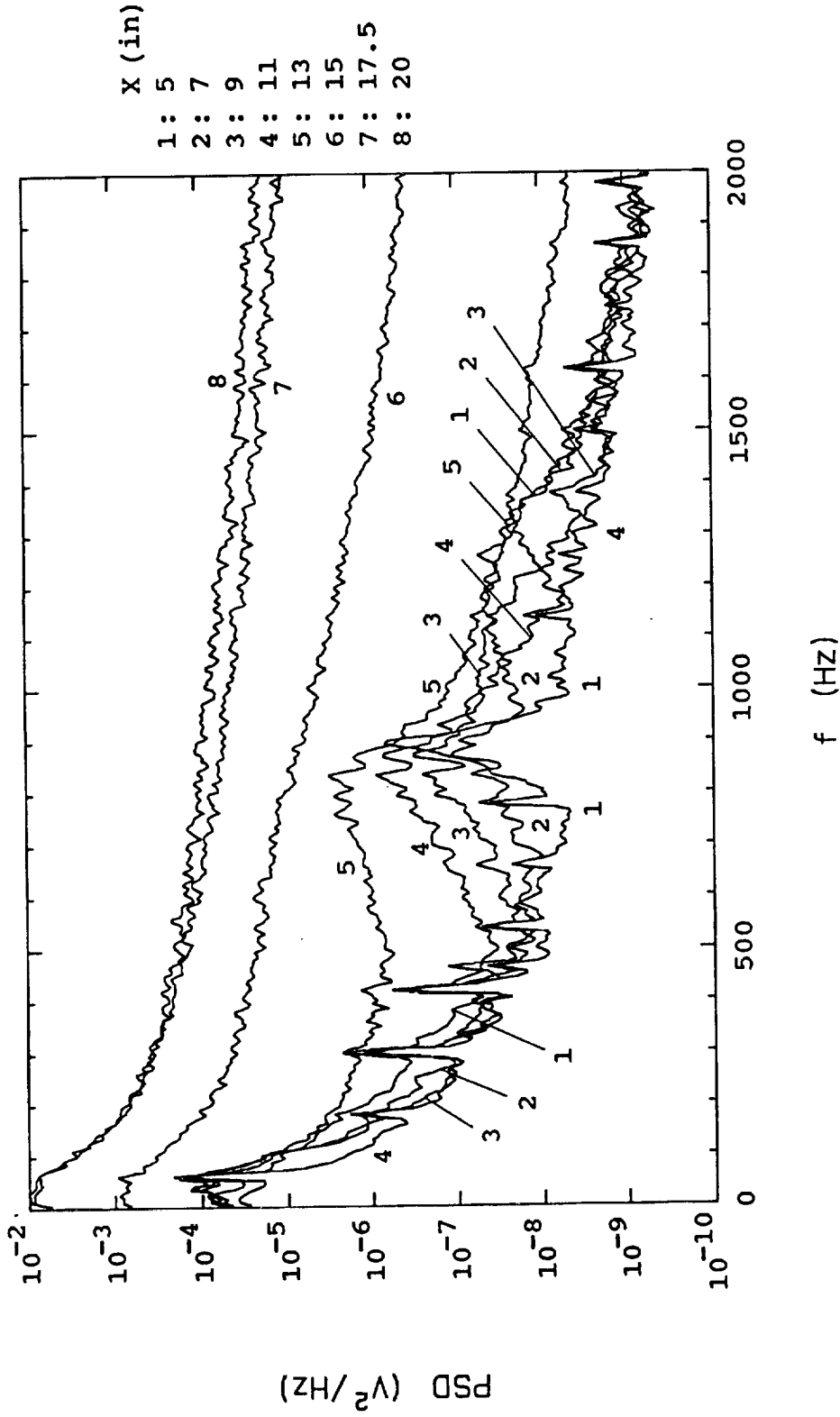


Fig. 52(a) Boundary layer spectra obtained at near-wall locations ( $Y_0$ ) for grid 0

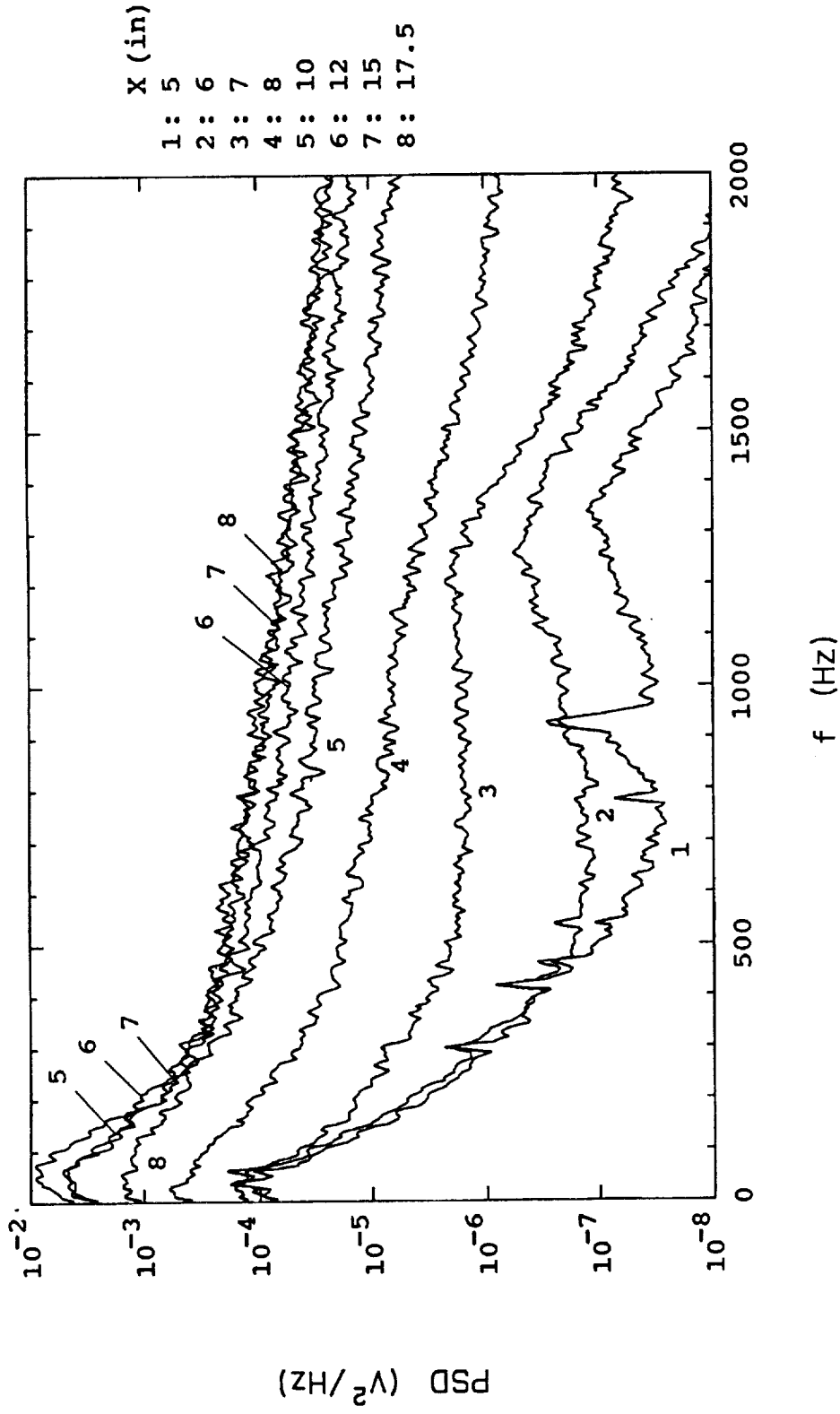


Fig. 52(b) Boundary layer spectra obtained at near-wall locations ( $Y_0$ ) for grid .5

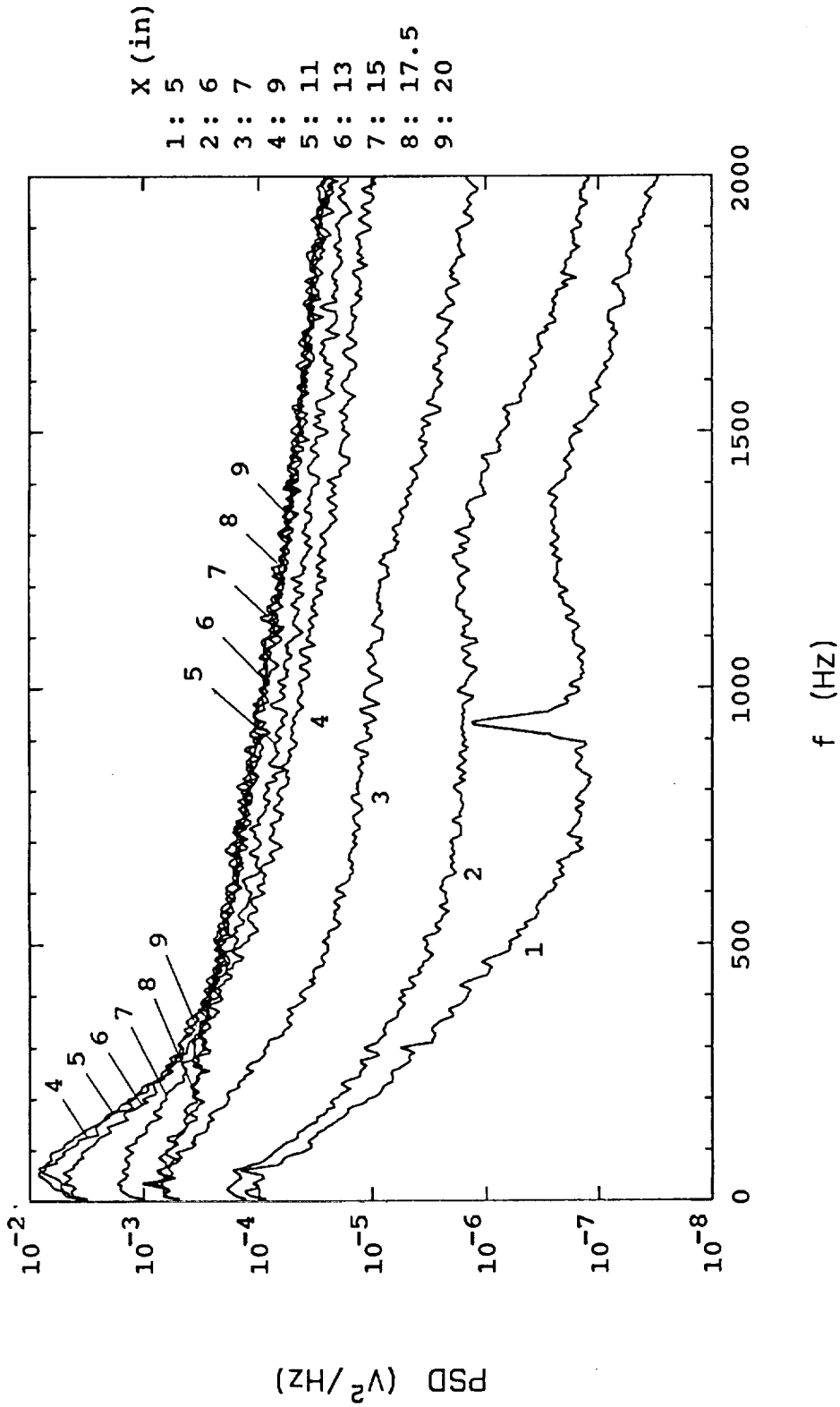


Fig. 52(c) Boundary layer spectra obtained at near-wall locations ( $Y_0$ ) for grid 1

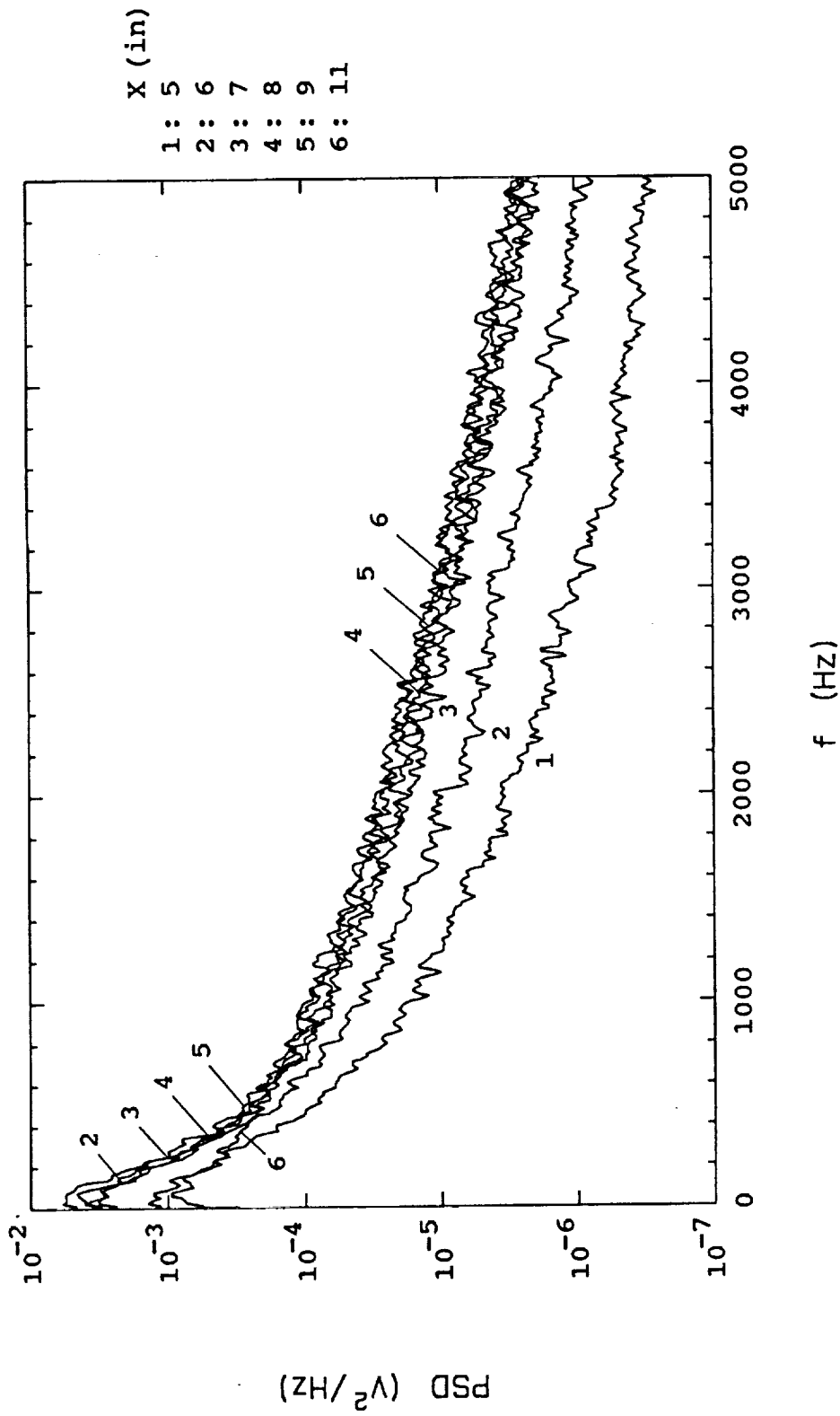


Fig. 52(d) Boundary layer spectra obtained at near-wall locations ( $Y_0$ ) for grid 2

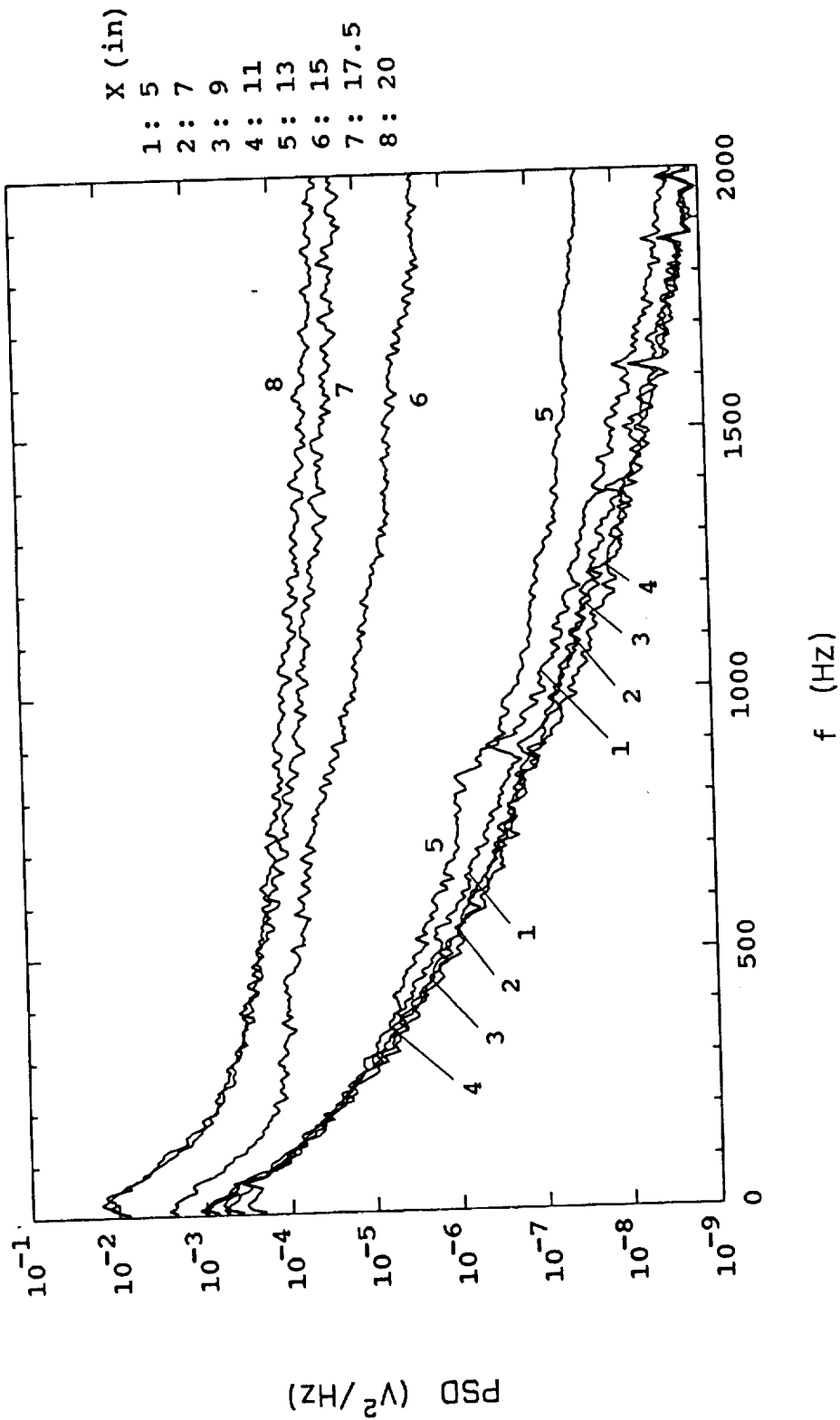


Fig. 53(a) Boundary layer spectra measured at locations where rms velocity reached maximum for grid 0

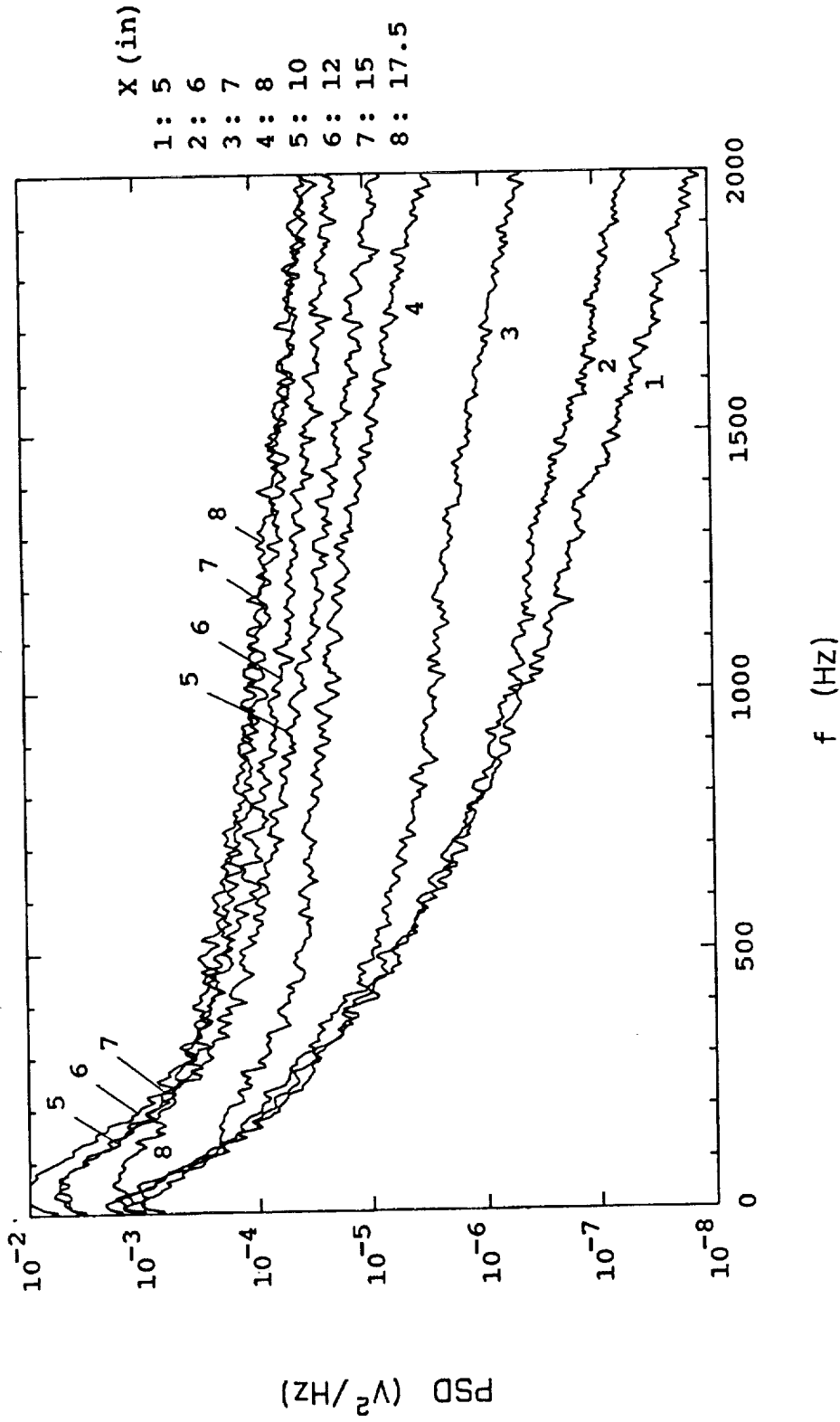


Fig. 53(b) Boundary layer spectra measured at locations where rms velocity reached maximum for grid .5

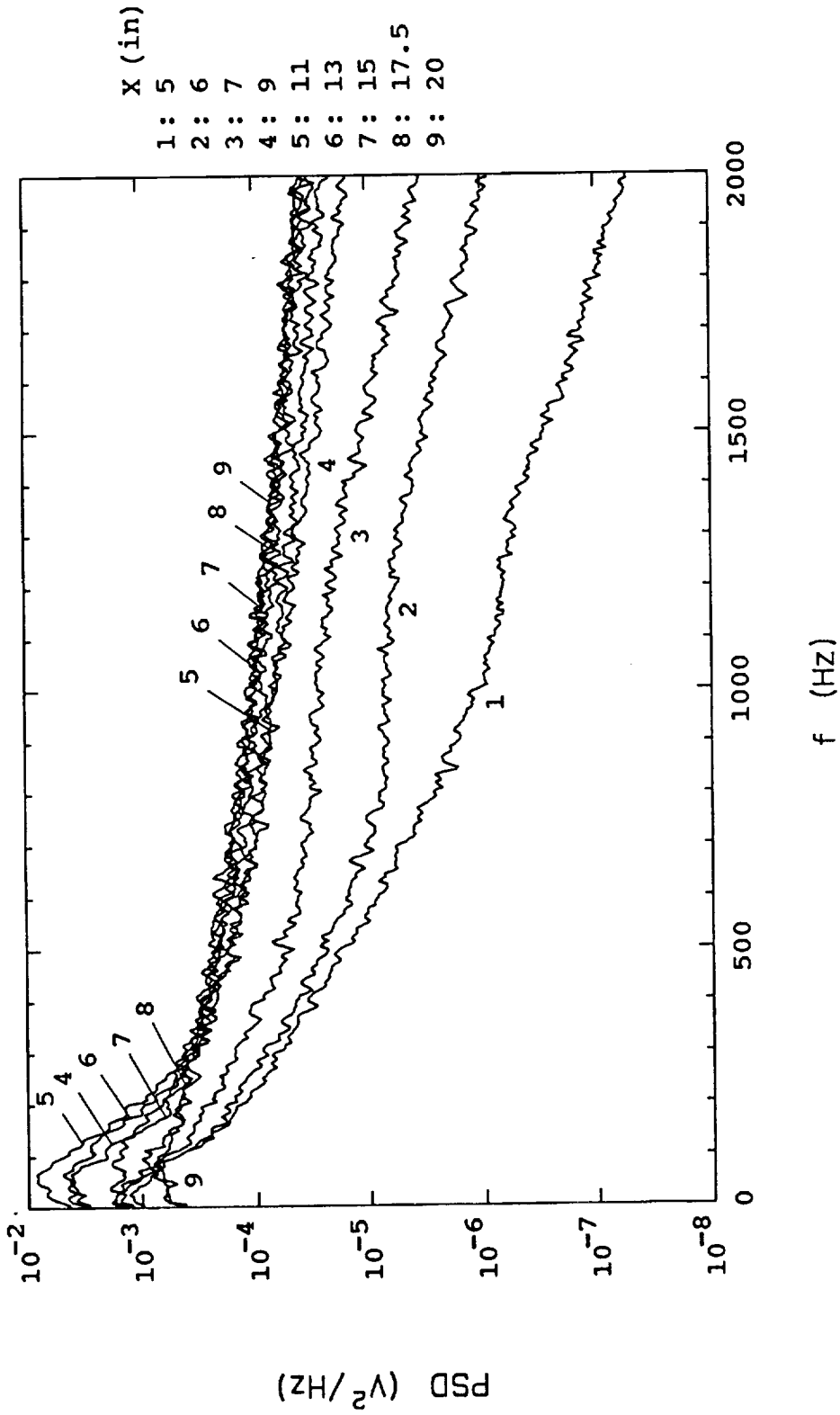


Fig. 53(c) Boundary layer spectra measured at locations where rms velocity reached maximum for grid 1

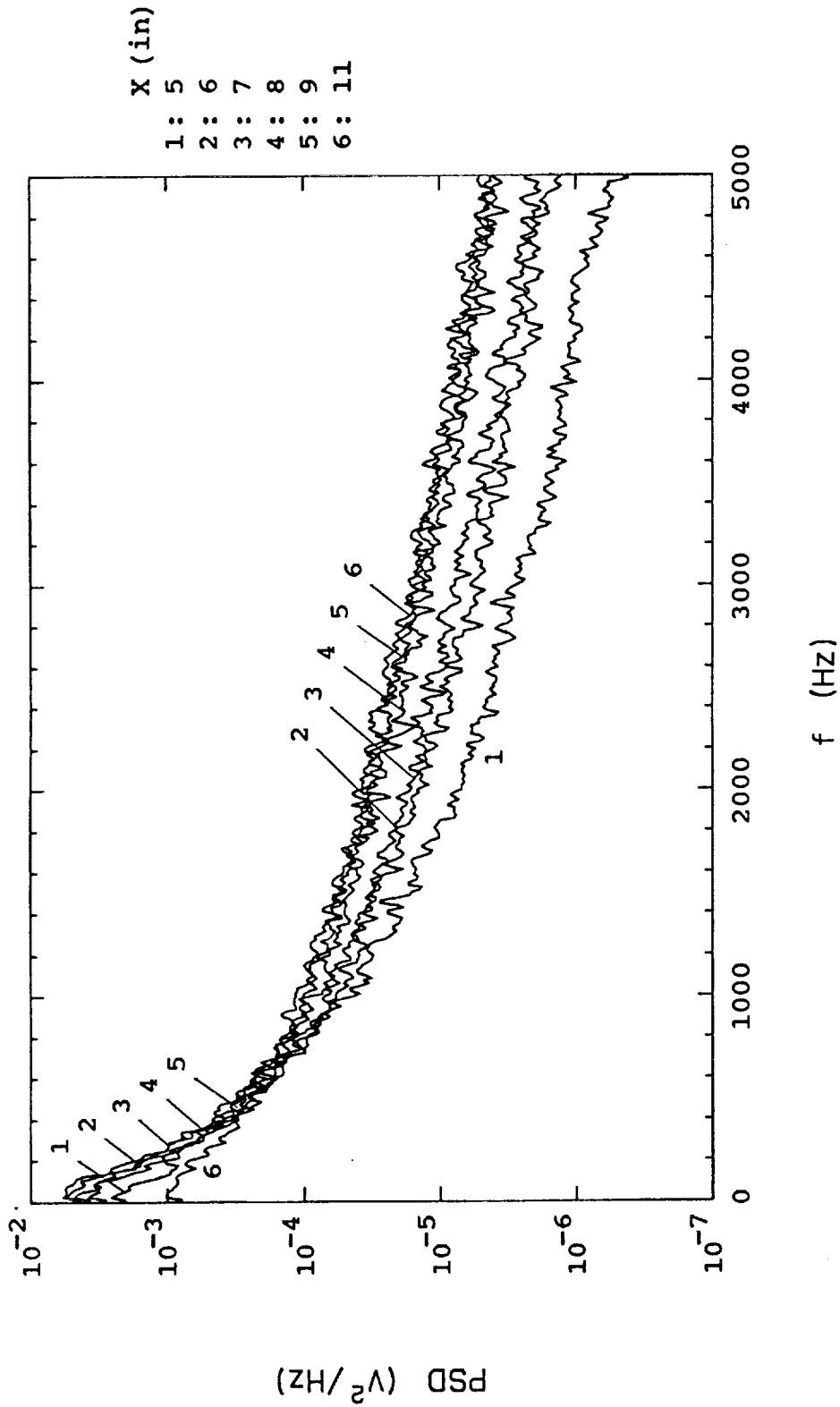


Fig. 53(d) Boundary layer spectra measured at locations where rms velocity reached maximum for grid 2

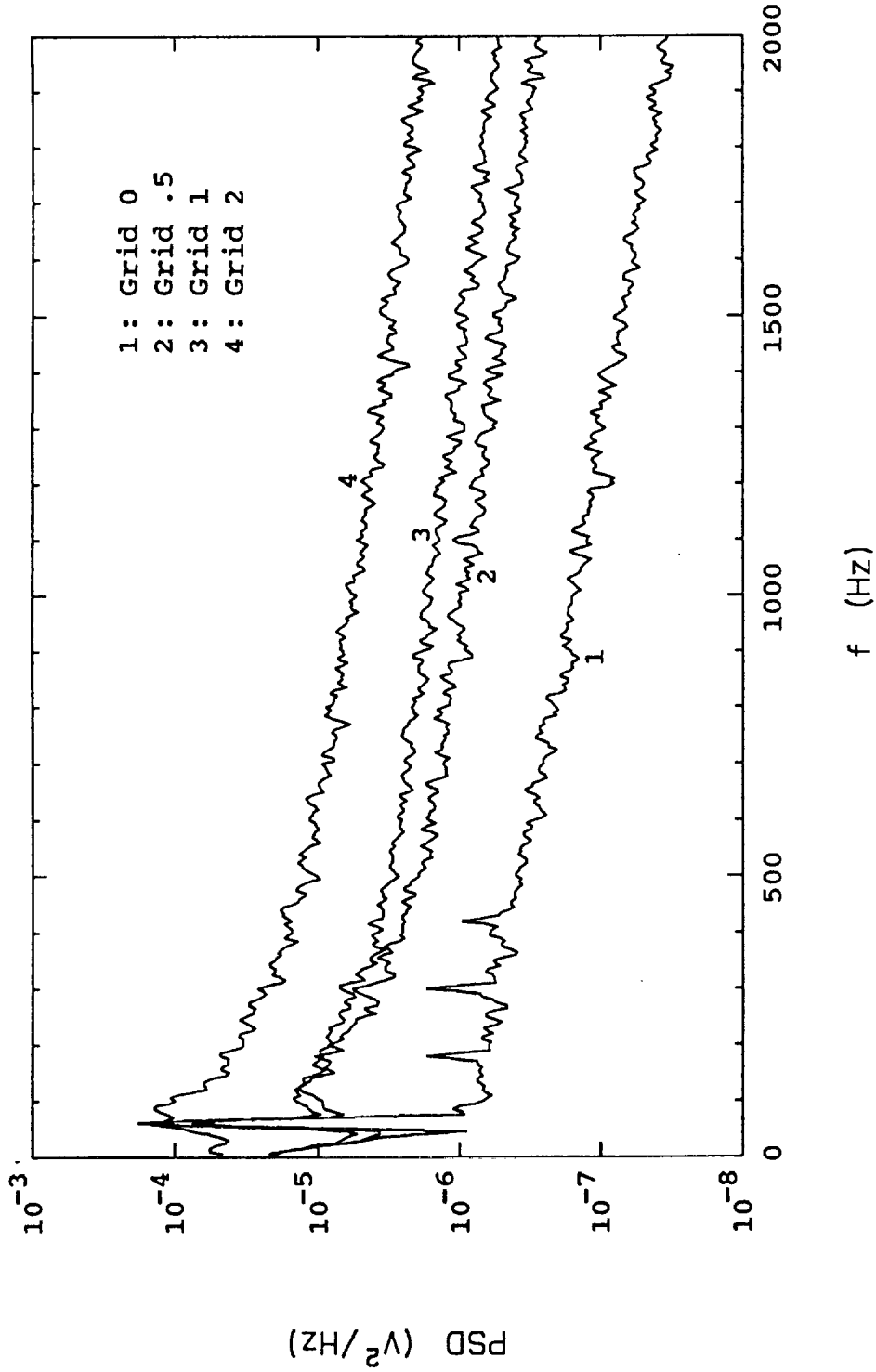


Fig. 54 Freestream spectra for 4 grids

1. Report No. NASA CR-187068		2. Government Accession No.		3. Recipient's Catalog No.	
4. Title and Subtitle Experimental Study of Boundary Layer Transition With Elevated Freestream Turbulence on a Heated Flat Plate				5. Report Date February 1991	
				6. Performing Organization Code	
7. Author(s) Ki-Hyeon Sohn and Eli Reshotko				8. Performing Organization Report No. None	
				10. Work Unit No. 505-62-52	
9. Performing Organization Name and Address Case Western Reserve University Department of Mechanical and Aerospace Engineering Cleveland, Ohio 44106				11. Contract or Grant No. NAG3-230	
				13. Type of Report and Period Covered Contractor Report Final	
12. Sponsoring Agency Name and Address National Aeronautics and Space Administration Lewis Research Center Cleveland, Ohio 44135-3191				14. Sponsoring Agency Code	
15. Supplementary Notes Project Manager, Frederick F. Simon, Internal Fluid Mechanics Division, NASA Lewis Research Center.					
16. Abstract A detailed investigation to document momentum and thermal development of boundary layers undergoing natural transition on a heated flat plate was performed. Experimental results of both overall and conditionally sampled characteristics of laminar, transitional and low Reynolds number turbulent boundary layers are presented. Measurements were acquired in a low-speed, closed-loop wind tunnel with a freestream velocity of 100 ft/s and zero pressure gradient over a range of freestream turbulence intensities (TI) from 0.4% to 6%. The distributions of skin friction, heat transfer rate and Reynolds shear stress were all consistent with previously published data. Reynolds analogy factors for $Re_\theta < 2300$ were found to be well predicted by laminar and turbulent correlations which accounted for an unheated starting length. The measured laminar value of Reynolds analogy factor was as much as 53% higher than $Pr^{-2/3}$ . A small dependence of turbulent results on TI was observed. Conditional sampling performed in the transitional boundary layer indicated the existence of a near-wall drop in intermittency, pronounced at certain low intermittencies, which is consistent with the cross-sectional shape of turbulent spots observed by others. Non-turbulent intervals were observed to possess large magnitudes of near-wall unsteadiness and turbulent intervals had peak values as much as 50% higher than were measured at fully turbulent stations. Non-turbulent and turbulent profiles in transitional boundary layers cannot be simply treated as Blasius and fully turbulent profiles, respectively. The boundary layer spectra indicate predicted selective amplification of T-S waves for $TI \approx 0.4\%$ . However, for $TI \approx 0.8\%$ and $1.1\%$ , T-S waves are localized very near the wall and do not play a dominant role in the transition process.					
17. Key Words (Suggested by Author(s)) By-pass transition Heat transfer Flat plate			18. Distribution Statement Unclassified - Unlimited Subject Category 34		
19. Security Classif. (of this report) Unclassified		20. Security Classif. (of this page) Unclassified		21. No. of pages 265	22. Price* A12